ENGINEERING ECONOMICAL MEMBRANE MATERIALS FOR

AGGRESSIVE SOUR GAS SEPARATIONS

A Dissertation
Presented to
The Academic Faculty

by

Carine Saha Kuete Achoundong

In Partial Fulfillment
of the Requirements for the Degree
Doctor of Philosophy in the
School of Chemical and Biomolecular Engineering

Georgia Institute of Technology
December 2013

ENGINEERING ECONOMICAL MEMBRANE MATERIALS FOR

AGGRESSIVE SOUR GAS SEPARATIONS

Approved by:

Dr. William Koros, Advisor
School of Chemical and Biomolecular
Engineering
Georgia Institute of Technology

Dr. Karl Jacob
School of Materials Science and
Engineering
Georgia Institute of Technology

Dr. Carson Meredith
School of Chemical and Biomolecular
Engineering
Georgia Institute of Technology

Dr. Sankar Nair
School of Chemical and Biomolecular
Engineering
Georgia Institute of Technology

Dr. Krista Walton
School of Chemical and Biomolecular
Engineering
Georgia Institute of Technology

Date Approved: August 27th, 2013

This dissertation is dedicated to my better half,
my husband Frank Achoundong

To my loving parents,
Mr. Martin Kuete and Mrs. Christine Kuete

And to my brothers and sisters particularly,
Mr. Kuete Eric and Mr. Kuete Yves

Without their loving support,
I definitely would not have been where I am today.

ACKNOWLEDGEMENTS

First and foremost, I would like to thank God for inspiring me to do this work, for putting the right people along my way to support me and for giving me the strength to overcome all the challenges I have encountered in the past four years of my life; I am beyond grateful.

Second, I would also like to thank my advisor Dr. William Koros for giving me the opportunity to work on something so great, for believing and trusting in my abilities, for getting the best out of me, and for being patient with me, especially during the first two years of my research. I am so grateful to have selected him as an advisor because he is such an outstanding researcher and mentor. Working under Dr. Koros' supervision has taught me the value of the quality of research results, but also how to be a resourceful and an efficient researcher. Therefore, I can never thank him enough for giving me such an opportunity.

Special thanks to all my committee members, Dr. Sankar Nair, Dr. Carson Meredith, Dr. Karl Jacob, Dr. Krista Walton. I am grateful for your constructive feedback, your valuable inputs, and your willingness to review and make suggestions on my work.

A good family support is important to surviving a rigorous graduate school program at Georgia Tech. I have been fortunate to be one of the children of the Kuete family as my parents have sacrificed their lives for myself and my other siblings. I would not have made it this far without their emotional, moral and financial supports. I hope

that I can live up to your expectations and that I have made you proud. I could never imagine having any other parents than you.

Frank Achoundong, the loving husband that God has generously given me, has been my rock and my biggest supporter from day one. He's been patient, a great listener, and has been very supportive when I had to work late at night or on weekends. He has given me the outmost confidence in myself when I needed it. He knows how to get the best out of me by challenging me to go beyond my potential; he makes me a better person, a better researcher, and I would not have been here without him. Thank you for not allowing me to give up when things got rough.

To my brother Eric Tafopa Kuete who took care of me when I first moved into the US. He gave me the foundation and challenged me when I got my Bachelors to reach even higher. I kept that speech he's given at my graduation dinner in mind. I hope that I have now gone as far as he would have wanted me. To my brother Yves Wamba Kuete, the one whom has inspired me to join Georgia Tech, and the only family member who actually understands my scientific life; I would like to thank you for always trusting and believing in me and making learning such an exciting experience. I would also like to thank all my family and friends, particularly my younger brother Nelson Kuete, my sisters Liliane Kuete and Christelle Kuete, my brother Desire Kuete, my aunt Suzanne Kuemo, Bruno Njiensi, my friends Ingrid Yamndzi and Raffaella Belinga, and my aunt-in-law and her husband Mr. and Mrs. Djiatsa for their emotional support during difficult times.

It is unusual to have parents-in-law like the ones I have. I am grateful to Dr. Gaston Achoundong and Mrs. Fauste Achoundong for taking such great interest in my

studies, for being so supportive during these years. I could not have wished for better in-laws. I would also like to mention my brothers and sister-in law who were also very supportive.

I would also like to express my gratitude to my long list of friends at Georgia Tech, with whom I have formed such a lifelong bond during my years of graduate school. You have made my experience at GT much more exciting than I could ever imagine. Nitesh Bhuwania, I would like to thank you for being such an amazing friend and colleague. Having you the office for the last two years, has made my life so much better. I would like to thank you for the discussions and contributions you've made to my work. I will miss going out for coffee with you. Jose Baltazar, Christine Flemming, Andac Armutlulu, Dr. Wilmarie Medina-Ramos, Deepraj Ghosh, Dr. Sandeep Mora, I don't know where to begin to let you know much I appreciate your friendship. Without you guys, I don't know what my life at GT would have been. We have gone through the qualifiers and proposal together, we've celebrated so many birthdays and weddings, and we have had so many lunches and dinners. I will miss all of it. Jose and Andac thank you for helping me with my XPS measurements. I would like to thank Christine Flemming for always organizing and keeping us in check at all times and for sharing lab equipment with me. Deepraj, thank you for always finding all the resources we needed and Wilmarie, thank you for all the great tips you gave me for thesis formatting. I would also like to thank Dr. Omoyemen Esekhile for being so supportive during my first years of grad school, showing me the ropes, for being an amazing friend, and for making my transition in the Koros group a bit smoother.

Finally, I would also like to thank all the Koros group members in particular Dr. Oguz Karvan and Dr. JR Johnson for building our H_2S facility. Thank you for all the troubleshooting you've done for us and for all the great technical discussions. I would like to thank my H_2S fellows, Dr. Justin Vaughn and Brian Kraftschik who were always willing to help, to share equipment, and to have many work related discussions. I appreciate having you guys as H_2S partners. I would also like to thank Shweta Karwa for allowing me to use her equipment to help me wrap-up experiments. I would also like to mention Steven Burgess for his willingness to sacrifice his own work to help me with DMA measurements and Dr. Canghai Ma for not only allowing me to use his permeation system during the later years of my PhD but also for a few measurements he has made for me. I would also like to mention Dr. Josh Thompson for synthesizing DDR sieves for me during my first years and Dr. Ryan Lively for helping me proofread my proposal and paper. I would like to thank Michelle Harden for placing orders on our behalf, especially those rush orders and for all the other great things she does behind the scene that goes unnoticed. I would also like to thank Dr. Mita Das and Dr. Olanrewaju who strongly encouraged me to join this research group.

TABLE OF CONTENTS

LIST OF TABLES

LIST OF FIGURES

SUMMARY

Natural gas is one of the cleanest and most useful of all energy sources, with consumption expected to grow by 39% from 2010 to 2035. Over 30% of natural gas wells in the United States contain impurities requiring removal before distribution. Such impurities not only reduce the quality of this important resource, but they also corrode pipelines. Among these impurities, hydrogen sulfide (H_2S) and carbon dioxide (CO_2), known as "acid gases", are the most important. Roughly 25% of proven resources contain unacceptable concentrations of either CO_2 or both CO_2 and H_2S. Hydrogen sulfide presents an even greater challenge than CO_2 because of its highly toxic nature so its specification level is lower than that of carbon dioxide. Typical pipeline specifications in the US require that natural gas be purified below 4 ppm and below 2% for H_2S and CO_2, respectively. Current technologies for removing such impurities are successful but energy intensive. Membrane processes could supplement or replace the current technologies. Membranes provide higher energy efficiency, ease of process scale-up, great operational flexibility, and environmental safety; however, limitations that include higher losses of the primary component CH_4 must be tackled. Only a few studies have considered simultaneous removal of CO_2 and H_2S using membranes; moreover, due to the hazardous nature of H_2S, prior studies have generally focused on low concentrations of H_2S. However, well-head pressures can be as high as 1000 psia with H_2S concentrations exceeding 5%. Realistic high concentrations and pressures of acid gases may contribute to excess loss of the key component methane (CH_4) due to membrane separation impairment.

The goal is of this project was to identify principles to guide the development of high performance dense film membranes for natural gas sweetening using hydrogen sulfide and carbon dioxide gas mixtures as models under aggressive sour gas feed conditions. To achieve this goal, three objectives were developed to guide this research. The first objective was to study the performance of cellulose acetate (CA) and an advanced crosslinkable polyimide (PDMC) dense film membrane for H_2S separation from natural gas. The second objective was to engineer those polymers to produce membrane materials with superior performance as measured by efficiency, productivity, and plasticization resistance, and the third objective was to determine the separation performance of these engineered membrane materials under more aggressive, realistic natural gas feeds, and to perform a detailed transport analysis of the factors that impact their performance.

Work on the first objective showed that in neat CA, penetrant transport is controlled by both the solubility and mobility selectivity, with the former being more dominant, leading to a high overall CO_2/CH_4 (33) and H_2S/CH_4 (35) ideal selectivities. However, in uncrosslinked PDMC, H_2S/CH_4 selectivity favored sorption only, whereas CO_2/CH_4 selectivity favored both mobility and sorption selectivity, leading to a high CO_2/CH_4 (37) but low H_2S/CH_4 (12) ideal selectivities. However, the latter polymer showed more plasticization resistance for CO_2.

In the second objective, both materials were engineered. A new technique referred to as "*GCV-Modification*" was introduced in which cellulose acetate was grafted using vinyltrimethoxysilane (VTMS), then hydrolyzed and condensed to form a polymer network. PDMC was also covalently crosslinked to enhance its performance. GCV-

Modified CA showed significant performance improvements for H_2S and CO_2 removal; the permeability of CO_2 and H_2S were found to be 139 and 165 Barrer, respectively, which represented a 30X and 34X increase compared to the pristine CA polymer. The H_2S/CH_4 and CO_2/CH_4 ideal selectivities were found to be 39 and 33, respectively. Crosslinked PDMC showed a higher CO_2/CH_4 selectivity of 38 with a better plasticization resistance for CO_2 and H_2S.

In the third objective, these materials were tested under aggressive ternary mixtures of $H_2S/CO_2/CH_4$ with both vacuum and nonvacuum downstream. Even under aggressive feed conditions, GCV-Modified CA showed better performance vs. PDMC, and it remained were fairly stable, making it a potential candidate for aggressive sour gas separations, not only because of its significantly higher productivity, which will help decrease the surface area needed for separation, thereby reducing operating costs, but also because of the lower cost of the raw material GCV-Modified CA compared to PDMC.

CHAPTER 1: INTRODUCTION AND MOTIVATION

1.1 Natural Gas Processing

World natural gas consumption is projected to increase from 111 trillion cubic feet in 2008 to 169 trillion cubic feet in 2035, which represents more than a 50% increase as shown in Figure 1.1 [1]. Natural gas remains the fuel of choice for many regions of the world in the electric power and industrial sectors, despite the global recession of 2009 [1]. One of the reasons for this trend is its relatively low carbon footprint compared to other fossil fuels, which makes it an attractive option for nations interested in reducing greenhouse gas emissions. These advantages make natural gas one of the cleanest, safest, and most efficient energy sources [2, 3].
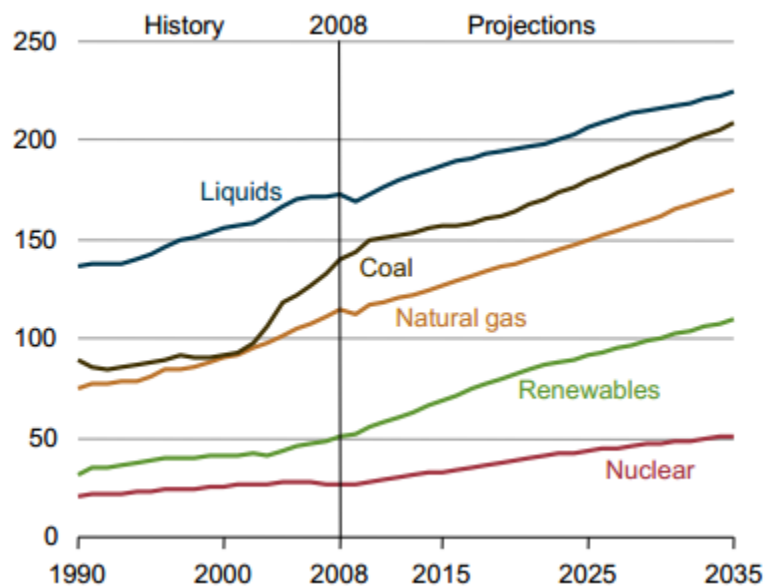
Figure 1.1: Projected world energy consumption by fuel, 1990-2035 (quadrillion Btu) [1]. Methane is the primary component in natural gas, accounting for 30-90% of the total [4].

Raw natural gas composition varies substantially from one source to another [5]. Although the composition of the raw gas varies widely, the composition of the gas delivered to the pipeline and to end-users is tightly regulated. Therefore, before its distribution to consumers or delivery to pipelines, natural gas must be treated to remove impurities. Over 30% of the gas produced and over 40% of proven raw natural gas reserves are subquality, due to the presence of significant amounts of impurities such as hydrogen sulfide (H_2S), carbon dioxide (CO_2), water (H_2O), and nitrogen (N_2) [6, 7]. These impurities, especially CO_2 and H_2S not only increase compression costs or reduce the heating value of the gas, but they are also corrosive to gathering and transmission lines, compressors, pneumatic instruments, and distribution equipment. Special alloy pipes will therefore be required for transport unless these acid gases are removed, significantly increasing costs in remote applications where current purification methods at the well head may not be feasible. This required treatment makes natural gas processing the largest market for industrial gas separation processes and equipment [5]. Recently, H_2S removal has received more attention, because in certain areas in the US, Canada, the Middle East, and the Far East, oil and gas reservoirs contain high levels of H_2S as well as CO_2 at varying levels. Typical pipeline specifications in the US (Table 1.1) require that natural gas be purified below 4 ppm and below 2 mol% for H_2S and CO_2, respectively [5]. Therefore, it is imperative to find a purification technology that will not only be economically feasible and energy efficient, but also sustainable and environmentally sound, with ability for widespread use.

Table 1.1: Natural gas composition specifications for delivery to US pipelines [4, 5, 7]

Component	Specification (US)
Carbon Dioxide	<2%
Hydrogen Sulfide	<4 ppm
Water	<120 ppm
Inert Gases (He, N_2)	<4%
C_{3+} Content	950-1050 Btu/scf; Dew Point <-20°C

1.2 Current Sweetening Techniques

Natural gas is usually considered "sour" if the hydrogen sulfide content exceeds 5.7 milligrams of H_2S per cubic meter of natural gas (~4 ppm). The process for removing hydrogen sulfide from sour gas is commonly referred to as "sweetening" the gas. The terms "acid gas" and "sour gas" are often used interchangeably; but in reality, a sour gas is any gas that contains hydrogen sulfide in considerable amounts, whereas an acid gas is any gas that contains significant amounts of acid gases such as carbon dioxide or hydrogen sulfide. Thus, carbon dioxide by itself is an acid gas but it is not a sour gas. The removal of "acid gases" is conventionally achieved by absorption of these gases in solvents like monoethanolamine (MEA), diethanolamine (DEA), diisopropanolamine (DIPA), diglycolamine (DGA), or methyldiethanolamine (MDEA). The process is known as the "amine" or the Girdler process [8]. The gas is run through a contactor, which contains the amine solution, and due to the solution affinity for acid gases, it absorbs CO_2 and H_2S preferentially over CH_4. A typical amine process is depicted in Figure 1.2.
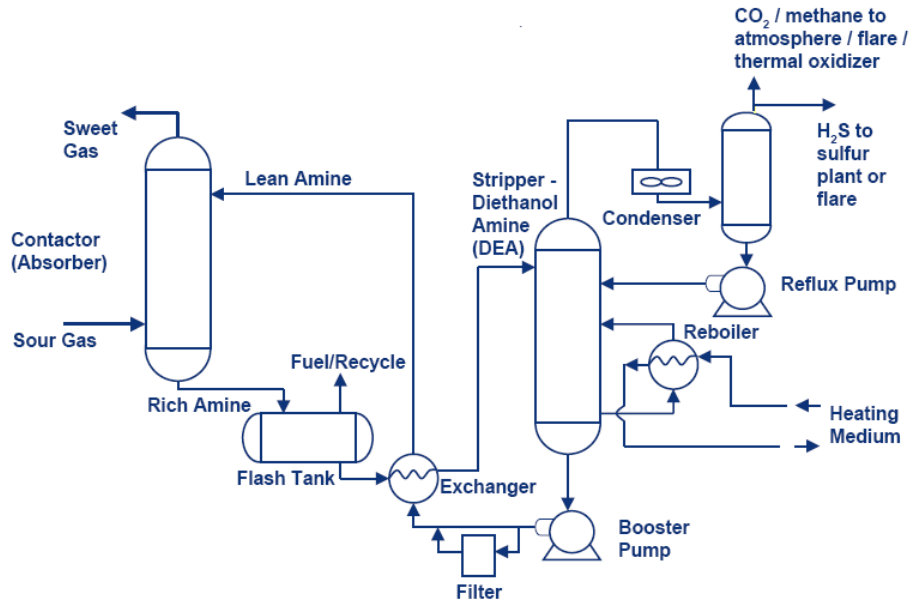
Figure 1.2: Typical amine absorption process for acid gas removal.

When the amine solution is saturated, the acid gases are flashed off as the solution is thermally regenerated. Most plants handling large volumes of sour gas containing greater than about 200 ppm hydrogen sulfide use this amine-based technology for acid gas removal [9]. For low-volume streams containing less than 100 ppm of hydrogen sulfide, scavenging or sulfur recovery processes like Sulfa-Scrub, Sulfa-Check, Chemsweet, Suertron 600, solid iron sponge or solid zinc oxide are used as an alternative or as a polishing step following any process [9-14]. In these techniques, H₂S is adsorbed on a solid compound and the adsorbed gas is converted to a less harmful waste product. However, many scavengers present substantial disposal problems - in some states, the spent scavenger constitutes toxic waste. Even though amine absorption is one of the most widely used techniques for treating natural gas, it has drawbacks [15]. In addition to high energy costs associated with thermal regeneration, the mechanical equipment (heaters, aerial coolers, pumps, etc.) in an amine plant require frequent quality checks and

4

maintenance, making operational reliability one of the weakest features of the costly technology.

1.3 Membranes for Gas Separations

While absorption processes are the main treatment technique for the removal of acidic gases from natural gases, polymeric membranes have gained acceptance during the past few decades [16]. Baker summarized the development of membrane gas separation technology in Figure 1.3 [17]. One of the first large industrial applications of gas separation membranes was launched in the 1980s by Permea (now a division of Air Products). Since then, membrane-based gas separation has grown into a $150 million per year business, and substantial growth in the future is likely [17]. Membrane separation processes offer many advantages that potentially include high energy efficiency, ability to be assembled into high surface area modules, small footprint, and a great operational flexibility for handling feeds streams of different compositions or flow rates in remote locations. In addition, membrane processes are environmentally safe and can typically operate at ambient temperature, which prevents energy losses related to heat exchange [15]. Polymeric membranes have already experienced success in a number of industrially relevant gas separations including nitrogen from air (blanketing or packaging of food, aircraft fuel tank blanketing, and underbalanced drilling), hydrogen recovery from ammonia, and natural gas purification [5]. However, a much larger potential market for membrane gas separation lies in separating mixtures containing condensable gases [17]. Commercial applications of gas separations using membranes are summarized in Table 1.2.
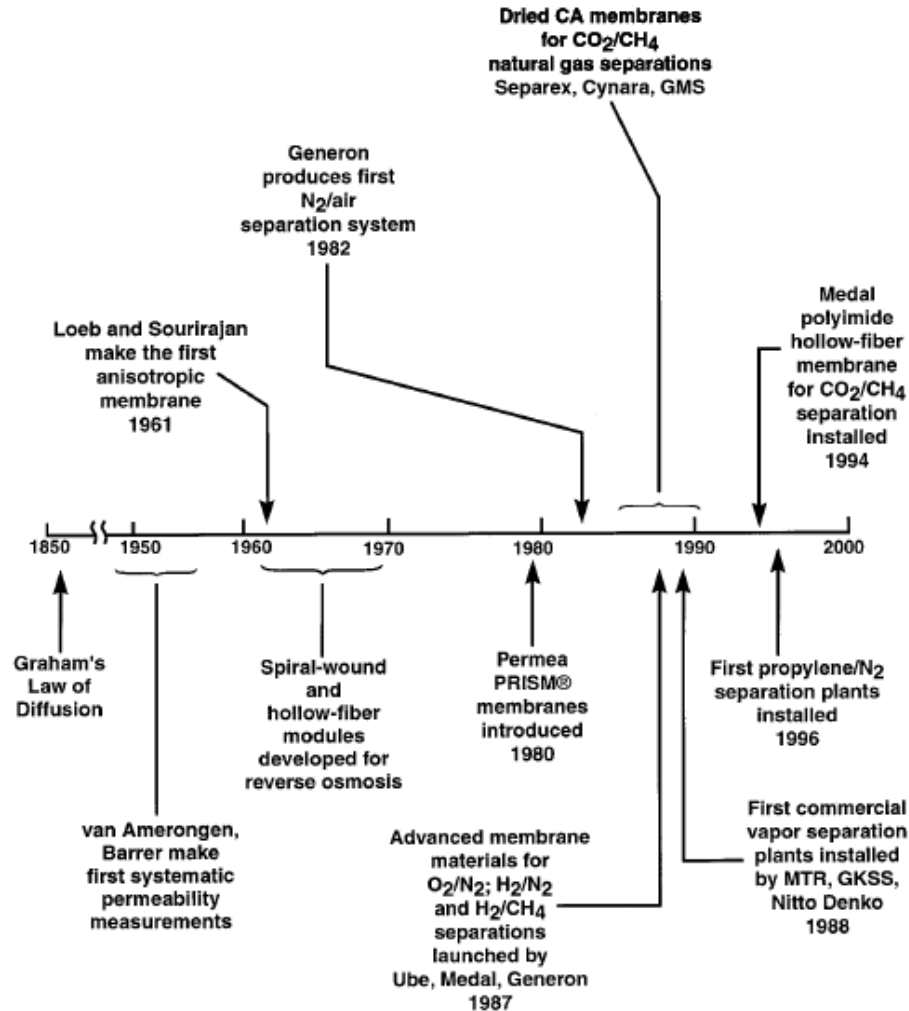
Figure 1.3: Evolution of membrane-based gas separation technologies [17].

Table 1.2: Current commercial applications of membrane-based gas separations [18, 19]

Common Gas Separations	Application
O_2/ N_2	N_2 enriched air, oxygen enrichment
H_2/Hydrocarbons	Refinery hydrogen recovery
H_2/ N_2	Ammonia purge gas
H_2/CO	Syngas ratio adjustment
CO_2/Hydrocarbons	Acid gas removal, landfill gas upgrading
H_2S /Hydrocarbons	Sour gas sweetening
H_2O /Air	Air dehumidification
H_2O /Hydrocarbons	Natural gas dehydration
He/Hydrocarbons	Helium separations
He/N_2	Helium recovery
Hydrocarbons/Air	Pollution control, hydrocarbon recovery

To become a dominant force, membrane technology requires the development of membrane materials with the following ideal characteristics [19-22]:

- ❖ High flux (high permeability, thin selective layer)

- ❖ High separation efficiency (high selectivity)

- ❖ High tolerance or durability to all feed components and process conditions

- ❖ Long-term mechanical stability

- ❖ Ability to be packaged in high surface area modules

- ❖ Excellent manufacturing reproducibility

- ❖ Low cost

Among all those criteria, high permeability (productivity) and selectivity (separation efficiency) are the first requirements that must be met to even be a contender. Research indicates that most membranes lose their selectivity and sometimes even their productivity in the presence of highly condensable, plasticizing gases such as H_2S and CO_2. This phenomenon will be explained in more details in the next chapter. To illustrate the productivity/efficiency criteria, Robeson pointed out that for a membrane material to be industrially competitive it must be within or near the commercially attractive region of the upper-bound [23, 24] curve. While CO_2 and H_2S removal from sour gas is the primary focus of this work, only the CO_2/CH_4 upper-bound is shown in Figure 1.4 since an accepted H_2S/CH_4 upper-bound line does not exist yet due to the limited amount of data available in literature.
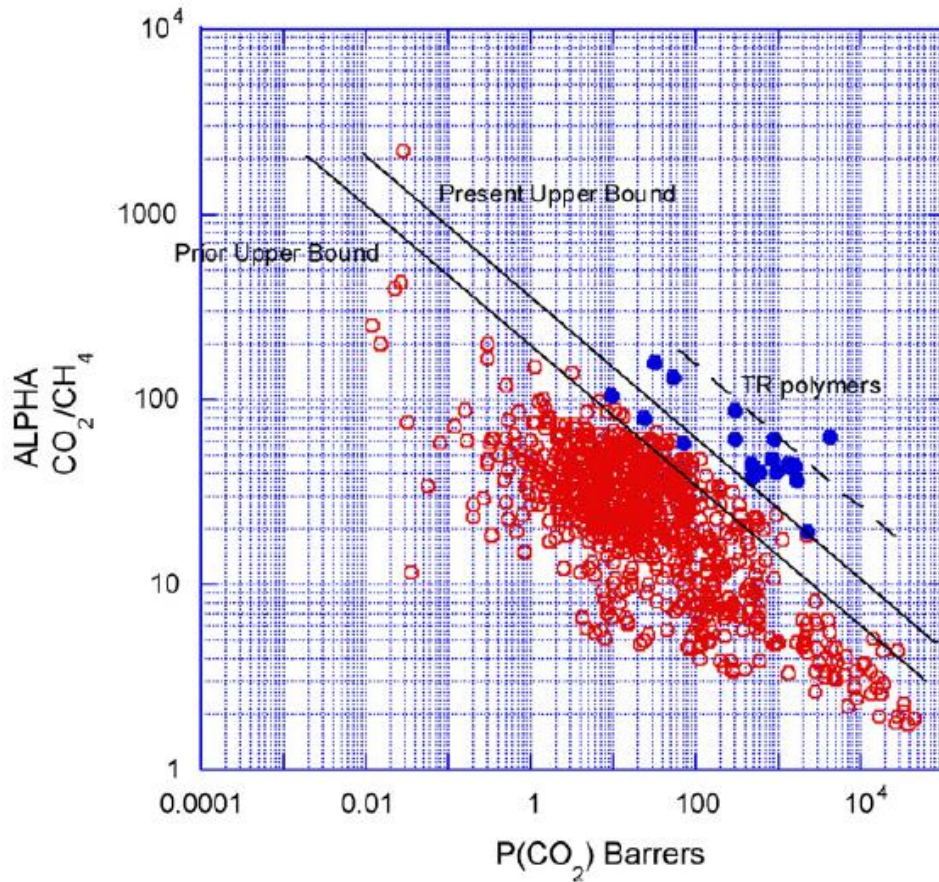
Figure 1.4: Robeson upper-bound tradeoff for CO_2/CH_4 separation [23].

Industrial applications of membrane for gas separations can be grouped into two categories [25]:

1. ***Separations using polymers that are more permeable to smaller penetrants in a gas mixture.*** The most feasible polymers used for CO_2/CH_4 application include stiff, glassy polymers with moderately high free volume with the ability to separate penetrant molecules based on their size. Commercially, the most widely practiced gas separations in this category include CO_2 removal from acid gas, air separation (O_2/N_2), and hydrogen recovery [17, 26]. Typical polymers used for these separations are cellulose acetate, polysulfone, aromatic polyimides,

aromatic polyamides, polycarbonates, polyphenylene oxide, and perfluoropolymers [4, 17, 27].

2. ***Separations requiring polymers that are more permeable to larger penetrants.*** The most feasible polymers used in this category are highly flexible, rubbery polymers or some ultra high free volume, glassy substituted polyacetylenes [25]. These polymers separate penetrant molecules based on their solubility rather than their size. Typical industrial applications for these materials include the removal of organic vapors from mixtures [25, 26] with light gases and the removal of H_2S from sour gas. Hydrogen sulfide can also be separated by glassy polymers but rubbery polymers proved to be the most feasible (solubility selectivity is maximized) [5]. One of the most common polymers used for these sorption selective separations is polydimethylsiloxane (PDMS), since it offers high diffusion coefficients [4].

1.3.1 Membranes for Acid Gas Removal

As noted above, one of the most common applications for membrane-based gas separation is the removal of acid gases, CO_2 and H_2S from natural gas. Almost 20% of natural gas wells in the US require acid gas treatment [5], and this is likely to grow if the low quality reserves become economically feasible [4, 19]. Typical CO_2 concentrations are in the range of 5% to 70% [4]. Membranes that are commercially available for CO_2/CH_4 separation include cellulose acetate, polyimides, and perfluoropolymers [4, 20]. For sour gas treatment, polyether block amide (PEBAX®), poly (ether urethane urea), poly (ether urethane) membranes, among others have been considered [28, 29]. Some of the challenges of these materials include plasticization of the polymer matrix which leads

to decreased separation performance if swelling is extreme. Cellulose acetate has been used commercially since the mid-to-late 1980s as shown in Figure 1.3. These materials were attractive mainly due to their low cost and versatility. They usually consist of a mixture of cellulose acetate, cellulose diacetate, and/or cellulose triacetate, depending on the degree of acetylation, and they make up 80% of the market for membranes in natural gas processing [4]; this makes them the industry standard for these separations. Some suppliers of cellulose acetate membranes include Cynara® (asymmetric hollow fiber modules), UOP Separex® (spiral wound modules), and W.R Grace (spiral wound modules) [5]. Even though these membranes dominate the market, they have major drawbacks that threaten their position, as new polymers with higher potential performance are becoming available. One of the most important problems cellulose acetate membranes face is their susceptibility to be plasticized either by CO_2 or some other highly condensable penetrant. Many researchers have reported various ways to stabilize these membranes against plasticization and improve separation performance [30, 31]. Polyimides have received considerable attention due to their good thermal and mechanical stability coupled with their high permeability for CO_2 and high CO_2/CH_4 selectivity. These materials are also easily assembled into hollow fibers membranes, making them very attractive as an alternative to cellulose acetate. In fact Baker [17] simulated an acid gas separation process with a polyimide as a substitute from cellulose acetate and he found an area reduction of ~40% and a recycle compressor duty reduction of ~35%, with a methane loss in the permeate reduction of 75%. However, these materials are more expensive than conventional cellulose acetate membranes, and are also susceptible to plasticization; in addition, they sometimes require costly pretreatment

to ensure the durability of the membrane [4]. Nevertheless, as more versatile, higher performance polyimide materials are being developed, a large increase their market share is possible over time. Rubbery polymers have a higher degree of segmental mobility, which gives them high productivities. They are also more solubility selective, which makes them strong candidates for H_2S removal. Even though their H_2S/CH_4 selectivities can be quite high (~74) for poly (ether urethane urea), their CO_2/CH_4 selectivities are not very competitive (~17) [29], and they are also susceptible to plasticization which makes them inadequate for an efficient separation. Therefore, rubbery-based processes can be inefficient for treating natural gas, especially when the CO_2 content is much more significant compared to H_2S. These membranes have been commercialized by MTR and GKSS. Figure 1.5 shows a picture of a sour gas processing membrane unit in British Columbia, Canada.

Figure 1.5: Sour gas processing unit in British Columbia, Canada [Courtesy of Membrane Technology and Research (MTR)].

1.3.2　Previous Research on Membranes for Acid/Sour Gas Separations

Whereas a significant number of studies have been focused on the removal of carbon dioxide from methane, only a few have focused on hydrogen sulfide removal. The main reason for this lack of study is the toxic and corrosive nature of the gas which requires a safe, state-of-the art laboratory with high levels of maintenance. In 1985, Klass and Landahl studied the separation of acid gases from methane with membranes such as Nylon 6, Nylon 6,6, polyvinyl alcohol (PVA), polyacrylonitrile (PAN) and also some rubbery membranes [7]. Although they achieved selectivities of about 200 for H_2S/CH_4, the permeabilities obtained were very low. In 1993, Bhide and Stern studied the effect of H_2S on the performance of CA membranes in removing acid gases from methane. They showed that at concentrations greater than 1% H_2S in a tertiary mixture of $H_2S/CO_2/CH_4$, not only CO_2 but also H_2S plasticizes the membrane [32, 33]. It was concluded that the combined effects of the two gases resulted in a loss of membrane efficiency. In 1997, Chatterjee et al. studied the permeation properties of membranes made of a group of polyurethanes (PU) and polyurethane-urea (PUU) [29]. They found a direct correlation between the permeability of CH_4, CO_2, and H_2S and their critical temperatures. Because critical temperature directly affects the solubility of gases in polymers, and diffusivities are only weak functions of size in rubbery polymers, they concluded that the permeation of those gases is controlled by their solubility. Although they obtained selectivities as high as 100 for H_2S/CH_4, their total feed pressure did not exceed 200 psia. This is not realistic as many gas wells pressures can reach pressures well above 1000 psia. It is also important to note that their studies involved gas mixtures with a maximum H_2S concentration of 12.5%. In 1997, Bhide et al. studied the separation properties of polyimide membranes based on 6FDA (hexafluoropropane dianhydride) [14]. They tried

to remove CO_2 from a ternary mixture of $H_2S/CO_2/CH_4$ at concentrations of 2.8-8%. They concluded that the selectivity of membranes improved in the presence of H_2S. While they pointed out that this phenomenon was unpredictable, they did not offer any explanation for their observations [28]. In 2006, Merkel and Toy studied hydrogen sulfide transport properties in fluorinated and nonfluorinated polymers [34]. They showed that fluorinated glassy polymers are more resistant to H_2S -induced plasticization than nonfluorinated polymers. This finding is relevant for the selection of polymer material for H_2S separation from natural gas. In 2008, Mohammadi et al. studied the acid gas permeation behavior through poly (ester urethane urea) membrane [28]. Although they achieved moderate selectivities of 43 for H_2S/CH_4, their studies were only performed with small H_2S concentration and feed pressures of up to 435 psia.

From these various studies, it can be concluded that rubbery polymers and glassy polymers both have their advantages and drawbacks. The common problem associated with H_2S and CO_2 separation from natural gas using glassy polymers is the swelling-induced plasticization of the membrane which leads to loss of membrane efficiency. In CA membrane, the presence of water vapor was proven to be harmful to the performance of the membrane, which in practice is solved by drying the feed to the membrane before processing. Rubbery polymers may have proven to yield high selectivities but because of their high free volume and high chain mobility, they may not be as efficient under realistic feeds. This is especially true for cases when both CO_2 and H_2S are present, which is common. In summary, there is a need to develop materials that can simultaneous separate H_2S and CO_2 efficiently under real processing conditions. It is important to point

out that none of the above studies were performed under such real, aggressive process conditions that include high pressures and high concentrations of H_2S.

1.3.3   Challenges in Sour Gas Treatment

This work focuses on the simultaneous separation of CO_2 and H_2S from natural gas. The challenge in this separation is depicted in Figure 1.6. The difference in size between CO_2 and CH_4 is higher than the difference in size between H_2S and CH_4, which makes CO_2 more diffusion selective, whereas the difference in condensability between H_2S and CH_4 is higher compared to CO_2 and CH_4, which makes H_2S more solubility selective polymers. This is the reason why rubbery polymers, as discussed previously, have been preferred over glassy polymers for H_2S separation and glassy polymers have been widely used for CO_2 separation. However, one of the most attractive things is that cellulose acetate has the ability to separate both successfully, which makes it especially attractive. These challenges will be addressed in this work. First, the industrial standard polymer, cellulose acetate, is studied, and then compared to a high performance crosslinkable polyimide known as PDMC. Crosslinking will be examined for both polymers as a means to suppress plasticization and increase overall separation performance. Realistic feed conditions such as high concentrations and pressures of acid gases, as well as nonvacuum downstream studies will also be examined. The focus of this work will be on dense film membranes as a "proof of concept" study, which is the precursor for the development of hollow fiber membrane modules in a subsequent study.
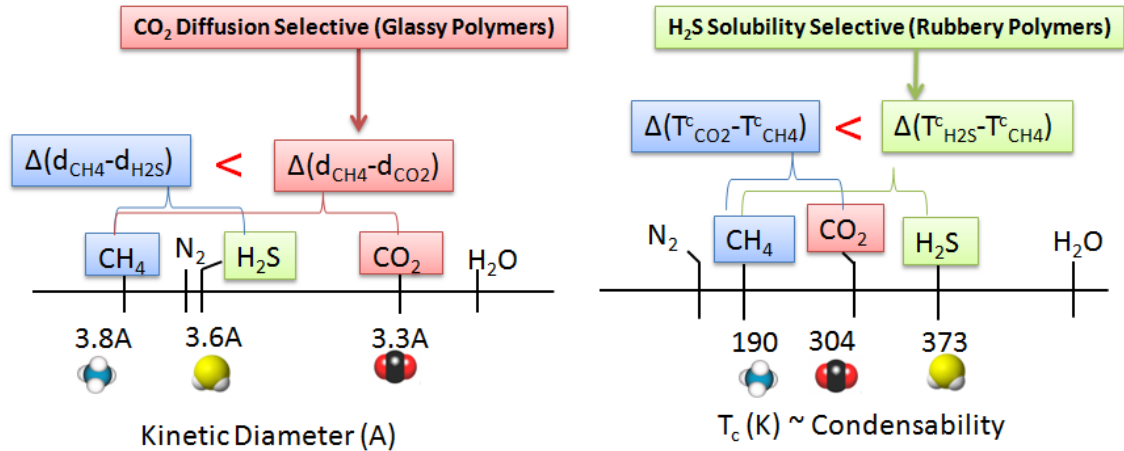
Figure 1.6: Schematic representation of the challenge in CO_2 and H_2S removal from natural gas showing relative size and condensability differences [35-37].

1.4 Research Objectives

The *overall goal of this project is to identify principles to guide the development of high performance dense film membranes for natural gas sweetening using hydrogen sulfide and carbon dioxide gas mixtures as models under aggressive sour gas feed conditions of up to 1000 psia.*

(1) Study the performance of cellulose acetate and an advanced crosslinkable polyimide (PDMC) dense film membrane for H_2S separation from natural gas.

As discussed previously, there is a great deal of data available in literature on CO_2/CH_4 separations using these two materials but only a limited on data is available for H_2S. It is crucial to understand the fundamental transport properties of H_2S in these materials in order to enhance their separation performance.

(2) Engineer the polymer in objective 1 to produce membrane materials with superior performance as measured by efficiency, productivity, and plasticization resistance.

15

Once the CO_2 and H_2S transport properties are evaluated, new materials will be engineered and synthesized based on the identified need.

(3) Determine the separation performance of the engineered membrane in objective 2 under more aggressive, realistic natural gas feeds, and perform a detailed transport analysis of the factors that impact their performance.

Sour gas treatment at the wellhead can reach pressure exceeding 700 psig; therefore testing the viability of the developed materials under those aggressive realistic conditions is important to assess their true separation performance. An analysis of the transport parameters governing these separations will provide insight into their typical operating range in order to use them effectively.

1.5 Dissertation Outline

This dissertation is divided into seven chapters, including this chapter. The second chapter will cover some background on gas transport mechanisms in polymers, as well as some common terminology used in this dissertation such as parameters used to assess membrane performance. Chapter 2 will also identify some challenges in membrane-based gas separations such as plasticization and approaches that have been considered by previous researchers such as crosslinking. The third chapter will cover the materials and equipments used in this study as well as the experimental methods. Techniques used to characterize polymer properties will be discussed in more detail. The fourth chapter will report preliminary studies conducted on the conventional cellulose acetate polymer and on a high performance polyimide (PDMC), focusing especially on the fundamental transport of H_2S through these materials. General CO_2, H_2S, and CH_4 transport

parameters will be reported. Pure gas and mixed gas studies will be discussed both with vacuum and nonvacuum downstream. The fifth chapter will introduce a new modification technique called the "*GCV-Modification*" technique, which was inspired by the results of Chapter 4. All synthesis details of this material as well as other methods that were considered will be addressed. This technique involves grafting and crosslinking of a silane (vinyltrimethoxysilane) to residual hydroxyl groups in cellulose acetate. The sixth chapter will cover the transport of CO_2 and H_2S in the GCV-Modified CA material and in the crosslinked PDMC material. Pure gas and mixed gas studies with both vacuum and nonvacuum downstream will be discussed, and all the transport parameters will be reported. The final chapter will cover summarize the findings in this work and will provide recommendations for future work.

1.6 References

[1] International Energy Outlook 2011, in, U.S. Energy Information Administration, Washington, D.C., 2011.

[2] K. Schoots, R. Rivera-Tinoco, G. Verbong, B. van der Zwaan, Historical variation in the capital costs of natural gas, carbon dioxide and hydrogen pipelines and implications for future infrastructure, Int J Greenh Gas Con, 5 (2011) 1614-1623.

[3] Y. Xiao, B.T. Low, S.S. Hosseini, T.S. Chung, D.R. Paul, The strategies of molecular architecture and modification of polyimide-based membranes for CO2 removal from natural gas—A review, Progress in Polymer Science, 34 (2009) 561-580.

[4] C.A. Scholes, G.W. Stevens, S.E. Kentish, Membrane gas separation applications in natural gas processing, Fuel, 96 (2012) 15-28.

[5] R.W. Baker, K. Lokhandwala, Natural gas processing with membranes: An overview, Ind Eng Chem Res, 47 (2008) 2109-2121.

[6] H.S. Meyer, Volume and distribution of subquality natural gas in the United States, GasTIPS, 6 (2000).

[7] J. Hao, P.A. Rice, S.A. Stern, Upgrading low-quality natural gas with H2S- and CO2-selective polymer membranes - Part II. Process design, economics, and sensitivity study of membrane stages with recycle streams, J Membrane Sci, 320 (2008) 108-122.

[8] J.G. Speight, The Chemistry and Technology of Petroleum, Fourth Edition, Taylor & Francis, 2010.

[9] R.W. Baker, K.A. Lokhandwala, Acid Fractionation Process, in, United States, 1996.

[10] R.W. Baker, K.A. Lokhandwala, Sour Gas Treatment Process, in, United States, 1995.

[11] T.E. Cooley, A.B. Coady, Removal of H2S and/or CO2 from a Light Hydrocarbon Stream by Use of Gas Permeable Membrane, in, United States, 1978.

[12] D.L. Klass, C.D. Landahl, Gas Sweetening by Membrane Permeation, in, United States, 1985.

[13] K.A. Lokhandwala, R.W. Baker, Sour Gas Treatment Process Including Membrane and Non-membrane Treatment Steps, in, United States, 1995.

[14] S.A. Stern, H. Kawakami, A.Y. Houde, G. Zhou, Material and Process for Separating Carbon Dioxide from Methane, in, United States, 1997.

[15] B.D. Bhide, A. Voskericyan, S.A. Stern, Hybrid processes for the removal of acid gases from natural gas, J Membrane Sci, 140 (1998) 27-49.

[16] H. Savoji, M.P. Chenar, M. Soltanieh, T. Matsuura, S. Tabe, Removal of hydrogen sulfide from methane using commercial polyphenylene oxide and Cardo-type polyimide hollow fiber membranes (vol 28, pg 902, 2011), Korean J Chem Eng, 28 (2011) 1311-1311.

[17] R.W. Baker, Future directions of membrane gas separation technology, Ind Eng Chem Res, 41 (2002) 1393-1411.

[18] R.D. Noble, S.A. Stern, Membrane Separations Technology: Principles and Applications, Elsevier Science, 1995.

[19] W.J. Koros, R. Mahajan, Pushing the limits on possibilities for large scale gas separation: which strategies?, J Membrane Sci, 175 (2000) 181-196.

[20] W.J. Koros, G.K. Fleming, Membrane-Based Gas Separation, J Membrane Sci, 83 (1993) 1-80.

[21] R.W. Baker, Membrane technology and applications, 3rd ed., John Wiley & Sons, Chichester, West Sussex ; Hoboken, 2012.

[22] W.J. Koros, M.W. Hellums, Gas Separation Membrane Material Selection Criteria - Differences for Weakly and Strongly Interacting Feed Components, Fluid Phase Equilibr, 53 (1989) 339-354.

[23] L.M. Robeson, The upper bound revisited, J Membrane Sci, 320 (2008) 390-400.

[24] L.M. Robeson, Correlation of separation factor versus permeability for polymeric membranes, J Membrane Sci, 62 (1991) 165-185.

[25] B.D. Freeman, I. Pinnau, A.C.S.D.o.P.M. Science, Engineering, A.C.S. Meeting, Polymer membranes for gas and vapor separation: chemistry and materials science, American Chemical Society, 1999.

[26] D.R. Paul, I.U.P. ÍAmpol′skiĭ, Polymeric Gas Separation Membranes, Taylor & Francis, 1994.

[27] P. Bernardo, E. Drioli, G. Golemme, Membrane Gas Separation: A Review/State of the Art, Ind Eng Chem Res, 48 (2009) 4638-4663.

[28] T. Mohammadi, M.T. Moghadam, M. Saeidi, M. Mahdyarfar, Acid gas permeation behavior through poly(ester urethane urea) membrane, Ind Eng Chem Res, 47 (2008) 7361-7367.

[29] G. Chatterjee, A.A. Houde, S.A. Stern, Poly(ether urethane) and poly(ether urethane urea) membranes with high H2S/CH4 selectivity, J Membrane Sci, 135 (1997) 99-106.

[30] S.S. Kulkarni, S.F. Yates, A.X. Swamikannu, Cross-linked Gas Selective Membranes, in, Allied-Signal Inc., United States, 1990.

[31] J.J. Chiou, S. Kulprathipanja, D.A. Lesch, C. Liu, S.T. Wilson, Plasticization Resistant Membanes, in, UOP LLC, United States, 2010.

[32] B.D. Bhide, S.A. Stern, Membrane Processes for the Removal of Acid Gases from Natural-Gas .1. Process Configurations and Optimization of Operating-Conditions, J Membrane Sci, 81 (1993) 209-237.

[33] B.D. Bhide, S.A. Stern, Membrane Processes for the Removal of Acid Gases from Natural-Gas .2. Effects of Operating-Conditions, Economic-Parameters, and Membrane-Properties, J Membrane Sci, 81 (1993) 239-252.

[34] T.C. Merkel, L.G. Toy, Comparison of hydrogen sulfide transport properties in fluorinated and nonfluorinated polymers, Macromolecules, 39 (2006) 7591-7600.

[35] D.W. Breck, Zeolite Molecular Sieves: Structure, Chemistry and Use, 3 ed., John Wiley & Sons, New York, 1974.

[36] S. Matteucci, Y. Yampolskii, B.D. Freeman, I. Pinnau, Transport of Gases and Vapors in Glassy and Rubbery Polymers, in: Materials Science of Membranes for Gas and Vapor Separation, John Wiley & Sons, Ltd, 2006, pp. 1-47.

[37] J. Vaughn, Development and Evaluation of Aromatic Polyamide-imide Membranes for H2S and CO2 Separations from Natural Gas, in: School of Chemical and Biomolecular Engineering, Georgia Instituteof Technology, Atlanta, 2013.

CHAPTER 2: BACKGROUND AND THEORY

2.1 Gas Transport Through Glassy Polymeric Membranes

2.1.1 Penetrant Diffusion in Polymers

Transport properties determine a polymer's ability to move through some medium or to have some penetrant medium move between its constituent segments [1]. Gas transport can be achieved using membranes based on one of the following three transport mechanisms: Knudsen-diffusion, solution-diffusion, and molecular sieving as illustrated in Figure 2.1. In Knudsen diffusion, diffusing molecules collide with the pore walls more frequently than with other molecules, especially when the distance between molecular collisions is much greater than the pore diameter [2]. Even though membranes that favor this mechanism have some specialty applications, such membranes are not industrially attractive due to their low selectivities [3]. Ultramicroporous molecular sieving membranes have pore dimensions similar to those of small molecules (pores < 7Å), and in this process, molecules are separated based on size exclusion [3-5]. These materials have received attention due to their high productivities and selectivities [6-8]. Among those three mechanisms, sorption-diffusion describes the permeation of a small penetrant molecule through a nonporous (dense) polymer membrane, and will be the only case discussed in this work. This transport mechanism is based on both sorption and diffusivity factors. Diffusivity selectivity favors the smaller molecule and sorption selectivity favors the most condensable one.
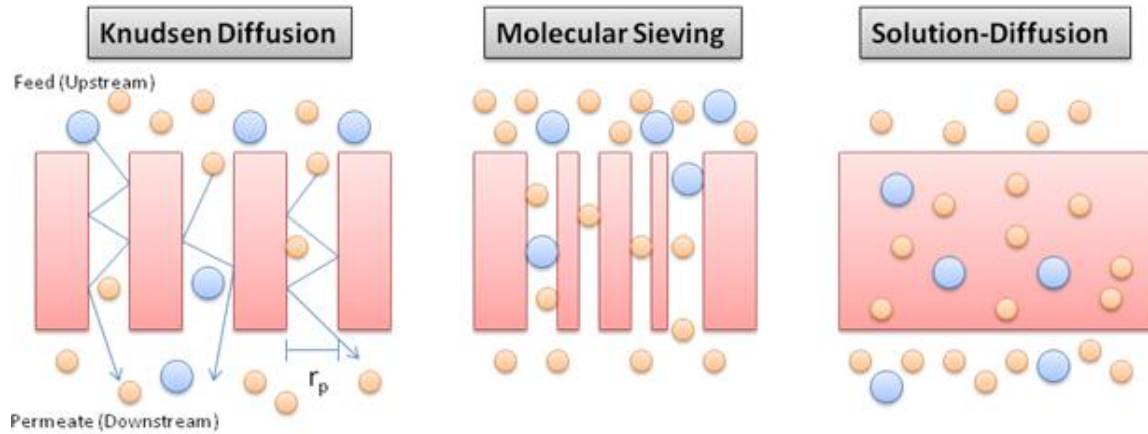
Figure 2.1: Schematic of membrane-based gas separations main transport mechanisms.

The sorption-diffusion mechanism for transport in polymers was first quantitatively expressed by Graham [9]. In its view ofthe process for a penetrant to diffuse, a minimum characteristic packet of unoccupied volume is required. Penetrant molecules vibrate inside local cavities in the polymer matrix at frequencies much higher frequencies than the frequency of the polymer chain motion. The penetrant diffuses by jumping between packets of unoccupied volume through transient gaps, created by the thermally agitated motions of the chain segments. A schematic of this diffusion process is illustrated in Figure 2.2, where a gap of sufficient size is generated to allow the penetrant to move into, with subsequent collapse of the cage that previously housed the penetrant [1]. The diffusion coefficient of a penetrant molecule through an isotopic medium (equal in all six directions) can be written as [3]:

$$D = \frac{f\lambda^2}{6}$$
2.1

where f is the average jumping frequency and λ is the average jump length. The lifetime, size , and shape of these volume packets and the transient gaps that connect them are dependent upon the micromotions of the polymeric medium [1]. If the size of

the gap is larger than the critical dimension of the penetrant molecule, a diffusive jump can be taken but if it is too small compared to the size of the molecule, a jump is prevented. The size of the opening gaps in glassy polymers is narrowly distributed, thereby allowing a more selective environment for penetrant diffusion, which explains why these materials are more diffusion selective [1].
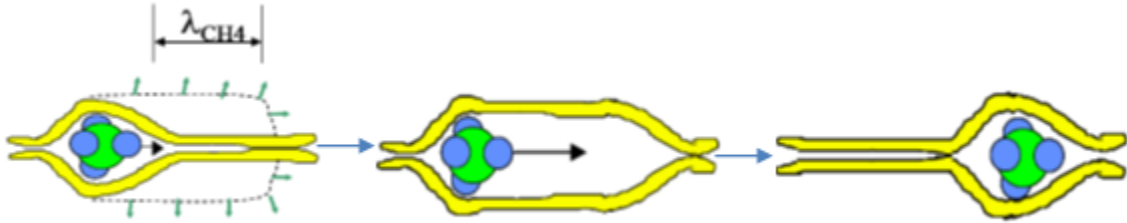
Figure 2.2: Cartoon of transient gap formation and collapse for penetrant diffusion in nonporous polymers.

2.1.2 Permeation

As mentioned earlier, the mechanism of permeation in dense membranes involves a sorption-diffusion mechanism (Figure 2.3) consisting of three steps where a given penetrant is first: (1) sorbed or adsorbed on the upstream boundary (high pressure) side of the membrane, then (2) actively diffuses through the membrane down a chemical potential gradient to the downstream boundary (low pressure) side of the membrane, where it is finally (3) desorbed or evaporated from the downstream boundary [1, 10]. The driving force for the process is related to the concentration difference created by the partial pressure of the permeating gases on the upstream and downstream sides of the membrane [3].
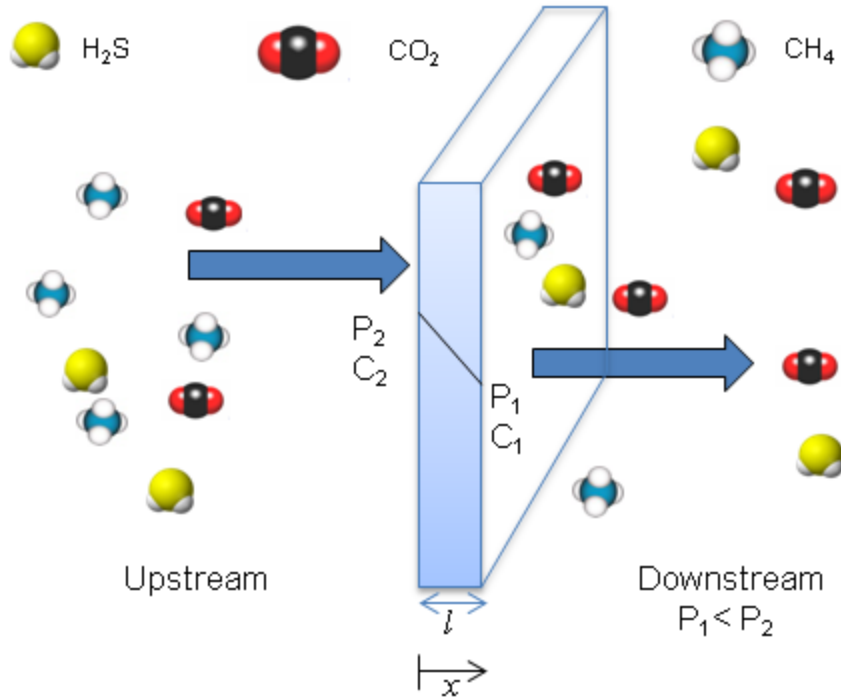
Figure 2.3: Schematic of sorption-diffusion process for CO_2, H_2S, and CH_4 separation through a dense polymer membrane.

The rate of gas permeation through a membrane is described by the permeability coefficient *P.* The permeability of a given gas *A* is defined as the observed steady-state flux N_A divided by the partial pressure difference ($\Delta p = p_1\text{-}p_2$) across the membrane normalized by the membrane thickness *l* as shown in Equation 2.2. The permeability coefficient provides an overall measure of the ease of transporting a given gas penetrant through the polymer material.

$$P_A = \frac{N_A \times l}{\Delta p_A}$$ 2.2

The permeability coefficient is commonly expressed in Barrer, where

$$1\,\text{Barrer} = 1 \times 10^{-10} \frac{\text{cm}^3(\text{STP})\,\text{cm}}{\text{cm}^2 \text{sec cmHg}}$$ 2.3

In non-ideal mixtures, (i.e. CO_2 and H_2S-containing mixtures at high pressures) as is the case in this study, the pressures appearing in Equation 2.2 are replaced by fugacities to yield:

$$P_A = \frac{N_A \times l}{\Delta f_A}$$

2.4

If bulk flow is a factor in the x-direction as shown in Figure 2.3, the flux of gas A through the membrane, N_A relative to a fixed coordinate can be written as:

$$N_A = -D\left(\frac{dC}{dx}\right) + w_A\left(N_A + N_p\right)$$

2.5

where C is the concentration of component A in the polymer, D is the diffusion coefficient, and $\frac{dC}{dx}$ is the concentration gradient in the polymer [1, 11, 12]. This situation can be important even when an actual pressure gradient does not exist within the membrane if the diffusive flux is high. The term N_p can be set to zero since the membrane is presumably immobile at steady-state relative to the fixed frame of reference, Equation 2.5 becomes:

$$N_A = -\frac{D}{1-w_A}\left(\frac{dC}{dx}\right)$$

2.6

By combining Equation 2.4 and 2.6, the following expression is obtained:

$$P_A = -\frac{D \times l}{(1-w_A) \times (f_2 - f_1)}\left(\frac{dC}{dx}\right)$$

2.7

Integrating both sides from $x = 0$, $C = C_2$ to $x = l$, $C = C_1$ gives:

$$P_A \int_0^l \frac{1}{l}\, dx = \frac{1}{f_2 - f_1}\int_{C_2}^{C_1} \frac{D}{1-w_A}\, dC$$

2.8

Equation 2.8 can be simplified to yield:

$$P_A = \frac{1}{f_2 - f_1} \int_{C_1}^{C_2} \frac{D}{1-w_A} \, dC = [\bar{D}_A] \times \frac{C_2 - C_1}{f_2 - f_1} \qquad 2.9$$

where $\bar{D}_A$ is the concentration-average diffusion coefficient defined by the following expression:

$$[\bar{D}_A] = \frac{1}{C_2 - C_1} \int_{C_1}^{C_2} \frac{D}{1-w_A} \, dC \qquad 2.10$$

The permeability can be expressed as the product of a diffusivity (kinetic factor) and a solubility coefficient (thermodynamic factor) [1]:

$$P_A = [\bar{D}_A] \times [\bar{S}_A] \qquad 2.11$$

The solubility coefficient indicates how much gas can be taken up by a membrane when equilibrated with a given gas fugacity [13]. The solubility coefficient can found by combining Equation 2.9, 2.10, and 2.11 as:

$$\bar{S}_A = \frac{C_2 - C_1}{p_2 - p_1} \qquad 2.12$$

The separation performance of a membrane is determined by its permselectivity. For an ideal binary gas mixture permeating through a membrane, the ideal selectivity can be written as a ratio of permeabilities, when the downstream pressure is negligible relative to the upstream pressure, viz.,

$$\alpha_{A/B} = \frac{P_A}{P_B} \qquad 2.13$$

Bearing in mind Equation 2.11, the ideal selectivity can be partitioned into diffusivity and solubility selectivity as follows:

$$\alpha_{A/B} = \left[\frac{D_A}{D_B}\right] \times \left[\frac{S_A}{S_B}\right] = \alpha_{A/B}^D \times \alpha_{A/B}^S \qquad \text{2.14}$$

In the case of mixed gas feeds where there may be plasticization as well as competitive interactions between the permeating gases and the polymer, the separation factor $\alpha_{A/B}^*$ is used to describe the separation and is defined by [14]:

$$\alpha_{A/B}^* = \frac{y_A / y_B}{x_A / x_B} \qquad \text{2.15}$$

where y_A and y_B are the mole fraction of components A and B in the permeate (downstream), x_A and x_B are the mole fraction of components A and B in the feed (upstream). However, this separation factor does not fully account for the deviation from ideal gas phase behavior that highly condensable gases such as CO_2 and H_2S might exhibit, and a better indicator of the intrinsic membrane performance can be achieved to account for fugacity viz.,

$$\alpha_{A/B}^* = \frac{y_A / y_B}{\Delta f_A / \Delta f_B} \qquad \text{2.16}$$

where Δf_A and Δf_B are the fugacity driving force of component A and B between the feed and permeate sides of the membrane. By substituting fugacities expressions ($f_{i,2} = x_i \, \hat{\varphi}_{i,2} \, p_2$) for each penetrant, the following expression is obtained for the case of negligible downstream pressure:

27

$$\alpha_{A/B} = \left(\frac{y_A}{y_B}\right) \times \left(\frac{x_B}{x_A}\right) \times \left(\frac{\hat{\varphi}_{B,2}}{\hat{\varphi}_{A,2}}\right) \qquad \text{2.17}$$

where $\hat{\varphi}_{i,2}$ and $\hat{\varphi}_{i,1}$ are the fugacities coefficients of each component in the feed and in the permeate mixtures, respectively. For the case of non negligible downstream pressure, Equation 2.16 reduces to:

$$\alpha_{A/B} = \left(\frac{y_A}{y_B}\right) \times \left(\frac{x_B \hat{\varphi}_{B,2}\, p_2 - y_B \hat{\varphi}_{B,1}\, p_1}{x_A \hat{\varphi}_{A,2}\, p_2 - y_A \hat{\varphi}_{A,1}\, p_1}\right) \qquad \text{2.18}$$

2.1.3 Sorption

The concept of free volume is illustrated in Figure 2.4, which shows the specific volume of a polymer as function of temperature. In this concept, there are two different states in which amorphous polymers can be found: a glassy and a rubbery state. At high temperatures, the polymer is in a rubbery state. In both states, packing defects of polymer chains give rise to some unoccupied space (free volume) between the polymer chains.
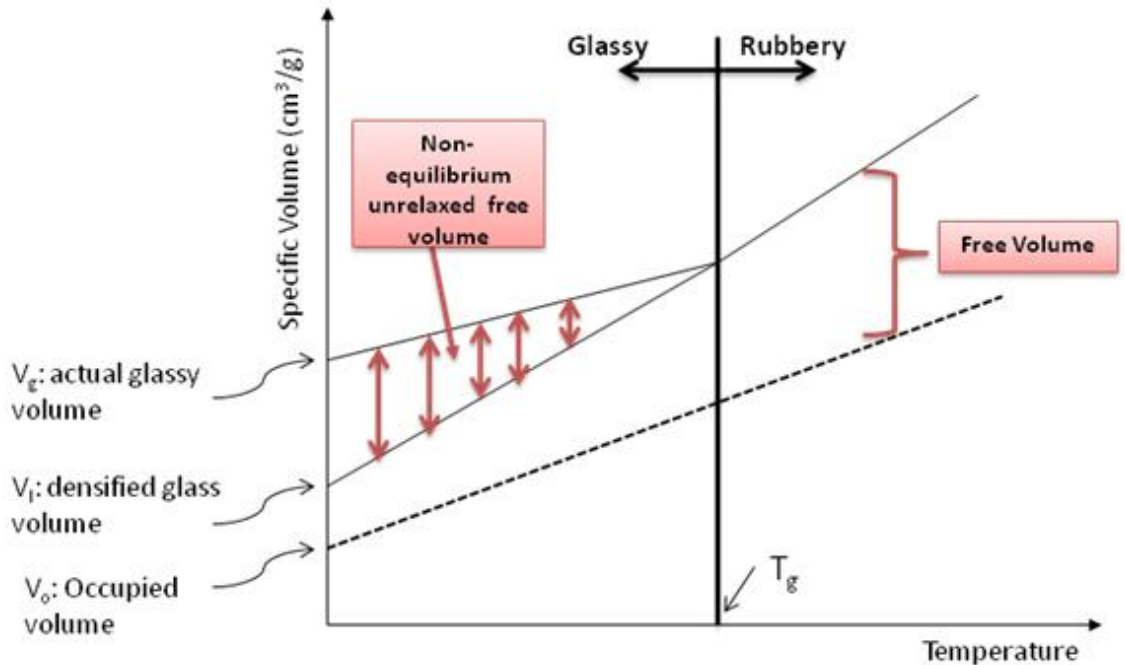
Figure 2.4: Schematic of the unrelaxed free volume concept in a glassy polymer.

Although this free volume is only a fraction of the total volume, it is sufficient to allow polymer segmental motion [4]. This free volume allows rubbery polymers to exhibit liquid-like characteristics, even though there are solid at the macroscopic level. As the polymer is cooled further, its free volume also decreases. At the glass transition temperature (T_g), the free volume is reduced to a critical extent which doesn't allow polymer chain segments to move freely. As segmental motion becomes extremely limited, the temperature falls below the T_g, and extra unrelaxed volume elements between the polymer chains are frozen into the polymer matrix, giving rise to an excess free volume [4]. This non-equilibrium excess free volume is defined as V_g-V_l and results from the inability of the polymer chain to quickly rearrange to reach equilibrium once it is cooled below the T_g [12], which leads to a low segmental mobility and long relaxation

times, causing glassy polymers to be in a non-equilibrium state [15]. This introduction of unrelaxed free volume causes the specific volume of a glassy polymer to be higher than the extrapolated specific volume of the polymer in a hypothetical liquid state [16]. Therefore, glassy polymers hypothetically contain two environments: (1) normal free volume elements caused by the packing defects of the groups making the polymer chains and (2) excess (unrelaxed) free volume gaps between polymer chain segments. As a result, sorption in glassy polymers is commonly described using the dual-mode sorption model, which is the combination of: a simple dissolution or Henry's mode in the dense equilibrium domain analogous to that observed above the T_g (rubbery state), and sorption at the microcavities (filling of the nonequilibrium excess free volume or "holes"), which may be formulated as a simple Langmuir adsorption [12, 13] as illustrated in Figure 2.5. Analytically, the dual mode model can be expressed as [17, 18]:

$$C = C_D + C_H = k_D f + \frac{C_H' b f}{1 + b f} \qquad 2.19$$

where C is the total concentration of penetrant in the polymer, C_D is the dissolved mode penetrant concentration, C_H is the penetrant concentration in the Langmuir mode, k_D is the Henry's law constant, C_H' is the hole saturation constant or Langmuir sorption capacity, and b is the hole affinity constant or the Langmuir affinity parameter. The parameter k_D characterizes sorption of penetrants in the densified regions that comprise most of the polymer or the level of dissolution that the penetrant can achieve. The Langmuir capacity is proportional to the maximum concentration of penetrant molecules in the unrelaxed domains and can be considered to be a measure of the non-equilibrium

30

or excess free volume of the polymer [14]. This parameter depends strongly on the condensability of the penetrant because it determines the relative efficiency with which the component can use the available volume [11].

Dual-Mode

$$C = C_D + C_H = k_d P + \frac{b C_H' p}{1 + bp}$$

Langmuir

$$C_H = \frac{b C_H' p}{1 + bp}$$

Henry

$$C_D = k_d P$$

slope = k_d
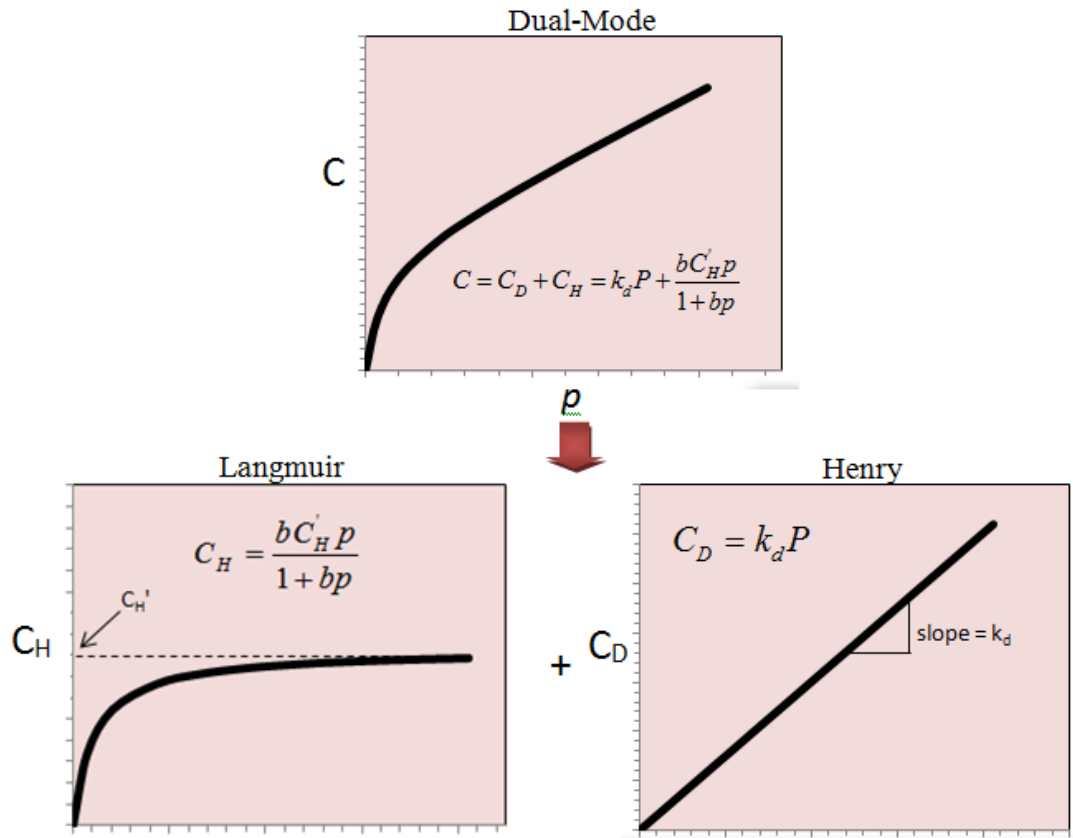
Figure 2.5: Schematic representation of the dual-mode sorption model capturing Henry's and Langmuir's contributions.

Koros et al. extended this dual-mode model to account for sorption in binary gas mixtures at concentrations below which plasticization occurs [19, 20]. This model accounts for the possibility of competitive sorption between penetrants for the fixed unrelaxed volume in the Langmuir domain. This competitive effect may lead in a significant decrease of the overall sorption of a given penetrant when the concentration of the other penetrant is increased. The model is analytically described by Equations 2.20 and 2.21.

$$C_A = k_{D_A} f_A + \frac{C'_{H_A} b_A f_A}{1 + b_A f_A + b_B f_B} \qquad\qquad 2.20$$

$$C_B = k_{D_B} f_B + \frac{C'_{H_B} b_B f_B}{1 + b_A f_A + b_B f_B} \qquad\qquad 2.21$$

In these equations, all the pure components parameters can be used directly for the mixture, under the assumption that the influence that the plasticizing effects have on k_D are negligible as well as the interactions between the two penetrants influence on C_H' and b of each component [20].

2.1.4 Effect of Free Volume

The specific free volume (V_f) can be written as the difference between the specific volume of the glass (V_g) and the occupied specific volume of the polymer chains (V_o) [21]:

$$V_f = V_g - V_o = V_g - 1.3V_W \qquad\qquad 2.22$$

where V_W is the van der Waals volume, since the occupied volume was estimated from the van der Waals group contribution method such as those given by van Krevelen [22]. The fractional free volume (*FFV*) can be defined as the ratio of the specific free volume to the occupied specific volume of the polymer as [10, 13, 14, 23]:

$$FFV = \frac{V_g - V_o}{V_g} \qquad\qquad 2.23$$

As discussed earlier, there exists a non-equilibrium "unrelaxed" excess free volume in glassy polymers. A parameter used to represent that excess volume can be obtained from a dual-mode fit of a sorption isotherm of a given gas penetrant A as follows [14]:

$$\upsilon_{ex} = \frac{C_H' \upsilon_A}{22400} \qquad 2.24$$

where is υ_A the molar volume of the liquid-like penetrant. As an example, υ_{CO_2} is equal to 55 cm^3/mol [24]. Previous researchers suggested that there exist good correlations between diffusion and permeability coefficients and reciprocal free volume [25-27]. Therefore, the diffusion coefficient of gas molecules in polymers obey the following equation [13, 14]:

$$D = A \exp\left[\frac{-B}{FFV}\right] \qquad 2.25$$

where A and B are empirical constants, which vary from one gas to another and from one polymer to another. Gas solubility coefficient in polymers vary over a much narrower range than diffusivity, and the effect of free volume is generally much weaker than on diffusivity [12, 14], and as a practical matter, the permeability coefficient can directly be correlated with fractional free volume as [23, 26]:

$$P = A \exp\left[\frac{-B}{FFV}\right] \qquad 2.26$$

where A and B are empirical constants, which depends only on temperature and penetrant type.

2.1.5 Effect of Temperature

The diffusion of small penetrant molecules in polymers is a thermally activated process where the diffusion coefficient can be expressed by an Arrhenius-type relation, at temperatures away from thermal transitions in the polymer [28-30]:

$$D = D_0 \exp\left(\frac{-E_d}{RT}\right) \qquad 2.27$$

where D_o is the pre-exponential factor, E_d is the activation energy required for diffusion, R is the universal gas constant, and T is the absolute temperature. The solubility coefficient can be expressed via a Van't Hoff type equation [31]:

$$S = S_0 \exp\left(\frac{-\Delta H_S}{RT}\right) \qquad 2.28$$

where S_o is the pre-exponential factor and ΔH_S is the heat of solution or enthalpy of sorption. The dissolution of a penetrant molecule into a polymer matrix can be described as a two-step thermodynamically process: (1) penetrant condensation and (2) creation of a molecular scale gap of sufficient size to accommodate the penetrant or mixing of the condensed penetrant with polymer molecules [12, 14]. The heat of solution can be written as

$$\Delta H_S = \Delta H_{condensation} + \Delta H_{mixing} \qquad 2.29$$

where $\Delta H_{condensation}$ is the enthalpy of condensation of the penetrant and ΔH_{mixing} is the partial molar enthalpy of mixing of the condensed penetrant within the polymer matrix. For highly condensable gases such as CO_2 and H_2S, ΔH_S is usually negative due to the large contribution of $\Delta H_{condensation}$ to Equation 2.29, and as a result the solubility decreases with increasing temperature. Since the energy associated with the condensation step is the dominant contribution, gas solubility often scales with measures of gas condensability such as gas critical temperature and gas normal boiling point. Permeability is defined in Equation 2.11 as the product of solubility coefficient and diffusion coefficient, substituting Equation 2.27 and 2.28 into 2.11 gives the following expression for permeability:

$$P = P_0 \exp\left(\frac{-E_P}{RT}\right) \qquad 2.30$$

where P_o is the pre-exponential factor and E_p is the activation energy required for permeation is defined as:

$$E_p = E_d + \Delta H_S \qquad 2.31$$

2.1.6 Effect of Polymer Crystallinity on Gas Transport

Semi-crystalline polymers have tortuosity caused by the presence of the typically impenetrable crystalline domains. The effect of crystallinity on solubility is based on the assumption that penetrant molecules are only soluble in the amorphous regions of the polymer [1]. The solubility coefficient is proportional to the amorphous volume fraction

of the material and the intrinsic solubility coefficient for the completely amorphous material [32, 33].

$$S = \Phi_A S_A \qquad\qquad 2.32$$

However, the effects of crystallinity on the diffusion coefficient can be much more complex, since the crystallites may act as both impermeable barriers to transport (forcing penetrant to follow a tortuous path) and as chain motions restrictors in amorphous regions of the polymer [1, 32]. For glassy polymers, the diffusion coefficient was estimated as [32]:

$$D = \frac{D_A}{\tau\beta} \approx \frac{D_A}{(1/\Phi_A)\beta} \approx D_A \Phi_A \qquad\qquad 2.33$$

where D_A is the diffusion coefficient of the gas for a totally amorphous polymer, β, is the chain immobilization factor and it is usually taken to be equal to 1 for glassy polymers, the tortuosity τ, can be a function of crystallite size, shape, and orientation. The effect of crystallinity on permeability for this simple two-phase becomes:

$$P = \Phi_A^2 P_A \qquad\qquad 2.34$$

2.2 Permeation Modeling in Glassy Polymers

2.2.1 Partial Immobilization Model

Koros et al. [34, 35] found that penetrant molecules in the two different populations have different inherent mobilities and the so-called "partial immobilization" model accounts for that fact by expressing Fick's law as:

36

$$N = -D_D \frac{\partial C_D}{\partial x} - D_H \frac{\partial C_H}{\partial x} \qquad\qquad 2.35$$

where N is the total diffusive flux, and D_D and D_H are the local diffusion coefficients in the two different environments. This model further predicts the permeability of a single gas measured with an upstream fugacity f_2 and negligible downstream fugacity f_1 as follows:

$$P = k_D D_D \left[1 + \frac{FK}{1 + bf_2} \right] \qquad\qquad 2.36$$

where

$$F \equiv D_H / D_D \qquad\qquad 2.37$$

and

$$K \equiv C_H' b / k_D \qquad\qquad 2.38$$

Parameters such as k_D, b, and C_H' can be obtained by conducting sorption experiments as discussed in the next chapter and D_D and D_H can be found by plotting P versus $1/(1+bf_2)$ [34, 36]. An expression for the effective (apparent) diffusion coefficients were derived assuming that D_D and D_H are exponential functions of the penetrant concentration in polymers [37].

$$D_{eff} = D_D \left[\frac{1 + FK/(1+bf)^2}{1 + F/(1+bf)^2} \right] \qquad\qquad 2.39$$

To consider the possible molecular meaning of the coefficients D_D and D_H, Barrer identified that the molecules can execute diffusive movements within their respective

modes (Henry's or "dissolved" and "hole" or Langmuir) through the four following ways [38]:

1. D→D: This represents a jump of a penetrant from one dissolved mode to another dissolved mode via a chemical potential gradient. The diffusion coefficient of this jump is denoted D_{DD}.

2. D→H: This represents a jump of a penetrant from one dissolved mode to an empty hole via a chemical potential gradient. This jump is dependent upon the availability of a hole, and the probability of finding a hole adjacent to the dissolved penetrant. The diffusion coefficient of this jump is denoted D_{DH}.

3. H→D: This represents a jump of a penetrant from a hole to a dissolved mode via a chemical potential gradient. The diffusion coefficient of this jump is denoted D_{HD}.

4. H→H: This represents a jump of a penetrant from a hole to another hole via a chemical potential gradient. This jump is dependent upon the availability of a hole, and the probability that the two holes are adjacent. The diffusion coefficient of this jump is denoted D_{HH}.

For the case of mixed gas sorption, assuming local equilibrium in which all penetrants at a local level at any distance through the membrane in the x-direction of diffusion, the polymer have equal chemical potential and the permeability is defined as [20]:

$$P_A = k_{D_A} D_{D_A} \left[1 + \frac{F_A K_A}{1 + b_A f_A + b_B f_B} \right]$$

2.40

$$P_B = k_{D_B} D_{D_B} \left[1 + \frac{F_B K_B}{1 + b_A f_A + b_B f_B} \right] \qquad 2.41$$

If the downstream pressure is not neglected, the permeability becomes [20, 39]

$$P_A = \frac{k_{D_A} D_{D_A}}{\left(f_{A2} - f_{A1} \right)} \left[\left(f_{A2} - f_{A1} \right) + F_A K_A \left(\frac{f_{A2}}{1 + b_A f_{A2} + b_B f_{B2}} - \frac{f_{A1}}{1 + b_A f_{A1} + b_B f_{B1}} \right) \right] \quad 2.42$$

$$P_B = \frac{k_{D_B} D_{D_B}}{\left(f_{B2} - f_{B1} \right)} \left[\left(f_{B2} - f_{B1} \right) + F_B K_B \left(\frac{f_{B2}}{1 + b_A f_{A2} + b_B f_{B2}} - \frac{f_{B1}}{1 + b_A f_{A1} + b_B f_{B1}} \right) \right] \quad 2.43$$

2.2.2 Bulk Flow Model (Frame of Reference)

Small molecule transport through a dense polymeric medium was described earlier using Fick's first law of diffusion. However when speaking of diffusional flux, it is necessary to specify a reference frame from which the diffusion process is to be observed [1]. Two frames of reference can be defined: fixed and moving. In the fixed frame of reference, the mass flux relative to a fixed coordinates results from two contributions: a concentration gradient contribution (true molecular diffusion) and a bulk flow contribution [40]. In the moving frame of reference, the mass average bulk velocity is typically used as the reference for the diffusional velocity [41]. In membrane transport, a fixed reference frame is used because permeation is being measured with respect to the membrane because it is presumably immobile at steady-state. When dealing with gas penetrants, using mass flux unit instead of molar flux unit is more convenient because the molar volume of the

penetrants might not be readily available [41]. This gives the following expression for permeability:

$$P_A = \frac{22400 \times n_A \times l}{M_A \times \Delta f_A} \qquad 2.44$$

where M_A is the molecular weight of gas A and n_A is the observed mass flux. The mass fluxes in a mixture can be given by:

$$n_A = \frac{-\rho D_{D_A}\left(\dfrac{d\omega_{m,A}}{dx}\right)}{\left[1-\left(1+\dfrac{1}{r}\right)\omega_{m,A}\right]} \qquad 2.45$$

$$n_B = \frac{-\rho D_{D_B}\left(\dfrac{d\omega_{m,B}}{dx}\right)}{\left[1-\left(1+\dfrac{1}{r}\right)\omega_{m,B}\right]} \qquad 2.46$$

$$r = \frac{n_A}{n_B} \ , \ (n_A > n_B) \qquad 2.47$$

By combining Equation 2.44, 2.45, 2.46, and 2.47, and integrating using the following boundary conditions, Equation 2.48 and 2.49 are derived:

$$x = 0, f_A = f_{A2}; f_B = f_{B2}; \omega_A = \omega_{m,A2}; \omega_B = \omega_{m,B2}$$
$$x = l, f_A = f_{A1}; f_B = f_{B1}; \omega_A = \omega_{m,A1}; \omega_B = \omega_{m,B1}$$

$$P_A = \left(\frac{22400 \times \rho \times D_{D_A}}{M_A \times \Delta f_A}\right)\left(\frac{1}{1+1/r}\right)\ln\left[\frac{1-\omega_{m,A1}\left(1+1/r\right)}{1-\omega_{m,A2}\left(1+1/r\right)}\right] \qquad 2.48$$

$$P_B = \left(\frac{22400 \times \rho \times D_{D_B}}{M_B \times \Delta f_B} \right) \left(\frac{1}{1+1/r} \right) \ln \left[\frac{1 - \omega_{m,B1}(1+1/r)}{1 - \omega_{m,B2}(1+1/r)} \right] \qquad 2.49$$

where ρ is the polymer density. In the case of zero permeate pressure, the above expressions reduce to:

$$P_A = \left(\frac{22400 \times \rho \times D_{D_A}}{M_A \times \Delta f_A} \right) \left(\frac{1}{1+1/r} \right) \ln \left[\frac{1}{1 - \omega_{m,A2}(1+1/r)} \right] \qquad 2.50$$

$$P_B = \left(\frac{22400 \times \rho \times D_{D_B}}{M_B \times \Delta f_B} \right) \left(\frac{1}{1+1/r} \right) \ln \left[\frac{1}{1 - \omega_{m,B2}(1+1/r)} \right] \qquad 2.51$$

where

$$\omega_{m,A} = \frac{k_{D_A} f_A M_A}{22400 \rho} \times \left(1 + \frac{F_A K_A}{1 + b_A f_A + b_B f_B} \right) \qquad 2.52$$

$$\omega_{m,B} = \frac{k_{D_B} f_B M_B}{22400 \rho} \times \left(1 + \frac{F_B K_B}{1 + b_A f_A + b_B f_B} \right) \qquad 2.53$$

2.3 Penetrant Induced Plasticization

Penetrant-induced plasticization of polymers in the context of membranes is defined as a significant increase in the diffusion coefficient of a penetrant caused by the swelling of polymer chains, when exposed to high concentrations of highly condensable gases [42-45]. Penetrant molecules with higher critical temperatures like H_2S and CO_2 are more

capable to induce swelling, because they are considerably more soluble, particularly in glassy polymers [37, 46-48], and this phenomenon is illustrated in Figure 2.6.
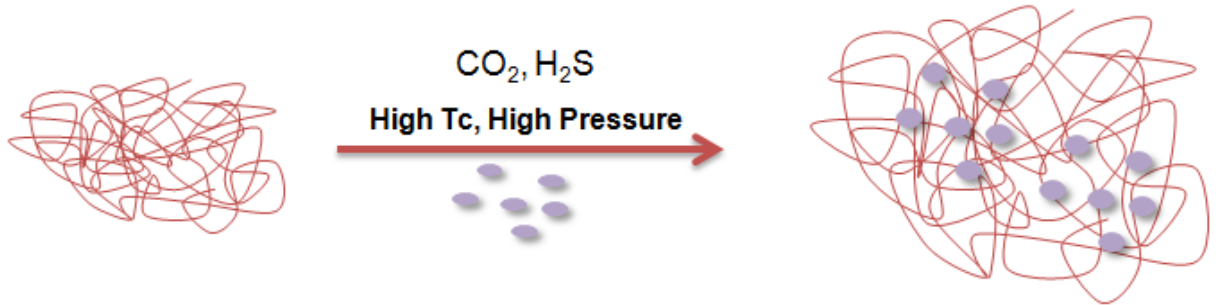
Figure 2.6: Cartoon representation of the penetrant-induced plasticization phenomenon in polymers.

The key result of swelling is a loss in size and shape discrimination of the polymer matrix. The degree of swelling typically increases as the partial pressure of the penetrant gas is increased. At much higher pressures, microvoid saturation processes are essentially complete and additional sorption simply swells and plasticizes the membrane, making it more rubberlike [11]. As a result, the increase in polymer chain segmental motion due to swelling creates a bias toward larger, less selective transient gaps, which allows both gases in a separation pair to permeate through the membrane at increased rates, with a greater increase in flux for the slow gas. The apparent result of this effect is an increase in permeability followed by a loss of selectivity due to an increase in polymer free volume. The effect of this plasticization phenomenon on the polymer separation performance is illustrated in Figure 2.7. This undesirable event is accompanied by changes in mechanical behavior, physical properties, and as a result, membrane efficiency. Therefore, knowledge of this phenomenon is critical for processing applications [49]. This

phenomenon can be superimposed on the "bulk flow" phenomenon discussed in 2.2.2, so the behavior can be quite complex when a large degree of swelling exists.
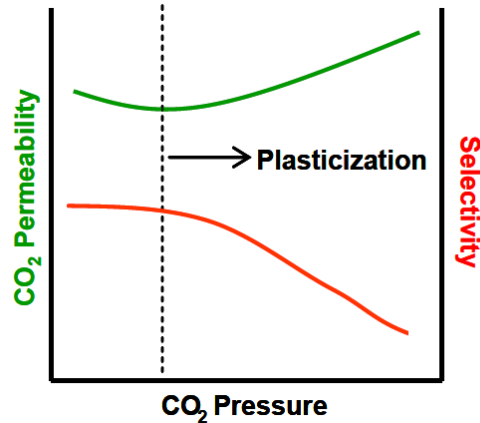
Figure 2.7: Schematic representation of the plasticization effect on polymer separation performance.

2.4 Polymer Crosslinking

Many researchers have shown that it is possible to stabilize polymer membranes against plasticization and to suppress bulk flow effects through the use of chemical crosslinking to minimize swelling and thereby maintain attractive membrane properties in the presence of aggressive feeds [45, 50-56]. Crosslinking creates an interwoven polymer network in which the polymer chains are much less susceptible to be influenced by outside penetrants relative to their uncrosslinked form, thereby reducing polymer segmental mobility [12]. Crosslinking may not in principle stabilize a membrane to an specific penetrant pressure, but will provide improved plasticization resistance over uncrosslinked membranes [45, 50-52]. Among all the crosslinking techniques, photocrosslinking and chemical crosslinking are the most common [55, 57-59]. Staudt-

Bickel et al. found that by chemically crosslinking 6FDA-*m*PD/DABA 9:1 via available carboxylic acid groups with ethylene glycol as the crosslinking agent, the swelling effects due to CO_2 can be significantly reduced [53]. Wind et al. also increased the CO_2 plasticization resistance by crosslinking 6FDA-DAM:DABA 2:1 with various agents [44]. Similarly, Hillock et al. showed that crosslinking 6FDA-DAM: DABA 3:2 using 1,3-propanediol as a crosslinking agent resulted in a significantly higher CO_2 permeability and slightly higher selectivity for the CO_2/CH_4 separation, with higher CO_2 plasticization resistance [60].

2.5 References

[1] W.J. Koros, W. Madden, Transport Properties, in Encyclopedia of Polymer Science and Technology, 3rd ed., John Wiley & Sons, 2004.

[2] E.L. Cussler, Diffusion: Mass Transfer in Fluid Systems, Cambridge University Press, 2009.

[3] W.J. Koros, G.K. Fleming, Membrane-Based Gas Separation, J Membrane Sci, 83 (1993) 1-80.

[4] R. Baker, Membrane Technology and Applications, Wiley, 2012.

[5] G. van der Donk, Inorganic Microporous Membranes for Gas Separation in Fossil Fuel Power Plants, Forschungszentrum Julich GmbH - Zentralbibliothek, Verlag, 2007.

[6] L.R. Xu, M. Rungta, W.J. Koros, Matrimid (R) derived carbon molecular sieve hollow fiber membranes for ethylene/ethane separation, J Membrane Sci, 380 (2011) 138-147.

[7] J.E. Koresh, A. Soffer, THE CARBON MOLECULAR-SIEVE MEMBRANES - GENERAL-PROPERTIES AND THE PERMEABILITY OF CH4/H-2 MIXTURE, Separ Sci Technol, 22 (1987) 973-982.

[8] D.Q. Vu, W.J. Koros, S.J. Miller, High pressure CO2/CH4 separation using carbon molecular sieve hollow fiber membranes, Ind Eng Chem Res, 41 (2002) 367-380.

[9] T. Graham, On The Law of Diffusion of Gases, The Philosophical Magazine and Journal, 2 (1833) 175.

[10] R.E. Kesting, A.K. Fritzsche, Polymeric gas separation membranes, Wiley, New York, 1993.

[11] W.J. Koros, R.T. Chern, Separation of Gaseous Mixtures Using Polymer Membranes, in Handbook of Separation Process Technology, Wiley-Interscience, New York, 1987.

[12] K. Ghosal, B.D. Freeman, Gas separation using polymer membranes: an overview, Polymers for Advanced Technologies, 5 (1994) 673-697.

[13] D.R. Paul, Y.P. Yampolskii, Polymeric Gas Separations Membranes, CRC Press, Boca Raton, 1994.

[14] B. Freeman, Y. Yampolskii, I. Pinnau, Materials Science of Membranes for Gas and Vapor Separation, Wiley, 2006.

[15] S. Alexander Stern, Polymers for gas separations: the next decade, J Membrane Sci, 94 (1994) 1-65.

[16] W. Madden, THE PERFORMANCE OF HOLLOW FIBER GAS SEPARATION MEMBRANES IN THE PRESENCE OF AN AGGRESSIVE FEED STREAM, in: Chemical Engineering, Georgia Institute of Technology, Atlanta, 2005.

[17] W.R. Vieth, J.M. Howell, J.H. Hsieh, Dual Sorption Theory, J Membrane Sci, 1 (1976) 177-220.

[18] W.J. Koros, D.R. Paul, A.A. Rocha, Carbon-Dioxide Sorption and Transport in Polycarbonate, J Polym Sci Pol Phys, 14 (1976) 687-702.

[19] W.J. Koros, Model for Sorption of Mixed Gases in Glassy-Polymers, J Polym Sci Pol Phys, 18 (1980) 981-992.

[20] W.J. Koros, R.T. Chern, V. Stannett, H.B. Hopfenberg, A Model for Permeation of Mixed Gases and Vapors in Glassy-Polymers, J Polym Sci Pol Phys, 19 (1981) 1513-1530.

[21] D.R. Paul, I.U.P. ͡IAmpolʹskiĭ, Polymeric Gas Separation Membranes, Taylor & Francis, 1994.

[22] D.W. van Krevelen, K. te Nijenhuis, Properties of Polymers: Their Correlation with Chemical Structure; their Numerical Estimation and Prediction from Additive Group Contributions, Elsevier Science, 2009.

[23] J.Y. Park, D.R. Paul, Correlation and prediction of gas permeability in glassy polymer membrane materials via a modified free volume based group contribution method, J Membrane Sci, 125 (1997) 23-39.

[24] I. Pinnau, C.G. Casillas, A. Morisato, B.D. Freeman, Long-term permeation properties of poly(1-trimethylsilyl-1-propyne) membranes in hydrocarbon-vapor environment, J Polym Sci Pol Phys, 35 (1997) 1483-1490.

[25] Y. Maeda, D.R. Paul, Effect of Antiplasticization on Gas Sorption and Transport .3. Free-Volume Interpretation, J Polym Sci Pol Phys, 25 (1987) 1005-1016.

[26] W.M. Lee, Selection of barrier materials from molecular structure, Polymer Engineering & Science, 20 (1980) 65-69.

[27] A. Thran, G. Kroll, F. Faupel, Correlation between fractional free volume and diffusivity of gas molecules in glassy polymers, Journal of Polymer Science Part B: Polymer Physics, 37 (1999) 3344-3358.

[28] L.M. Robeson, Polymer membranes for gas separation, Curr Opin Solid St M, 4 (1999) 549-552.

[29] S.C. George, S. Thomas, Transport phenomena through polymeric systems, Progress in Polymer Science, 26 (2001) 985-1017.

[30] B.D. Freeman, Basis of permeability/selectivity tradeoff relations in polymeric gas separation membranes, Macromolecules, 32 (1999) 375-380.

[31] R.M. Barrer, Permeation, diffusion and solution of gases in organic polymers., T Faraday Soc, 35 (1939) 0628-0643.

[32] D.H. Weinkauf, D.R. Paul, Effects of Structural Order on Barrier Properties, in: Barrier Polymers and Structures, American Chemical Society, 1990, pp. 60-91.

[33] J. Comyn, Polymer Permeability, Springer, 1985.

[34] W.J. Koros, A.H. Chan, D.R. Paul, Sorption and Transport of Various Gases in Polycarbonate, J Membrane Sci, 2 (1977) 165-190.

[35] W.J. Koros, D.R. Paul, Transient and Steady-State Permeation in Poly(Ethylene Terephthlate) above and Below the Glass-Transition, J Polym Sci Pol Phys, 16 (1978) 2171-2187.

[36] D.R. Paul, W.J. Koros, Effect of Partially Immobilizing Sorption on Permeability and Diffusion Time Lag, J Polym Sci Pol Phys, 14 (1976) 675-685.

[37] S. Zhou, S.A. Stern, The Effect of Plasticization on the Transport of Gases in and through Glassy-Polymers, J Polym Sci Pol Phys, 27 (1989) 205-222.

[38] R.M. Barrer, Diffusivities in Glassy-Polymers for the Dual Mode Sorption Model, J Membrane Sci, 18 (1984) 25-35.

[39] M.J. Thundyil, Y.H. Jois, W.J. Koros, Effect of permeate pressure on the mixed gas permeation of carbon dioxide and methane in a glassy polyimide, J Membrane Sci, 152 (1999) 29-40.

[40] J. Welty, Fundamentals of Momentum, Heat, and Mass Transfer, Wiley, 2001.

[41] H.D. Kamaruddin, W.J. Koros, Some observations about the application of Fick's first law for membrane separation of multicomponent mixtures, J Membrane Sci, 135 (1997) 147-159.

[42] B. Freeman, Y. Yampolskii, Membrane Gas Separation, Wiley, 2011.

[43] A.Y. Houde, S.S. Kulkarni, M.G. Kulkarni, Permeation and Plasticization Behavior of Glassy-Polymers - a Waxd Interpretation, J Membrane Sci, 71 (1992) 117-128.

[44] J.D. Wind, Improving Polyimide Membrane Resistance to Carbon Dioxide Plasticization in Natural Gas Separations, in: Chemical Engineering, The University of Texas at Austin, Austin, 2002, pp. 232.

[45] W.J. Koros, J.D. Wind, C. Staudt-Bickel, D.R. Paul, Solid-state covalent cross-linking of polyimide membranes for carbon dioxide plasticization reduction, Macromolecules, 36 (2003) 1882-1888.

[46] J.S. Chiou, J.W. Barlow, D.R. Paul, Plasticization of Glassy-Polymers by Co2, J Appl Polym Sci, 30 (1985) 2633-2642.

[47] T. Visser, G.H. Koops, M. Wessling, On the subtle balance between competitive sorption and plasticization effects in asymmetric hollow fiber gas separation membranes, J Membrane Sci, 252 (2005) 265-277.

[48] M. Wessling, S. Schoeman, T. Boomgaard van den, C.A. Smolders, Plasticization of gas separation membranes, Gas Separation & Purification, 5 (1991) 222-228.

[49] M.F. Kemmere, T. Meyer, Supercritical Carbon Dioxide: in Polymer Reaction Engineering, Wiley, John & Sons, 2005.

[50] A. Bos, I.G.M. Punt, M. Wessling, H. Strathmann, Plasticization-resistant glassy polyimide membranes for CO2/CH4 separations, Sep Purif Technol, 14 (1998) 27-39.

[51] C. Cao, T.S. Chung, Y. Liu, R. Wang, K.P. Pramoda, Chemical cross-linking modification of 6FDA-2,6-DAT hollow fiber membranes for natural gas separation, J Membrane Sci, 216 (2003) 257-268.

[52] Y. Liu, T.S. Chung, R. Wang, D.F. Li, M.L. Chng, Chemical cross-linking modification of polyimide/poly(ether sulfone) dual-layer hollow-fiber membranes for gas separation, Ind Eng Chem Res, 42 (2003) 1190-1195.

[53] C. Staudt-Bickel, W.J. Koros, Improvement of CO2/CH4 separation characteristics of polyimides by chemical crosslinking, J Membrane Sci, 155 (1999) 145-154.

[54] H.Y. Zhao, Y.M. Cao, X.L. Ding, M.Q. Zhou, J.H. Liu, Q. Yuan, Poly(ethylene oxide) induced cross-linking modification of Matrimid membranes for selective separation of CO2, J Membrane Sci, 320 (2008) 179-184.

[55] A. Bhattacharya, J.W. Rawlins, P. Ray, Polymer Grafting and Crosslinking, Wiley, 2008.

[56] W.J. Koros, R. Mahajan, Pushing the limits on possibilities for large scale gas separation: which strategies?, J Membrane Sci, 175 (2000) 181-196.

[57] H. Kita, T. Inada, K. Tanaka, K. Okamoto, Effect of Photo-Cross-Linking on Permeability and Permselectivity of Gases through Benzophenone-Containing Polyimide, J Membrane Sci, 87 (1994) 139-147.

[58] Y. Liu, C.Y. Pan, M.X. Ding, J.P. Xu, Gas permeability and permselectivity of photochemically crosslinked copolyimides, J Appl Polym Sci, 73 (1999) 521-526.

[59] A. Bhattacharya, B.N. Misra, Grafting: a versatile means to modify polymers: Techniques, factors and applications, Progress in Polymer Science, 29 (2004) 767-814.

[60] A.M.W. Hillock, S.J. Miller, W.J. Koros, Crosslinked mixed matrix membranes for the purification of natural gas: Effects of sieve surface modification, J Membrane Sci, 314 (2008) 193-199.

CHAPTER 3: MATERIALS AND EXPERIMENTAL PROCEDURES

3.1 Abstract

This chapter lists all materials used in this study including polymers, solvents, silane agents, catalysts, and gases. The polymers used were cellulose acetate and PDMC (propanediol monoester crosslinkable). Dense film formation will be described in details along with the techniques used to characterize them. The characterization of cellulose acetate will not be discussed in detail here because it is well documented in literature. However, some characterization of the monoesterified 6FDA-DAM: DABA (3:2) will be discussed as well as PDMC crosslinking protocol. On the other hand, the grafting and crosslinking protocols of cellulose acetate will be discussed in the next chapter because it is a new technique that has not been explored previously. In addition, all equipment and procedures used, including permeation set-up and sorption system will be provided as well. All equipment related to the safe handling of H_2S is also discussed.

3.2 Materials

3.2.1 Polymers

The structures of polymers used in this study are summarized in Table 3.1. Cellulose acetate with 39.7 wt% acetyl content (degree of substitution (DS) of 2.45) and an average M_n of ~50,000 was obtained from Sigma-Aldrich. The degree of substitution is the number of acetyl groups per repeat unit and it is calculated using Equation 3.1 [1].

$$DS = \frac{162W}{100M - [(M-1)W]}$$

3.1
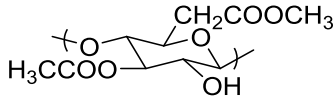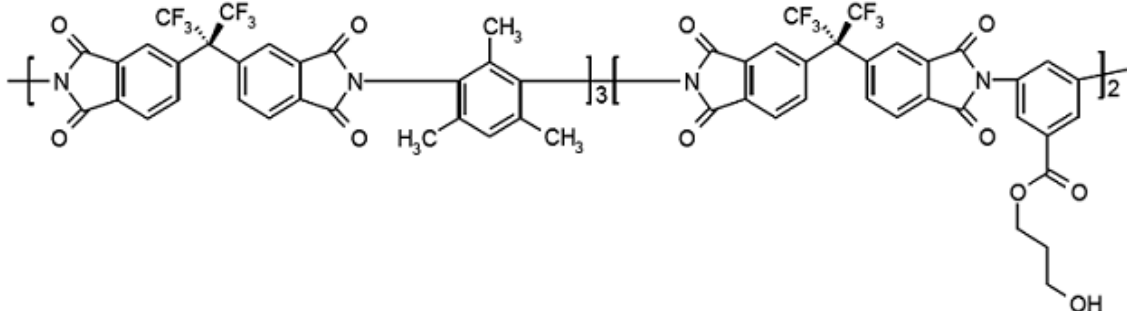
In this equation, W is the percent acetyl content and M is the molecular weight of the acetyl ($COCH_3$) group. The other polymer used in this study is PDMC, a robust, crosslinkable polyimide with a propyl monoester chain attached to the DABA groups in 6FDA-DAM: DABA (3:2). The polymer precursor 6FDA-DAM: DABA (3:2) was obtained from Akron Polymer Systems, Inc. This material was monoesterified in-house as described below by using the previously reported synthesis routes [2-4].

3.2.2 Synthesis of the Crosslinkable PDMC Polymer

The polyimide 6FDA-DAM:DABA (3:2) is synthesized via a polycondensation reaction where the dianhydride, 4, 4'-(hexafluoroisopropylidene) diphthalic anhydride (6FDA), the diamines, 2,4,6-trimethyl-1,3-diaminobenzene (DAM), and the carboxylic acid, 3,5-diaminobenzoic acid (DABA) were all added in solution [5-7]. In this reaction, polyamic acid is produced as the precursor to the polyimide. The second step is the thermal imidization step where the produced polyamic acid is heated to form the imide rings on the polyimide as shown in Figure 3.1. The high temperature used helps drive dehydration of precursor to induce ring closure. Previous researchers showed that the 3:2 DAM: DABA monomer ratio gave superior CO_2/CH_4 performance and a higher CO_2 plasticization resistance [2, 8, 9]. This material was obtained from an outside vendor as discussed previously. However, the final synthesis step, which is a monoesterification via the reaction of 1, 3-propanediol with the pendant carboxylic acid group on the DABA moiety, with water given off as a by-product was synthesized in-house as shown in Figure 3.2. This step was carried out in solution prior to the dense film membrane

formation and produced the uncrosslinked PDMC polymer. More details on this synthesis

can be found elsewhere [2-4].

Table 3.1: Structure of cellulose acetate and PDMC polymers used in this work

Cellulose Acetate (DS=2.45)	
6FDA-DAM:DABA (3:2) **P**ropane **D**iol **M**onoester **C**rosslinkable (PDMC)	
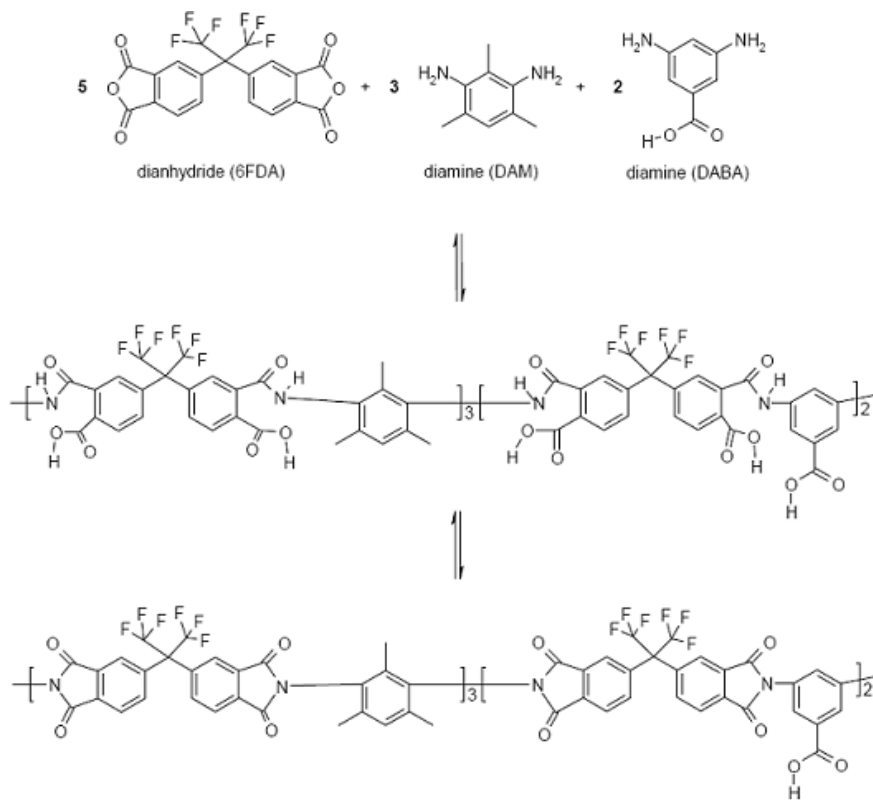
Figure 3.1: Reaction mechanism for the synthesis of 6FDA-DAM: DABA (3:2).

51
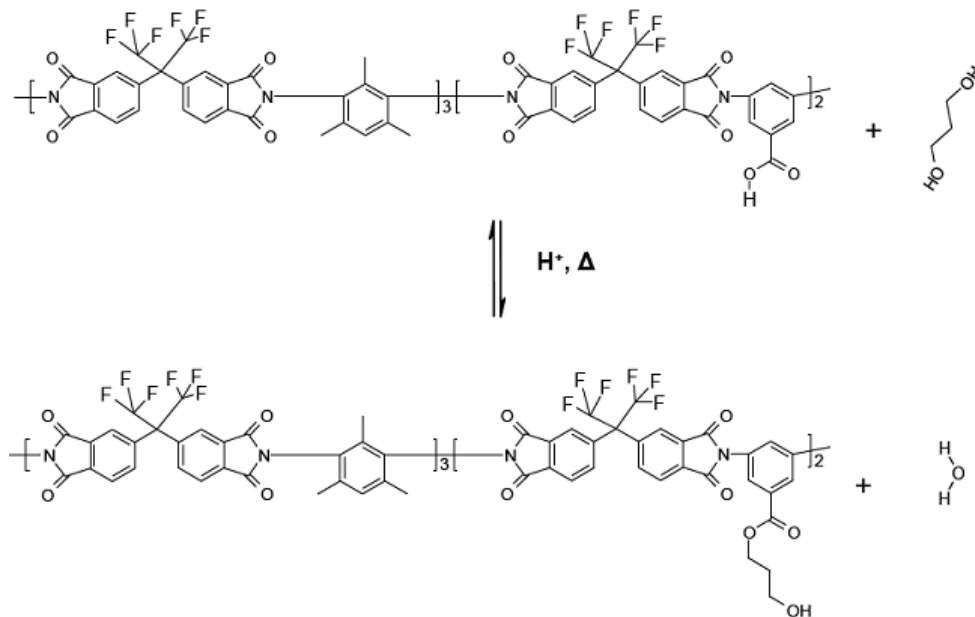
Figure 3.2: Monoesterification reaction for the synthesis of uncrosslinked PDMC.

3.2.3 Solvents

All solvents used in this study were purchased from Sigma Aldrich and are summarized in Table 3.2. Their primary purpose was to dissolve the polymers for membrane formation.

3.2.4 Silane Agents and Catalysts

The silanes used were also obtained from Sigma Aldrich and their properties are summarized in Table 3.3. Vinyltrimethoxysilane (VTMS), and trimethoxysilane (TMS), were all liquids at room temperature, while dicumyl peroxide (DCP) was a solid and was stored between 2-8°C. These materials are discussed in more details in Chapter 5.

Table 3.2: Structure of solvents used in this work
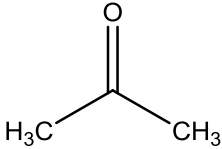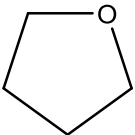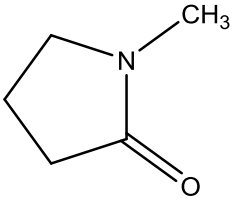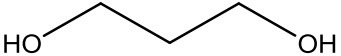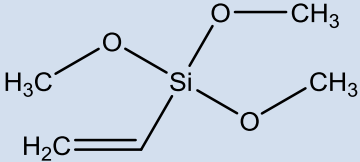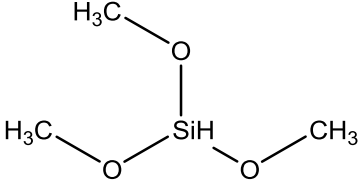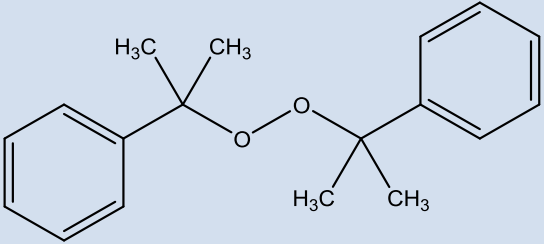
Solvent	Boiling Point (°C)	Structure
Acetone (≥99.5%)	56°C	
Tetrahydrofuran (THF) anhydrous, ≥99.9%	65-67°C	
N-Methylpyrrolidone (NMP) anhydrous, ≥99.5%	202°C	
1,3-Propanediol (98%)	214°C	

Table 3.3: Structure and Properties of silane agents and catalysts used in this study

Chemical	bp or mp (°C)	Density (g/cc)	Structure
Vinyltrimethoxysilane (VTMS) 98%	123°C (bp)	0.968	
Trimethoxysilane (TMS) 95%	81°C (bp)	0.96	
Dicumyl Peroxide (DCP) 98%	39-41°C (mp)	1.56	

3.2.5 Gases

Carbon Dioxide (CO_2) and Methane (CH_4) gases with 99.999% purity were obtained from Airgas, whereas hydrogen sulfide (H_2S) gas was obtained from Praxair with 99.6% purity. The kinetic diameter and critical temperature of these gases are shown in Table 3.4. The specialty gas mixtures used in this study were all obtained from Praxair and are summarized in Table 3.5.

Table 3.4: Kinetic diameters and critical temperatures of gases used in this study [10, 11].

Gas	Kinetic Diameter (Å)	Critical Temperature (K)
CH_4	3.8	190
CO_2	3.3	304
H_2S	3.6	373

Table 3.5: Gas mixtures used in this study

	H_2S	CO_2	CH_4
Mixture 1	5.0%	-	95%
Mixture 2	10%	-	90%
Mixture 3	10%	20%	70%
Mixture 4	20%	20%	60%
Mixture 5	-	50%	50%

3.2.6 Other Materials

As required by EHS, additional PPE (personal protective equipment) was used for handling H_2S. An air-purifying respirator (APR) was used for protection against toxic gases like H_2S. A North® Silicone 7700 Series Half Mask APR equipped with North® Organic Vapor/Acid Gas Cartridges, both obtained from Airgas was worn before entering

the lab. In addition, a Gas Alert Clip Extreme H$_2$S monitor from BW Honeywell was worn at all times while working in the lab to detect any abnormal H$_2$S concentrations. Both of these pieces of equipment are shown in Figure 3.3.

Figure 3.3: Half-mask APR respirator (left) and H$_2$S detector (right) used in this study.

3.3 Dense Film Membrane Fabrication

3.3.1 Formation of Cellulose Acetate Dense Films

Cellulose acetate powder was first dried under vacuum at 100°C for 24 hrs to remove any sorbed moisture. The polymer powder was then dissolved in acetone to make a 15-20 wt% solution. The dense film was formed using a knife casting method in a sealed glove bag (Glass-col LLC, Terre Haute, IN). The bag was first swept with N$_2$ gas to eliminate any impurities; it was then saturated with acetone for 4 hours prior to casting to reduce the rate of solvent evaporation upon casting [12]. This pre-saturation of the vapor space prevents irregularities or defects caused by excessively rapid evaporation. After this step,

the polymer solution was cast onto a clean glass plate using a 250-500μm stainless steel gap knife as shown in Figure 3.4, and the solvent was allowed to evaporate for 24 hrs before removing the film from the plate. The film was then dried under vacuum at 100°C for 24 hrs to remove residual solvent.
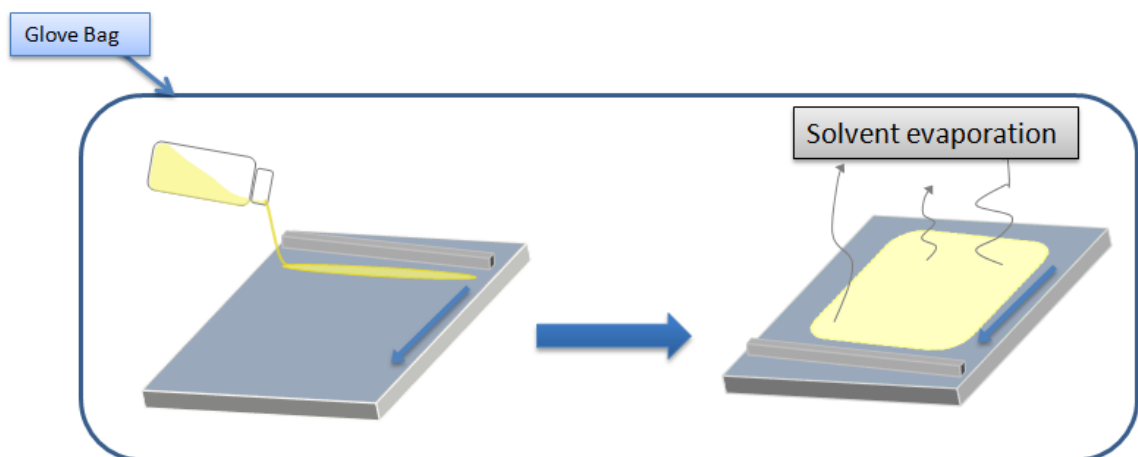
Figure 3.4: Schematic of the dense film knife casting setup.

3.3.2 Formation of Uncrosslinked PDMC Films

The same procedure described above was used to cast the PDMC films. The PDMC polymer powder was dried at 100°C to remove any sorbed moisture. After drying, the polymer was dissolved in Tetrahydrofuran (THF) to make a 15-20 wt% solution. The bag was purged with N_2 gas to eliminate any impurities; it was then saturated with THF for 4 hours prior to casting. The polymer-containing solution was cast (using a 250-500μm stainless steel gap knife) onto a clean glass plate previously treated with Glassclad®18 (Gelest, Inc) to facilitate the removal of the film from the plate after solvent evaporation. The film was then dried under vacuum at 100°C for 24 hrs to remove residual solvent.

3.3.3 Formation of Crosslinked PDMC Films

The crosslinking was achieved via a transesterification reaction as shown in Figure 3.5. Samples of the above dried uncrosslinked PDMC films were heated at 220° and 295°C under vacuum for 24 hrs to induce thermal crosslinking as described by previous researchers [2, 3]. The films were slowly cooled down to room temperature after heating.
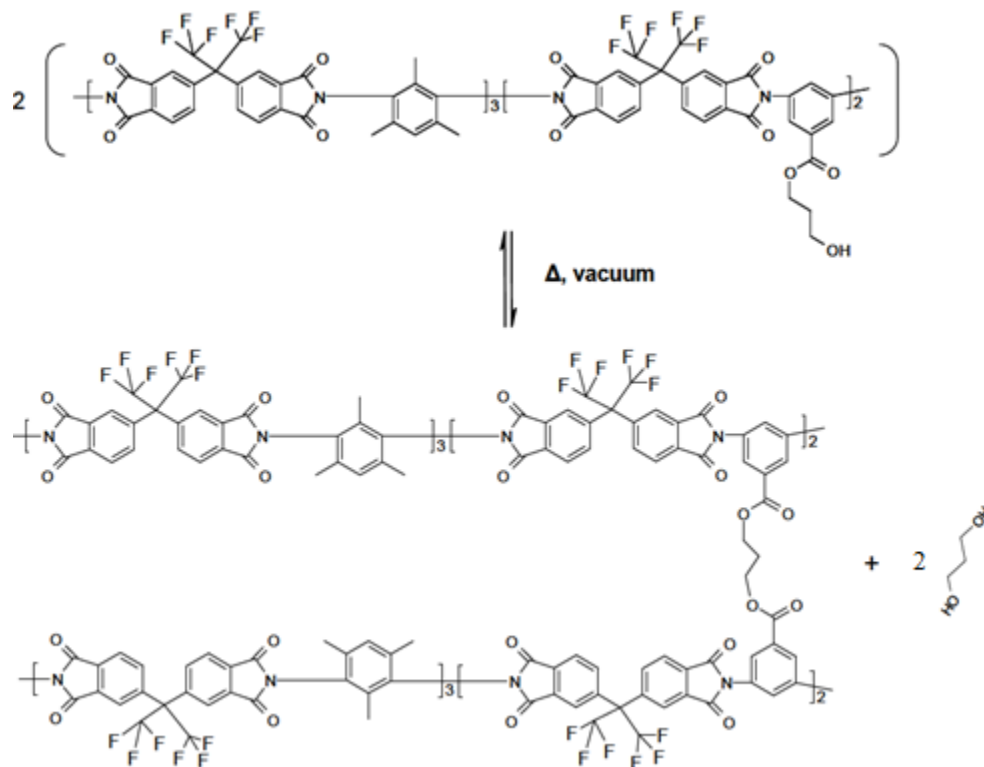
Figure 3.5: Transesterification or thermal crosslinking mechanism of PDMC films.

3.4 Membrane Characterization Techniques

3.4.1 Fourier Transform Infrared Spectroscopy (FTIR)

The infrared spectra (FTIR-ATR) were measured using a Bruker Tensor 27 FT-IR spectrometer (Bruker Corp, Billerica, MA) equipped with a Harrick MVP 2 Series™ ATR (Harrick Scientific Products Inc., Pleasantville, NY.). Each sample was analyzed

using 128 scans with a scanner velocity of 10 kHz with a resolution of 4 cm^{-1} and 6 mm aperture setting. Each sample was scanned from 370-4000 cm^{-1} with KBr as the beamsplitter. This technique was used to confirm the chemistry of the polymers and silanes used in this study and to understand the chemistry of the modified membrane in Chapter 5.

3.4.2 Nuclear Magnetic Resonance Spectroscopy (NMR)

The NMR results presented here were measured at the Georgia Tech NMR Center by Johannes Leisen using a high resolution Bruker DSX300 solid-state spectrometer. ^{13}C solid state NMR spectra were recorded at a ^{13}C frequency of 75 MHz, ^1H 90 degree pulse length of 5 µs, MAS at 10 kHz, VACP (variable amplitude CP) with a ramp on ^1H ranging from 85-100%, 1ms contact time, and repetition delay of 4s. ^{13}C solid-state NMR was used to identify how the carbon atoms are bonded in the modified CA structure discussed in Chapter 5. The ^{29}Si measurements were carried out with a ^{29}Si frequency of 59.6 MHz, ^1H 90 degree pulse length 5 µs, MAS at 10 kHz with regular CP (no ramp in the contact pulse), a contact time of 3000 µs and repetition delay of 5s. ^{29}Si has a natural isotropic abundance of 4.7%, a nuclear spin of ½, and a magnetic moment that is slightly lower than that of ^{13}C, leading to a lower resonance frequency. The referencing in ^{29}Si NMR is mostly done relative to tetramethylsilane (TMS) due to their low boiling point, inert nature, and short relaxation time [28]. Negative values of the ^{29}Si shift are due to low frequency and high field compared to TMS. This technique was used to identify and/or confirm the structure of newly synthesized polymers such as the one described in Chapter 5.

3.4.3 Thermogravimetric Analysis (TGA)

TG curves were obtained from STA 409PC Luxx from NETZSCH, Burlington, MA. The samples were heated at a rate of 10°K/min from 25°C to 800°C in argon at a flow rate of 30 ml/min. This technique was used to study the thermal stability of polymers used.

3.4.4 Differential Scanning Calorimetry (DSC)

DSC curves were obtained from a DSC Q200 from TA Instruments. Aluminum pans were used for the samples and reference, under a nitrogen atmosphere with a flow rate of 50 ml/min. The samples were first heated from 40°C to 250°C at a rate of 10°C/min, then were kept at 250°C for 2 mins, and finally cooled to 40°C at 10°C/min. This technique was used to determine thermal phase and glass transitions in the materials.

3.4.5 Dynamic Mechanical Analysis (DMA)

Dynamic Mechanical analysis was done using a DMA Q800 from TA Instruments. Operations conditions were: heating rate of 3°C/min from 100°C-250°C, a fixed frequency of 3 Hz in air using the tensile geometry clamp. This technique was mainly used to determine the glass transition temperature and to identify transitions corresponding to other molecular motions in the polymers under study.

3.4.6 X-Ray Diffraction (XRD)

X-rays diffraction patterns were obtained using a PANalytical X'Pert Pro with a Ni filter and Cu Kα radiation source of wavelength 1.54Å. Measurements were made from 5° to

60° using an X'celerator detector. The technique was used to determine the amorphous structure of thin polymer films.

3.4.7 Gas Chromatography-Mass Spectrometry (GC-MS)

The instrument used in for GC-MS measurements was a Micromass AutoSpec M, and the GC was an Agilent 6890 with an Agilent 6890 autosampler. The GC column was a J&W DB 5MS, 30m x 0.25mm, with a 0.25µm film thickness. One µL of the sample solution was injected at a split ratio of 50:1, and the carrier gas was helium. The initial column temperature was 30°C, and after a 1-minute hold, the temperature was ramped to 300°C at 15°C/min, with a 6-minute hold at 300°C. This technique was used to analyze the chemical composition of the liquid residues from the reaction presented in Chapter 5.

3.4.8 X-Ray Photoelectron Spectroscopy (XPS)

XPS results presented here were measured using a Thermo K-alpha XPS using aluminum (Al) Kα radiation, a 100µm spot size, and a 50 eV pass energy. This technique was used to characterize the atomic composition of the thin polymer films surfaces.

3.4.9 Elemental Analysis

Elemental analysis of the GCV-Modified and the neat CA samples were performed by Columbia Analytical Services, Inc., located in Tucson, AZ. The samples were grinded prior to analysis. The Si wt% was obtained using the total dissolution method. The C and H wt% were obtained by combustion, and the O wt% was obtained by pyrolysis.

3.4.10 Density Column Gradient

A Techne DC-1 density gradient column was used to measure the density of uncrosslinked, crosslinked PDMC, and modified CA films. This technique helped obtain reliable density measurements down to three decimal places (0.001 g/cc). The column was filled with both a low and a high density $Ca(NO_3)_2$ solutions, and calibrated weights spanning the density range selected were also added in the column. Once an approximately linear density gradient was established, the samples were introduced. The density of the sample was determined based on the known densities of the calibrated weights and the linearity of the column.

3.4.11 Gel Content

This technique was used to determine the degree of crosslinking of the films [13, 14]. In the gel content experiment, the polymer films were first dried and weighted; they were then immersed in NMP solvent and heated to 100°C for 24 hrs to dissolve the soluble fraction. The solution was filtered and the insoluble gel was dried at 250°C overnight to remove the excess solvent. The film residue was weighed. The gel content was calculated using Equation 3.2 :

$$\text{Gel Content} = \frac{m_{\text{residue}}}{m_{\text{initial}}} \times 100\%$$

3.2

3.5 Characterization of Uncrosslinked and Crosslinked PDMC Films

The degree of monoesterification was estimated using ^{1}H solid state NMR. Previous researchers used ^{1}H solution NMR to quantify the monoester conversion. The only

difference is that liquid samples yield sharper signals than solids, so the spectra of solids will typically show signals wider than their chemical shift range. Figure 3.6 shows the ^{1}H solid state NMR of uncrosslinked PDMC. In ^{1}H solution NMR, the methylene proton (circled in red on Figure 3.6) closest to the DABA gives a signal around 4.6 ppm, whereas the aromatic proton from the DAM moiety gives a signal around 7.3 ppm [3, 4, 15] . In this ^{1}H NMR spectrum, peaks are identified in similar chemical shift ranges. The monoester conversion was found by taking the ratio of the methylene proton peak to the aromatic proton from the moiety, and the monoester conversion was found to be ~90%. This high conversion from the monoester reaction was adequate to obtain high crosslinking conversions, as previous researchers showed that at least a 50% monoester conversion was necessary to achieve a 100% conversion in solid-state crosslinking [15].
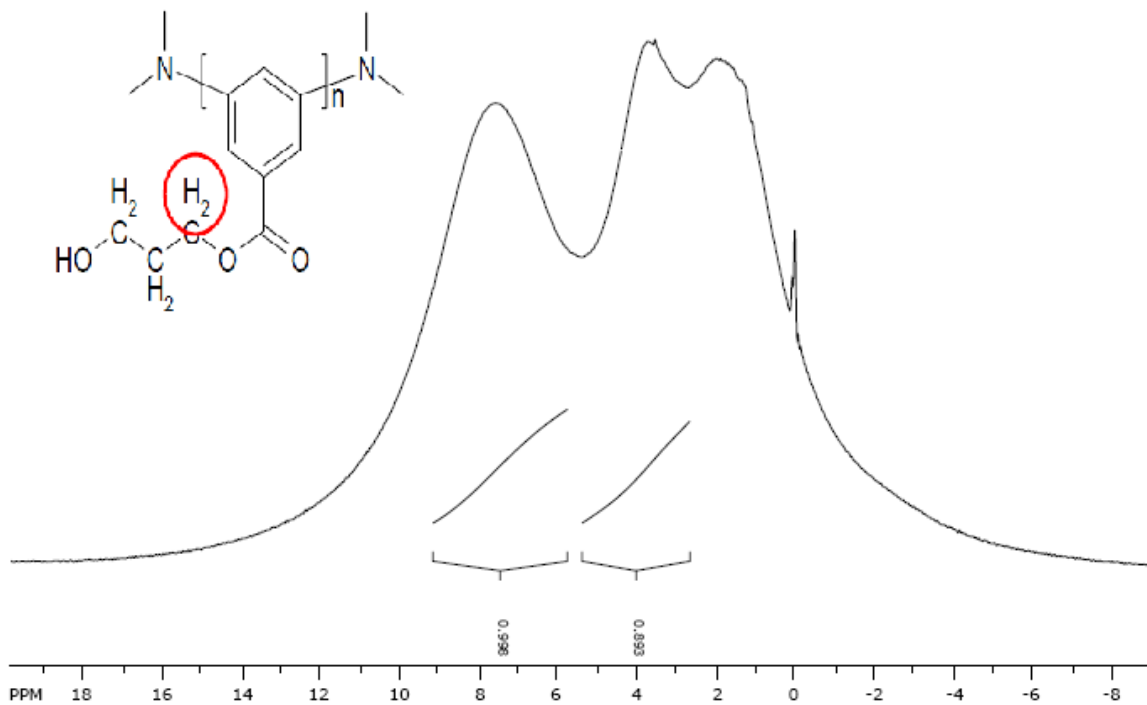
Figure 3.6: ^{1}H Solid state NMR analysis of uncrosslinked PDMC.

The gel content of crosslinked PDMC films was measured to determine the degree of crosslinking and is shown in Table 3.6 along with their densities. The increase in density with increasing crosslinking temperature is in good agreement with previously reported studies [3, 15]. This trend is likely due to the densification of the polymer matrix during the elimination of the propanediol group during the transesterification reaction.

Table 3.6: Density of uncrosslinked and crosslinked PDMC films

	Density (g/cc)	Gel Content (%)
Uncrosslinked PDMC	1.393±0.0015	-
Crosslinked PDMC @ 220°C	1.398±0.0019	96.1±0.23%
Crosslinked PDMC @ 295°C	1.400±0.0021	99.8±0.11%

3.6 Permeation Testing

3.6.1 Film Masking

This step was designed to prepare the film for permeation testing. In this masking step, an area of the large polymer film with no visible defects was cut and sandwiched between two circular pieces of aluminum tape. The films thicknesses were measured using a micrometer. The sandwiched film was then mounted into a stainless steel permeation cell and sealed with a bigger diameter aluminum foil piece. The contours were covered with a black Duralco 4525 epoxy (Cortronics Corp., Brooklyn, NY) as shown in Figure 3.7 to prevent any high pressure gas from bypassing the aluminum tape seal. The epoxied film was cured at 35°C overnight. The available film area for gas permeation was measured

using the Photoshop software before closing the cell. The upstream and downstream sides of the cell were equipped with two rubber O-rings of different diameters to provide a good seal to avoid any gas leaks. The cell was then closed, loaded onto the permeation system described in the next section.
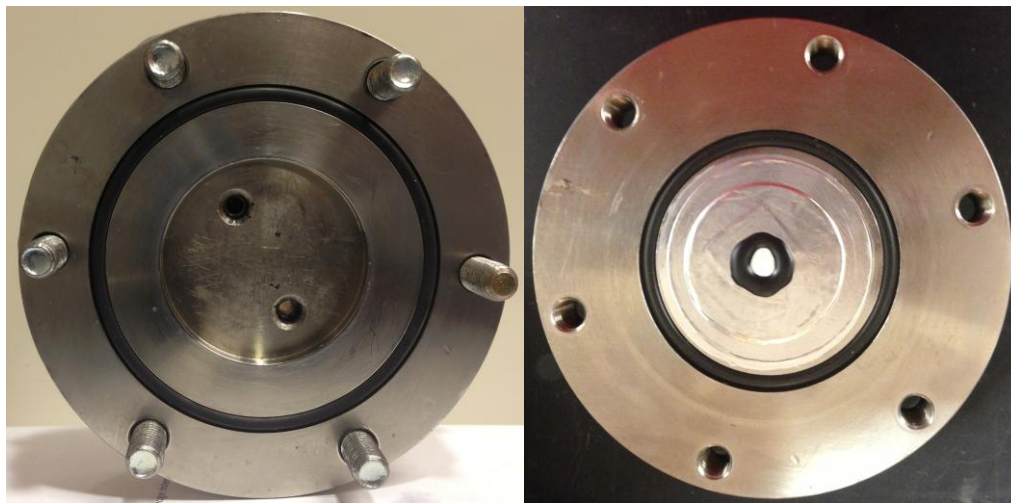
Figure 3.7: Actual picture of the top (left) and bottom (right) of a permeation cell.

3.6.2 Permeation System Design

Single and mixed gas steady state permeabilities were measured via an isochoric (constant volume), variable pressure system as previously described [16-18]. A schematic of the system used in this study is shown in Figure 3.8. This system was modified from the previously reported systems in order to (1) ensure high safety when handling H_2S gas mixtures as described in section 3.4.3 and (2) to allow nonvacuum permeate measurements. Major components of this system are described in Table 3.7. Components L and K were added to allow nonvacuum permeate measurements. The system was connected to a Varian 450-GC gas chromatograph for downstream mixed gas sampling.

The ISCO syringe pump was used to obtain a desired high pressure unattained by the cylinder regulator and to help maintain a low stage cut during mixed gas experiments as discussed later. The fan heater was used to regulator the temperature inside the permeation box to keep the system isothermal. The entire system was connected to Swagelok 316 SS stainless tubing of either ¼"OD or 1/8" OD.

Table 3.7: Constant-volume permeation system major components

Components	Vendor
A. Retentate Shutoff Valve	Swagelok Double Sealed Bellows Valve
B. Pneumatically-actuated Feed Valve	Swagelok Pneumatic Actuated Bellows Valve
C. Upstream Pressure Transducer	Honeywell (2000 psia max. pressure)
D. Retentate Metering Valve	Swagelok Back Pressure Regulator
E. 500mL Ballast Volume	-
F. Feed Isolation Valve	Swagelok Double Sealed Bellows Valve
G. Pressure Adjusting Vent Valve	Swagelok Double Sealed Bellows Valve
H. Feed Input Valve	Swagelok Double Sealed Bellows Valve
J. Upstream/Downstream Isolation Valve	Swagelok Double Sealed Bellows Valve
K. 5000 torr Downstream Isolation Valve	Swagelok Short Handle Bellows Valve
L. 5000 torr Pressure Transducer	MKS Instruments, Inc
M. 50 torr Pressure Transducer	MKS Instruments, Inc
N. Pneumatically-actuated GC Isolation Valve	Swagelok
O. 50 torr Downstream Isolation Valve	Swagelok Double Sealed Bellows Valve
P. Syringe Pump	1015 mL D Series Syringe Pump (Teledyne Isco)
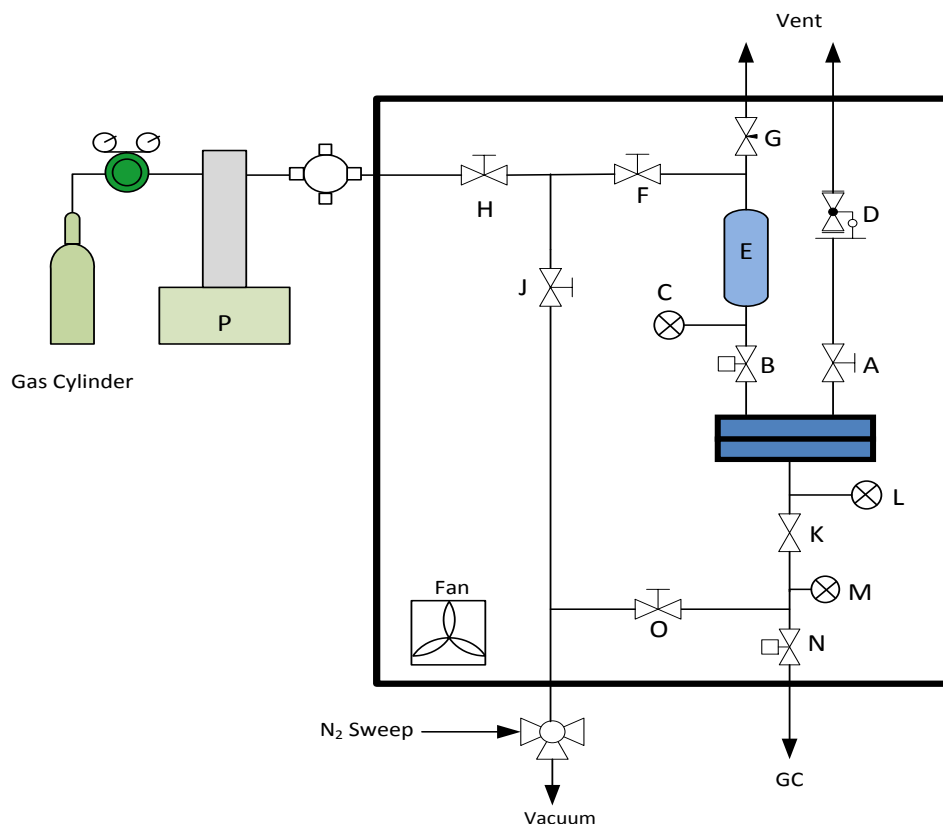
Figure 3.8: Schematic of the dense film permeation apparatus used in this study.

3.6.3 Additional Permeation System Design for Safe H₂S Handling

Because H_2S is a toxic gas, further modifications were made to ensure its safe handling [19]. The two pneumatically-actuated valves (B and N) in Figure 3.8 were controlled by the LabVIEW® program for additional safety; the downstream actuated valve was programmed to shut down when the downstream pressure reached the maximum transducer pressure (50 torr) to avoid over-pressurization that may damage the transducers or to prevent unintended release of high amounts of H_2S. The permeation box was enclosed in a large ventilated cabinet made of Plexiglass (Figure 3.9) as a secondary compartment to prevent H_2S exposure if a leak was to occur in the system. This cabinet

was linked to a negative pressure overhead duct, which was connected to a vertical packed bed H_2S scrubber (Indusco Environmental Services, Inc), equipped with a recirculation system designed to pump a 20-25wt% sodium hydroxide scrubbing solution from the sump to the spray headers.
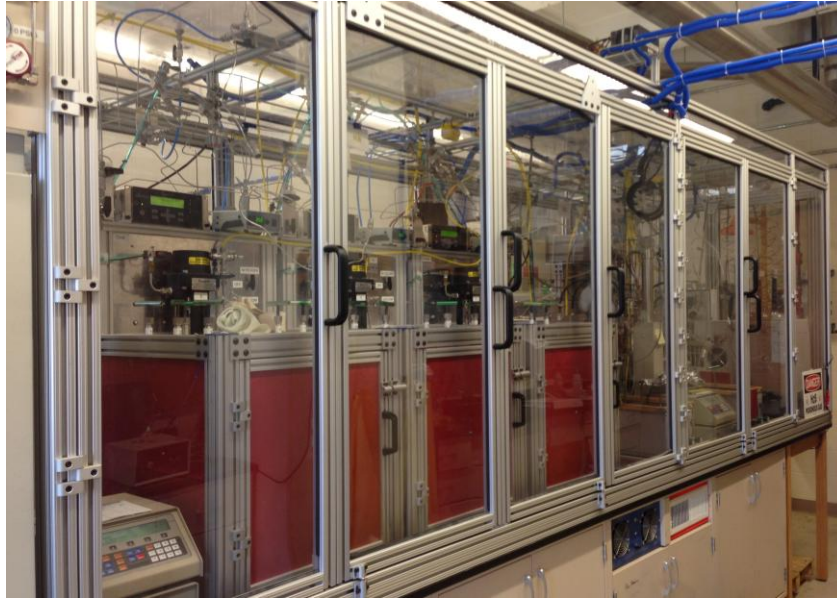
Figure 3.9: Picture of the Plexiglass enclosed permeation systems for safe H_2S handling.

3.6.4 Permeation Testing Procedure

3.6.4.1 Pure Gas Testing

Before the beginning of the experiment, vacuum was pulled on the upstream and the downstream sides to degas both the lines and the film, and to minimize the leak rate. This degassing step was achieved by sequentially opening valves O, K, and J. Many researchers reported membrane degassing times ranging from a few hours to several days depending on the system under study [20, 21]. In this case, degassing times ranging from

12-72 hrs was used depending on the gas to be removed. Once the system was vacuumed, all the upstream and downstream valves were closed and the pressure rise was recorded using LabVIEW® for ~0.5 – 2 hrs. The system leak rate (dp/dt) was obtained from the slope of the plot of pressure vs. time. After the leak rate was obtained, valves K and O were opened, keeping the downstream under vacuum to ensure that the permeate pressure was always lower than the upstream to prevent the film from breaking. The feed valves H and F were opened to fill the upstream ballast volume with gas. Once the upstream reached the desired pressure, valve O was closed (while valve K remained open) in the case of vacuum permeate measurements. However, for nonvacuum downstream, valve K was closed. Valve B was then opened on the LabVIEW® program to introduce gas on the upstream side of the membrane. As the gas diffused through the membrane to the permeate side, the permeate pressure was recorded on the using the LabVIEW® program until steady-state was reached. The upstream pressure was maintained constant throughout the experiment and also recorded using LabVIEW®, mainly to ensure that there were no leaks on the upstream. A downstream pressure vs. time plot was then generated using the data collected. In general, because of the tendency of both CO_2 ad H_2S to plasticize the membrane, measurements were conducted sequentially, in the order of increasing condensability: $CH_4 < CO_2 < H_2S$.

3.6.4.2 Mixed Gas Testing

The same procedure described in the previous section was used when dealing with multicomponent gas mixtures. The feed pressure and retentate flow were maintained by keeping the stage cut below 1% using the ISCO syringe pump and the retentate metering

valve. The syringe pump was maintained at constant pressure and the gas was fed at the same rate as the retentate vented through the metering valve. The stage cut is the fraction of a feed mixture that is allowed to permeate through the membrane. A low stage cut was used to prevent concentration polarization on the upstream in order to maintain a constant driving force across the membrane during the experiment. Once the system reached steady-state, the GC isolation valve N was opened to send a sample to the GC to obtain the permeate gas composition. The downstream isolation valve was closed (K or N) to allow the pressure to rise again and the permeate gas was sampled each time after steady-state was reached. This was repeated as many times as possible to ensure consistency in the results.

3.6.5 Pure Gas Permeation Analysis

The transient period of permeation can be characterized to obtain the time lag Θ, which was used to predict the time period for the system to reach steady-state. This period was typically taken after 10-15 Θ, after which data collection was stopped. The steady-state used in this study was well above the mathematically 4-6 Θ predicted steady-state [22]. The time lag was obtained by taking the zero-pressure time intercept of the steady-state linear fit as depicted in Figure 3.10. The time lag Θ, the diffusivity D, and the membrane thickness l are related through Equation 3.3. Even though the time lag was not necessary to evaluate permeability and solubility data, it was widely used as a data consistency check to ensure that the experimentally observed values are consistent with Fick's law predictions [23].

$$D = \frac{l^2}{6\Theta} \qquad 3.3$$
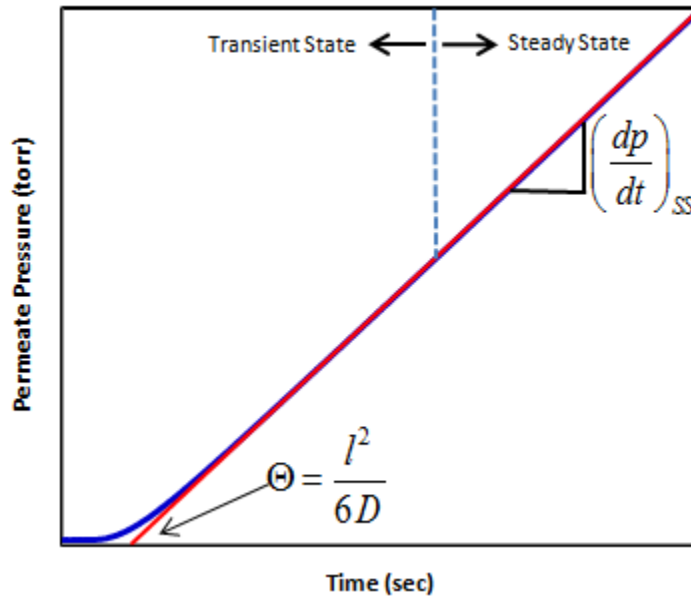
Figure 3.10: Transient permeation plot for gas transport rates determination.

The permeability coefficient was calculated using Equation 3.4:

$$P(Barrer) = \frac{\left\{\left(\dfrac{dp}{dt}\right)_{SS} - \left(\dfrac{dp}{dt}\right)_{leak}\right\}\left(\dfrac{torr}{\sec}\right) \times V_d(cm^3) \times l(cm) \times V_{STP}\left(\dfrac{cm^3(STP)}{mol}\right)}{\Delta f(psia) \times \left(\dfrac{psia}{5.1715 cmHg}\right) \times R\left(\dfrac{cm^3 torr}{mol.K}\right) \times T(K) \times A(cm^2) \times 1 \times 10^{-10}\left(\dfrac{cm^3(STP).cm}{cmHg.cm}\right)} \qquad 3.4$$

V_d : Downstream volume

V_{STP} : Standard molar volume $\cong 22{,}413 \ cm^3(STP)$/mol

l : Membrane thickness

R : Universal gas constant $\cong 62{,}356 \ cm^3 torr$/mol K

Let: $\left(\dfrac{dp}{dt}\right)_{net} = \left(\dfrac{dp}{dt}\right)_{SS} - \left(\dfrac{dp}{dt}\right)_{leak}$

By substituting standard values shown above, we obtain the following simplified expression for the permeability coefficient of a component *i* in the case of a ***negligible permeate pressure***:

$$P_i(Barrer) = \frac{6.95 \times 10^8 \times \left(\dfrac{dp}{dt}\right)_{net} \left(\dfrac{torr}{\sec}\right) \times V_d(cm^3) \times l(cm)}{f_{i,u}(psia) \times T(K) \times A(cm^2)}$$

3.5

$f_{i,u}$: Fugacity of component i upstream

$f_{i,u} = \varphi_{i,u} p_{T,u}$

$p_{T,u}$: Total upstream pressure

$\varphi_{i,u}$: Fugacity coefficient of component i in the feed at pressure $p_{T,u}$

In the case of **nonvacuum permeate**, the permeability coefficient becomes:

$$P_i(Barrer) = \frac{6.95 \times 10^8 \times \left(\dfrac{dp}{dt}\right)_{net} \left(\dfrac{torr}{\sec}\right) \times V_d(cm^3) \times l(cm)}{\left(f_{i,u} - f_{i,d}\right)(psia) \times T(K) \times A(cm^2)}$$

3.6

$f_{i,d}$: Fugacity of component i downstream

$f_{i,d} = \varphi_{i,d} p_{T,d}$

$p_{T,d}$: Total downstream pressure

$\varphi_{i,d}$: Fugacity coefficient of component i in the permeate at pressure $p_{T,d}$

The above expression can be further simplified to give Equation 3.7. It was particularly important to adjust the pressures for fugacity because of the highly condensable gases used in this study. The fugacity coefficients of the pure gases were calculated from the Peng Robinson equation of state, specifically using the Lewis Fugacity Rule equation. The calculated coefficients are shown in Appendix D.

$$P_i(Barrer) = \frac{6.95 \times 10^8 \times \left(\dfrac{dp}{dt}\right)_{net} \left(\dfrac{torr}{\sec}\right) \times V_d(cm^3) \times l(cm)}{\left(\varphi_{i,u} \times p_{T,u} - \varphi_{i,d} \times p_{T,d}\right)(psia) \times T(K) \times A(cm^2)}$$

3.7

3.6.6 Mixed Gas Permeation Analysis

In the case of multicomponent permeation, with *vacuum downstream*, the pressure rise was adjusted to account for each gas contribution to the overall flow to give rise to Equation 3.8:

$$P_i(Barrer) = \frac{6.95 \times 10^8 \times y_i \left(\dfrac{dp}{dt}\right)_{net} \left(\dfrac{torr}{\sec}\right) \times V_d(cm^3) \times l(cm)}{\left(x_i \, \hat{\varphi}_{i,u} \, p_{T,u}\right)(psia) \times T(K) \times A(cm^2)}$$

3.8

y_i : Mole fraction of component i downstream

x_i : Mole fraction of component i upstream

$\hat{\varphi}_{i,u}$: Fugacity of component i in the feed mixture at pressure $p_{T,u}$

$p_{T,u}$: Total Upstream Pressure

$f_{i,u} = x_i \, \hat{\varphi}_{i,u} \, p_{T,u}$

The mixed gas selectivity of a gas i over a gas j, with *vacuum downstream*, was calculated using Equation 3.9.

$$\alpha_{i/j} = \frac{P_i}{P_j} = \left(\frac{y_i}{y_j}\right) \times \left(\frac{x_j}{x_i}\right) \times \left(\frac{\hat{\varphi}_{j,u}}{\hat{\varphi}_{i,u}}\right)$$

3.9

For the case of *nonvacuum permeate*, Equation 3.6 was corrected to give Equation 3.10:

$$P_i(Barrer) = \frac{6.95 \times 10^8 \times y_i \left(\dfrac{dp}{dt}\right)_{net} \left(\dfrac{torr}{\sec}\right) \times V_d(cm^3) \times l(cm)}{\left(x_i \, \hat{\varphi}_{i,u} \, p_u - y_i \, \hat{\varphi}_{i,d} \, p_d\right)(psia) \times T(K) \times A(cm^2)}$$

3.10

$\hat{\varphi}_{i,d}$: Fugacity of component i in the downstream mixture at pressure p_d

p_d : Total Downstream Pressure

$f_{i,d} = y_i \, \hat{\varphi}_{i,d} \, p_d$

The mixed gas selectivity with ***nonvacuum downstream*** was calculated using Equation 3.11.

$$\alpha_{i/j} = \frac{P_i}{P_j} = \left(\frac{y_i}{y_j} \right) \times \left(\frac{x_j \, \hat{\varphi}_{j,u} \, p_{T,u} - y_j \, \hat{\varphi}_{j,d} \, p_{T,d}}{x_i \hat{\varphi}_{i,u} \, p_{T,u} - y_i \, \hat{\varphi}_{i,d} \, p_{T,d}} \right) \qquad 3.11$$

The fugacity coefficients of all gases in the mixtures of Table 3.5 that were used in this study can be found in Appendix D. The full rigor Peng Robinson equation of state in ThermoSolver was used to obtain those coefficients.

3.7 Sorption Testing

3.7.1 Sorption System Design

The solubility coefficients and the sorption capacities of all the polymers studied were measured using the pressure decay method. As discussed in Chapter 2, glassy polymers solubility coefficients are obtained using the dual-mode sorption model. The design of the sorption apparatus was slightly modified from previously reported systems [2, 15, 24, 25] as shown in Figure 3.11. The apparatus is composed of two main compartments: the reservoir and the sample cell. Other components are listed in Table 3.8. As discussed in the case of permeation, the system was also enclosed in a large ventilated cabinet made of Plexiglass to avoid hazardous exposure to H_2S in case there was a leak. The pneumatically-actuated sample cell (valve C) was controlled by the LabVIEW®

software. The sample cell housed the membrane, the pressure transducers were used to measure the pressure in each compartment at all times during the experiment. The entire apparatus was kept in silicone oil bath to provide an isothermal system and the temperature was carefully monitored.
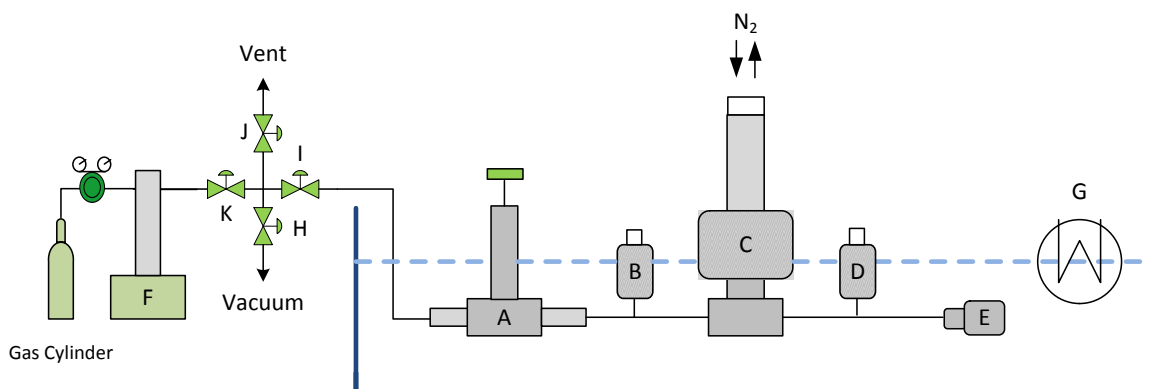
Figure 3.11: Pressure-decay sorption apparatus.

Table 3.8: Pressure-decay sorption system components list

Component	Vendor
A. Reservoir Isolation Valve	Swagelok
B. Reservoir Pressure Transducer	Ametek Aerospace (1000 psia limit)
C. Pneumatic Sample Cell Valve	Swagelok
D. Sample Cell Pressure Transducer	Ametek Aerospace (1000 psia limit)
E. Sample Cell	Swagelok
F. Syringe Pump	D Series Isco (Teledyne)
G. Heating Element with Temperature Controller	Polyscience
H, I, J, and K: Short Handle Bellows Valves	Swagelok

3.7.2 Sorption Testing Procedure

To begin the experiment, the polymer film was first dried under vacuum to remove any sorbed moisture; the film was weighed and loaded inside the sample cell. The system was degassed for sufficient time to eliminate any gas present in the lines and in the membrane (vacuum time ranged from 12-48 hrs depending on the gas used). This was done by manually opening valves H, I, A, by selecting vacuum under the drop-down menu shown in Figure 3.12, and then clicking start to automatically open valve C. Once the system was evacuated, all valves were closed. The LabVIEW® program was programmed to collect data every 1-5 sec, the reservoir equilibrium interval time was set between 30 – 90 mins, and valve C open interval time was set at 1 sec for all experiments. Once programmed, valves K, I, and A were manually opened to introduce gas into the reservoir. Once gas entered the reservoir, valve A was closed and the reservoir pressure was allowed to equilibrate. After valve A programmed equilibration time elapsed, the pneumatically-actuated valve C was automatically opened for 1 sec to allow gas to enter the sample cell. LabVIEW® recorded the pressure change over time in both the reservoir and the cell. Data collection was manually stopped once the system reached equilibrium.
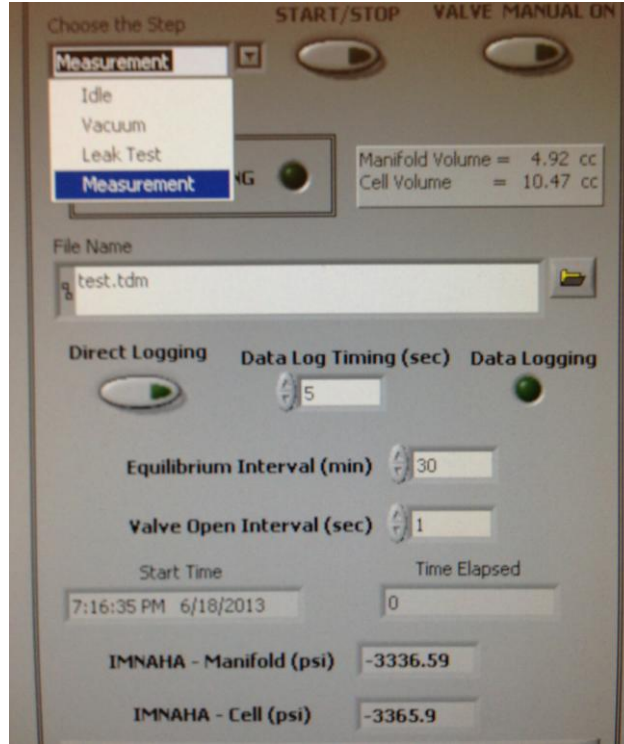
Figure 3.12: Screenshot of LabVIEW® interface for sorption measurements.

3.7.3 Sorption Data Analysis

The amount of moles sorbed by the polymer was calculated by doing a simple mole balance on the sample cell as shown in Equation 3.12.

$$n_{sorbed} = \left(n_{R,i} - n_{R,f}\right) + \left(n_{C,i} - n_{C,f}\right) \qquad 3.12$$

n_R : Initial and final moles of gas in the reservoir
n_C : Initial and final moles of gas in the sample cell

By substituting the ideal gas law into the equation, the following expression was derived to obtain the moles of gas sorbed.

$$n_{sorbed} = \frac{1}{RT} \times \left[V_R \left(\frac{P_{R,i}}{Z_{R,i}} - \frac{P_{R,f}}{Z_{R,f}} \right) + \left(V_C - V_P\right) \left(\frac{P_{C,i}}{Z_{C,i}} - \frac{P_{C,f}}{Z_{C,f}} \right) \right] \qquad 3.13$$

76

$$n_{sorbed} \equiv \left[mol \right]$$

$$V_R, V_C, V_P \equiv \left[cm^3 \right] : \text{Reservoir, cell, and polymer volumes}$$

Z: Compressibility factor

$$R \cong 1206 \, cm^3 psia \, / \, mol \, K$$

The compressibility factors of the gases used in study are shown in Appendix D. The sorbed concentration was calculated to determine the solubility coefficient using Equation 3.14.

$$C_{sorbed} \left[\frac{cm^3 (STP)}{cm^3} \right] = \frac{n_{sorbed} \left[mol \right] \times V_{STP} \left[\frac{cm^3}{mol} \right]}{V_P \left[cm^3 \right]} \qquad 3.14$$

3.8 References

[1] Degree of Substitution, in: Encyclopedia of Polymer Science and Technology, John Wiley & Sons, Inc., 2002.

[2] I.C. Omole, Crosslinked Polyimide Howllow Fiber Membranes for Agressive Natural Gas Feed Streams, in, Georgia Institute of Technology, PhD Thesis, 2008.

[3] A.M.W. Hillock, Crosslinkable Polyimide Mixed Matrix Membranes For Naural Gas Purification, in, Georgia Institue of Technology, PhD Thesis, 2005.

[4] C. Ma, Highly Productive Ester Crosslinkable Composite Hollow Fiber Membranes for Aggressive Natural Gas Separations, in: School of Chemical and Biomolecular Engineering, Georgia Institute of Technology, Atlanta, 2012, pp. 167.

[5] G.R. Husk, P.E. Cassidy, K.L. Gebert, Synthesis and Characterization of a Series of Polyimides Derived from 4,4'-[2,2,2-Trifluoro-1-(Trifluoromethyl)Ethylidene]-Bis[1,3-Isobenzofurandione], Macromolecules, 21 (1988) 1234-1238.

[6] M.I. Bessonov, V.A. Zubkov, Polyamic Acids and Polyimides: Synthesis, Transformations, and Structure, CRC Press, 1993.

[7] M.K. Ghosh, K.L. Mittal, Polyimides: Fundamentals and Applications, Taylor & Francis, 1996.

[8] A.M.W. Hillock, W.J. Koros, Cross-Linkable Polyimide Membrane for Natural Gas Purification and Carbon Dioxide Plasticization Reduction, Macromolecules, 40 (2007) 583-587.

[9] D.W. Wallace, C. Staudt-Bickel, W.J. Koros, Efficient development of effective hollow fiber membranes for gas separations from novel polymers, J Membrane Sci, 278 (2006) 92-104.

[10] D.W. Breck, Zeolite Molecular Sieves: Structure, Chemistry and Use, 3 ed., John Wiley & Sons, New York, 1974.

[11] S. Matteucci, Y. Yampolskii, B.D. Freeman, I. Pinnau, Transport of Gases and Vapors in Glassy and Rubbery Polymers, in: Materials Science of Membranes for Gas and Vapor Separation, John Wiley & Sons, Ltd, 2006, pp. 1-47.

[12] R.W. Baker, Membrane technology and applications, 3rd ed., John Wiley & Sons, Chichester, West Sussex ; Hoboken, 2012.

[13] H. Mao, U.o. Minnesota, Nanoporous Polymers with Functionalized One-dimensional and Three-dimensional Channels from Ordered Block Copolymer Templates, University of Minnesota, 2006.

[14] D. Klempner, V. Sendijarevi′c, R.M. Aseeva, Handbook of Polymeric Foams and Foam Technology, Hanser Gardner Publications, 2004.

[15] J.D. Wind, Improving Polyimide Membrane Resistance to Carbon Dioxide Plasticization in Natural Gas Separations, in: Chemical Engineering, The University of Texas at Austin, Austin, 2002, pp. 232.

[16] S. Damle, W.J. Koros, Permeation Equipment for High-Pressure Gas Separation Membranes, Ind Eng Chem Res, 42 (2003) 6389-6395.

[17] T.T. Moore, S. Damle, P.J. Williams, W.J. Koros, Characterization of low permeability gas separation membranes and barrier materials; design and operation considerations, J Membrane Sci, 245 (2004) 227-231.

[18] K.C. O'Brien, W.J. Koros, T.A. Barbari, E.S. Sanders, A new technique for the measurement of multicomponent gas transport through polymeric films, J Membrane Sci, 29 (1986) 229-238.

[19] C.S.K. Achoundong, N. Bhuwania, S.K. Burgess, O. Karvan, J.R. Johnson, W.J. Koros, Silane Modification of Cellulose Acetate Dense Films as Materials for Acid Gas Removal, Macromolecules, 46 (2013) 5584-5594.

[20] S. Shu, Engineering the Performance of Mixed Matrix Membranes for Gas Separations, in, Georgia Institute of Technology, PhD Thesis, 2007.

[21] T.T. Moore, Effects of materials, processing, and operating conditions on the morphology and gas transport properties of mixed matrix membranes, in: Chemical Engineering, The University of Texas at Austin, Austin, 2004, pp. 283.

[22] D.R. Paul, A.T. DiBenedetto, Diffusion in amorphous polymers, Journal of Polymer Science Part C: Polymer Symposia, 10 (1965) 17-44.

[23] W.J. Koros, R.T. Chern, Separation of Gaseous Mixtures Using Polymer Membranes, in Handbook of Separation Process Technology, Wiley-Interscience, New York, 1987.

[24] W.J. Koros, D.R. Paul, Design Considerations for Measurement of Gas Sorption in Polymers by Pressure Decay, J Polym Sci Pol Phys, 14 (1976) 1903-1907.

[25] O. Esekhile, Mixed Matrix Membranes for Mixture Gas Separation of Butane Isomers, in: School of Chemical and Biomolecular Engineering, Georgia Institute of Technology, Atlanta, 2011.

CHAPTER 4: TRANSPORT OF ACID GASES IN NEAT CELLULOSE ACETATE AND UNCROSSLINKED PDMC DENSE FILM MEMBRANES

4.1 Abstract

This chapter focuses on assessing the performance of neat cellulose acetate (CA), the industrial and uncrosslinked PDMC, which has shown promising results for CO_2/CH_4 separations. Both polymers are compared against one another for the potential simultaneous removal of CO_2 and H_2S from aggressive sour gas streams. The permeability of neat CA to H_2S was found to be similar to CO_2, resulting in a high H_2S/CH_4 selectivity. On the other hand, the permeability of H_2S in uncrosslinked PDMC was more than 1.5 times lower than CO_2, giving it a low H_2S/CH_4 selectivity. Both materials had low plasticization resistance to H_2S compared to other gases due to their high solubility in H_2S. Furthermore, despite the size difference between H_2S and CH_4, the H_2S/CH_4 mobility selectivity was only slightly higher than unity, suggesting strong penetrant-polymer interactions. It was hypothesized that H_2S diffusion is governed by additional factors other than its kinetic diameter and that polar interaction with the polymer may introduce an additional energy barrier that must be overcome for the penetrant to execute a diffusive jump. To verify the validity of this hypothesis, the energetics of gas sorption and permeation in these materials was studied. Those temperature dependence experiments revealed that the activation energy of diffusion of H_2S in uncrosslinked PDMC is higher than CH_4, suggesting that H_2S tend to show strong affinity for available sorption sites. Therefore, H_2S transport is governed by its polar physiochemical interactions with the polymer. Neat CA followed the generally observed trend of higher activation energy of diffusion and permeation with increasing penetrant

kinetic diameter. It was also found that in neat CA, penetrant transport is controlled by both the solubility and mobility selectivity, with the former being more dominant, leading to a high overall CO_2/CH_4 and H_2S/CH_4 selectivities. However, in uncrosslinked PDMC, H_2S/CH_4 selectivity favors solubility only, whereas CO_2/CH_4 selectivity favors both mobility and solubility selectivity, even though diffusivity selectivity is more dominant. This leads to a low H_2S/CH_4 and a high CO_2/CH_4 selectivity. Binary and ternary mixed gas tests revealed that H_2S/CH_4 selectivity increases with increasing pressure and increasing H_2S concentration in the feed stream. In the ternary gas mixtures, this increase in H_2S/CH_4 is accompanied by a loss in H_2S/CH_4 selectivity. The permeability of H_2S was higher in feeds of higher H_2S concentrations. This result was attributed to both competitive sorption effects and an increase in chain local segmental mobility. These mixed gas results showed that these materials are promising candidate for the simultaneous removal of CO_2 and H_2S from natural gas if their performance could be further improved.

4.2 Pure Gas Permeation

Single gas permeation tests were typically conducted at 65 psia and 35°C except during plasticization resistance tests. Table 4.1 shows the pure gas permeability coefficients of CH_4, CO_2, and H_2S in neat CA and uncrosslinked PDMC dense films. Permeability data for dense (homogeneous) cellulose acetate (CA) membranes for single CH_4 and CO_2 have been reported previously by many researchers [1, 2].

81

Table 4.1: Single gas permeability and selectivity of neat CA and uncrosslinked PDMC at 65 psia and 35°C

Polymer	Permeability (Barrer)			Ideal Selectivity	
	CH_4	CO_2	H_2S	CO_2/CH_4	H_2S/CH_4
Neat CA	0.14±0.03	4.65±0.65	4.86±0.78	33.2±1.51	34.7±1.43
Neat CA [1]	0.13	4.75	-	36.5	
Neat CA [2]	0.085	3.11	-	36.6	-
Uncrosslinked PDMC	0.83±0.07	30.4±0.90	11.7±0.93	36.7±1.14	14.1±1.02

It can be seen from Table 4.1 that the measured values in this study agree well with previous studies with a small deviation. It should be noted that film preparation procedures, including casting conditions, solvent evaporation rate, thermal history, and dryness influence the transport properties [1]. Therefore, the slight deviation could be the result of any of those factors listed. Glassy polymers are not in a state of equilibrium, and prior history influences current and future performance [3]. Pure H_2S gas data in the pressure range studied is not available in reported literature, due to its highly toxic nature; however, it has been measured in this lab with the high safety equipments as discussed in Chapter 3, and the permeation results are presented in Table 4.1. The permeability of H_2S in neat CA is slightly greater than that of CO_2 at the same pressure, even though H_2S have a higher kinetic diameter. This is because the polymer matrix was significantly swollen at that pressure, due to the high polarity and condensability of H_2S. This higher H_2S permeability led to the higher H_2S/CH_4 ideal selectivity compared to the CO_2/CH_4 ideal selectivity. The uncrosslinked CO_2 and CH_4 are more than 6 times higher than neat CA, in part because of the presence of the bulky $-CF_3$ group, which inhibits chain packing and create a more permeable matrix, resulting in a high fractional free volume. As expected, the permeability increases with decreasing kinetic diameter $(CO_2>H_2S>CH_4)$ in uncrosslinked PDMC. The H_2S permeability is more than 60% lower

than CO_2 in uncrosslinked PDMC compared to neat CA. At first one may be tempted to conclude that PDMC may have a higher plasticization resistance to H_2S. However, as discussed below, the H_2S sorption isotherms showed that both materials are swollen at very low pressures. On the other hand, previous researchers have shown that there may be unfavorable interactions between H_2S and fluorinated polymers, which result in a lower H_2S solubility and therefore permeability [4]. Sorption results as discussed later may help validate those claims. The pure gas permeation isotherms of CH_4, CO_2, and H_2S are shown in Figures 4.1, 4.2, and 4.3, respectively. These figures suggest that CH_4 does not swell either polymer at pressures well above 400 psia, which is expected due to its noncondensable nature. Figure 4.2 shows that CO_2 plasticizes neat CA and uncrosslinked PDMC at pressures between 100-200 psia, which is consistent with the values reported by previous researchers [2, 5, 6]. The high conditioning effect by CO_2 in CA is the result of its interaction with the carbonyl group and the hydrogen bonding with the hydroxyl groups. A much higher conditioning by H_2S is observed in both materials as shown in Figure 4.3. Both materials are plasticized at much lower than 10 psia. The reason for this higher conditioning may be due to its higher condensability and polarity compared to CO_2, which will make it more soluble with a greater tendency to swell the polymers at low pressures. To measure the relative contribution of solubility in the observed results, sorption measurements were conducted as discussed below.
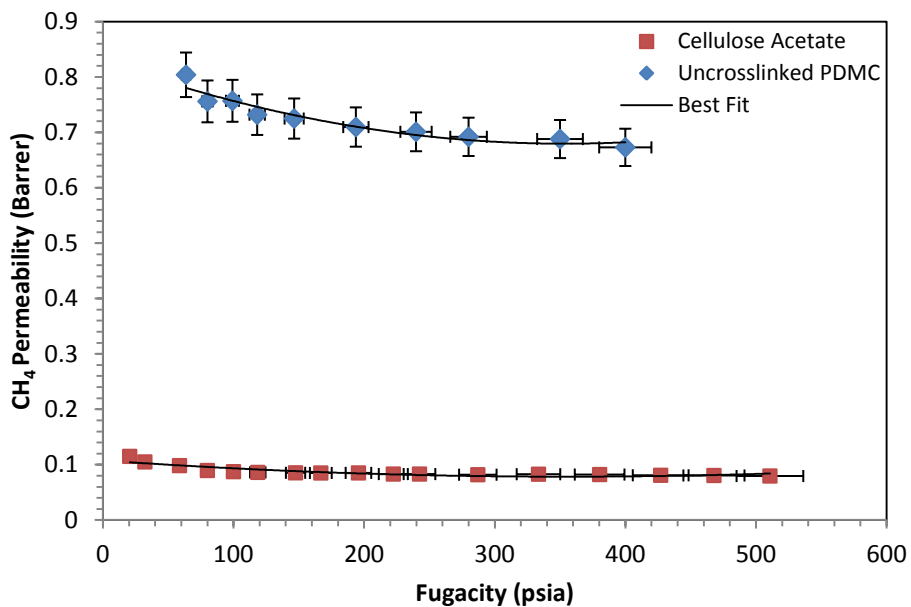
Figure 4.1: Pure CH_4 permeation isotherm at 35°C for neat CA and uncrosslinked PDMC.
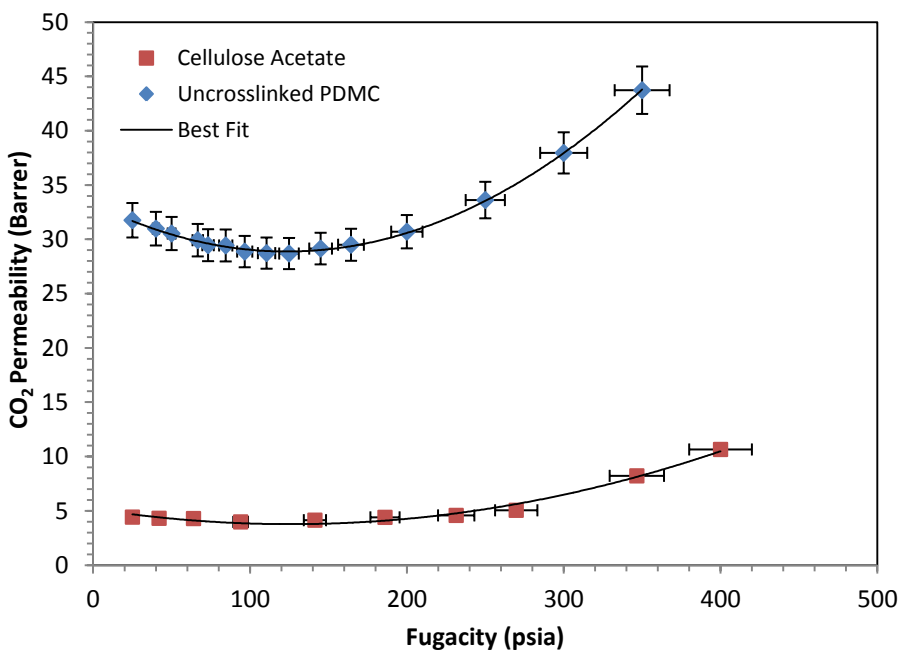
Figure 4.2: Pure CO_2 permeation isotherm at 35°C for neat CA and uncrosslinked PDMC.
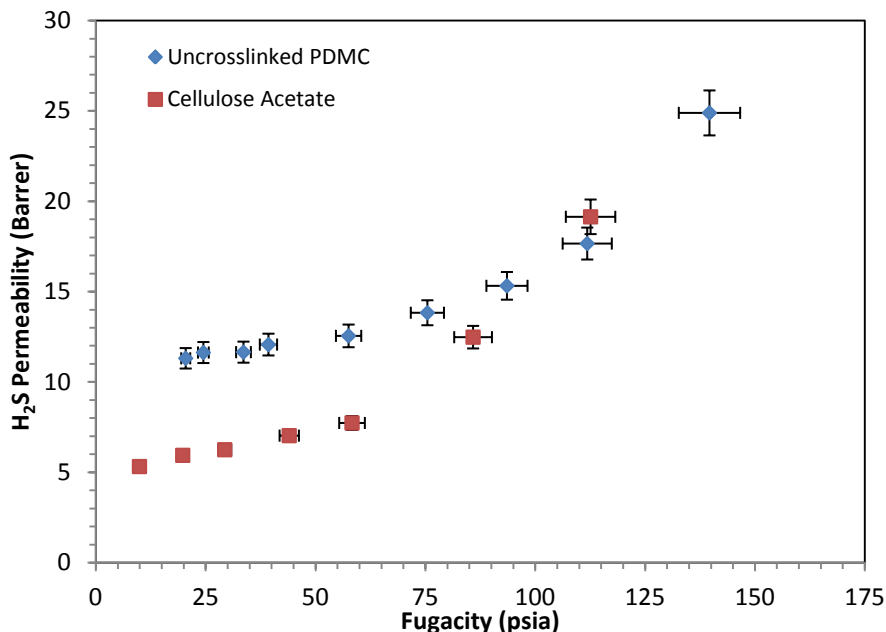
Figure 4.3: Pure H$_2$S permeation isotherm at 35°C for neat CA and uncrosslinked PDMC.

4.3 Pure Gas Sorption

Sorption isotherms of CH$_4$, CO$_2$, and H$_2$S components were measured at 35°C using the protocol outlined in Chapter 3. The results are shown in Figures 4.4 and 4.5. Table 4.2 lists the sorption parameters obtained from those isotherms using the dual-mode sorption model. This model suggests that once microcavities become saturated at sufficiently high pressures, the ordinary dissolution becomes the main solution mechanism [7, 8]. The sorption isotherms of both materials agree well with the dual-mode model judging its concavity, except for the case of CO$_2$ and H$_2$S at high pressures when the materials become significantly swelled. For H$_2$S in neat CA, an upward deviation is observed above ~100 psia and in uncrosslinked PDMC, the deviation is observed above ~150 psia. The swelling in this case is characterized by an upswing in the concentration isotherm. At such pressures, the dual-mode fit can no longer be applied and no quantitative

conclusions can be made beyond that point. Similar upward deviation for pure H_2S was also observed by previous researchers in our group [9, 10].

Table 4.2: Pure CH_4, CO_2, and CH_4 sorption parameters of neat CA and uncrosslinked PDMC at 35°C

Polymer	CH_4				CO_2				H_2S			
	k_d (10^{-2})	b (10^{-2})	C_H'	K	k_d (10^{-1})	b (10^{-2})	C_H'	K	k_d (10^{-1})	b (10^{-1})	C_H'	K
Neat CA	1.80	1.25	2.01	1.39	1.50	8.80	8.01	4.70	4.94	2.15	16.11	7.61
Uncrosslinked PDMC	1.82	0.40	20.23	4.45	1.07	1.86	29.27	5.09	6.64	4.38	27.33	18.1

k_d is in $cm^3(STP)/cm^3psia$, b is in $psia^{-1}$, and C_H' is in $cm^3(STP)/cm^3$ polymer

Table 4.2 shows that Langmuir sorption capacity (C_H') of all gases in neat CA is much lower than that of the same gases in uncrosslinked PDMC. This implies a larger preexisting "hole" or microcavities volume in the uncrosslinked PDMC, which explains the much higher fractional free volume of PDMC compared to CA. Furthermore, the value of K, which measures the amount of gas immobilized in the microcavities relative to the amount dissolved, is much higher for uncrosslinked PDMC.
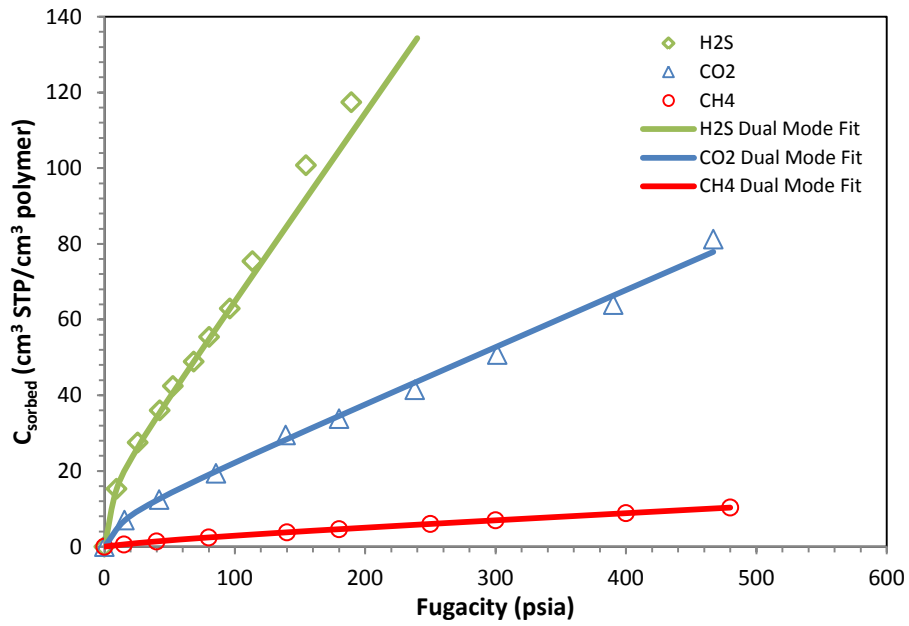
Figure 4.4: Pure CH$_4$, CO$_2$, and H$_2$S sorption isotherm at 35°C in neat CA.
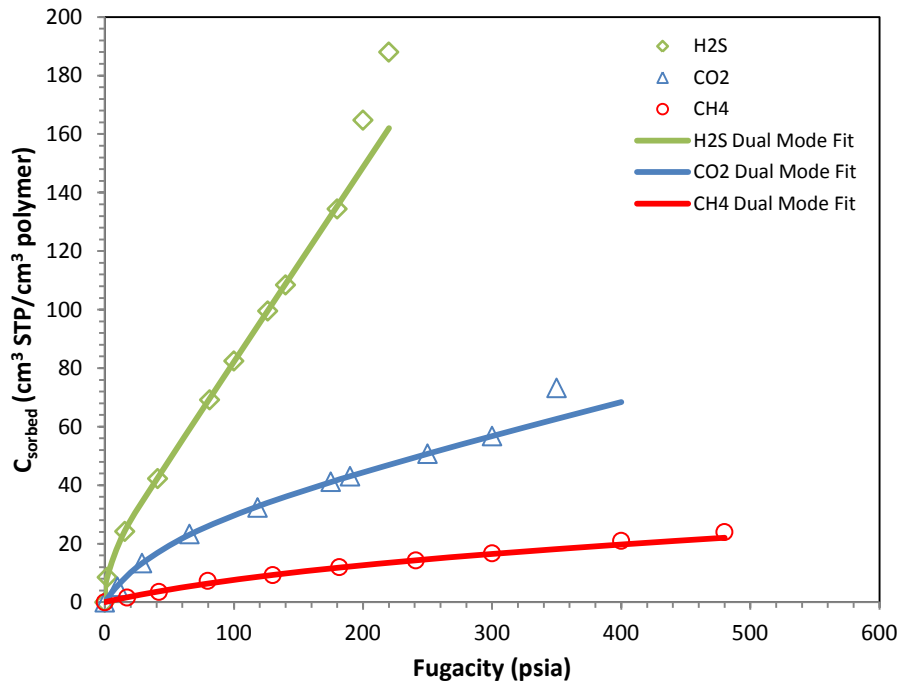
Figure 4.5: Pure CH$_4$, CO$_2$, and H$_2$S sorption isotherm at 35°C in uncrosslinked CA.

As discussed in Chapter 2, the permeability coefficient is defined as the product of the diffusion coefficient and the sorption coefficient; therefore, the selectivity can be decoupled into mobility and solubility selectivity. Using the permeation and sorption results, the kinetic (diffusion) and thermodynamic (solubility) individual contributions were calculated and are shown in Table 4.3. Details on the calculation of the parameters in Table 4.3 can be found in Appendix F.

Table 4.3: Diffusion coefficient (D), solubility coefficient (S), diffusion selectivity (α_D), and solubility selectivity (α_S) of neat CA and uncrosslinked PDMC at 35°C and 65 psia

Polymer	D (10^{-9} cm^2/sec)			S (10^{-2} cm^{3}STP/cm^{3}psia)			α_D		α_S	
	CH_4	CO_2	H_2S	CH_4	CO_2	H_2S	CO_2/CH_4	H_2S/CH_4	CO_2/CH_4	H_2S/CH_4
Neat CA[a]	1.95	7.91	3.11	3.45	27.78	70.66	4.06	1.59	8.05	20.48
Neat CA[b]	2.11	8.62	3.44	3.19	25.49	72.52	4.09	1.63	7.99	22.73
Uncrosslinked PDMC[a]	4.64	40.61	5.12	9.25	38.73	118.06	8.75	1.10	4.19	12.76
Uncrosslinked PDMC[b]	5.20	44.58	5.65	8.25	35.28	107.02	8.57	1.09	4.28	12.97

a. D was measured by the time-lag method and S was calculated from P=DS
b. S was measured by pressure-decay sorption and D was calculated from P=DS

As expected, the diffusion coefficient increases with decreasing penetrant kinetic diameter for both materials. Similarly, the sorption coefficient increases with increasing penetrant critical temperature in both materials. As mentioned previously, previous studies using fluorinated polymers for H_2S/CH_4 separations have found that H_2S-fluorine interactions are the main cause for the low H_2S/CH_4 observed [4]. In those materials the sorption coefficient of CO_2 is similar or higher than that H_2S even though the latter is much more condensable. However, in this case, the sorption coefficient of H_2S is ~3 times higher than CO_2 in both neat CA and uncrosslinked PDMC. Thus, in these two materials the solubility coefficient increases with increasing critical temperature. It hypothesized that favorable carbonyl and hydrogen bonding with hydroxyl groups on the

DABA moiety with H_2S overshadows any unfavorable interactions with the fluorine containing groups. The diffusion coefficient of all three gases in uncrosslinked PDMC is higher than the diffusion coefficient of the same gases in neat CA, which is expected as PDMC has a much higher backbone stiffness and matrix free volume. The CO_2/CH_4 mobility selectivity in uncrosslinked PDMC is almost two times higher than neat CA, which is expected. However, both the CO_2/CH_4 and H_2S/CH_4 sorption selectivities in neat CA are higher than in uncrosslinked PDMC. On the other hand, the H_2S/CH_4 mobility selectivity in neat CA is about 1.5 times higher than in PDMC. The mobility selectivity of the latter polymer is only slightly higher than one, despite the significant difference in size between the molecules. This result may be due to the hydrogen bonding of the highly polar H_2S with hydroxyl groups in the polymer chains, which may lead to a lower diffusion coefficient due to the tendency of H_2S molecules to "stick" to the sorption sites. This "sticky" assumption can lead to a higher than expected activation energy of diffusion of H_2S. To test the validity of this "sticky" diffusion hypothesis, temperature dependence tests were conducted and will be discussed later in this Chapter. The difference in the observed performance of these materials can be summarized as follows:

(a) In neat CA, the CO_2/CH_4 and H_2S/CH_4 selectivities are controlled by both solubility selectivities and mobility selectivities, even though the solubility selectivity is more dominant. This leads to high overall CO_2/CH_4 and H_2S/CH_4 selectivities.

(b) In uncrosslinked PDMC, the H_2S/CH_4 overall selectivity is controlled mostly by the solubility selectivity, whereas the CO_2/CH_4 selectivity is controlled by both factors, even though the diffusivity selectivity is dominant. This leads to a low H_2S/CH_4 and a high CO_2/CH_4 selectivity.

4.4 Pure Gas Permeation Modeling

As discussed in Chapter 3, Koros et al. [11, 12] found that penetrant molecules in the Henry's and Langmuir populations have different inherent mobilities and the so-called "partial immobilization" model accounts for that fact by expressing the permeability coefficient in terms of both the local diffusion coefficients D_D and D_H in the local two environments as shown in Equation 2.36, for the case of zero downstream pressure.

$$P = k_D D_D \left[1 + \frac{FK}{1 + bf_2} \right] \qquad 2.36$$

The local CH_4 and CO_2 diffusion coefficients were determined for both materials and are shown in Table 4.4. The coefficients D_D and D_H were found by plotting permeability versus $1/(1+bf_2)$ as shown in Appendix F [11, 13]. It should be noted that equation 2.36 is based on the assumption that the polymer is not significantly plasticized by the penetrant gas; therefore, these coefficients can only be determined from the permeation isotherm data before plasticization has occurred. This limitation is the reason why these local diffusion coefficients could not be determined for H_2S since they plasticize at much lower pressures. Figure 4.6 and 4.7 show the effective diffusion coefficient as a function of pressure calculated using the values of Table 4.4.

Table 4.4: Local diffusion coefficients D_D and D_H of CH_4 and CO_2 in neat CA and uncrosslinked PDMC at 35°C

Polymer	D_D (10^{-9} cm^2/sec)		D_H (10^{-9} cm^2/sec)		F = D_H / D_D	
	CH_4	CO_2	CH_4	CO_2	CH_4	CO_2
Neat CA	3.33	13.32	1.07	3.94	0.32	0.30
Uncrosslinked PDMC	18.66	127.2	1.59	7.56	0.085	0.059
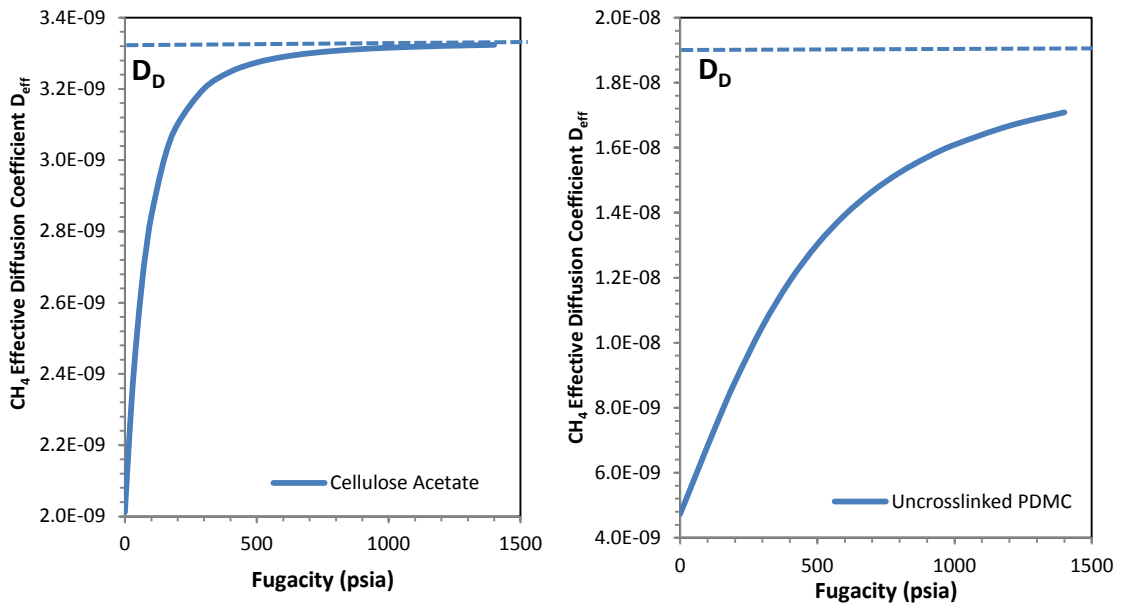
Figure 4.6: Effective diffusion coefficient of CH_4 in neat CA and uncrosslinked PDMC.
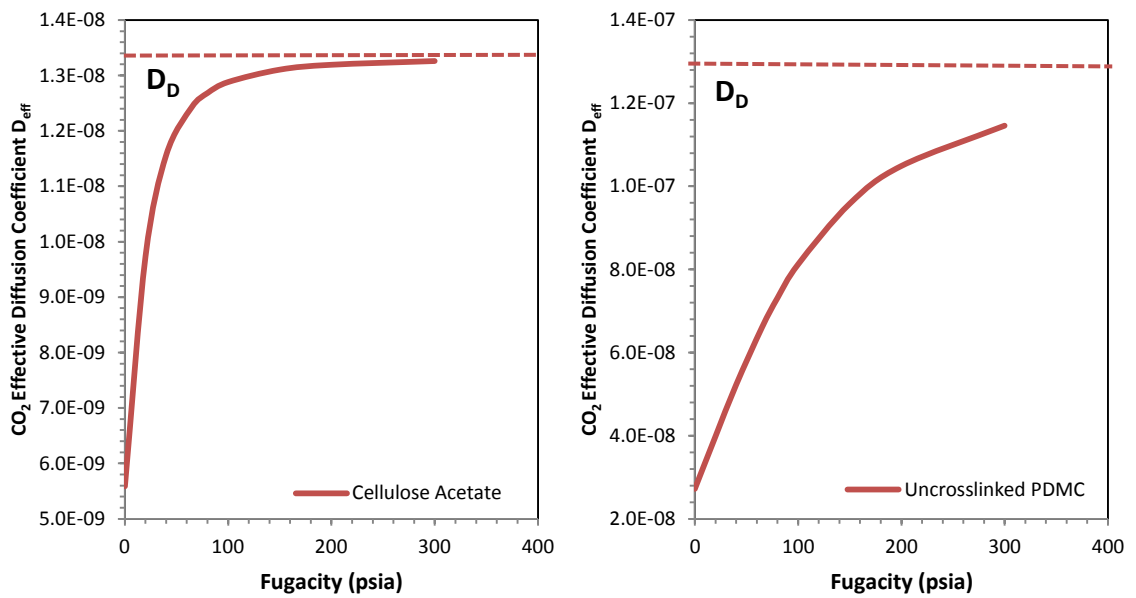
Figure 4.7: Effective diffusion coefficient of CO_2 in neat CA and uncrosslinked PDMC.

It can be observed that $D_D > D_H$ which is similar to the trend observed by previous researchers in a variety of glassy polymers [2, 11, 14-16]. It means that the dissolved mode has a higher mobility than the Henry's mode for both gases. The lower value of F (a measure of the degree of immobilization) for CO_2 may be due to the apparent "trapping" caused by its sorption in the microvoid regions [14, 17]. In the glassy polymers, the diffusion coefficient is usually a function of increasing sorbed concentration or pressure. It can be inferred from Figure 4.6 and Figure 4.7 that at lower pressures, a high fraction of penetrant sorbs into the Langmuir sites and as discussed previously, penetrants in these domains have a lower mobility than in the Henry's domain ($D_D > D_H$). As the pressure rises, an increasingly higher amount of penetrant sorbs into the Henry's regions, which increases the mobility of the total concentration sorbed. At very high pressures, sorption occurs primarily in the Henry's domain as the Langmuir sites become saturated, making diffusivity almost independent of concentration. Therefore, the effective diffusion coefficient is lower than the local diffusivity in the Henry's domain, which is independent of concentration. The shape of the effective diffusivity concentration dependent curve of neat CA is steeper than its corresponding PDMC curve. This can be explained by the lower total sorption coefficient of both CO_2 and CH_4 in CA compared to PDMC. The lower Langmuir capacity of these gases in CA causes the holes to be saturated at a faster rate than PDMC, thereby entering the dissolved region much more quickly than PDMC. Furthermore, as shown in Table 4.2, the amount of penetrant immobilized in the microcavities relative to the amount dissolved (K) is much higher for uncrosslinked PDMC. It should be noted that when the proportion of penetrant in the "holes" is equal to the amount of penetrant in the dissolved region, that is

K = 0, the effective coefficient is also equal to the local diffusion coefficient in the Henry's domain regardless of the pressure.

4.5 Binary Gas Permeation

Since single gas permeation often overpredicts the separation performance compared to what would be observed under realistic conditions, binary gas tests were conducted with uncrosslinked PDMC and cellulose acetate at 35°C. Figure 4.8 and Figure 4.9 represent the H_2S and CH_4 permeability isotherms in the two binary mixtures for the two polymers. Figure 4.10 shows the H_2S/CH_4 selectivity of both polymers in those binary mixtures. Figure 4.8 shows a decrease in H_2S permeability followed by a small upswing in permeability for both materials in the two mixtures. There is no significant upswing in H_2S permeability as expected from the pure H_2S isotherm in Figure 4.3, even at pressures up to 700 psia in both mixtures. These results are surprising since the feed H_2S fugacity for both polymers exceeds the plasticization pressure as measured in pure gas tests in Figure 4.3. Similar trends have been observed by previous researchers with the same mixture [9, 10]. Figure 4.9 shows that the CH_4 permeability decreases in uncrosslinked PDMC in both mixtures throughout the pressure range studied. It is reduced to more than 35% of its pure gas value at ~700 psia. However, in neat CA, the CH_4 permeability passes through a minimum and then slightly increases at higher pressures. It increases to more than 50% of its pure value in the 5%H_2S mixture and to more than 95% of its pure value in the 10%H_2S mixtures at ~700 psia. It should be noted that the permeability of CH_4 decreases at a much faster rate in uncrosslinked PDMC than in neat CA at low pressures. The constant CH_4 permeability reduction with increasing pressure in

93

uncrosslinked PDMC may be due to the fact that PDMC has more Langmuir sites due to its higher fractional free volume compared to neat CA; this is evident by the higher Langmuir sorption capacity of all three gases in PDMC as shown in Table 4.2. This may suggest that the Langmuir sites in PDMC become saturated at much higher pressures and concentrations and H_2S may "outcompete" CH_4 for those fixed number of Langmuir sites, thereby reducing its permeability. These competitive sorption effects can be captured by Equation 2.39 and 2.40 for vacuum downstream in mixed gas feeds, as discussed in Chapter 2.

$$P_A = k_{D_A} D_{D_A} \left[1 + \frac{F_A K_A}{1 + b_A f_A + b_B f_B} \right] \tag{0.1}$$

$$P_B = k_{D_B} D_{D_B} \left[1 + \frac{F_B K_B}{1 + b_A f_A + b_B f_B} \right] \tag{0.2}$$

This dual-mode competitive model suggests that the permeability of one penetrant gas will decrease as the partial pressure of the co-penetrant increases. In this case, the permeability of CH_4 in PDMC keeps decreasing with increasing partial pressure of H_2S even at pressures up to 700 psia, which leads to an increase in H_2S/CH_4 selectivity. The latter increases to more than 40% of its pure gas value in uncrosslinked PDMC at ~700 psia. This result suggests that the Langmuir sorption sites may still not be saturated at those conditions. Because both materials plasticize at low H_2S pressures, the results obtained could not be compared against the predictions from the dual-mode model. The constant decrease in CH_4 permeability coupled with a rather small change in H_2S permeability with increasing pressure causes an increase in the overall H_2S/CH_4 selectivity in uncrosslinked PDMC. In CA, the increase in H_2S permeability at higher

94

pressures surpasses the increase in CH_4 permeability, leading to an overall increase in H_2S/CH_4 selectivity with increasing pressure. This higher increase in H_2S permeability may due to both an increase in chain segmental mobility at higher pressures, and an increase in the effective diffusion coefficient. A way to verify the latter claim might be to obtain values of D_D and D_H in these materials. However, it is difficult to obtain to those parameters because they are swelled by the H_2S penetrant at very low pressures. Kraftschik et al. attempted to model a similar behavior in annealed 6FDA-DAM:DABA (3:2) using the partial immobilization model with and without bulk flow contribution without success, indicating a much complex effect [10]. Nevertheless, the increase in H_2S/CH_4 selectivity with increasing pressure is a desirable result. It should also be noted from Figure 4.10 that higher H_2S (10% versus 5%) concentrations in the feed mixture also lead to a slightly higher H_2S/CH_4 selectivity for both materials over the entire pressure range studied.
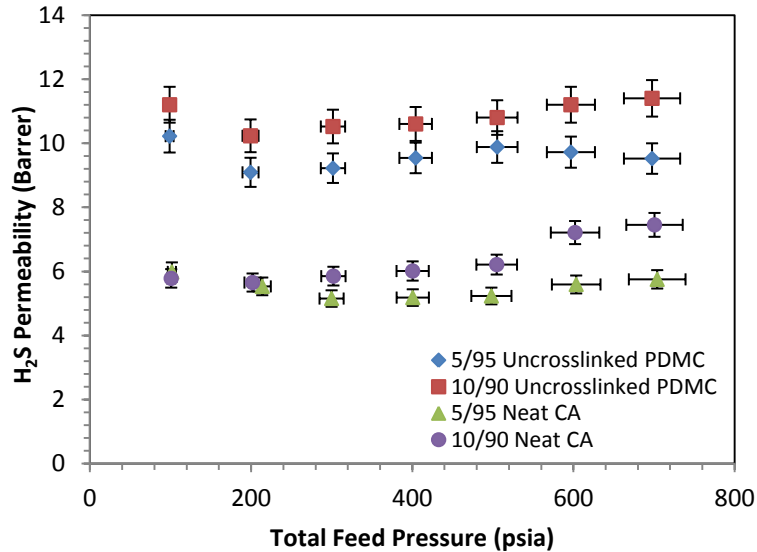
Figure 4.8: H_2S permeability in binary 5%H_2S/95CH_4 and 10%H_2S/90%CH_4 mixtures in neat CA and uncrosslinked PDMC.
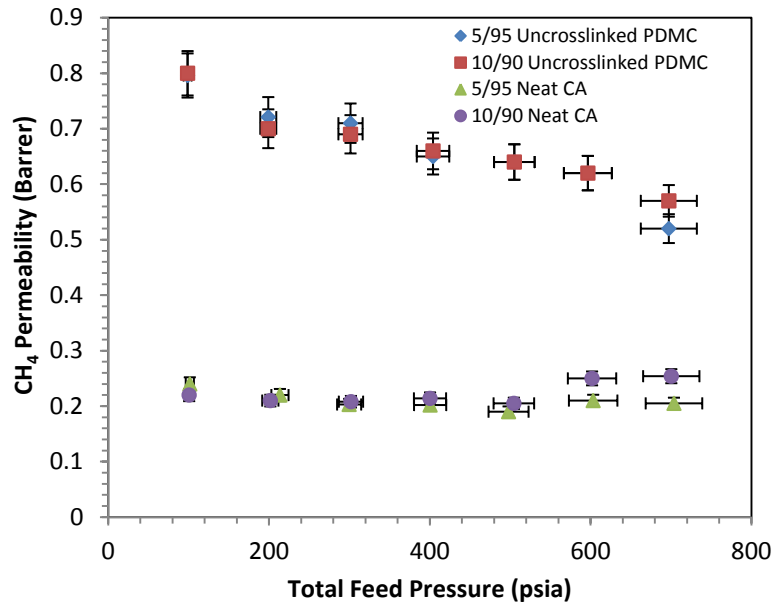
Figure 4.9: CH_4 permeability in binary $5\%H_2S/95CH_4$ and $10\%H_2S/90\%CH_4$ mixtures in neat CA and uncrosslinked PDMC.
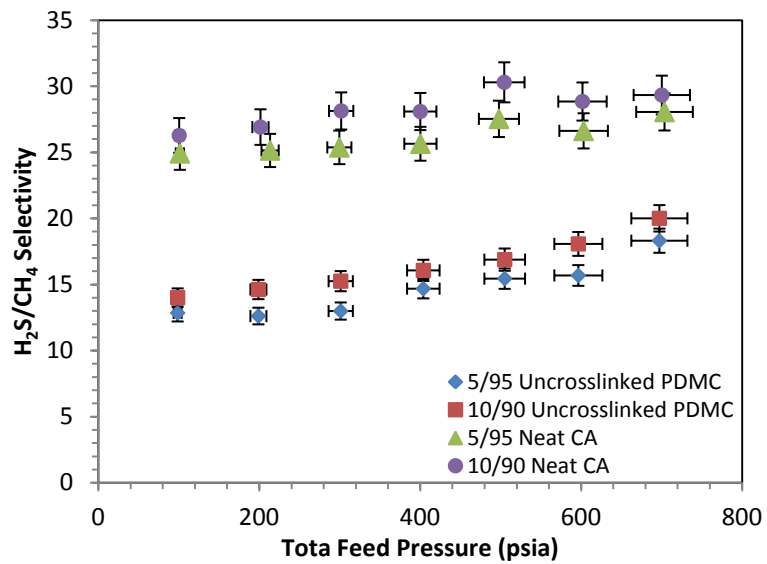
Figure 4.10: H_2S/CH_4 selectivity in binary $5\%H_2S/95CH_4$ and $10\%H_2S/90\%CH_4$ mixtures in neat CA and uncrosslinked PDMC.

4.6 Ternary Gas Permeation

In addition to binary mixtures, permeation tests were also conducted in two $H_2S/CO_2/CH_4$ ternary gas mixtures of 10%/20%/70% and 20%/20%/60% at the same temperature of 35°C. These mixtures mimic aggressive feeds for which these materials are expected to be utilized. Figure 4.11, 4.12, and 4.13 represent the CH_4, CO_2, and H_2S permeability isotherms in the two ternary mixtures in both polymers. It can be seen that the H_2S permeabilities rise at a much faster rate than observed in the previous binary mixtures discussion, but H_2S/CH_4 selectivity increases with increasing pressure and H_2S concentration. In addition, the CH_4 permeability is not suppressed as it was previously. Rather, like CO_2, it briefly goes through a minimum and then quickly rises. This may be explained by the introduction of CO_2 in the feed mixture, which can compete more effectively for the available Langmuir sorption sites than CH_4 could. It can be seen from Figure 4.14 and 4.15 that as the CO_2/CH_4 selectivity decreases, the H_2S/CH_4 selectivity increases. This may indicate the dominance of H_2S for the sorption sites due to the high affinity coefficient for H_2S in these materials, making them more H_2S selective at those pressures. It is more difficult to assess where plasticization occurs in such a complex system when compared to pure and binary systems. In fact, plasticization may favor H_2S/CH_4 selectivity by increasing H_2S sorption capacity, because as mentioned in Chapter 1, H_2S separation is a solubility-selective process. This is illustrated by the slight increase in H_2S/CH_4 selectivity with increasing H_2S feed concentration. The CO_2/CH_4 selectivity decreases by more than 50% of its ideal selectivity in neat CA compared to only ~30% in uncrosslinked PDMC at ~800 psia. The permeability of H_2S in the 20/20/60 mixture is higher than in the 10/20/70 mixture in the two polymers. This is

likely due to its higher concentration, which allows it to "outcompete" other gases. This increase in H_2S permeability is accompanied by a lower CH_4 permeability than it would have been otherwise. The combination of these competitive sorption effects with an increase in chain mobility causes the diffusivity of H_2S to increase much more than CH_4, leading to an increase in overall H_2S/CH_4 selectivity with increasing H_2S concentration in the feed. It can be concluded from these mixed gas experiments that the CO_2/CH_4 and H_2S/CH_4 membrane efficiencies are a strong function of feed pressure and concentrations. As the H_2S feed concentration increases, the CO_2/CH_4 selectivity decreases while the H_2S/CH_4 selectivity increases because when H_2S is present at higher concentrations, it effectively blocks CH_4 molecules by preventing them from occupying some of sorption sites. This effect is greater in CH_4 than in CO_2 because of the smaller difference in condensability between CO_2 and H_2S, making CO_2 molecules more competitive than CH_4. It leads to the conclusion that H_2S is much more dependent on both diffusion and dual-mode sorption effects than other gases, mainly due to its higher sorption capacity. One should point out that these aggressive feed mixtures at the pressures tested are well above those reported from previous researchers for H_2S removal [18, 19].
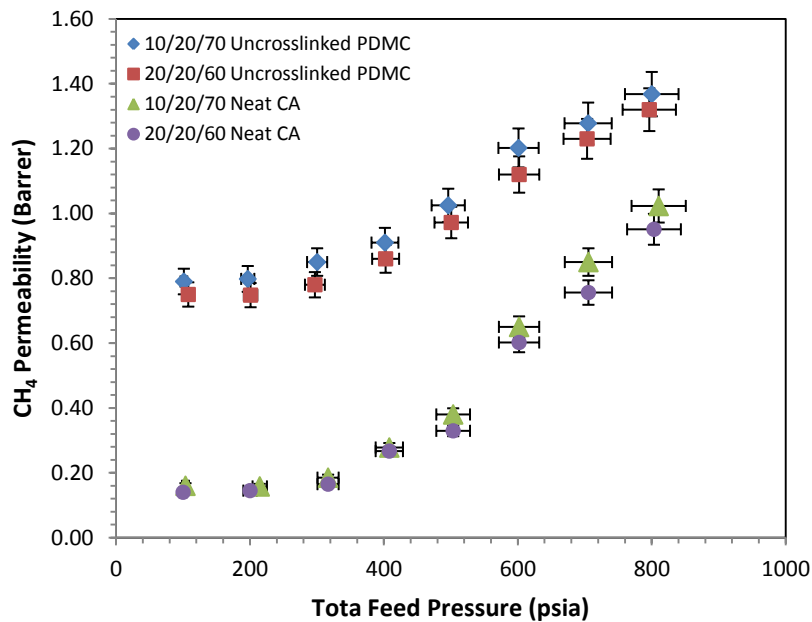
Figure 4.11: CH_4 permeability in ternary $10\%H_2S/20\%CO_2/70\%CH_4$ and $20\%H_2S/20\%CO_2/60\%CH_4$ mixtures in neat CA and uncrosslinked PDMC.
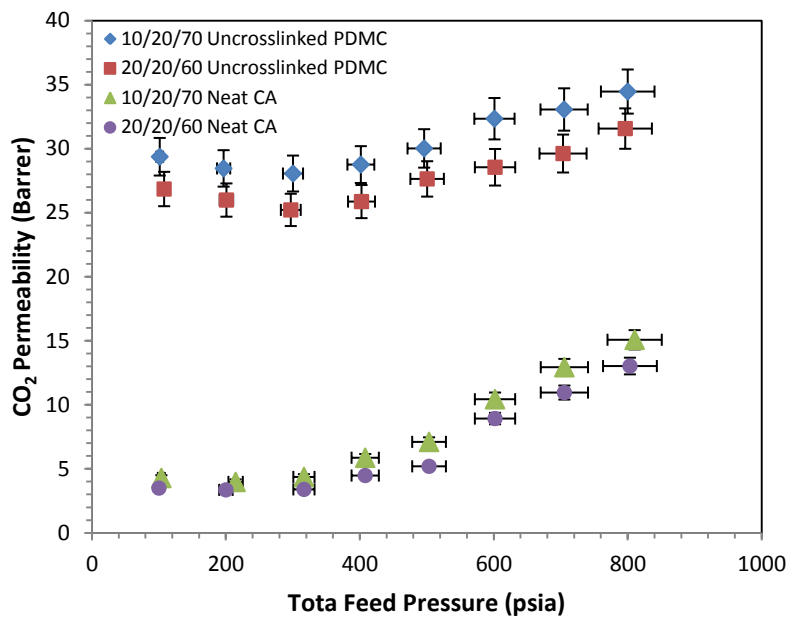
Figure 4.12: CO_2 permeability in ternary $10\%H_2S/20\%CO_2/70\%CH_4$ and $20\%H_2S/20\%CO_2/60\%CH_4$ mixtures in neat CA and uncrosslinked PDMC.

99
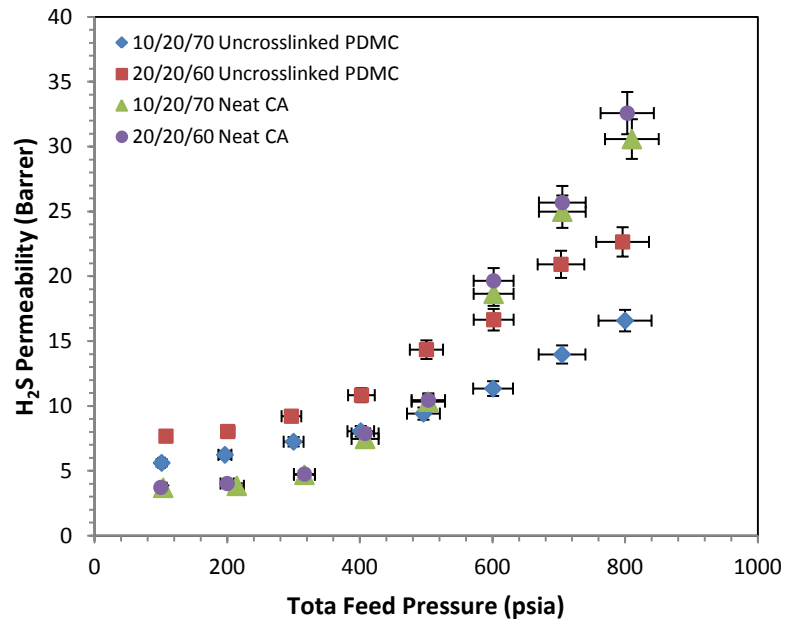
Figure 4.13: H$_2$S permeability in ternary 10%H$_2$S/20%CO$_2$/70%CH$_4$ and 20%H$_2$S/20%CO$_2$/60%CH$_4$ mixtures in neat CA and uncrosslinked PDMC.
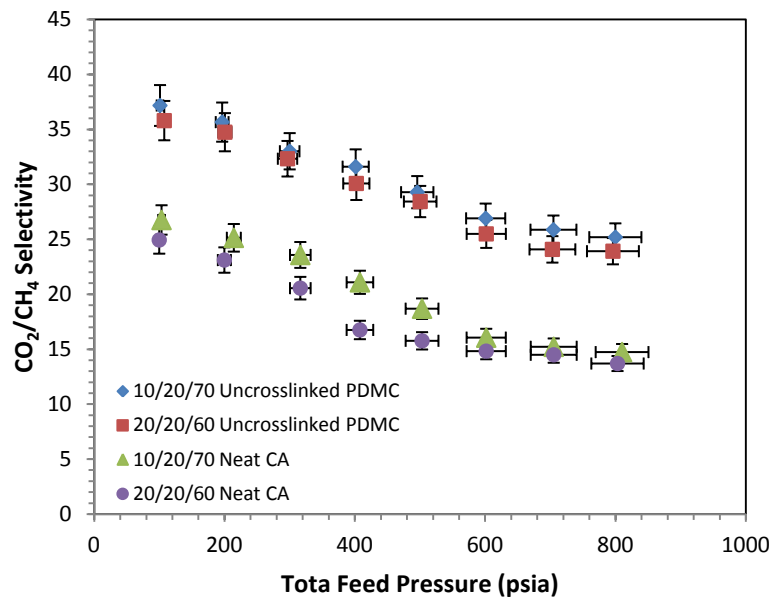
Figure 4.14: CO$_2$/CH$_4$ selectivity in ternary 10%H$_2$S/20%CO$_2$/70%CH$_4$ and 20%H$_2$S/20%CO$_2$/60%CH$_4$ mixtures in neat CA and uncrosslinked PDMC.
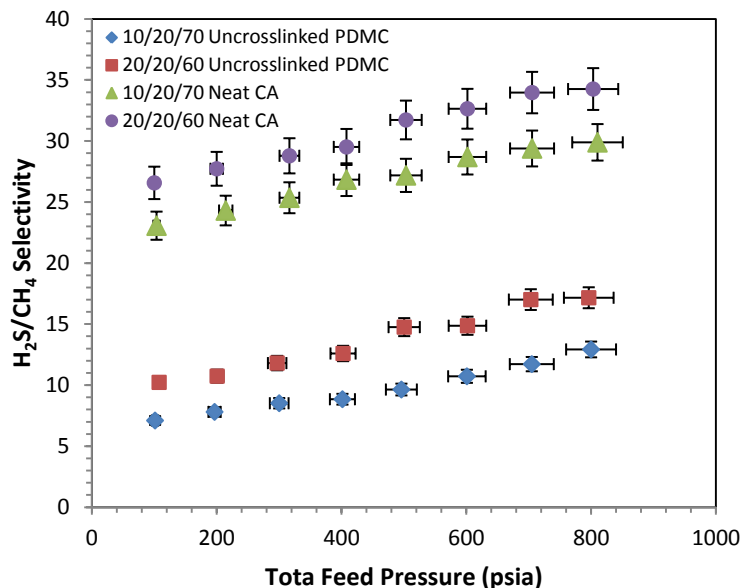
Figure 4.15: H_2S/CH_4 selectivity in ternary $10\%H_2S/20\%CO_2/70\%CH_4$ and $20\%H_2S/20\%CO_2/60\%CH_4$ mixtures in neat CA and uncrosslinked PDMC.

4.7 Energetics of Penetrant Diffusion and Sorption

The permeation, sorption, and diffusion of small molecules in polymers are all thermally activated processes. It was shown in the previous sections that H_2S had lower than expected permeability and mobility selectivity in PDMC. The H_2S/CH_4 mobility selectivity of the latter polymer was found to be only slightly higher than unity, despite the larger difference in size between the molecules. It was hypothesized that it could be the result of penetrant-polymer interactions that may lower the diffusion coefficient due to the tendency of H_2S molecules to "stick" in the Langmuir sites, which may lead to a higher than expected activation energy of diffusion of H_2S. Mohammadi et al. [19] showed that H_2S permeation increases with temperature to a much greater extent than CO_2 and CH_4 for a poly (ester urethane urea) rubber, indicating E_p is positive for all three gases, and that the energy of diffusion for H_2S is higher than that of CH_4. Xu et al. also

showed that the activation energy of diffusion of CO_2 was higher than O_2 in a series of polyamide-imides, giving it a lower diffusivity. Costello also observed similar results for the same gas pair in a number of polycarbonates [20]. To test the validity of this "sticky" diffusion hypothesis in uncrosslinked PDMC, temperature dependence tests were conducted. The permeability of H_2S, CO_2, and CH_4 was measured at 35°C, 50°C, 60°C, and 75°C at 65 psia in neat CA and uncrosslinked PDMC. Similarly, the solubility of H_2S, CO_2, and CH_4 was measured at 35°C, 50°C, and 60°C in both polymers. The activation energy of permeation was obtained by taking the slope of ln P versus 1/T in accordance with Equation 2.30 as shown in Figure 4.16. The enthalpy of solution was found by plotting ln S versus 1/T (Figure 4.17) as derived from the van't Hoff expression in Equation 2.28. Finally, the activation energy of diffusion was calculated using equation 2.31. These plots show an increase in permeability with increasing temperature, revealing that the activation energy of permeation is positive. On the other hand, the temperature dependence on solubility plot reveals that solubility decreases with increasing temperature, suggesting that sorption is an exothermic process. The values obtained are summarized in Table 4.5 and detailed calculations can be found in Appendix F.

$$D = D_o \exp\left(\frac{-E_d}{RT}\right) \qquad\qquad 2.27$$

$$S = S_o \exp\left(\frac{-\Delta H_S}{RT}\right) \qquad\qquad 2.28$$

$$P = P_o \exp\left(\frac{-E_p}{RT}\right) \qquad\qquad 2.30$$

$$E_p = E_d + \Delta H_s \qquad\qquad 2.31$$
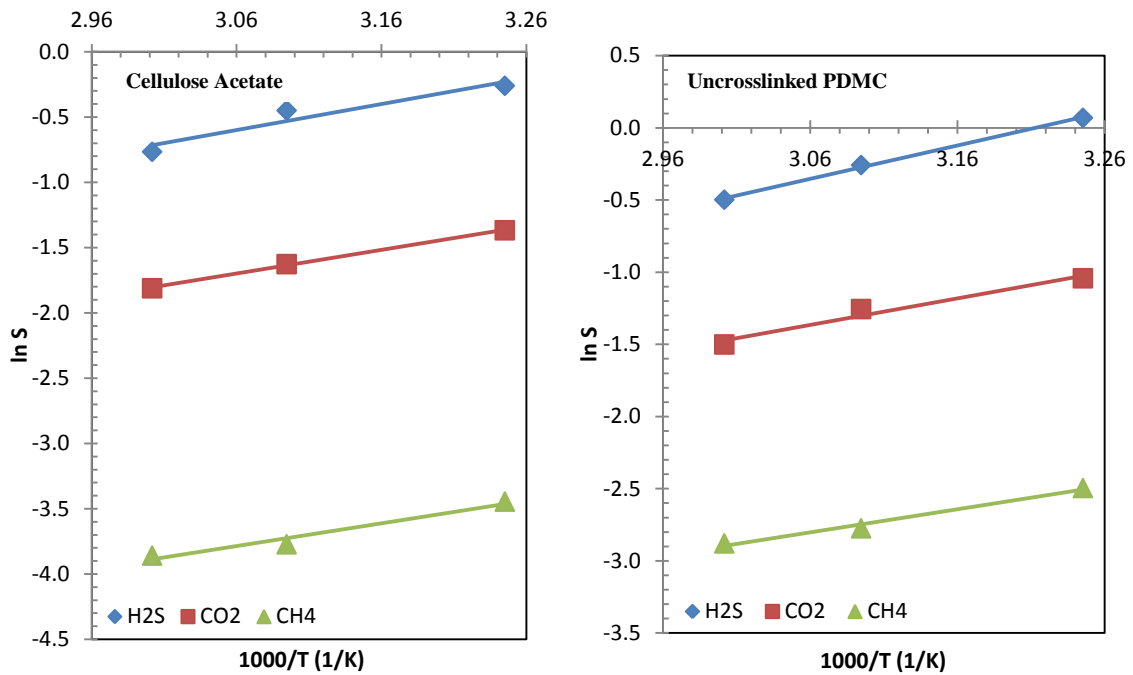
Figure 4.16: Temperature Dependence of H_2S, CO_2, and CH_4 on solubility in neat CA and uncrosslinked PDMC at 65 psia.
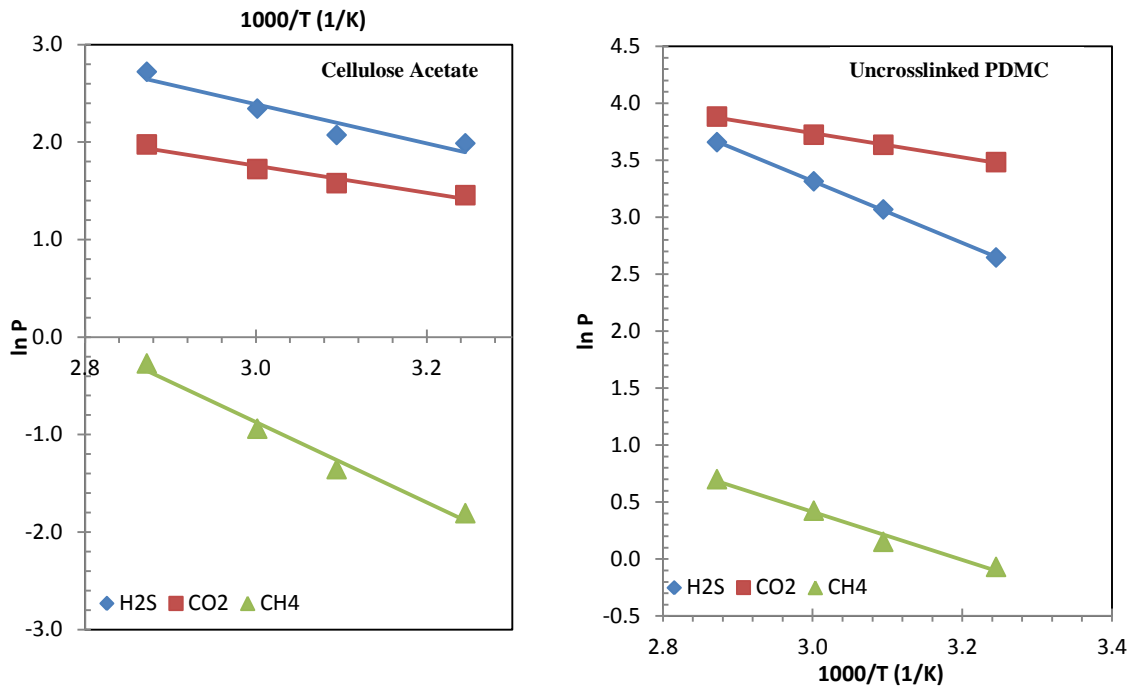
Figure 4.17: Temperature Dependence of H_2S, CO_2, and CH_4 on permeability in neat CA and uncrosslinked PDMC at 65 psia.

Table 4.5: Activation energies of permeation and diffusion, and heat of sorption of H_2S, CO_2, and CH_4 in neat CA and uncrosslinked PDMC at 65 psia

Parameters	Cellulose Acetate			Uncrosslinked PDMC		
	H_2S	CO_2	CH_4	H_2S	CO_2	CH_4
E_p (kJ/mol)	24.29	11.59	34.24	22.08	8.84	18.32
ΔH_s (J/mol)	-16.61	-15.08	-14.49	-19.24	-15.29	-13.33
E_d (J/mol)	40.90	26.67	48.73	41.32	24.13	31.65
D (10^{-9}cm^2/sec)	3.28	8.32	2.51	6.91	46.6	5.50
S (10^{-2}cm^{3}STP/cm^3 psia)	80.7	25.6	3.13	107.8	35.9	81.7
P (Barrer)	5.11	4.12	0.15	14.4	32.3	0.87

*D, S, and P were calculated using equations 2.27, 2.28, and 2.30 at T=35°C

Table 4.5 shows that the activation energy of permeation increases with increasing size of the penetrant molecule (CH_4>H_2S>CO_2) in neat CA, which is the generally observed trend as the energy required for gap openings that could allow large molecules such as CH_4 (3.8Å) to go through should be higher than that of a smaller molecule like H_2S (3.6Å) since it is a larger molecule. However, the same trend is not observed for uncrosslinked PDMC, which follows this order of increasing activation energy of permeation: H_2S>CH_4>CO_2. This translates into H_2S having a higher activation energy of diffusion than CH_4, suggesting that interactions between H_2S molecules and the polymer lead to large differences in H_2S diffusivity vs. that of CH_4. Therefore, the higher activation energy of diffusion of H_2S observed in PDMC reveals that it has strong specific interactions with the polymer sorption sites, thereby providing an additional resistance to diffusional jumps. This additional resistance adds to the simple-size-based resistance to diffusional jumps for H_2S. The specific interactions of H_2S with the sorption sites could be the result of its polarity and condensability. These results explain the lower H_2S permeability and H_2S/CH_4 mobility selectivity PDMC.

On the other hand, the enthalpy of solution follows the generally observed trend as it increases with increasing critical temperature in both materials. The activation energy of diffusion of each molecule is higher in CA than in PDMC, due to the fact that the latter is has a higher stiffness and free volume, therefore a more "open" structure than its counterpart. The heat of sorption of H_2S is more exothermic than for CO_2 and CH_4, consistent with its higher condensability.

4.8 Assessing Materials Performance

As mentioned previously, most studies for H_2S/CH_4 separation focused on rubbery polymers, due H_2S's high condensability. Rubbery polymers are typically described as amorphous and highly viscous materials that behave as high molecular weight liquids [3, 21-23]. Their backbone typically consists of long repeat units of flexible linkages such as, $-CH_2-$, $-COO-$, $-O-$, Si-O, and $-NH$. These groups increase the polymer's polarity and leads to the high solubility observed with highly polar molecules such as H_2S. Rubbery polymers that have been studied for sour gas separations include Pebax® (polyamide co-ether) [18, 24, 25], poly (ether urethane) [18], poly (ether urethane urea) [18], silicone rubber (PDMS) [24, 26, 27], and poly (ester urethane urea) [19]. These materials showed high H_2S/CH_4 selectivities but low CO_2/CH_4. It is important to compare their performance with the glassy polymers used in this study to understand what modification will be needed to compete with these materials, mainly to increase permeability and H_2S/CH_4 selectivity. The pure, binary, and ternary gas results obtained in the previous sections were plotted on a productivity-selectivity trade-off curve and compared to these materials [28, 29]. The pure CO_2 and H_2S performance of neat CA and uncrosslinked

PDMC and their mixed gas performance are plotted in Figure 4.18 and 4.19. The mixed gas data points are only reported as 700 psia because it simulates realistic feed conditions. It should be noted that there is no upper-bound line yet due to the limited amount of data available in literature for this gas pair. These trade-off curves show that PDMC is a great candidate for CO_2 removal as shown by previous researchers, as it lies on the trade-off curve even with aggressive $10\%\,H_2S$ and $20\%\,H_2S$ feed concentrations at 700 psia. Therefore, there is significant potential for this material if its permeability could be further improved by thermal crosslinking for example. On the other hand, CA showed great potential for H_2S removal as its H_2S/CH_4 is good, even under aggressive H_2S feeds. These observations led to the conclusion that cellulose acetate could still be a better choice for this separation because it favors both solubility and diffusivity; it possess good CO_2/CH_4 and H_2S/CH_4 selectivity. Therefore, if its permeability could be substantially improved without significant loss in selectivity, it may be a more economically feasible choice. One approach could be introducing bulky groups in the main chain to increase free volume [30]. On the other hand, PDMC showed promise since it has a high overall productivity and its performance and resistance to plasticization could be improved by crosslinking as previous researchers have shown [5, 6]. Engineering cellulose acetate via a grafting and crosslinking with a silane [30] will be explored in the next Chapter and the performance of these engineered materials will be assessed in Chapter 6.
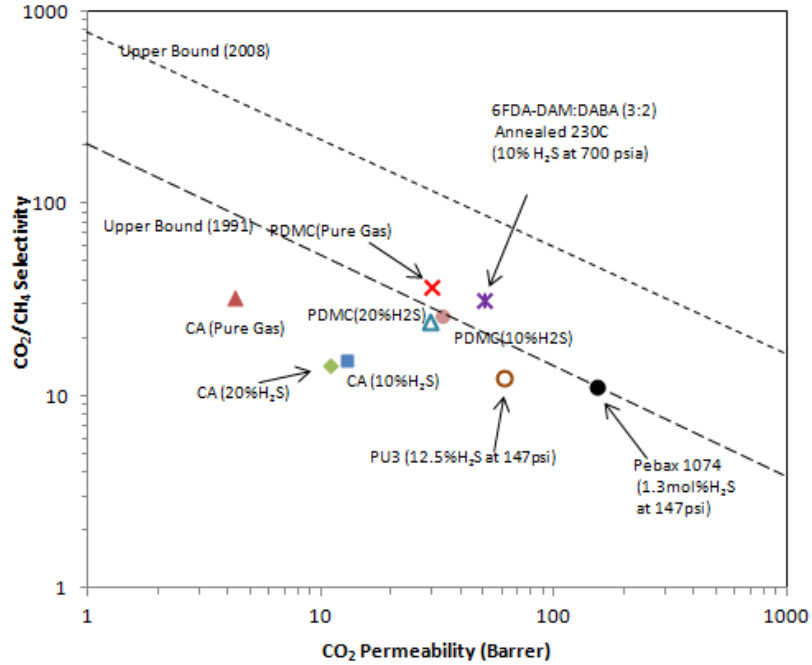
Figure 4.18: CO$_2$/CH$_4$ Permeability-selectivity tradeoff curve comparison of neat CA and uncrosslinked PDMC to other materials [10, 18].
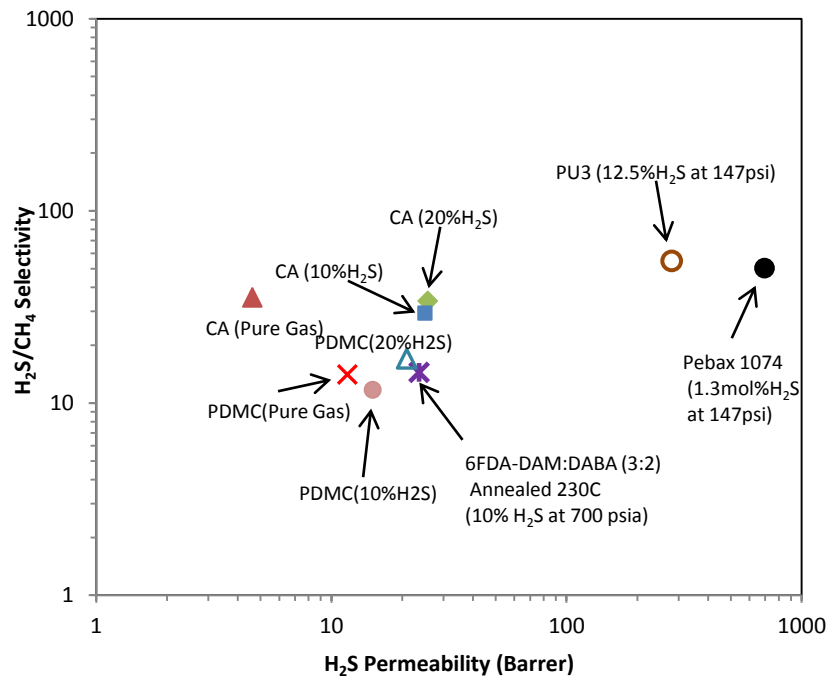
Figure 4.19: H$_2$S/CH$_4$ Permeability-selectivity tradeoff curve comparison of neat CA and uncrosslinked PDMC to other materials [10, 18].

4.9 References

[1] A.C. Puleo, D.R. Paul, S.S. Kelley, The effect of degree of acetylation on gas sorption and transport behavior in cellulose acetate, J Membrane Sci, 47 (1989) 301-332.

[2] A.Y. Houde, S.S. Kulkarni, M.G. Kulkarni, Permeation and Plasticization Behavior of Glassy-Polymers - a Waxd Interpretation, J Membrane Sci, 71 (1992) 117-128.

[3] D.R. Paul, I.U.P. I͡Ampolʹskiĭ, Polymeric Gas Separation Membranes, Taylor & Francis, 1994.

[4] T.C. Merkel, L.G. Toy, Comparison of hydrogen sulfide transport properties in fluorinated and nonfluorinated polymers, Macromolecules, 39 (2006) 7591-7600.

[5] A.M.W. Hillock, W.J. Koros, Cross-Linkable Polyimide Membrane for Natural Gas Purification and Carbon Dioxide Plasticization Reduction, Macromolecules, 40 (2007) 583-587.

[6] A.M.W. Hillock, Crosslinkable Polyimide Mixed Matrix Membranes For Naural Gas Purification, in, Georgia Institue of Technology, PhD Thesis, 2005.

[7] W.R. Vieth, J.M. Howell, J.H. Hsieh, Dual Sorption Theory, J Membrane Sci, 1 (1976) 177-220.

[8] S.A. Stern, A.H. Demeringo, Solubility of Carbon-Dioxide in Cellulose-Acetate at Elevated Pressures, J Polym Sci Pol Phys, 16 (1978) 735-751.

[9] J. Vaughn, Development and Evaluation of Aromatic Polyamide-imide Membranes for H2S and CO2 Separations from Natural Gas, in: School of Chemical and Biomolecular Engineering, Georgia Instituteof Technology, Atlanta, 2013.

[10] B. Kraftschik, W.J. Koros, J.R. Johnson, O. Karvan, Dense film polyimide membranes for aggressive sour gas feed separations, J Membrane Sci, 428 (2013) 608-619.

[11] W.J. Koros, A.H. Chan, D.R. Paul, Sorption and Transport of Various Gases in Polycarbonate, J Membrane Sci, 2 (1977) 165-190.

[12] W.J. Koros, D.R. Paul, Transient and Steady-State Permeation in Poly(Ethylene Terephthlate) above and Below the Glass-Transition, J Polym Sci Pol Phys, 16 (1978) 2171-2187.

[13] D.R. Paul, W.J. Koros, Effect of Partially Immobilizing Sorption on Permeability and Diffusion Time Lag, J Polym Sci Pol Phys, 14 (1976) 675-685.

[14] S.M. Jordan, W.J. Koros, G.K. Fleming, The Effects of Co2 Exposure on Pure and Mixed Gas Permeation Behavior - Comparison of Glassy Polycarbonate and Silicone-Rubber, J Membrane Sci, 30 (1987) 191-212.

[15] M.J. Thundyil, Y.H. Jois, W.J. Koros, Effect of permeate pressure on the mixed gas permeation of carbon dioxide and methane in a glassy polyimide, J Membrane Sci, 152 (1999) 29-40.

[16] H.D. Kamaruddin, W.J. Koros, Some observations about the application of Fick's first law for membrane separation of multicomponent mixtures, J Membrane Sci, 135 (1997) 147-159.

[17] S.A. Stern, H.L. Frisch, The Selective Permeation of Gases through Polymers, Annu Rev Mater Sci, 11 (1981) 523-550.

[18] G. Chatterjee, A.A. Houde, S.A. Stern, Poly(ether urethane) and poly(ether urethane urea) membranes with high H2S/CH4 selectivity, J Membrane Sci, 135 (1997) 99-106.

[19] T. Mohammadi, M.T. Moghadam, M. Saeidi, M. Mahdyarfar, Acid gas permeation behavior through poly(ester urethane urea) membrane, Ind Eng Chem Res, 47 (2008) 7361-7367.

[20] L.M. Costello, Temperature Dependence of Gas Sorption and Transport Properties, in: Chemical Engineering, University of Texas at Austin, Austin, 1994.

[21] B. Freeman, Y. Yampolskii, I. Pinnau, Materials Science of Membranes for Gas and Vapor Separation, Wiley, 2006.

[22] Properties and Behavior of Polymers, Wiley, 2012.

[23] J. Brandrup, E.H. Immergut, Polymer handbook, Interscience Publishers, 1966.

[24] K.A. Lokhandwala, R.W. Baker, Sour Gas Treatment Process Including Membrane and Non-membrane Treatment Steps, in, United States, 1995.

[25] R.W. Baker, K.A. Lokhandwala, Sour Gas Treatment Process, in, United States, 1995.

[26] S.A. Stern, B.D. Bhide, Permeability of Silicone Polymers to Ammonia and Hydrogen-Sulfide, J Appl Polym Sci, 38 (1989) 2131-2147.

[27] B. Wilks, M.E. Rezac, Properties of rubbery polymers for the recovery of hydrogen sulfide from gasification gases, J Appl Polym Sci, 85 (2002) 2436-2444.

[28] L.M. Robeson, Correlation of separation factor versus permeability for polymeric membranes, J Membrane Sci, 62 (1991) 165-185.

[29] L.M. Robeson, The upper bound revisited, J Membrane Sci, 320 (2008) 390-400.

[30] C.S.K. Achoundong, N. Bhuwania, S.K. Burgess, O. Karvan, J.R. Johnson, W.J. Koros, Silane Modification of Cellulose Acetate Dense Films as Materials for Acid Gas Removal, Macromolecules, 46 (2013) 5584-5594.

CHAPTER 5: GCV-MODIFICATION OF CELLULOSE ACETATE FILMS AS MATERIALS FOR SOUR GAS REMOVAL

5.1 Abstract

This chapter introduces the modification of cellulose acetate (CA) using vinyltrimethoxysilane (VTMS), a technique referred to as *GCV-Modification* [1]. The modification technique is a three step protocol that involves grafting of the silane agent via residual hydroxyls groups in CA in the first step, then hydrolysis of the unreacted methoxy groups to form silanols in the second step, and condensation of the silanols groups to induce crosslinking in the last step. This technique was developed to obtain a lower cost, fairly high performance material for sour gas removal. Extensive characterization has been conducted on the material to support the proposed reaction mechanism and to understand the material properties. It was found that the GCV-Modified CA material was more amorphous, had a lower glass transition temperature (T_g) with fair thermal stability, and a higher flexibility compared to neat CA. The reaction conditions and selection will be described in detail as well as the use of other silane agents and catalysts considered. These studies showed that the vinyl substituent contributed to the higher polymer flexibility observed. The effect of different reaction times and temperatures on the silicon content and gel content will also be discussed. It was found that increasing reaction time and temperature, results in higher silicon loading and higher gel content in the membrane. It was also found that finding the right the balance between having higher silicon loading while maintaining the membrane appearance and stability will be a critical step when dealing with scaling up the technique. Therefore, further optimization will be required when transferring the

technology to asymmetric hollow fibers, which even though is beyond the scope of this study, is the ultimate goal.

5.2 Introduction

Many researchers have used silane crosslinking of polyethylene (PE) methods to improve its insulation properties [2-7]. Even though a number of silanes can be used in this process, the most common silane used is vinyltrimethoxysilane (VTMS) [6, 8]. Since PE has no functional groups available for crosslinking, dialkyl peroxides are used extensively to initiate the reaction, with dicumyl peroxide (DCP) as the most common [2, 6, 7, 9]. Previous researchers crosslinked PE by first grafting the polymer at the vinyl end by initiating the reaction with DCP at 200°C, and then using water in the presence of a catalyst to crosslink the polymer [2, 9, 10]. This technique was successful in increasing thermal and mechanical properties of PE. However, it had not been used previously for natural gas separation. The modification presented here is intended to develop a material capable of enhancing the polymer properties for membrane-based sour gas separations.

5.3 Synthesis of GCV-Modified Cellulose Acetate Films

In this technique, cellulose acetate is modified via grafting of vinyltrimethoxysilane (VTMS) to residual –OH groups, followed by moisture hydrolysis of the methoxy groups on the silane, and with condensation of those silanols to form a crosslinked polymer network, as shown in Figure 5.1. In the first step, a dried CA dense film was immersed in neat VTMS in a 1:100 by weight CA: VTMS ratio and placed in a 40mL Teflon bomb, which was inserted in a sealed stainless-steel autoclave. The autoclave was put in the

oven at 200°C for 24 hrs. After the 24 hrs reaction, the vessel was cooled down to room temperature, and the modified film was removed and dried in a vacuum oven at 150°C for 24 hrs, to remove excess VTMS. The grafted polymer was then exposed to moisture in ambient air with a relative humidity of ~25% for 48 hrs. This likely caused the unreacted methoxy groups to hydrolyze and to form silanols, which subsequently condensed to form siloxane bonds, inducing crosslinking of the polymer chains as illustrated in Figure 5.1. A comparison of a few properties of the films before and after modification is shown in Table 5.1. It includes the film thickness and weight change, and its density. Since the modification is believed to include a combination of grafting and crosslinking, the term "GCV" was used to denote the modification of CA by **G**rafting and **C**rosslinking using **V**TMS. While we will focus mostly on the GCV-Modified CA in this chapter, many other conditions were explored shown were considered as well before identifying the preferred protocol. These less desired approaches include the use of a DCP catalyst in the GCV-Modification procedure, and the use of a different grafting agent, trimethoxysilane (TMS). The reaction conditions of these different procedures are summarized in Table 5.2 along with some terminologies.

Table 5.1: Comparison of the properties of GCV-Modified CA and neat CA

	Weight (g)	Thickness (µm)	Density (g/cc)
Neat CA	0.150-0.30	75-85	1.312±0.0024
GCV-Modified CA	0.175-0.35	97-110	1.272±0.0026
Δ%	16.7%±1.15	30%±1.23	3.05%±0.0208

Table 5.2: Silane modification of CA at different reaction conditions

Terminology	Reaction Conditions	Reactant Ratio	Drying Conditions
GCV-Modified	1 day at 200°C	1:100 CA:VTMS	1 day at 150°C
GCV-DCP-Modified	1 day at 150°C	1:100:0.1 CA:VTMS:DCP	1 day at 150°C
GCT-Modified	1 day at 150°C	1:100 CA:TMS	1 day at 150°C

Step 1: VTMS Grafting
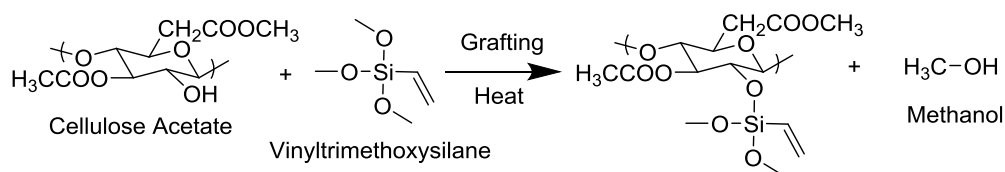
Step 2: Hydrolysis
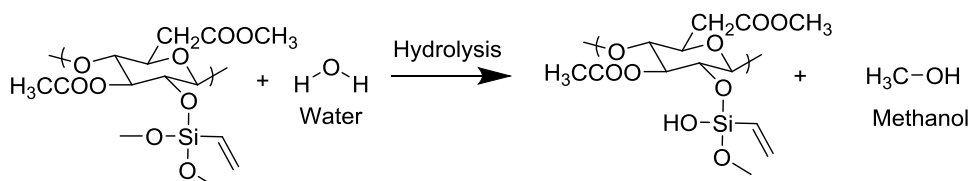
Step 3: Crosslinking
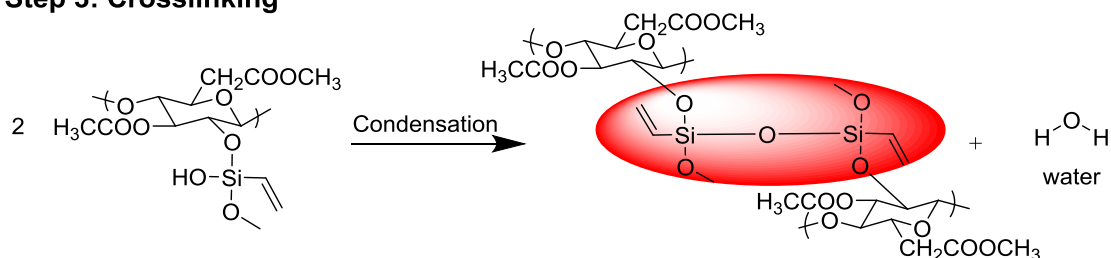
Figure 5.1: Reaction Mechanism of the GCV-Modification of cellulose acetate films.

5.4 Synthesis and Characterization of GCV-DCP-Modified Cellulose Acetate Films

Initially, it was envisioned that the vinyl bond on VTMS would open to induce grafting on that side of the VTMS (as done in the case of PE crosslinking). With this in mind, a reaction temperature of 150°C for 24 hrs was chosen using the DCP catalyst in a 1:100:0.1 ratios. The 24 hrs reaction time was selected to allow adequate time for the reaction with minimal diffusion limitations. It appeared that the resulting film from this initial study opened the vinyl group and the resulting film was brittle, cloudy, and had undesirable properties. Even though the resulting GCV-DCP-Modified film was brittle, it was characterized it using FTIR and NMR to understand the resulting outcome.

5.4.1 FTIR Analysis of GCV-DCP-Modified CA Films

The IR spectra of neat CA and VTMS are shown on Figure 5.2 and Figure 5.3 and their band assignments in Table 5.3 and Table 5.4, respectively. Some important features of the IR spectra of the GCV-DCP-Modified CA film (Figure 5.4) include: (1) a slight shift and a decrease in intensity in the –OH band in CA around 3469 cm^{-1}, (2) a decrease in the band that occurs in neat VTMS at 1410 cm^{-1}, a disappearance of the bands at 1011 and 968 cm^{-1}, and the merging of the doublet at 811 and 769 cm^{-1}. These bands were characteristic of the vinyl group present in the VTMS structure but, (3) the band at 2842 and 1191 cm^{-1} characteristic of the Si-OCH$_3$ was not changed significantly.
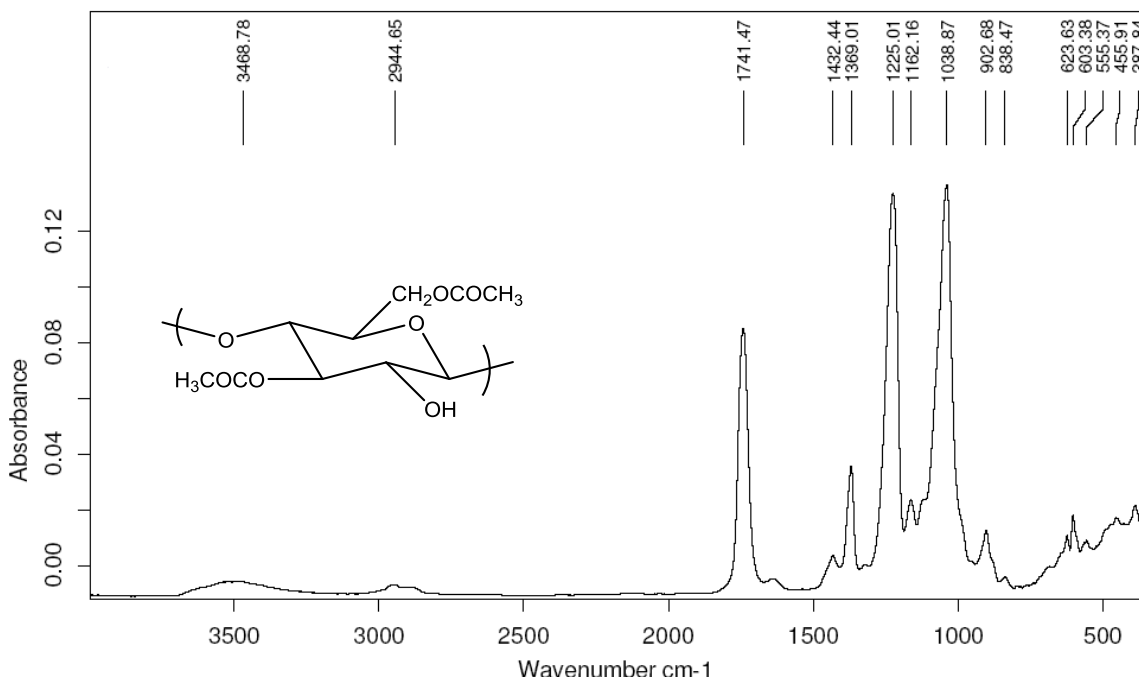
Figure 5.2: ATR-IR spectrum of neat cellulose acetate film.

Table 5.3: FTIR band assignments of neat cellulose acetate film [11, 12]

Wavenumber (cm^{-1})	Band Assignment
3467	-OH stretching (H-bonding)
2939	C-H stretching valence vibrations of –CH and –CH$_2$ groups
1739	C=O stretching of ester
1430	C-OH bending
1368	–CH$_3$ in plane bending (–CH$_3$ group from acetate group)
1223	C-O-C stretching of acetyl group
1161	C-O-C antisymmetric bridge stretching
1037	Ether linkage connecting neighboring glucopyranose rings
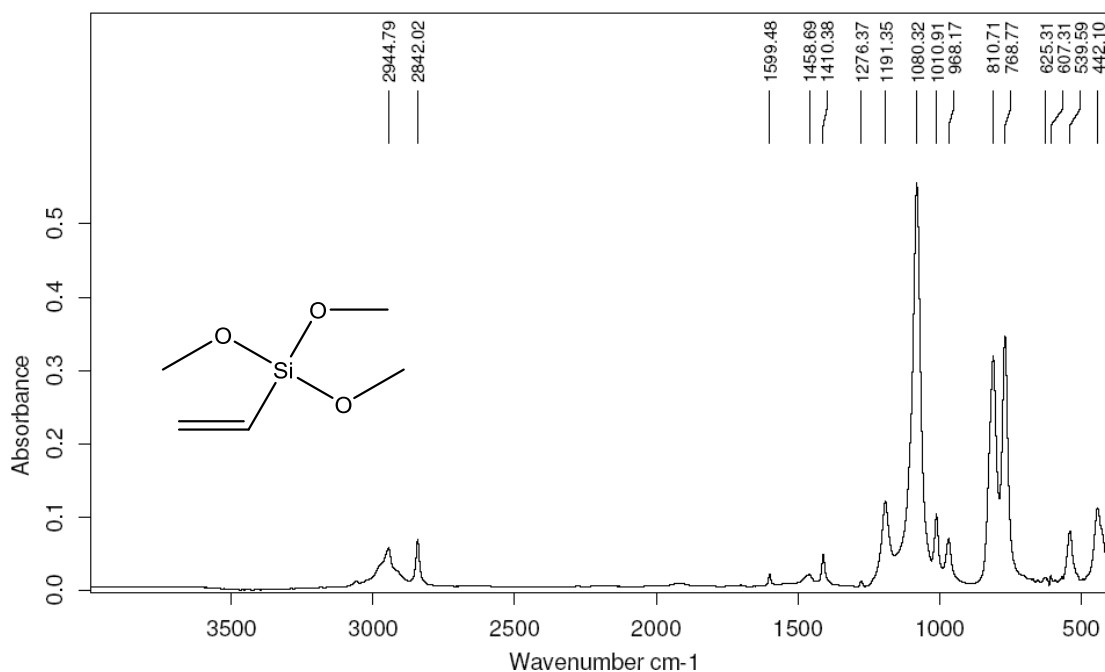
Figure 5.3: ATR-IR spectrum of neat VTMS liquid.

Table 5.4: FTIR band assignments of neat VTMS liquid [13, 14]

Wavenumber (cm^{-1})	Band Assignment
2945	CH_2 asymmetric stretch
2842	CH symmetric stretch ($Si-OCH_3$)
1599	C=C stretch
1410	CH_2 deformation ($Si-CH=CH_2$)
1191	$O-CH_3$ rocking ($Si-OCH_3$)
1080	Si-O-C stretch ($Si-OCH_3$)
1011	Vinyl CH_2 twist ($Si-CH=CH_2$)
968	Vinyl CH_2 wag ($Si-CH=CH_2$)
811	=CH & =CH_2 ($Si-CH=CH_2$)
769	=CH & =CH_2 ($Si-CH=CH_2$)
540	Vinyl C-H bend
443	C-Si-O bend

To refer to some band intensities as decreasing or increasing, all of the spectra used were carefully normalized with respect to one another for comparison. Therefore, it is reasonable to say that some peak are not being detected or have decreased in intensity relative to the others. Observation 1 shows that –OH groups have reacted, and observation 3 showed that some bands that are characteristic of the vinyl groups are no longer detected except from the ones at 1410 and at 443 cm^{-1}. To better quantify the latter observation, a band ratio analysis was used. Since the band at 1410 cm^{-1} is characteristic of the $Si-CH=CH_2$ bond and the band at 443 is characteristic of the C-Si-O bend in VTMS, their ratio in both VTMS and GCV-DCP-Modified CA was taken for comparison.

$$\left[\frac{Si-CH=CH_2\big|_{\text{at }1410cm^{-1}}}{C-Si-O\big|_{\text{at }443cm^{-1}}}\right]_{\text{in Neat VTMS}} = 0.529 \quad \text{and} \quad \left[\frac{Si-CH=CH_2\big|_{\text{at }1411cm^{-1}}}{C-Si-O\big|_{\text{at }443cm^{-1}}}\right]_{\text{in GCV-DCP-Modified CA}} = 0.105$$

This analysis showed that roughly 80% of the vinyl groups have reacted in the presence of the DCP catalyst. Similarly, the neat VTMS liquid has three bands that correspond to the Si-OCH$_3$ group: 2842, 1191, and 1080 cm^{-1}. Therefore, the ratio of any two of those peaks could also be taken and compared to the ratio of the same peaks in the GCV-DCP-Modified film. In this case, the bands at 1191 and 2842 cm^{-1} were used since the band at 1080 cm^{-1} merged with the one at 1039 cm^{-1} in neat CA and was therefore not useful.

$$\left[\frac{Si-OCH_3\big|_{\text{at }1191cm^{-1}}}{Si-OCH_3\big|_{\text{at }2842cm^{-1}}}\right]_{\text{in Neat VTMS}} = 1.25 \quad \text{and} \quad \left[\frac{Si-OCH_3\big|_{\text{at }1189cm^{-1}}}{Si-OCH_3\big|_{\text{at }2840cm^{-1}}}\right]_{\text{in GCV-DCP-Modified CA}} = 0.94$$

The ratio of those methoxy peaks have decreased by roughly 25% from the neat CA, indicating less of those groups have reacted compared to the vinyl groups.
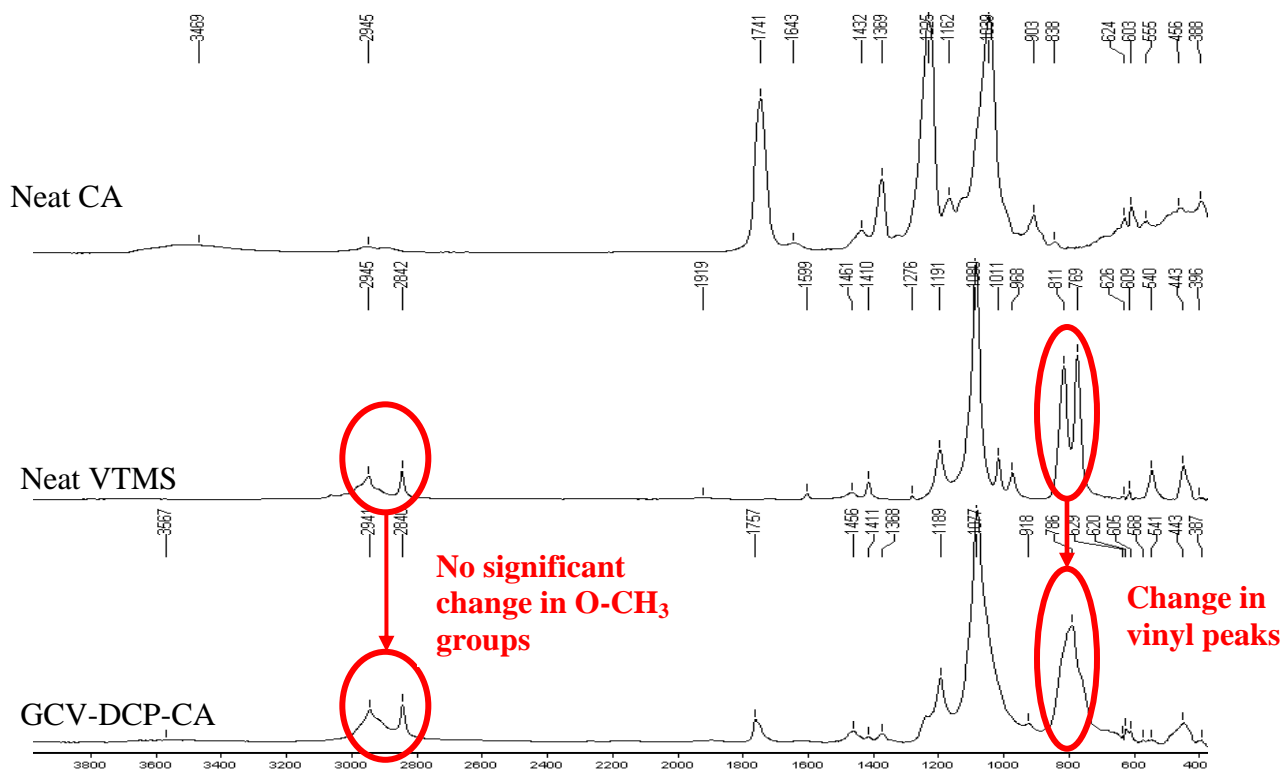
Figure 5.4: ATR-IR spectra of neat CA film (top), neat VTMS liquid (middle), and GCV-DCP-Modified CA film (bottom).

5.4.2 NMR Spectroscopy Analysis of GCV-DCP-Modified CA Films

The ^{13}C solid state NMR spectrum of neat CA is shown on Figure 5.5 while that of the GCV-DCP-Modified CA is shown on Figure 5.6. The carbons in CA are numbered and the chemical shifts of their functional groups are shown on Figure 5.5 [15]. Two new signals were generated for GCV-DCP-Modified CA around 130 -140 ppm. Those signals correspond to the carbons at either end of the carbon-carbon double bond, and are thus characteristic of the vinyl group. The signal detected around 50 ppm corresponds to the carbon-oxygen bond, which belongs to the unreacted $-OCH_3$ groups. Even though the vinyl bond signal is detected, it is nevertheless much smaller in intensity compared to

when no DCP is added as shown in Figure 5.10. It indicates that more vinyl groups opened when DCP was added. In addition, the intensity of the $-OCH_3$ groups is much higher compared to that of Figure 5.10, indicating that reaction happened more with the vinyl than the methoxy groups. These results show that during the GCV-DCP-Modification, the predominant reaction occurs with the vinyl groups, as also confirmed by the IR analysis above.
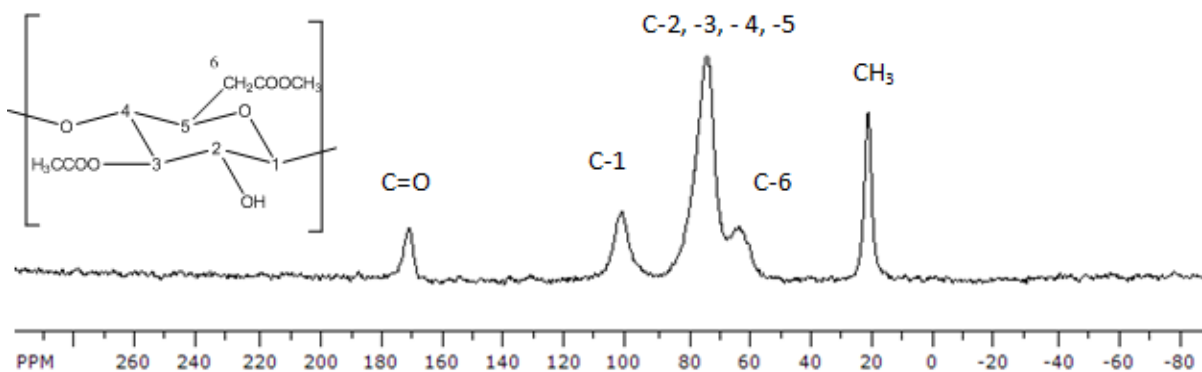
Figure 5.5: ^{13}C Solid state NMR of neat cellulose acetate film.
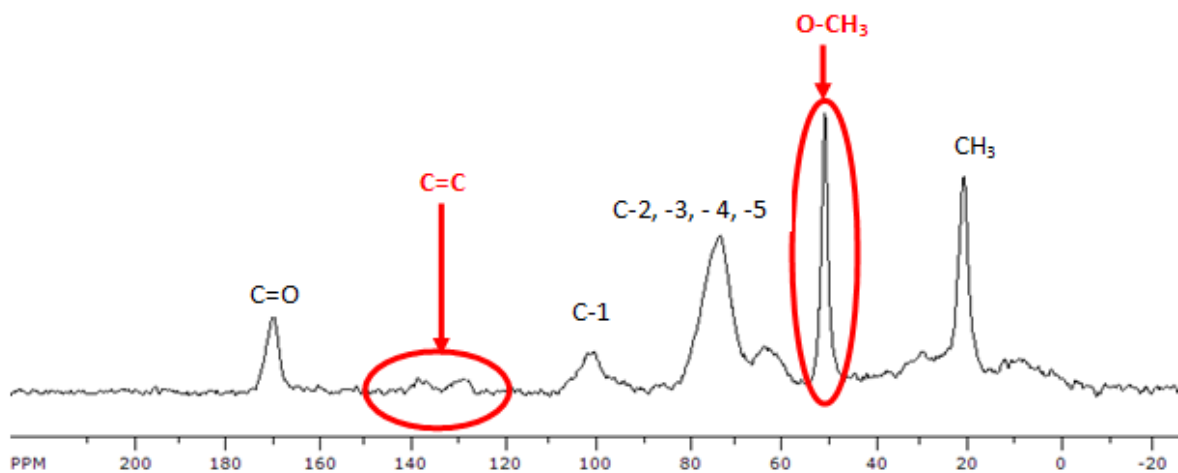
Figure 5.6: ^{13}C Solid Sate NMR of GCV-DCP-Modified cellulose acetate film.

Neat VTMS has a signal around -56 ppm [16], whereas the ethyltrimethoxysilane (ETMO) has a signal around -41 ppm [17, 18]. In Figure 5.7, there is a low signal around

120

-58 ppm and a strong signal around -43 ppm, which further supports the fact that some vinyl group have reacted. Furthermore, as shown in FTIR results, ~80% of the vinyl groups have reacted in the GCV-DCP-Modified CA, which explains the much lower signal around -58 ppm in Figure 5.7 compared to a much higher signal around -43 ppm.
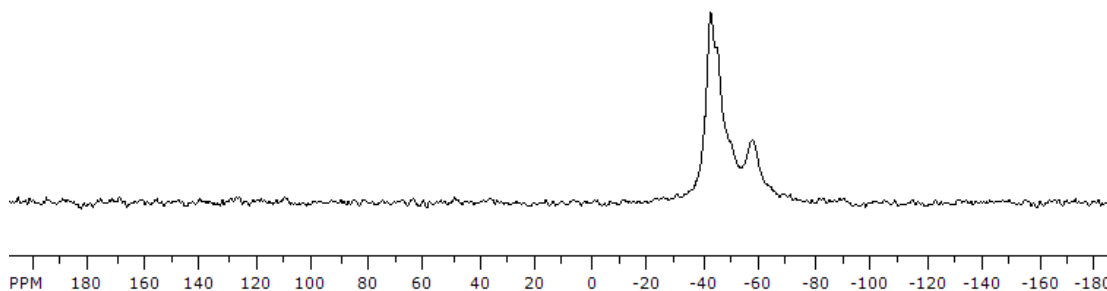
Figure 5.7: ^{29}Si Solid State NMR of GCV-DCP-Modified CA film.

These characterization techniques showed that the use of DCP led to dominant reaction with the vinyl groups. These effects caused the film to be brittle and thus not useful for this purpose. For these reasons, this synthesis protocol was not pursued any further. The brittleness that was observed with this DCP modified film may have been caused by the opening of the vinyl group which was originally hoped would add flexibility to the polymer to offset rigidification from the ultimate silanols crosslinking.

To consider the effect of eliminating possible crosslinking through the olefin functionality, the use of trimethoxysilane (TMS) instead of VTMS was explored. The difference between the VTMS and TMS lies in the replacement of the vinyl group in VTMS with hydrogen as illustrated in Chapter 3. It was found that the resulting film was also brittle and not useful as a membrane material as discussed in the next section.

5.5 Synthesis and Characterization of GCT-Modified Cellulose Acetate Films

The synthesis of GCT-Modified films was done using the conditions shown in Table 5.2. GCT-The resulting films were also brittle and cloudy with limited utility. By looking at the FTIR spectra of the resulting GCT-Modified membrane on Figure 5.8, the following observation were made: (1) the Si-OCH$_3$ bands at 2844, 1193, and 1085 cm^{-1} present in neat TMS are no longer detected, indicating that those methoxy groups reacted, (2) the band assigned to the Si-H group in TMS at 2199 cm^{-1} has reduced significantly. The three spectra were also normalized to facilitate comparison. By using a similar band ratio analysis as above, those observations were further analyzed.

$$\left[\frac{Si-H\big|_{at\ 2199cm^{-1}}}{Si-H\big|_{at\ 872cm^{-1}}}\right]_{in\ Neat\ TMS} = 0.206 \quad and \quad \left[\frac{Si-H\big|_{at\ 2220cm^{-1}}}{Si-H\big|_{at\ 831cm^{-1}}}\right]_{in\ GCT\text{-}Modified\ CA} = 0.043$$

In this case, a ~80% of the Si-H groups have reacted. The opening of the vinyl group and the resulting brittleness of the film in the GCV-DCP-Modified film and their absence in GCT-Modified, which resulted in a brittle film as well support the fact the vinyl groups are needed for the polymer to remain flexible for practical membranes. It may, of course, be possible to replace the vinyl groups with a simple ethyl group; however, these options were not pursued here but will be discussed in Chapter 7 as potential future routes.
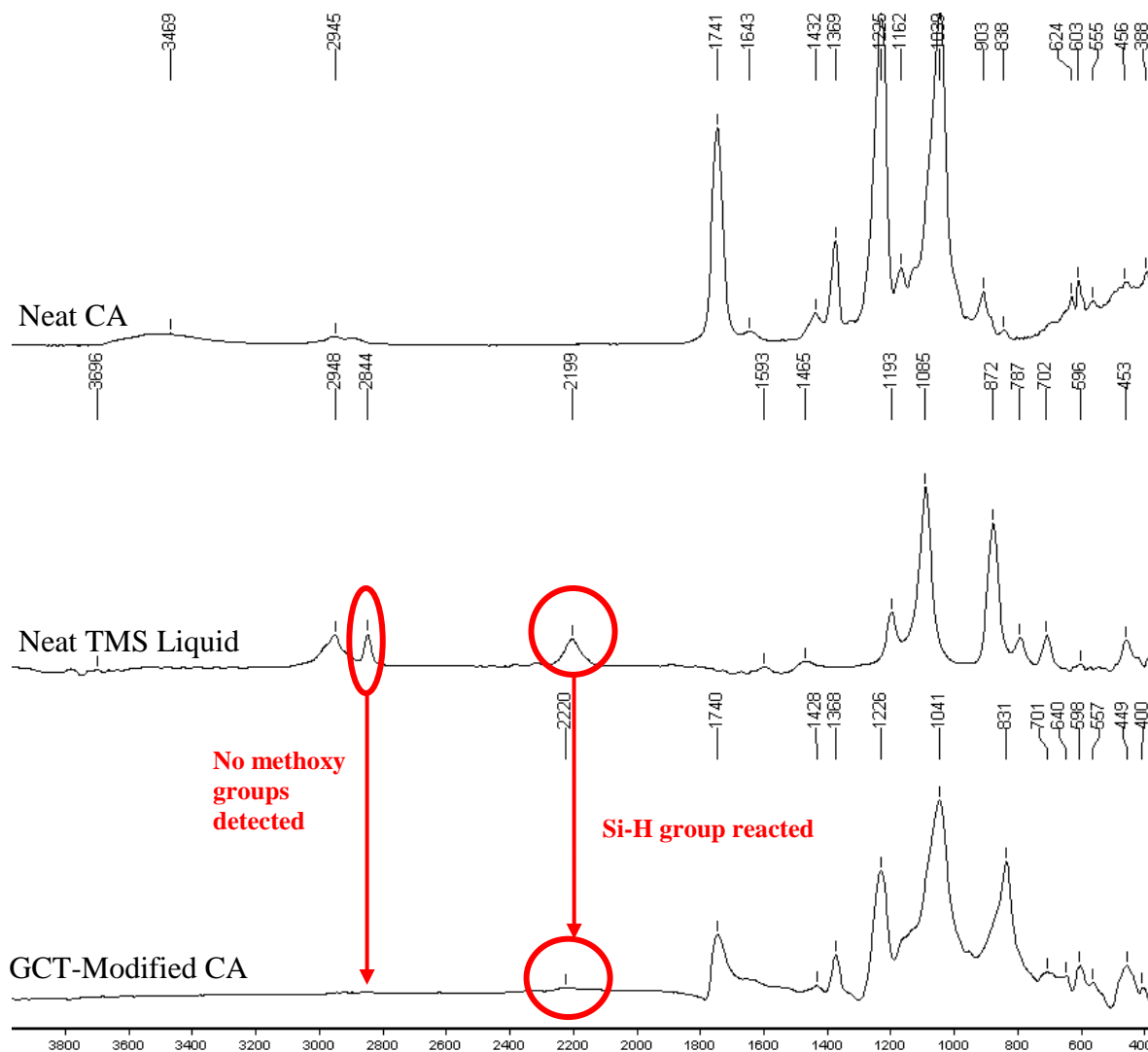
Figure 5.8: ATR-IR Spectra of neat CA film (top), neat TMS liquid (middle), and GCT-Modified CA film (bottom).

These studies showed that the vinyl group added flexibility to the polymer and their absence made the membrane unworkable. Therefore, the GCV-Modification was found to be the preferred protocol as it produced transparent, more flexible films with the best membrane performance as discussed in Chapter 6. The following section will focus on extensive characterization of this GCV-Modified material to not only confirm the proposed the reaction mechanism in Figure 5.1, but to also study the material mechanical and thermal properties.

5.6 Characterization of GCV-Modified Cellulose Acetate Films

5.6.1 FTIR Analysis of GCV-Modified CA Films

The IR spectrum of the GCV-Modified CA film is shown in Figure 5.9. Some important features of the GCV-Modified CA film in Figure 5.9 include: (1) a disappearance of the –OH band around 3469 cm^{-1}, (2) the appearance of bands at 2842 and 1191 cm^{-1}, characteristic of the unreacted –OCH$_3$ groups, (3) the appearance of the doublet at 811 and 769 cm^{-1}, characteristic of the vinyl group. A band ratio analysis was also used in this case to quantify the results. The neat VTMS liquid has three bands that correspond to the Si-OCH$_3$ group at 2842, 1191, and 1080 cm^{-1}. Therefore, the ratio of any two of those peaks could be taken and compared to the ratio of the same peaks in the GCV-Modified CA film. In this case, the bands at 1191 and 2842 cm^{-1} were used since the band at 1080 cm^{-1} appeared to have merged with the one at 1039 cm^{-1} in neat CA and was therefore not useful. These results indicate that approximately 85% of the methoxy groups in VTMS have reacted.

$$\left[\frac{Si-OCH_3\big|_{\text{at } 1191cm^{-1}}}{Si-OCH_3\big|_{\text{at } 2842cm^{-1}}}\right]_{\text{in neat VTMS}} = 1.25 \quad \text{and} \quad \left[\frac{Si-OCH_3\big|_{\text{at } 1191cm^{-1}}}{Si-OCH_3\big|_{\text{at } 2842cm^{-1}}}\right]_{\text{in GCV-Modified CA}} = 0.19$$

The same approach was used for the vinyl bands. The neat VTMS liquid has bands that correspond to the Si-CH=CH$_2$ group at 1599, 1410, 1011, and 968 cm^{-1}. In addition, =CH and =CH$_2$ bending bands occur at 811 and 769 cm^{-1}. In this case, the ratio of the bands at 811 and 769 cm^{-1} to the band at 1410 cm^{-1} were taken and compared with similar bands in the GCV-Modified CA film. As shown below, these two ratios have similar values,

124

indicating that most vinyl groups did not react, which was desirable in this case since it added flexibility in the polymer and had a positive effect on the permeation rate as we will discuss later.

$$\left[\frac{-CH\ \&=CH_{2}\big|_{at\ 769cm^{-1}\ and\ 811cm^{-1}}}{Si-CH=CH_{2}\big|_{at\ 1410cm^{-1}}} \right]_{in\ Neat\ VTMS} = 12.95 \quad and \quad \left[\frac{-CH\ \&=CH_{2}\big|_{at\ 782cm^{-1}\ and\ 818cm^{-1}}}{Si-CH=CH_{2}\big|_{at\ 1409cm^{-1}}} \right]_{in\ GCV\text{-}Modified\ CA} = 12.44$$

The gel content test done on this GCV-Modified CA film gave a value of 96.6±0.86%, which suggests that crosslinking occurred. However, since the siloxane (Si-O-Si) band usually occurs between 1000-1130 cm^{-1} and both CA (1039 cm^{-1}) and VTMS (1080 cm^{-1}) have bands around that region, it was difficult to assess whether the band in GCV-Modified CA at 1044 cm^{-1} confirmed the presence of the Si-O-Si bond. Therefore, the gel content was the only definitive evidence that crosslinking occurred in the GCV-Modified CA.
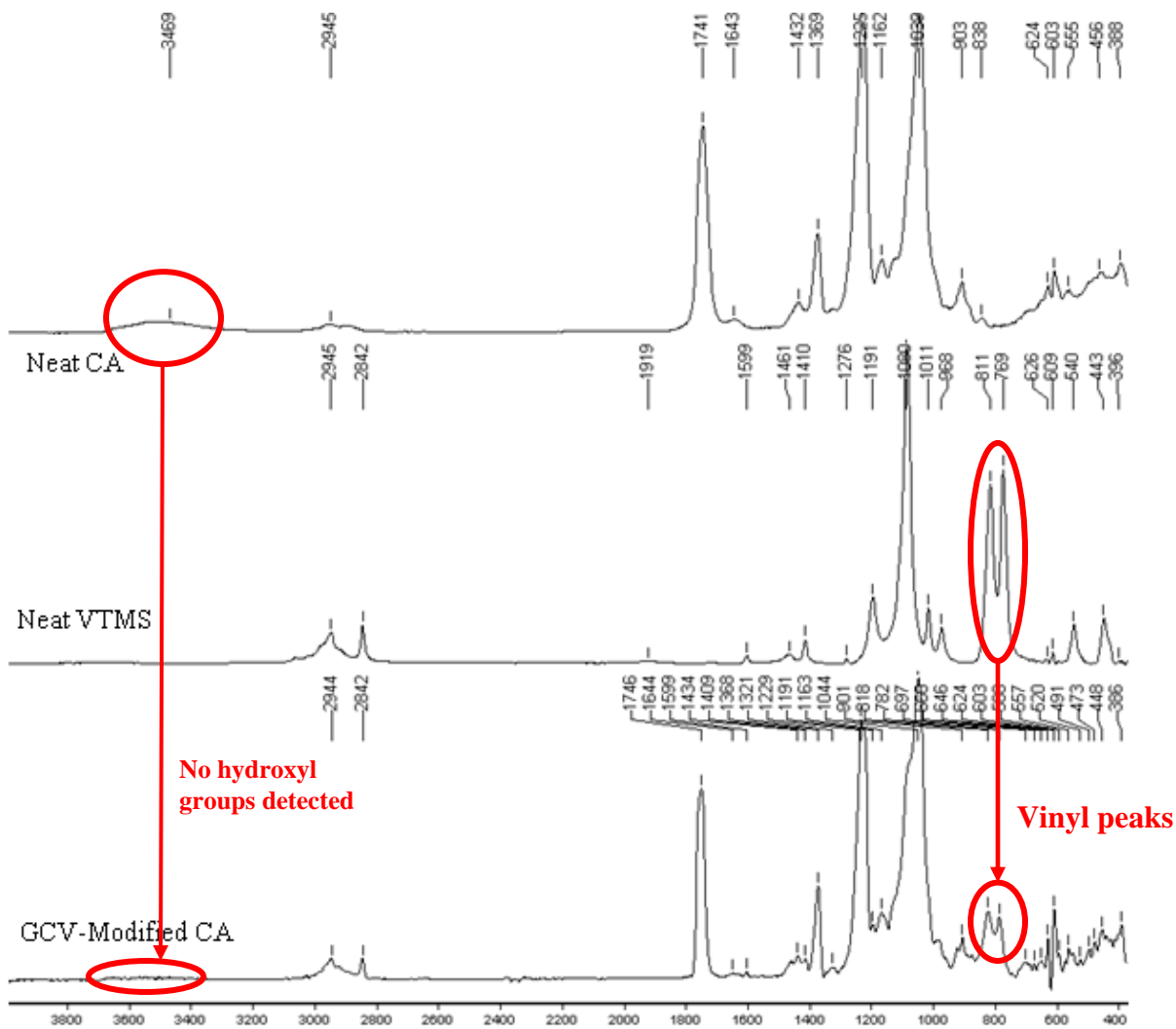
Figure 5.9: ATR-IR Spectra of neat CA film (top), neat VTMS liquid (middle), and GCV-Modified CA film (bottom).

5.6.2 NMR Spectroscopy Analysis of GCV-Modified CA Films

The ^{13}C NMR spectrum of the GCV-Modified film is shown in Figure 5.10. The ^{13}C NMR spectrum of the GCV-Modified CA generated two signals around 130 -140 ppm, which correspond to the vinyl carbons. The signal detected around 50 ppm as discussed previously corresponds to the unreacted methoxy groups. This result further supports our proposed reaction pathway of Figure 5.1.
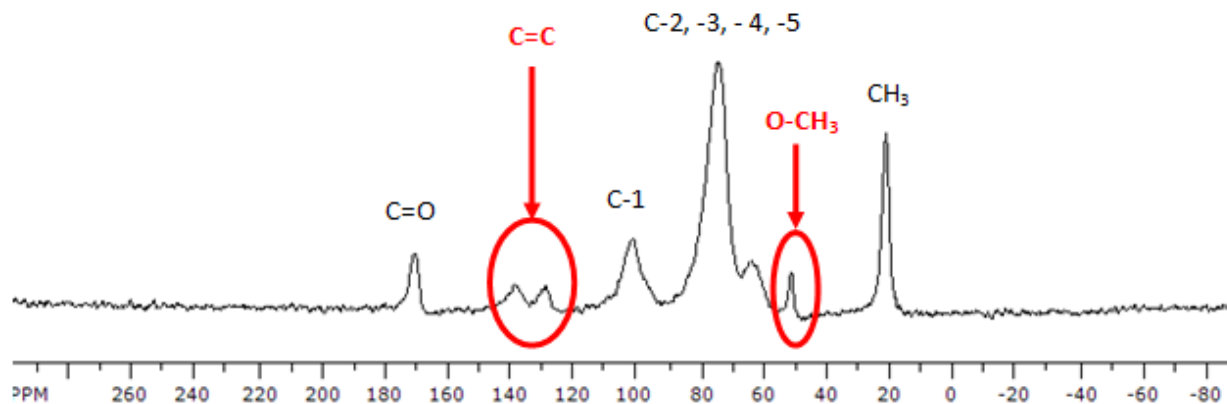
Figure 5.10. ^{13}C Solid state NMR of GCV-Modified CA dense film.

The ^{29}Si NMR spectrum of the GCV-Modified CA is shown in Figure 5.11. As noted previously, neat VTMS has a signal around -56 ppm, whereas the ethyltrimethoxysilane (ETMO) has a signal around -41 ppm. It shows that there is a strong signal around -58 ppm and a low signal around -43 ppm, which is the opposite of what happened for GCV-Modified CA film. This indicates that characteristic VTMS peak (vinyl) is still present in the GCV-Modified structure as expected from the IR results. Furthermore, these results suggest that VTMS does not just swell the polymer and crosslink with itself to form a gel. For example, if a silsesquioxane with a vinyl as the end group had formed, there would have been a signal -80 ppm [18, 19]. It should be noted that this does not mean that the grafted VTMS molecules have not grafted and crosslinked as shown in Figure 5.1, it simply means that a silica gel has not formed in this case, as it is generally the case with alkoxysilanes.
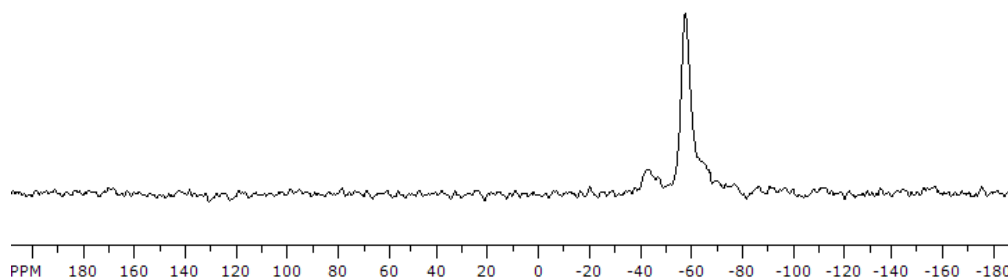
Figure 5.11: ^{29}Si Solid state NMR of GCV-Modified CA film.

5.6.3 DSC Analysis of GCV-Modified CA Films

The DSC scan of the neat CA and GCV-Modified CA films is shown in Figure 5.12. The average values of all runs are shown in Table 5.5. There was a roughly 40°C decrease in the glass transition temperature (T_g) from the neat CA to the GCV-Modified CA. Multiple effects led to the observed drop. While Maeda and Paul [20] showed that plasticizers tend to lower the T_g of the polymer, this decrease did not suggest that VTMS acted as an internal plasticizer. Rather, the main effect of grafting VTMS was to substitute the hydrogen-bonding hydroxyl groups in the neat CA which, as Kamide and Saito [21] showed, are mainly responsible for the stiff nature of CA. In general, crosslinking may or may not increase the T_g of a polymer depending on which polymer and which crosslinking agent is used [22]. For example, for rubbery polymers, crosslinking typically leads to increased T_g's [23]. However, previous researchers showed that covalent crosslinking of polyimides has a negligible impact on the T_g [24]. In this case, a significant decrease in the T_g was found, which suggests that factors that tend to lower the T_g override those promoting chain rigidity. Furthermore, bulky side groups tend to lower the T_g by inhibiting segmental packing, which in this case may be a

contributing factor to the resulting outcome [25]. The large endothermal peak between 50°C and 150°C in neat CA presumably represents evaporation of sorbed water [26], and in GCV-Modified CA represents methanol and water evolving during hydrolysis and condensation. By dividing the heat of vaporization of water (540 cal/g) by the area under the sorbed water endothermal peak in neat CA, the water content was estimated at about 3.3% prior to heating. This water loss was supported by the TG curve in Figure 5.14. Using the heat of fusion of a perfect cellulose triacetate crystallite (8.2 cal/g) [27], the crystallinity of neat CA was estimated to be about 33%. The melting transition observed in neat CA around 231°C was not evident in the GCV-Modified CA, and since melting characterizes crystalline polymers, it revealed the more amorphous nature of the GCV-Modified CA as we show later using XRD (Figure 5.15).
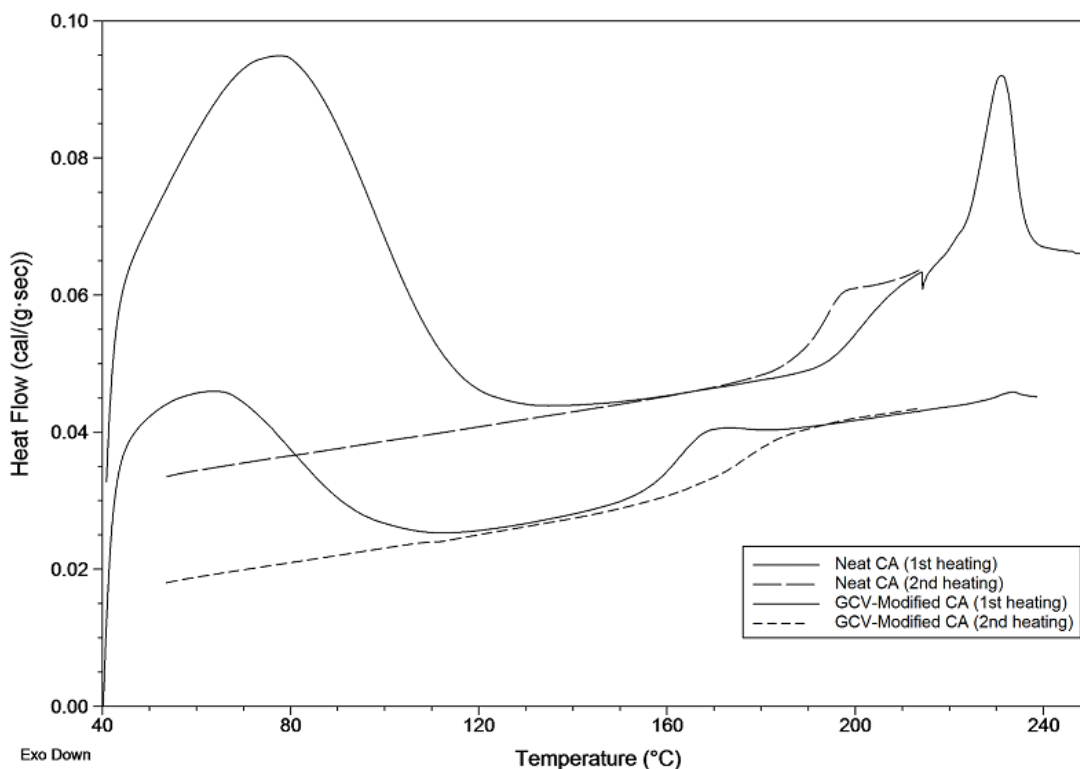
Figure 5.12: DSC curve of the Neat CA and GCV-Modified CA films.

5.6.4 DMA of GCV-Modified CA Films

The glass transition temperature of the polymer was also measured using DMA and was taken as the *tan δ* peak, as it is the one mostly used in literature; it occurs at the highest temperature. However, the loss modulus (E") peak and the onset of the storage modulus are also reported. The storage modulus (E') onset occurs at the lowest temperature and is related to the mechanical rigidity of the material, while the loss modulus peak is related to physical property changes (onset of segmental motion) in the material [28]. Figure 5.13 shows the DMA scan of the neat CA and GCV-Modified CA films. As expected, the T_g values measured by the DMA were higher than those measured using DSC, since DMA measurements are made at a higher frequency, which correspond to shorter time scales, which will shift the T_g to a higher value [29]. This is because the glass transition is a relaxation event involving the onset of chain segmental motion in the polymer, which is strongly dependent on the oscillation frequency [29]. For the same reason, the higher frequency of 3 Hz at which the measurements were made in this case also yielded slightly higher values than the values reported at 1 Hz in literature, as done by Puleo et al. [26] for example. The higher frequency was used to improve the signal-to-noise ratio. The average T_g value as measured by the *tan δ* peak was found to be 220.1°C for neat CA and 170°C for the GCV-Modified CA film. This 50°C reduction in the T_g is in good agreement with the DSC measurements reported above. The magnitude and shape of the tan delta peak at the T_g is higher for the GCV-Modified CA compared to neat CA, indicating a higher fraction of the amorphous phase in the modified material.

Table 5.5: Average T_g (°C) values of neat CA and GCV-Modified CA film using DSC and DMA

	Neat CA T_g (°C)	GCV-Modified CA T_g (°C)
DSC	202.1± 0.11	162.0± 0.16
DMA (E' onset)	196.5± 0.15	153.9±0.08
DMA (E" peak)	205.9± 0.00	157.5±0.93
DMA (tan δ peak)	220.1± 0.00	170.0± 0.64
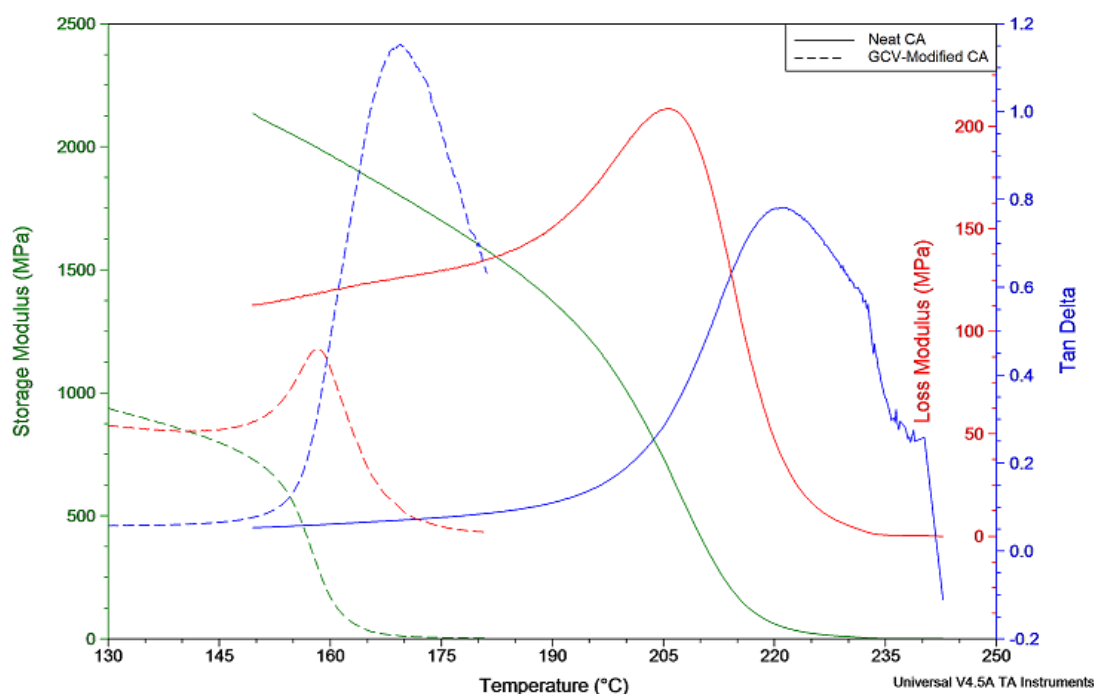
Figure 5.13. Dynamic mechanical spectrum of neat CA and GCV-Modified CA films at 3 Hz.

5.6.5 TGA of GCV-Modified CA Films

A comparison of the TG curves of the neat CA and the GCV-Modified CA film are shown on Figure 5.14. The initial weight loss in CA that occurred below 100°C was mainly due to moisture, and that occurring in GCV-Modified CA around 180°C may be due to the methanol evolving from unreacted methoxy groups. Therefore, the onset of weight loss of CA and GCV-Modified CA occurred around 340°C and 300°C,

131

respectively for both materials. The TG curve also shows that CA lost up to ~90% of its weight when heated to 800°C in an inert atmosphere compared to only ~73% for the GCV-Modified CA, reflecting additional residual mass introduced by the GCV technique. The difference in the residual masses between the two films was 16.6%±0.14, which closely matches the mass change of 16.7%±1.15 observed after the GCV-Modification procedure as shown in Table 5.1. However, both materials have similar degradation temperatures, slightly above 360°C, as reflected by the first derivative of the weight loss curve, which is an indication that they are both fairly thermally stable. The peak of the first derivative indicates the point of greatest rate of change on the weight loss curve [30].
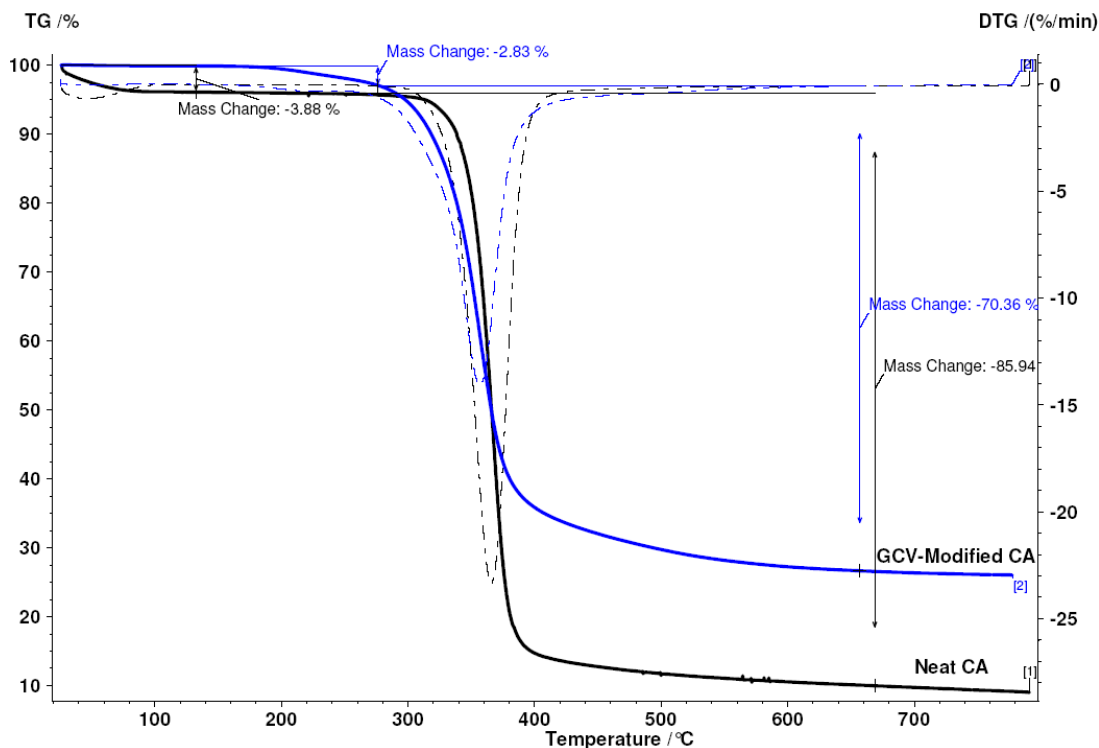
Figure 5.14: TG curve of neat CA and GCV-Modified CA dense film in Argon.

5.6.6 XRD Analysis of GCV-Modified CA Films

The XRD patterns of the neat CA and GCV-Modified CA are shown on Figure 5.15 and

it shows that there is a large difference in crystallinity and chain packing between the two

materials. Neat CA had two diffraction peaks at 2θ angles of 9.4 and 17.3°, which when

applying Bragg's law, corresponded to characteristic d-spacings of 9.44 Å and 5.13 Å,

respectively. The peak at 9.4° was quite sharp and more intense, revealing higher levels

of crystallinity and possibly more perfect crystallites. However, the GCV-Modified

pattern had only one peak at 23.4°, which corresponds to a lower characteristic d-spacing

of 3.80 Å. This peak presumably represented a shift from the peak at 17.3° in neat CA

and it was also broader, indicating that the modified material was more amorphous than

the neat CA consistent with higher permeation rate discussed later, which is explained by

the addition of the VTMS containing the Si-O bulky groups that made close chain

packing more difficult. Of course, it is well known that crystallinity reduces the overall

rate of permeation of semicrystalline polymers [31], due to suppression of both D_A and S_A

factors in the permeability equation.
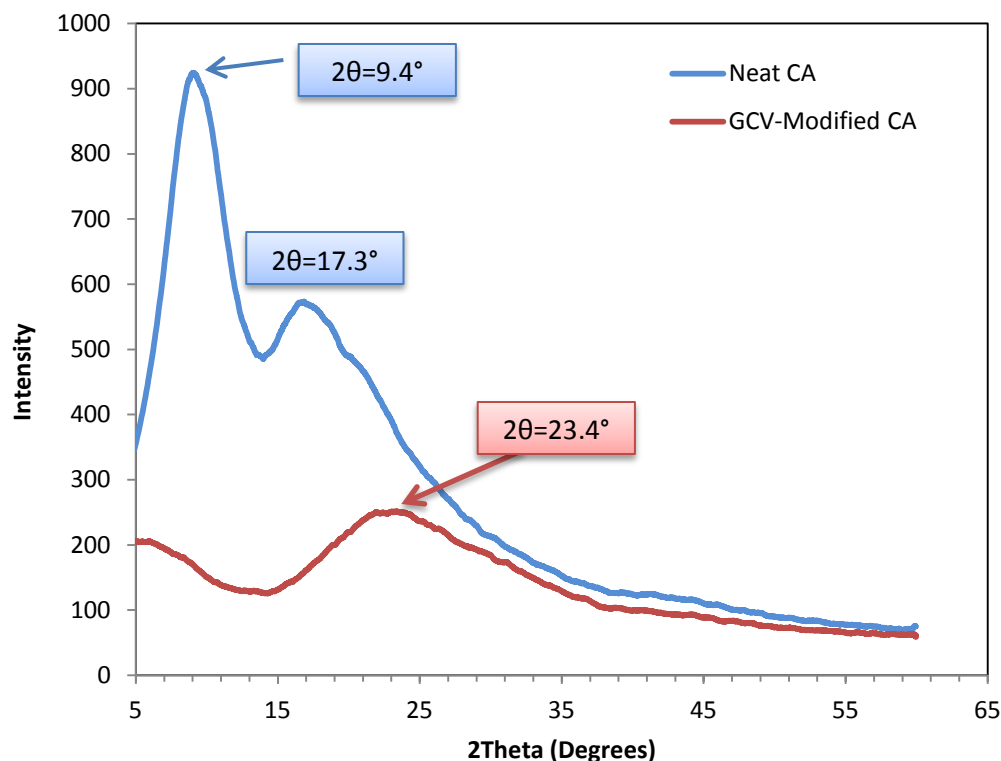
Figure 5.15: X-Ray diffraction pattern of neat CA and GCV-Modified CA dense film.

5.6.7 GC-MS Analysis of GCV-Modified CA Films

As hypothesized in Figure 5.1, methanol was a byproduct of the reaction in step 1 and this method was used to confirm the presence of methanol in the reaction liquid residue, since VTMS was used in excess. Figure 5.16 shows the total ion chromatogram (TIC) of neat VTMS liquid and Figure 5.17 shows the extracted ion chromatogram (XIC) for only the 31 ion in neat VTMS liquid, which is a marker for methanol. Figure 5.18 and Figure 5.19 show the TIC chromatograph of the GCV-Modified CA and the XIC chromatograms of the 31 ion, respectively. The mass spectrum of the GC peaks at 1.60 mins and 1.58 mins (which are when the methanol elutes) in the neat VTMS liquid and GCV-Modified liquid residue are shown in Figure 5.20. This technique is qualitative as it only showed that methanol evolved as the byproduct of the reaction. Even though the VTMS used in

this study was sure sealed, a trace amount of methanol was still detected in the neat liquid as shown in Figure 5.16. However, the magnitude of the peak in the GCV-Modified CA liquid residue was much higher than that of the neat VTMS, indicating that methanol evolved.
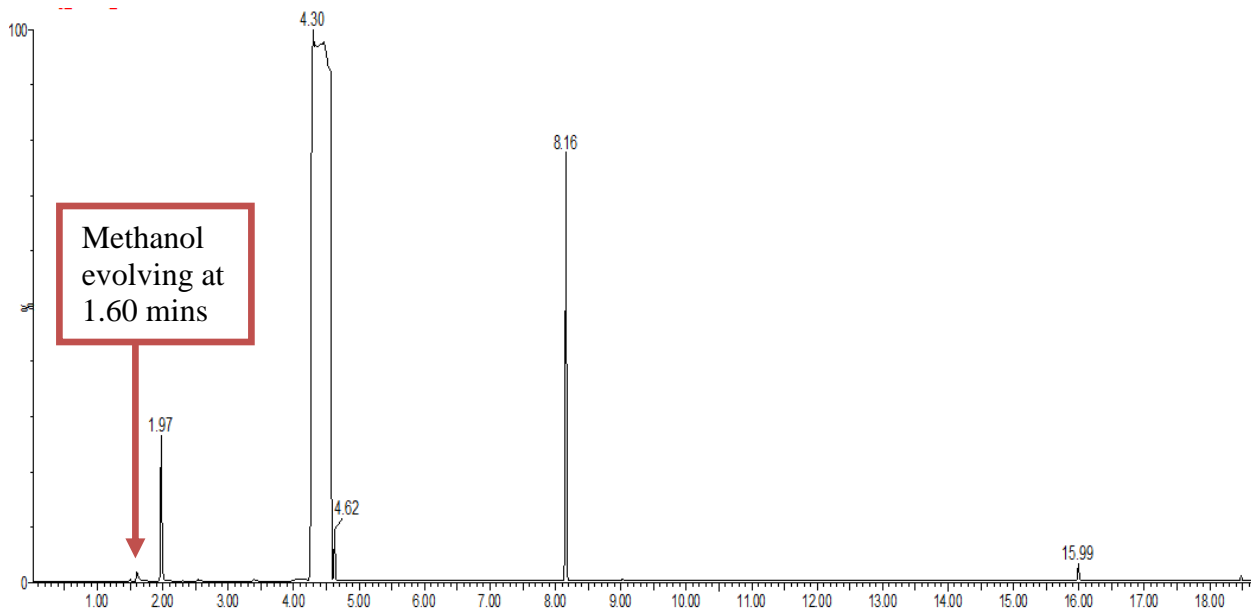
Figure 5.16: Total ion chromatogram (TIC) analysis of neat VTMS liquid.
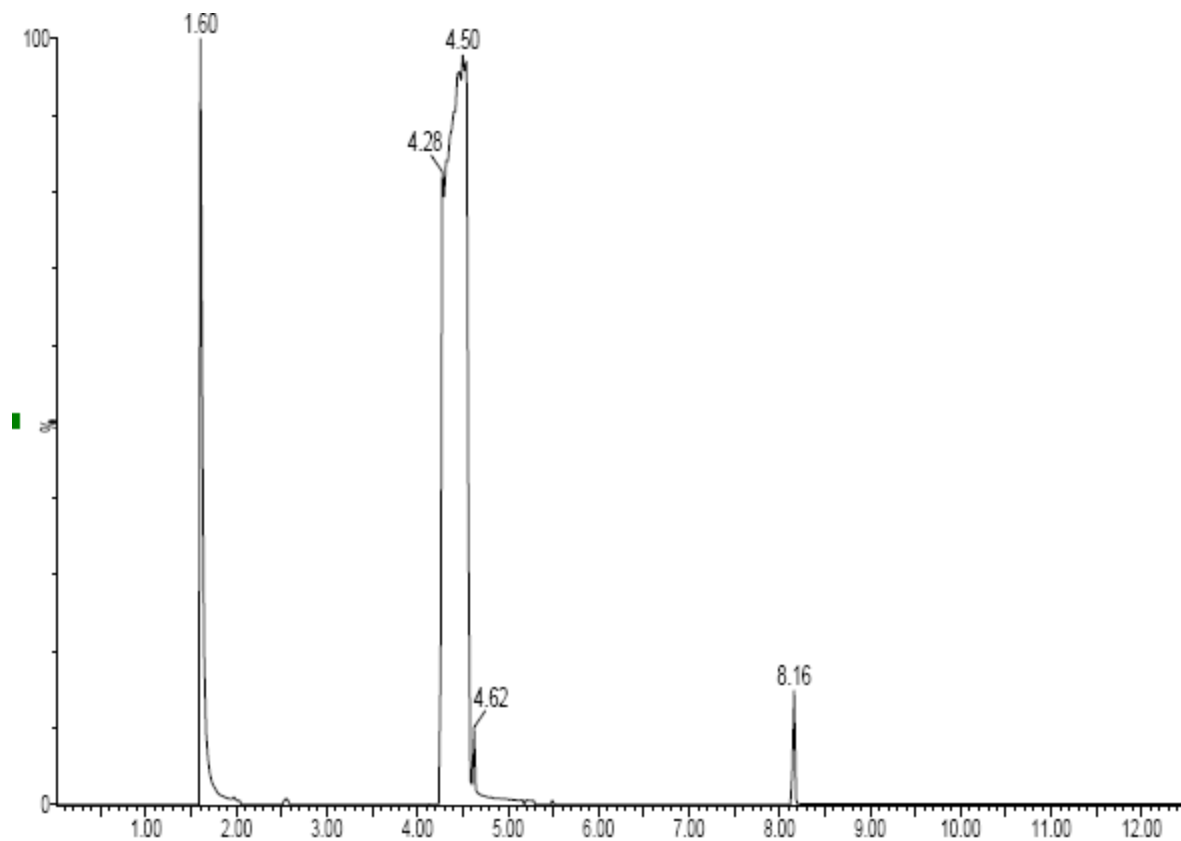
Figure 5.17: Extracted ion chromatogram (XIC) for the 31 ion in neat VTMS liquid.
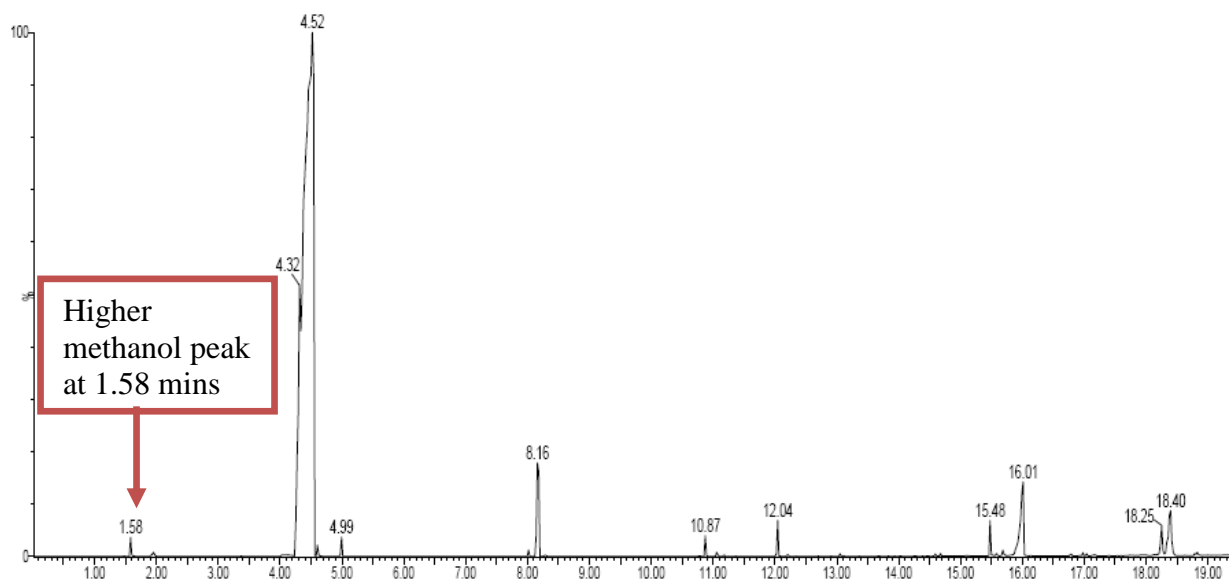
Figure 5.18: Total ion chromatogram (TIC) analysis of GCV-Modified liquid residue.
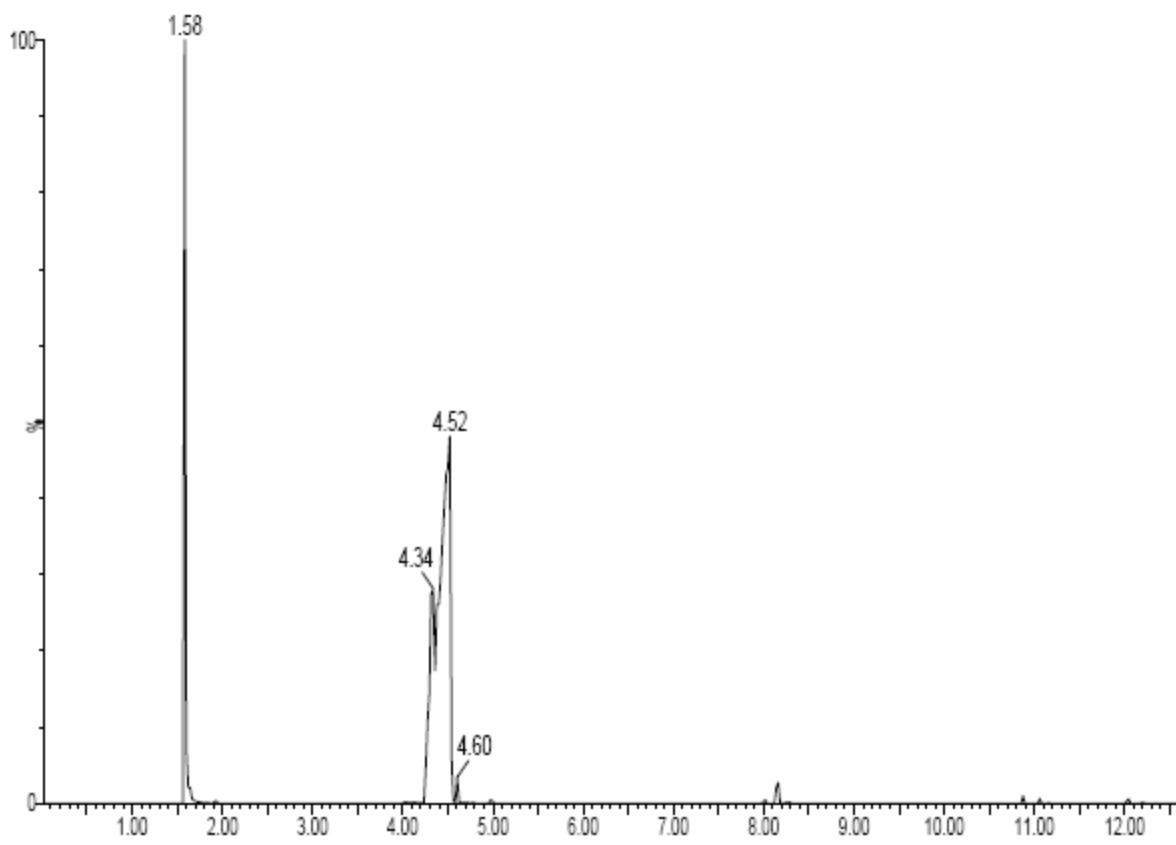
Figure 5.19: Extracted ion chromatogram (XIC) for the 31 ion in GCV-Modified liquid residue.
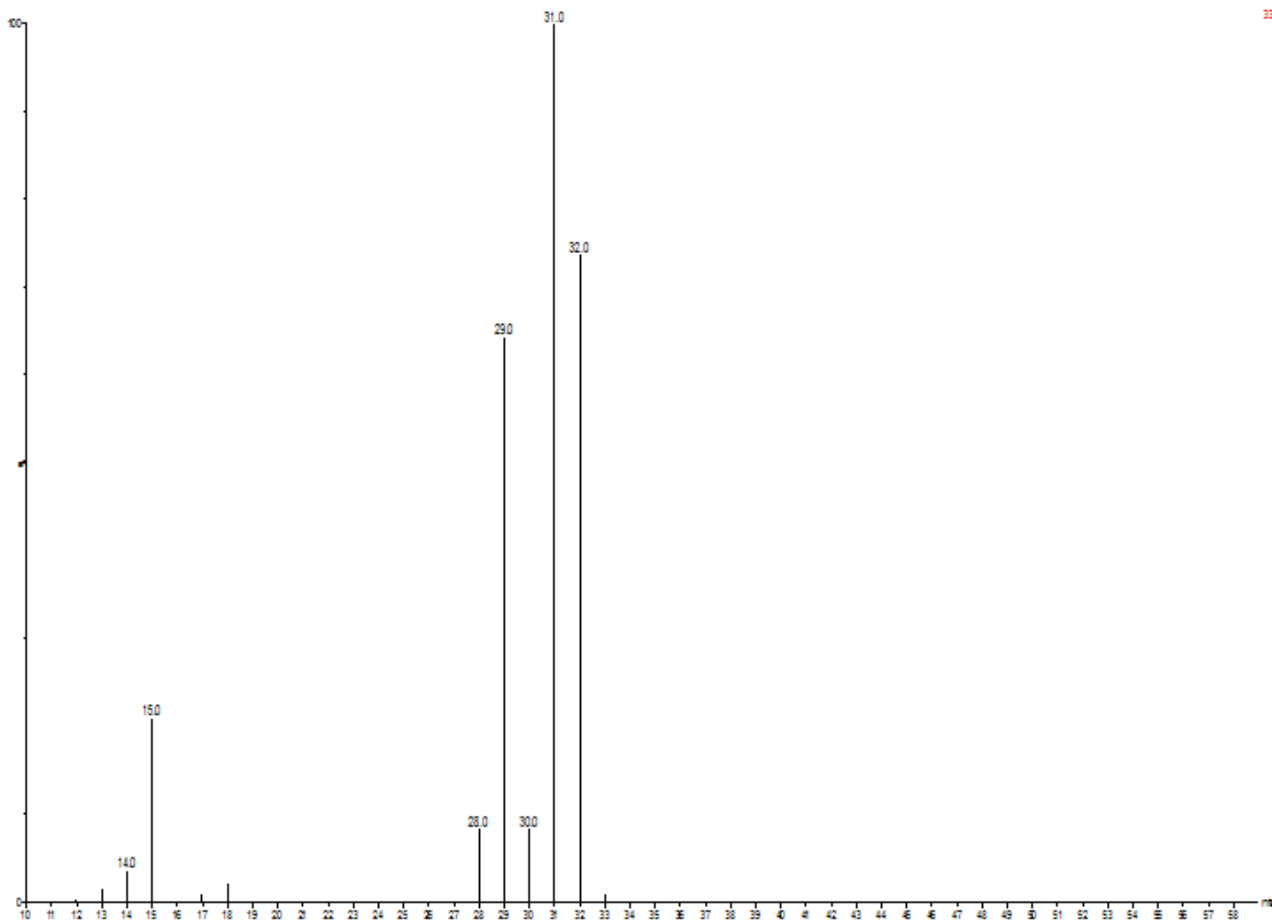
Figure 5.20: Mass spectrum of the GC peaks at 1.60 and 1.58 mins (methanol) in neat VTMS liquid and GCV-Modified liquid residue.

5.6.8 XPS Analysis of GCV-Modified CA Films

Table 5.6 shows the elemental composition of the GCV-Modified CA using XPS. Spot sizes of 100μm were measured at two different areas of the sample, both on the top surface and at the bottom surface to look at the distribution of the silicon atoms across the film surface. As shown in Table 5.6, there was an incorporation of $15.0 \pm 1.1\%$ Si in the GCV-Modified CA material.

Table 5.6: Elemental composition of GCV-Modified CA dense film by XPS (Atomic %)

	GCV-Modified CA				Neat CA
	Area 1 (Top)	Area 2 (Top)	Area 3 (Bottom)	Area 4 (Bottom)	
O1s	29.11	28.15	27.40	29.75	30.31
C1s	54.70	56.66	58.59	55.49	69.69
Si2p	16.19	15.19	14.01	14.76	-

5.7 Effect of Reaction Conditions on Silicon Loading and Gel Content

Many reaction conditions were studied to determine the ones that will yield the best separation performance. Table 5.7 shows the elemental composition of the GCV-Modified films as measured by Columbia Analytical Services. The results show that the silicon loading increases with increasing temperature and time, showing that both of these factors are the main drivers of this reaction. Sample E Si wt% increased by a factor of ~3.6 times compared to sample G when the reaction time was increased by 1 day; however, sample G was found to be unstable under those conditions, indicating that long reaction times at that temperature create other interactions. Theoretically, if 1 VTMS molecule grafts to every –OH group available per CA monomer, the Si wt% will be 2.04%. This value is the optimal loading if the VTMS molecule only graft at the hydroxyl end. Sample E, which is the case mostly discussed in this chapter and the next, has a Si wt% of 1.74%, which is close to the maximum loading of 2.04%, and the material maintained a desirable appearance and flexibility. By taking the ratio of these wt%, it was estimated that roughly 85% of the –OH groups were grafted with VTMS, which matches the value obtained with IR ratio analysis of the methoxy groups that have reacted. Sample F was also very close to the maximum Si loading and the film also retained its appearance; however that protocol was not pursued further because of the excessive

reaction time required to achieve that loading. This study showed that optimizing reaction time and temperature will be critical especially when scaling up the method to asymmetric hollow fibers since it is the most important step to test after this proof of concept study. Therefore, further optimization will be required directly on hollow fibers, but it is not anticipated that long reaction times and temperatures will be necessary as their actual separation skin is much smaller.

Table 5.7: Elemental composition of GCV-Modified CA films at different reaction conditions as measured by Columbia Analytical Services

Sample	Reaction Conditions	Carbon wt%	Hydrogen wt%	Oxygen wt%	Silicon wt%
Neat CA	-	48.65	5.31	46.04	-
Sample A	1 day at 150°C	48.75	5.55	45.12	0.58
Sample B	3 days at 150°C	48.61	5.41	45.36	0.62
Sample C	4 days at 150°C	48.12	5.53	45.35	1.00
Sample D	12 hrs at 200°C	48.09	5.49	45.20	1.12
Sample E	1 day at 200°C	48.84	5.68	43.74	1.74
Sample F	7 days at 150°C	47.66	5.75	44.16	2.05
Sample G	2 days at 200°C	45.43	5.96	42.30	6.31

The effect of silicon content on gel content was also studied to understand the correlation between the extent of crosslinking and the silicon loading. Table 5.8 shows that at lower silicon loading, the films dissolved when heated in NMP solvent at 100°C, indicating that the bonds formed during the reaction were not strong enough to overcome such conditions, and the film did not crosslink. However, at higher silicon loading, there was a positive correlation between the silicon loading and the gel content, and the values obtained indicate that material crosslinked. The difference between the highest and the

lowest gel content values was only about 5%, indicating that the gel content was not mainly a function of silicon loading.

Table 5.8: Effect of silicon loading (%) on gel content (%) in GCV-Modified CA films

	Silicon Loading (%)	Dissolved in NMP?	Gel Content (%)
Sample A	0.58	Yes	-
Sample B	0.62	Yes	-
Sample C	1.00	No	94.5
Sample D	1.12	No	95.8
Sample E	1.74	No	96.6
Sample F	2.05	No	97.1
Sample G	6.31	No	99.8

This chapter focused on the reaction mechanism and characterization of GCV-Modified CA films with varying reaction conditions, silane agents, and catalysts. The next chapter will focus on the separation performance of these GCV-Modified CA films in sour gas feeds.

5.8 References

[1] C.S.K. Achoundong, N. Bhuwania, S.K. Burgess, O. Karvan, J.R. Johnson, W.J. Koros, Silane Modification of Cellulose Acetate Dense Films as Materials for Acid Gas Removal, Macromolecules, 46 (2013) 5584-5594.

[2] J. Barzin, H. Azizi, J. Morshedian, Preparation of Silane-Grafted and Moisture Cross-Linked Low Density Polyethylene: Part I: Factors Affecting Performance of Grafting and Cross-Linking, Polymer-Plastics Technology and Engineering, 45 (2006) 979-983.

[3] H.C. Kuan, J.F. Kuan, C.C.M. Ma, J.M. Huang, Thermal and mechanical properties of silane-grafted water crosslinked polyethylene, J Appl Polym Sci, 96 (2005) 2383-2391.

[4] I. Kelnar, M. Schatz, Silane Cross-Linking of Pvc .2. Influence of Silane Type and Conditions on Cross-Linking by Water, J Appl Polym Sci, 48 (1993) 669-676.

[5] A.K. Sen, B. Mukherjee, A.S. Bhattacharyya, P.P. De, A.K. Bhowmick, Degradation of Silane-Cross-Linked and Peroxide-Cross-Linked Polyethylene and Ethylene Propylene Rubber, Polym Degrad Stabil, 36 (1992) 281-289.

[6] J. Morshedian, P.M. Hoseinpour, Polyethylene Cross-linking by Two-step Silane Method: A Review, Iran Polym J, 18 (2009) 103-128.

[7] H. Azizi, J. Morshedian, M. Barikani, Silane Grafting and Moisture Crosslinking of Polyethylene: The Effect of Molecular Structure, J Vinyl Addit Techn, 15 (2009) 184-190.

[8] T. Hjertberg, M. Palmlof, B.A. Sultan, Chemical-Reactions in Cross-Linking of Copolymers of Ethylene and Vinyltrimethoxy Silane, J Appl Polym Sci, 42 (1991) 1185-1192.

[9] J. Barzin, H. Azizi, J. Morshedian, Preparation of Silane-Grafted and Moisture Crosslinked Low Density Polyethylene. Part II: Electrical, Thermal and Mechanical Properties, Polymer-Plastics Technology and Engineering, 46 (2007) 305-310.

[10] H. Azizi, J. Morshedian, M. Barikani, Silane grafting and moisture crosslinking of polyethylene: The effect of molecular structure, Journal of Vinyl and Additive Technology, 15 (2009) 184-190.

[11] H. Lobo, J.V. Bonilla, Handbook of plastics analysis, Marcel Dekker, New York, 2003.

[12] D.N.S. Hon, N. Shiraishi, Wood and cellulosic chemistry, 2nd ed., Marcel Dekker, New York, 2001.

[13] Y.-S. Li, P.B. Wright, R. Puritt, T. Tran, Vibrational spectroscopic studies of vinyltriethoxysilane sol–gel and its coating, Spectrochimica Acta Part A: Molecular and Biomolecular Spectroscopy, 60 (2004) 2759-2766.

[14] G.S. Ahmed, M. Gilbert, S. Mainprize, M. Rogerson, FTIR analysis of silane grafted high density polyethylene, Plast Rubber Compos, 38 (2009) 13-20.

[15] S. Doyle, R.A. Pethrick, R.K. Harris, J.M. Lane, K.J. Packer, F. Heatley, C-13 Nuclear-Magnetic-Resonance Studies of Cellulose-Acetate in the Solution and Solid States, Polymer, 27 (1986) 19-24.

[16] M.C. Douskey, M.S. Gebhard, A.V. McCormick, B.C. Lange, D.W. Whitman, M.R. Schure, K. Beshah, Spectroscopic studies of a novel cyclic oligomer with pendant alkoxysilane groups, Prog Org Coat, 45 (2002) 145-157.

[17] R.J. Hook, A Si-29 NMR study of the sol-gel polymerisation rates of substituted ethoxysilanes, J Non-Cryst Solids, 195 (1996) 1-15.

[18] F. Devreux, J.P. Boilot, F. Chaput, A. Lecomte, Sol-Gel Condensation of Rapidly Hydrolyzed Silicon Alkoxides - a Joint Si-29 Nmr and Small-Angle X-Ray-Scattering Study, Phys Rev A, 41 (1990) 6901-6909.

[19] F. Uhlig, H.C. Marsmann, 29Si NMR Some Pratical Aspects, in: Gelest Catalog, Gelest, Inc, 2009, pp. 208-222.

[20] Y. Maeda, D.R. Paul, Effect of Antiplasticization on Selectivity and Productivity of Gas Separation Membranes, J Membrane Sci, 30 (1987) 1-9.

[21] K. Kamide, K. Okajima, M. Saito, Nuclear Magnetic-Resonance Study of Thermodynamic Interaction between Cellulose-Acetate and Solvent, Polym J, 13 (1981) 115-125.

[22] J. Brandrup, E.H. Immergut, Polymer handbook, Interscience Publishers, 1966.

[23] L.E. Nielsen, Cross-Linking-Effect on Physical Properties of Polymers, J Macromol Sci-Rev M, C 3 (1969) 69-&.

[24] J.D. Wind, Improving Polyimide Membrane Resistance to Carbon Dioxide Plasticization in Natural Gas Separations, in: Chemical Engineering, The University of Texas at Austin, Austin, 2002, pp. 232.

[25] D.R. Paul, I.U.P. ĪAmpol′skiĭ, Polymeric Gas Separation Membranes, Taylor & Francis, 1994.

[26] A.C. Puleo, D.R. Paul, S.S. Kelley, The effect of degree of acetylation on gas sorption and transport behavior in cellulose acetate, J Membrane Sci, 47 (1989) 301-332.

[27] L. Mandelkern, P.J. Flory, Melting and Glassy State Transitions in Cellulose Esters and Their Mixtures with Diluents, J Am Chem Soc, 73 (1951) 3206-3212.

[28] E. Turi, Thermal Characterization of Polymeric Materials, Elsevier Science, 1981.

[29] M.P. Sepe, R.T. Limited, Thermal Analysis of Polymers, Rapra Technology Limited, 1997.

[30] W. Brostow, Performance Of Plastics, Hanser Publishers ; Cincinnati, 2000.

[31] A.S. Michaels, R.B. Parker, Sorption and flow of gases in polyethylene, Journal of Polymer Science, 41 (1959) 53-71.

CHAPTER 6: TRANSPORT OF ACID GASES IN GCV-MODIFIED CA AND CROSSLINKED PDMC DENSE FILM MEMBRANES

6.1 Abstract

This Chapter focuses on evaluating the performance of GCV-Modified CA and crosslinked PDMC as potentially improved high performance materials for the separation of H_2S and CO_2 from aggressive sour gas feeds. A detailed transport analysis of the factors that impact the performance of these materials is also presented. It was found that GCV-Modified CA maintained similar H_2S/CH_4 (~39) and CO_2/CH_4 (~33) selectivities compared to the unmodified material; however the pure CO_2 and H_2S permeabilities were 139 and 165 Barrer, respectively, which are *more than an order of magnitude* higher than the neat polymer. PDMC was crosslinked at temperatures of 220°C and 295°C and it was found that increasing the degree of crosslinking resulted in higher permeabilities, improved CO_2/CH_4 selectivity, and better CO_2 and H_2S plasticization resistance. Therefore, the higher crosslinking temperature of 295°C was selected for further study. Crosslinked PDMC was found to have CO_2 and H_2S permeability of 86 and 22 Barrer, respectively with an improved CO_2/CH_4 selectivity of ~38 and a lower H_2S/CH_4 selectivity of ~10 compared to the uncrosslinked material. The increase in permeability observed in PDMC was due to the increase in free volume created by the propanediol crosslinker, which acts as a "spacer" between polymer chains. GCV-Modified CA was found to have a slightly higher CO_2 plasticization resistance than neat CA with no improvement for H_2S, and crosslinked PDMC was found to have a higher resistance to swelling of up to ~450 psia for CO_2 and up to ~90 psia for H_2S. The additional resistance to CO_2 swelling by GCV-Modified CA was found to be the result of its decreased

sorption capacity. The higher resistance to swelling observed in PDMC was due to the elimination of hydrogen bonding sites that promoted higher CO_2 and H_2S sorption and by the introduction of crosslinks that restrained swelling. Temperature dependence experiments revealed that the "stickiness" of H_2S observed in uncrosslinked PDMC was also apparent in crosslinked PDMC, but to a lower extent. Therefore, H_2S tendency to stick to sorption sites was found to be the result of hydrogen-bonding with hydroxyl groups on the DABA moiety and with carbonyl groups on 6FDA. Detailed analysis into the transport of GCV-Modified CA revealed that transport in this material is governed by the increase in segmental mobility of the polymer brought about its higher free volume created by the incorporation of the bulky Si-O groups into the polymer backbone and the elimination of crystalline regions that prevent sorption and diffusion in the crystalline fraction. Its higher H_2S/CH_4 selectivity with a maintained CO_2/CH_4 selectivity may be the result of the higher affinity of H_2S for the siloxane bridges, but also the size-discrimination ability of those siloxane-filled zones. Binary and ternary gas feeds were tested both with vacuum downstream and with 1 atm pressure downstream and the results showed that even under aggressive feed conditions, GCV-Modified CA showed the better performance vs. PDMC, and it remained were fairly stable, making it an immediate candidate for aggressive sour gas separations if it can be transformed into an asymmetric fiber. These findings could open new avenues for GCV-Modified CA as a lower cost, fairly high performance alternative even in non membrane applications.

6.2 Pure Gas Permeation

Table 6.1 shows the pure gas permeabilities of H_2S, CO_2, and CH_4 and ideal CO_2/CH_4 and H_2S/CH_4 selectivities for GCV-Modified CA [1] and crosslinked PDMC at 65 psia and 35°C. As mentioned in Chapter 3, PDMC was crosslinked at 220°C and 295°C to identify the condition with the best separation performance and plasticization resistance.

Table 6.1: Single gas permeability and selectivity of GCV-Modified CA and crosslinked PDMC at 65 psia and 35°C

Polymer	Permeability (Barrer)			Ideal Selectivity	
	CH_4	CO_2	H_2S	CO_2/CH_4	H_2S/CH_4
GCV-Modified CA	4.23±0.94	139.1±3.41	165.2±3.98	32.88±3.12	39.05±3.05
Crosslinked PDMC	1.52±0.14[a]	56.83±2.22[a]	18.11±2.09[a]	37.39±1.42[a]	11.91±1.08[a]
	2.30±0.13[b]	87.51±2.35[b]	22.31±2.05[b]	38.05±1.66[b]	9.70±1.27[b]

a. Crosslinking temperature is 220°C
b. Crosslinking temperature is 295°C

As it can be seen from Table 6.1, the permeabilities of H_2S, CO_2, and CH_4 in PDMC increase with an increasing degree of crosslinking. Similar results for CO_2 and CH_4 were observed by previous researchers [2-7].This higher permeability with a higher degree of crosslinking is believed to be the result of the increase in free volume created by propanediol, which acts as a "spacer" between polymer chains. Even though crosslinking generally decreases permeability, this suggests that the increase in free volume created by crosslinks overrides the reduced chain mobility. Therefore, crosslinking at higher temperature has a positive effect on both permeability and CO_2/CH_4 selectivity. The permeability of CO_2 and CH_4 increased by a factor of ~3 while H_2S permeability only increased by a factor of ~2. One of the reasons for this result may due to the "stickiness" of H_2S to sorption sites observed in the uncrosslinked material. This effect will be also

studied in detail later in this chapter. Nevertheless, these changes in permeabilities translated into a CO_2/CH_4 selectivity increase of ~4% with a H_2S/CH_4 selectivity decrease of roughly 45%. Even though the H_2S/CH_4 selectivity decreased, it is anticipated that this decrease may be compensated by the high productivity and polymer mechanical stability under aggressive feed conditions. In addition to the increase in free volume created by the introduction of propanediol between chains, the permeability increase may be explained by the fact that there is a significant decrease in hydrogen bonding due to the elimination of hydroxyl groups on the DABA moiety by their reaction and subsequent crosslinking with propanediol. While this overall increase in H_2S, CO_2, and CH_4 permeability and CO_2/CH_4 selectivity is a desirable outcome, the increase in the separation performance of GCV-Modified CA is quite remarkable as well. Table 6.1 shows a permeability increase by a factor of ~30 for CO_2 and CH_4 and by a factor of ~34 for H_2S for GCV-Modified CA compared to neat CA. Chapter 5 revealed that the GCV-Modified CA was less stiff with higher chain mobility (lower T_g). Therefore, the increase in permeability is hypothesized to be due to an increase in polymer free volume created by the introduction of the bulky Si-O bulky group into the main chain. This increase in H_2S, CO_2, and CH_4 permeabilities is accompanied by a less than 1% decrease in CO_2/CH_4 selectivity and an increase of 12.5% in H_2S/CH_4 selectivity. Silicon chemistry is quite versatile and complex. Silicon-containing polymers tend to have a relatively high intrinsic gas permeability compared to that of other types of polymers [8]. An interpretation of this permeability behavior requires knowledge of the sorption and diffusivity of these gases in this modified CA polymer and this will be addressed in the next sections.

6.3 Plasticization Resistance

Many researchers have shown that covalent crosslinking uses chemical bonds to link chains, increasing their stability in the presence of highly condensable gases such as CO_2 [2, 3, 5-7, 9-12]. The pure gas permeation isotherms of CH_4, CO_2, and H_2S in both polymers are shown in Figure 6.1, 6.2, and 6.3, respectively. As expected, CH_4 does not swell either polymer, even at high pressures. There is higher CO_2 and H_2S plasticization resistance based on differences between the uncrosslinked PDMC and the crosslinked PDMC material. In addition, crosslinked PDMC at 295°C shows a slight increase in H_2S plasticization resistance (~90 psia) compared to crosslinked PDMC at 220°C (~75 psia). Similarly, CO_2 does not plasticize crosslinked PDMC at 295°C until ~450 psia compared to ~350 psia for crosslinked PDMC at 220°C. These results make sense, because the higher susceptibility to plasticization is generally a result of the higher sorption of a penetrant in a polymer. In this case, the elimination of disruptable hydrogen bonding may make the crosslinked polymer less prone to plasticization. Carbon dioxide shows a higher resistance to swelling due to its lower sorption, caused by its lower critical temperature compared to H_2S. On the other hand, there is a slight improvement in CO_2 plasticization resistance for GCV-Modified CA compared to neat CA and no improvement noted for H_2S. One of the reasons for this behavior might be that there might be a constant or an increase in sorption of CO_2 and/or H_2S in the material. Sorption studies conducted on this material as shown in the next section show that H_2S has a higher sorption capacity compared to the unmodified CA with a slight lower CO_2 sorption capacity.
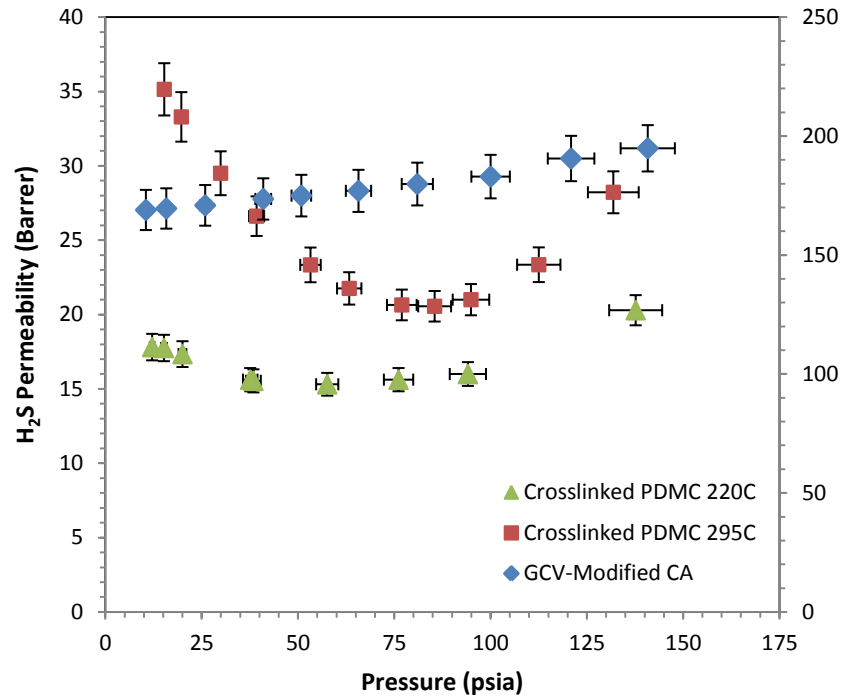
Figure 6.1: Pure H_2S permeation isotherm at 35°C for GCV-Modified CA (right axis) and crosslinked PDMC (left axis).
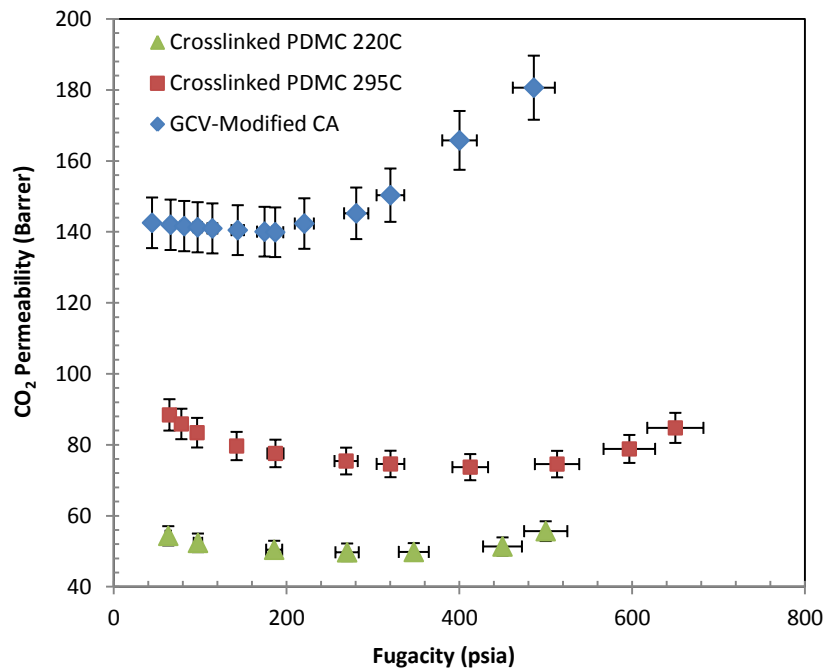
Figure 6.2: Pure CO_2 permeation isotherm at 35°C for GCV-Modified CA and crosslinked PDMC.
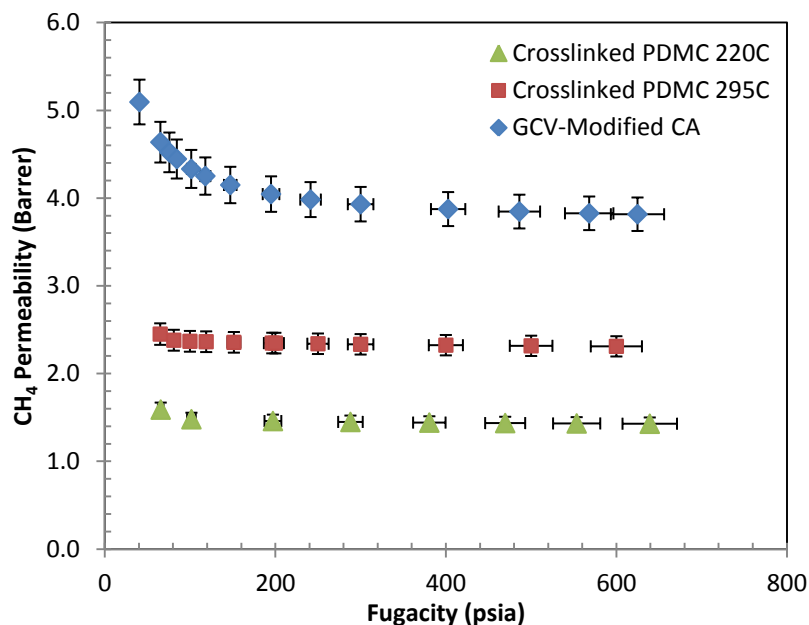
Figure 6.3: Pure CH_4 permeation isotherm at 35°C for GCV-Modified CA and crosslinked PDMC.

6.4 Pure Gas Sorption

Sorption isotherms of CH_4, CO_2, and H_2S were measured at 35°C using the procedure described in Chapter 3. The results are shown in Figure 6.4, Figure 6.5, and Figure 6.6. Table 4.2 lists the sorption parameters obtained from those isotherms using the dual-mode sorption model.

Table 6.2: Pure CH_4, CO_2, and CH_4 sorption parameters of GCV-Modified CA and crosslinked PDMC at 35°C

Polymer	CH_4			CO_2			H_2S		
	k_d (x10^{-2})	b (x10^{-2})	C_H'	k_d (10^{-1})	b (x10^{-2})	C_H'	k_d(x10^{-1})	b (x10^{-2})	C_H'
GCV-CA	1.50	10.82	0.47	1.59	4.40	5.65	6.63	2.09	8.84
Crosslinked PDMC 220°C	5.22	3.34	20.34	1.98	7.99	26.83	5.50	2.88	35.68
Crosslinked PDMC 295°C	7.85	3.23	24.63	1.51	4.67	41.48	5.30	2.65	37.80

k_d is in cm^3(STP)/cm^{3}psia, b is in psia^{-1}, and C_H' is in cm^3(STP)/cm^3 polymer
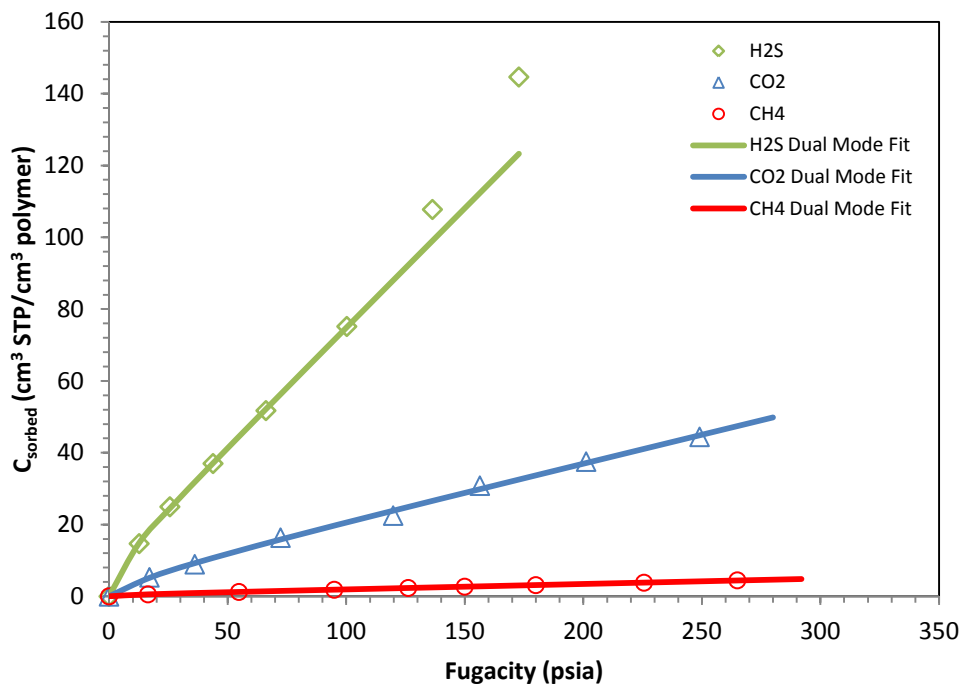
Figure 6.4: Pure CH_4, CO_2, and H_2S sorption isotherms at 35°C in GCV-Modified CA.
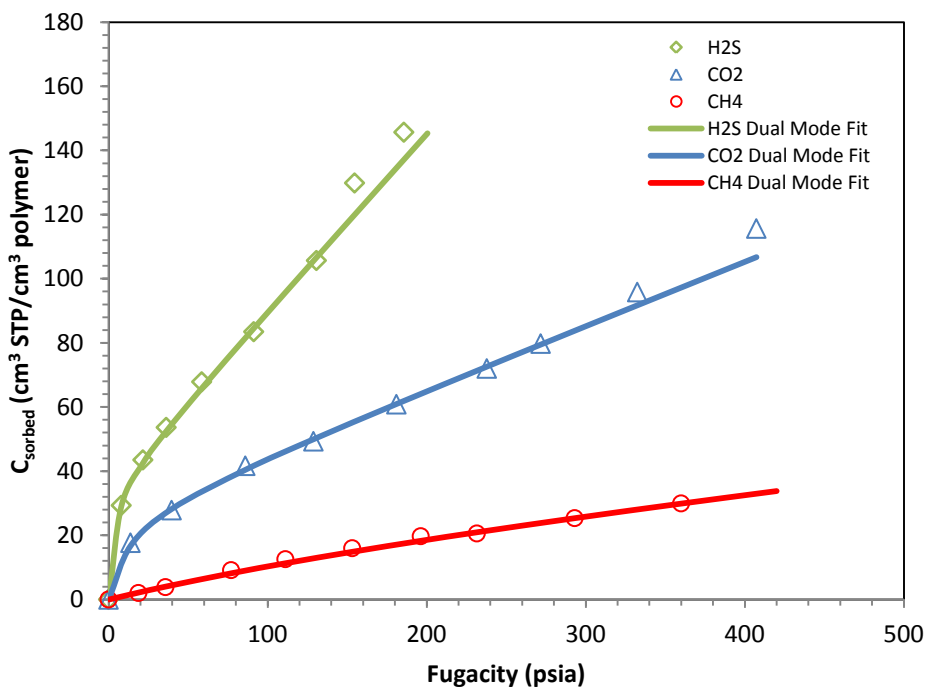
Figure 6.5: Pure CH_4, CO_2, and H_2S sorption isotherms at 35°C in crosslinked PDMC at 220°C.
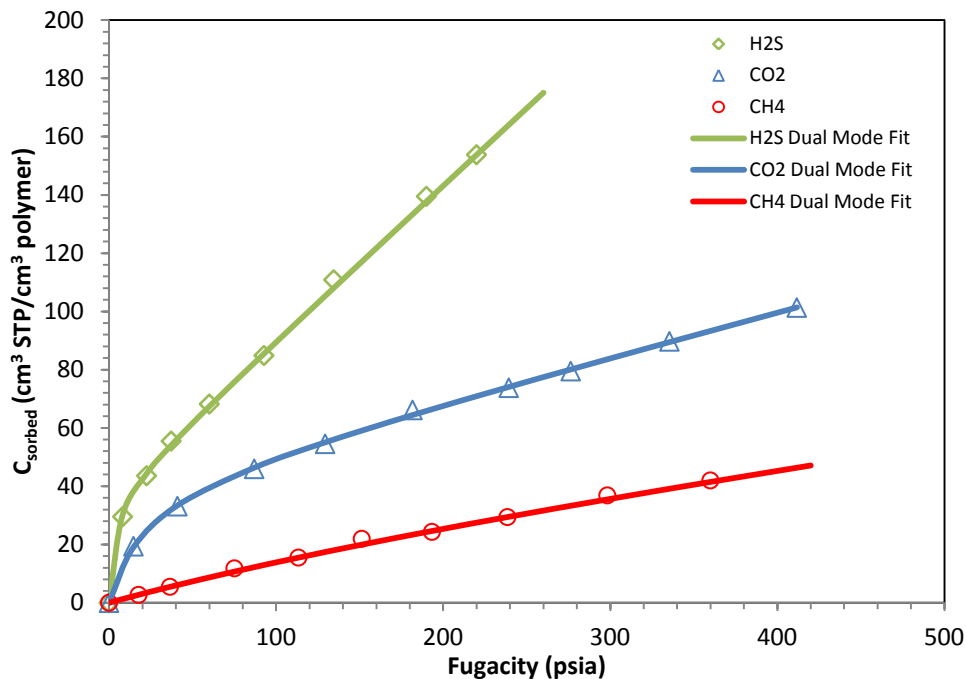
Figure 6.6: Pure CH_4, CO_2, and H_2S sorption isotherms at 35°C in crosslinked PDMC at 295°C.

The concave nature of the sorption isotherms is consistent with the so-called dual-mode sorption, with contributions from both Langmuir or "hole-filling" and Henry's law (dissolution) sorption modes. This is apparent at low to moderate pressures for all samples. At higher pressures, H_2S swelling in GCV-modified CA is apparent and marked by a deviation from the dual-mode fit, which is not observed for the crosslinked PDMC material. Table 6.2 shows that the Langmuir capacity constant C_H' increases as the degree of crosslinking increases; this suggests that propanediol molecules not only increase polymer free volume, but also its excess free volume. As discussed in Chapter 2, the "hole-filling" mode arises from sorption into the fixed amount of excess free volume in glassy polymers. This excess free volume results from chain packing defects in the polymer matrix, which means the introduction of "spacer" creates additional packing defects, which results in an increase in sorption into this mode. The Henry's law constant

(k_D) was also found to increase with increasing degree of crosslinking. Therefore, overall sorption in the crosslinked polymer is higher than its uncrosslinked counterpart. However, in GCV-Modified CA, the Henry's law dissolution constant increases (k_D), while the Langmuir capacity constant (C_H') decreases compared to neat CA. This may suggest that the primary mode of sorption in GCV-Modified CA occurs through the dissolved mode, and that this modified polymer has a lower excess free volume compared to neat CA. These single gas permeation and sorption experiments showed that crosslinked PDMC at 295°C had a higher permeability with an improved CO_2/CH_4 and small H_2S/CH_4 selectivity loss. The small H_2S/CH_4 selectivity loss is overridden by the higher CO_2 and H_2S plasticization resistance observed, since swelling is one of the most important setbacks in mixed gas feeds. Therefore, any reference to crosslinked PDMC will refer to crosslinked PDMC at 295°C beyond this point. It should be noted that in asymmetric fiber, it may not be practical to use 295°C; however, there will also be challenges in crosslinking CA in fiber form at 150-200°C. Therefore, what is being done in this study is considering both materials under their most attractive dense film conditions with the knowledge that asymmetric work remains to be done. As discussed in Chapter 2, the permeability coefficient is defined as the product of the diffusion coefficient and the sorption coefficient; therefore, the selectivity can be decoupled into mobility and sorption selectivity. Using the permeation and sorption results, the kinetic (diffusion) and thermodynamic (sorption) individual contributions were calculated and are shown in Table 6.3. Details on the calculation of the parameters in Table 6.3 can be found in Appendix F.

Table 6.3: Diffusion coefficient (D), sorption coefficient (S), diffusion selectivity (α_D), and sorption selectivity (α_S) of GCV-Modified CA and crosslinked PDMC at 35°C and 65 psia

Polymer	D (10^{-9} cm^2/sec)			S (10^{-2} cm^{3}STP/cm^{3}psia)			α_D		α_S	
	CH$_4$	CO$_2$	H$_2$S	CH$_4$	CO$_2$	H$_2$S	CO$_2$/CH$_4$	H$_2$S/CH$_4$	CO$_2$/CH$_4$	H$_2$S/CH$_4$
GCV-CA[a]	92.3	316.1	97.9	2.37	22.75	87.25	3.42	1.06	9.60	36.81
GCV-CA[b]	102.2	321.7	108.2	2.14	22.36	78.98	3.15	1.06	10.45	36.91
Crosslinked PDMC[a]	8.76	73.32	9.61	13.58	61.71	120.04	8.37	1.10	4.54	8.84
Crosslinked PDMC[b]	8.25	71.75	10.68	14.42	63.06	107.98	8.70	1.29	4.37	7.49

a. D was measured by the time-lag method and S was calculated from P=DS
b. S was measured by pressure-decay sorption and D was calculated from P=DS

Table 6.3 shows that for both CO$_2$/CH$_4$ and H$_2$S/CH$_4$ pairs, GCV-Modified CA is more sorption selective whereas crosslinked PDMC is more mobility selective for CO$_2$/CH$_4$ and also more sorption selective for the H$_2$S/CH$_4$ pair, despite the higher diffusion coefficient observed in the former polymer. The tendency toward plasticization of a polymer has been shown to increase with increasing sorption of the penetrant in the polymer [8]. The higher sorption of H$_2$S compared to other gases leads to the lower plasticization resistance observed in the GCV-Modified CA polymer, and the slight improvement in the CO$_2$ plasticization resistance may be the result of the CO$_2$ sorption decrease. It can also be concluded from Table 6.3 that the significant difference in the diffusion coefficient between the two materials, leads to the higher permeability observed in GCV-Modified CA. It should also be noted that there is a reasonable agreement between values obtained from time-lag or pressure-decay experiments and calculated values using the general permeability formula.

To better understand the changes in properties between the materials from their neat form to their modified or crosslinked form, Table 6.4 was constructed to show the changes in diffusion coefficient, sorption coefficient, diffusion selectivity, and sorption selectivity

between neat CA and GCV-modified CA, and between uncrosslinked and crosslinked PDMC. The changes in diffusivity selectivity of Table 6.4 were calculated based on the values obtained by the time-lag method and the changes in sorption selectivity were calculated based on the values obtained from the pressure-decay sorption experiments. Therefore, the changes in selectivity observed as shown in Table 6.1 and Table 4.1 might not exactly match the changes in properties observed. Table 6.4 and Table 6.5 were only built to give an overall picture of the changes in the materials performance.

Table 6.4: Changes in diffusion coefficient (ΔD), sorption coefficient (ΔS), diffusion selectivity ($\Delta\alpha_D$), and sorption selectivity ($\Delta\alpha_S$) between neat CA and GCV-Modified CA and between uncrosslinked and crosslinked PDMC at 65 psia and 35°C

Polymer	ΔD			ΔS			$\Delta\alpha_D$		$\Delta\alpha_S$	
	CH_4	CO_2	H_2S	CH_4	CO_2	H_2S	CO_2/CH_4	H_2S/CH_4	CO_2/CH_4	H_2S/CH_4
GCV-CA / Neat CA	▲ 47X	▲ 40X	▲ 31.5X	▼ 0.67X	▼ 0.88X	▲ 1.09X	▼ 0.84X	▼ 0.67X	▲ 1.31X	▲ 1.62X
Crosslinked PDMC / Uncrosslinked PDMC	▲ 1.9X	▲ 1.8X	▲ 1.9X	▲ 1.75X	▲ 1.79X	▲ 1.01X	▼ 0.96X	▲ 1.0X	▲ 1.02X	▼ 0.58X

Table 6.5: Changes in permeability coefficient (ΔP) and permselectivity ($\Delta\alpha_P$) between neat CA and GCV-Modified CA and between uncrosslinked and crosslinked PDMC at 65 psia and 35°C

Polymer	ΔP			$\Delta\alpha_P$	
	CH_4	CO_2	H_2S	CO_2/CH_4	H_2S/CH_4
GCV-CA / Neat CA	▲ 30.2X	▲ 29.9X	▲ 34X	▼ 0.99X	▲ 1.13X
Crosslinked PDMC / Uncrosslinked PDMC	▲ 2.77X	▲ 2.88X	▲ 1.91X	▲ 1.04X	▼ 0.69X

Table 6.4 shows that there is an overall increase in diffusion coefficient in both GCV-Modified CA and crosslinked PDMC compared to their unmodified counterparts, but the change is more drastic in GCV-Modified CA. This result confirms that there was an increase in free volume in the two materials, and the change was much higher in GCV-

CA. This increase in mobility is higher for CH_4 in GCV-Modified CA, leading to a loss in diffusivity selectivity for CO_2 and H_2S over methane. However, the sorption capacity of both CO_2 and CH_4 were 0.88X and 0.67X lower, respectively, while that of H_2S was 1.09X higher in the GCV-Modified CA polymer. This result suggests that the newly modified polymer had a much higher affinity for H_2S compared to the other gases. This decrease in CO_2/CH_4 diffusion selectivity with an increase in CO_2/CH_4 sorption selectivity only caused a less than 1% loss in overall CO_2/CH_4 selectivity in the GCV-Modified material. However, the much higher H_2S/CH_4 sorption selectivity increase compared to its diffusivity selectivity decrease, led to a 1.13X increase in overall H_2S/CH_4 selectivity as shown in Table 6.5. These results suggest that the introduction of the bulky Si-O group with vinyl substituent into the polymer backbone not only increased polymer mobility, it also increased its H_2S sorption, while slightly reducing both CO_2 and CH_4 solubilities, with the latter being affected the most.

6.5 Explaining the performance of GCV-Modified CA

In the previous section, key transport parameters governing the transport of H_2S, CO_2, and CH_4 in the novel GCV-Modified CA polymer were presented. In this section, the reasons behind the observed remarkable performance will be dissected in more depth. To do this, it is important to list the changes that were made from the neat polymer. Those changes are illustrated in Figure 6.7 and are listed below:

1. Substitution of the residual hydroxyl groups on neat CA with vinyltrimethoxysilane via grafting. This can be broken down into:

a. The introduction of vinyl substituent, which was shown to provide additional backbone flexibility, making it less brittle and therefore more processable, as discussed in Chapter 5.

b. The introduction of the bulky Si-O group into the main chain, which is believed to lead to an increase in free volume and in H_2S sorption, therefore contributes to the permeability and H_2S/CH_4 selectivity increase.

2. Creation of Si-O-Si flexible linkages via crosslinking of polymer network, which leads to the creation of selective siloxane areas within the polymer. This is believed to help the polymer remain selective.
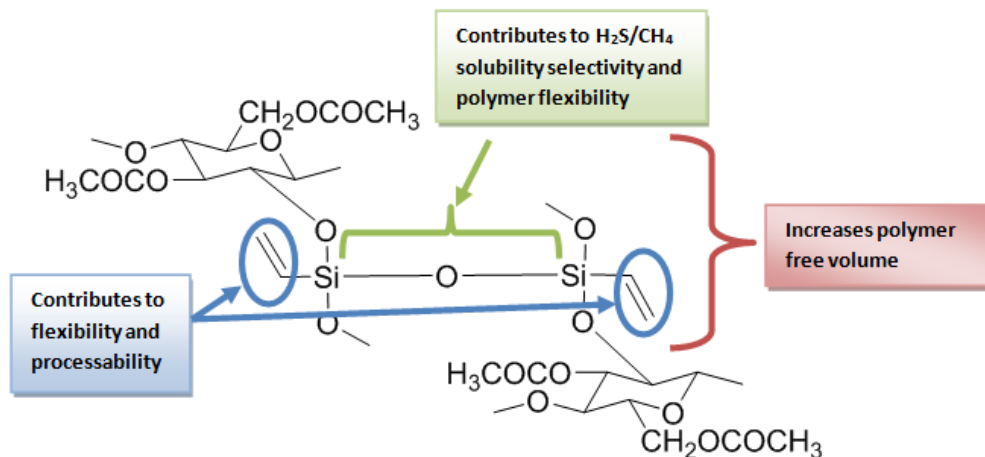
Figure 6.7: Effect of the GCV-Modification on polymer transport properties.

Bhide and Stern studied the permeation behavior of eleven different silicone-containing polymers, including PDMS in H_2S and they found that the substitution of the flexible Si-O bonds with stiffer bonds in the backbone chains resulted in a significant permeability decrease [8]. Wilks et al. showed that highly flexible Si-O linkages in the PDMS backbone are the basis of its high flexibility and high H_2S/CH_4 sorption selectivity [13].

Both atoms (Si and O) contribute to the great flexibility of the siloxane linkage [14]. These findings may help explain why the GCV-Modified CA polymer has a lower stiffness and a higher permeability.

Morita et al. have synthesized and characterized silyl derivatives of CA. They obtained CO_2 permeabilities as high as 160 Barrer, a 94X increase from the unmodified polymer for CA with a degree of substitution of 1.8 and an increase in CO_2 permeability by a factor of ~18 for DS = 2.46. However, the corresponding CO_2/CH_4 selectivities were 6.7 and 7.1, respectively. They found that the increase in permeability was brought about the increase in free volume and higher segmental motions of the chains. Those increases in permeability were accompanied by a decrease in polymer T_g as is the case in this study. It should be noted in their study, silanes used did not contain any Si-O bond and the polymer was not crosslinked. Therefore, no Si-O-Si bridges were formed. This is to show that the significant increase in permeability observed here is not unusual; however, the GCV-Modified CA has a higher H_2S/CH_4 selectivity with a minimum loss in CO_2/CH_4 selectivity. This can be attributed to the higher affinity of Si-O bonds to H_2S and the creation of Si-O-Si bridges, which are believed to help control swelling and sorption of CH_4 as observed in the pressure-decay experiments. There might be some micro-phase segregation created by the formation of the siloxane-filled channels in the GCV-Modified polymer, helping it maintain its size-discrimination ability; however, this is beyond the scope of this study. Many of the silicon-containing compounds that are of technologically relevant today were unknown a few decades ago and have originated from pure research; however, basic research helped generate additional unanswered questions so that there is

still much to be done in this field [15]. Even though, there have been tremendous developments in silicon-based materials over the past century, there is still much potential for new advanced materials, mainly based on the siloxane bond [16]. Therefore, additional research on this material may help further understand its properties.

Nevertheless, the various characterization techniques used, and the analysis of the diffusion and sorption coefficients of the GCV-Modified CA, indicates that the higher permeability observed is mainly brought about through the enhancement of diffusivity and not due to the increases in the sorption coefficients. However, the increase in H_2S/CH_4 selectivity was found to be due to the increase in sorption differences between penetrants, created by the higher affinity of the GCV-Modified polymer to H_2S compared to other gases and also by the size-discrimination ability of the siloxane-cages.

6.6 Pure Gas Permeation Modeling

As discussed in Chapter 3, Koros et al. [17, 18] expressed the permeability coefficient in terms of both the local diffusion coefficients D_D and D_H in the local two environments as shown in Equation 2.36, where the penetrant populations dissolved in the Henry's law and Langmuir domains are both mobile and their mobilities are characterized by the mutual diffusion coefficients D_D, and D_H, respectively.

$$P = k_D D_D \left[1 + \frac{FK}{1 + bf_2} \right] \qquad\qquad 2.36$$

The local CH_4 and CO_2 diffusion coefficients were determined for both materials and are shown in Table 6.1. However, only the local diffusion coefficient of H_2S in crosslinked PDMC was determined because GCV-Modified CA plasticizes at low H_2S pressures, and

Equation 2.36 is based on the assumption that the polymer is not significantly swelled by the penetrant gas. The coefficients D_D and D_H were found by plotting permeability versus $1/(1+bf_2)$ before the onset of plasticization as shown in Appendix F. Figure 6.8, 6.9, and 6.10 show the effective diffusion coefficient as a function of pressure prior to plasticization, calculated using the values of Table 6.6. These effective diffusion coefficient were calculated based on the Equation 2.39 below [19]:

$$D_{eff} = D_D \left[\frac{1 + FK / (1 + bf)^2}{1 + F / (1 + bf)^2} \right]$$

2.39

Table 6.6: Local diffusion coefficients D_D and D_H of CH_4, CO_2, and H_2S in GCV-Modified CA and crosslinked PDMC at 35°C

Polymer	D_D (10^{-8} cm²/sec)			D_H (10^{-9} cm²/sec)			$F = D_D / D_H$			K		
	CH_4	CO_2	H_2S	CH_4	CO_2	H_2S	CH_4	CO_2	H_2S	CH_4	CO_2	H_2S
GCV-CA	12.8	43.8	-	75.4	192	-	0.59	0.44	-	3.42	1.56	2.79
Crosslinked PDMC	1.49	24.0	1.91	0.89	19.8	4.45	0.06	0.08	0.23	1.01	12.9	18.9

Table 6.6 shows that $D_H < D_D$ for both polymers, which means that F<1, as observed for most penetrant-polymer systems [20, 21]. As mentioned in Chapter 4, F is used to represent the relative mobilities of the two populations. The shape of the effective diffusivity concentration dependent curve of GCV-Modified CA is steeper than its corresponding PDMC curve for all penetrants. This can be explained by the lower total sorption coefficient of those penetrants in GCV-Modified CA compared to crosslinked PDMC. The lower Langmuir capacity of these gases in GCV-Modified CA causes a faster "hole" saturation rate, leading to a faster diffusion onset into the dissolved mode compared to PDMC. It is important to note that the effective diffusion coefficient is lower than the local diffusivity in the Henry's domain in all cases.

160
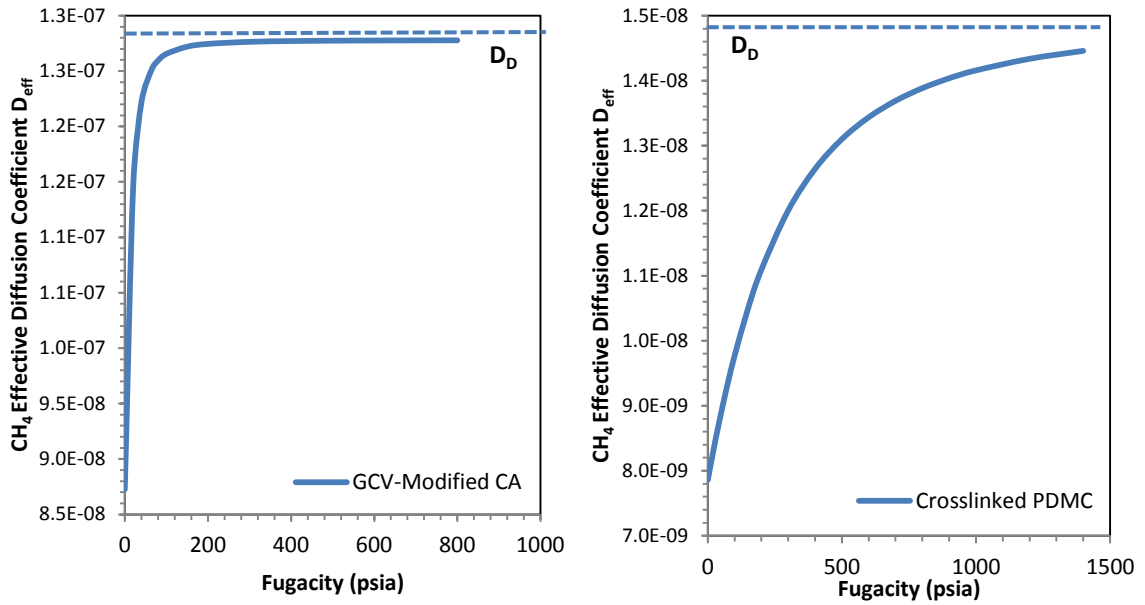
Figure 6.8: Effective diffusion coefficient of CH_4 in GCV-Modified CA and crosslinked PDMC Films.
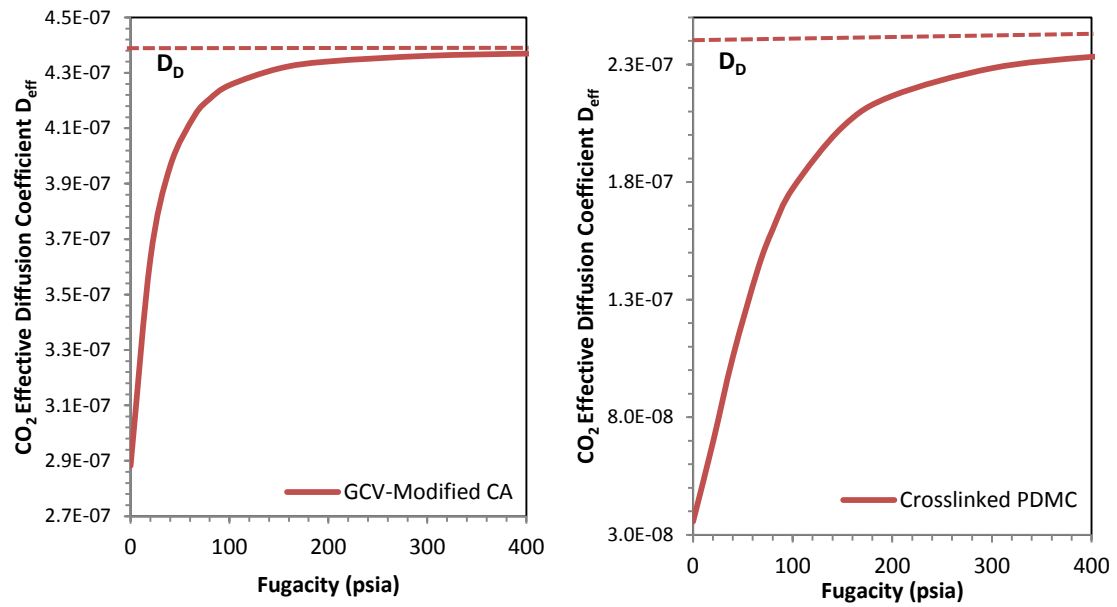
Figure 6.9: Effective diffusion coefficient of CO_2 in GCV-Modified CA and crosslinked PDMC Films.

161
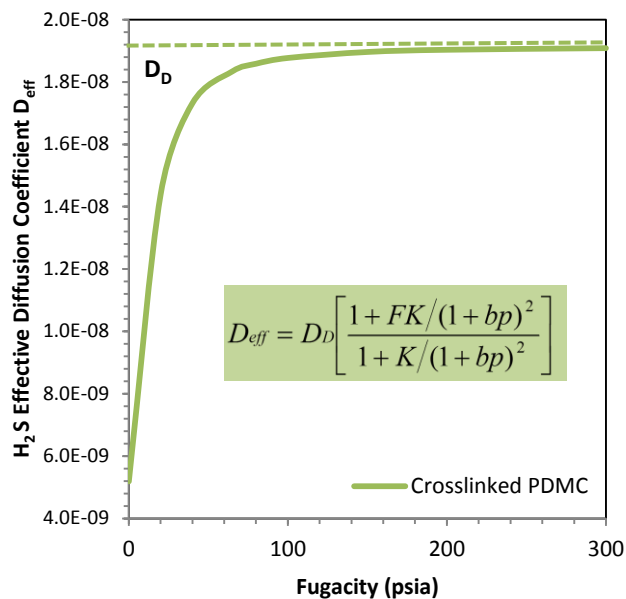
Figure 6.10: Effective diffusion coefficient of H_2S in crosslinked PDMC Films.

6.7 Energetics of Penetrant Diffusion and Sorption

As discussed in Chapter 2 and 4, the permeation, sorption, and diffusion of small molecules in polymers are all thermally moderated processes. It was shown in the previous sections that H_2S had a lower than expected permeability and mobility selectivity in PDMC. The H_2S/CH_4 mobility selectivity of the latter polymer was found to be only slightly higher than unity, despite the size difference between the molecules. It was hypothesized that this effect could be the result of penetrant-polymer interactions that may lower the diffusion coefficient due to the tendency of H_2S molecules to "stick" to the sorption sites, and this was shown to be true for uncrosslinked PDMC in Chapter 4. One of the reasons for this "stickiness" was hypothesized to be due to the hydrogen-bonding with carbonyl groups as well as hydroxyl groups on the DABA moiety in uncrosslinked PDMC. However, in crosslinked PDMC, most of these hydrogen sites have been eliminated through crosslinking. An analysis of the H_2S permeation and sorption

162

changes with temperature was conducted to acquire knowledge of diffusion, sorption, and permeation in crosslinked PDMC. In addition, GCV-Modified CA temperature studies were conducted to gain a better picture of the diffusion process in this polymer. The permeability of H_2S, CO_2, and CH_4 was measured at 35°C, 50°C, 60°C, and 75°C at 65 psia in neat CA and uncrosslinked PDMC. Similarly, the sorption of H_2S, CO_2, and CH_4 was measured at 35°C, 50°C, and 60°C in both polymers. The activation energy of permeation was obtained by taking the slope of ln P versus 1/T in accordance with Equation 2.30 as shown in Figure 6.12. The enthalpy of solution was found by plotting ln S versus 1/T (Figure 6.11) as derived from the van't Hoff expression in Equation 2.28. These plots show an increase in permeability with increasing temperature, revealing that the activation energy of permeation is positive. The temperature dependence on sorption plot reveals that sorption decreases with increasing temperature both materials, suggesting that sorption is an exothermic process. The values obtained are summarized in Table 6.7 and detailed calculations can be found in Appendix F. The activation energy of diffusion of CO_2, CH_4, and H_2S in GCV-CA is much lower than it was in neat CA, consistent with a higher free volume as mentioned previously. Similarly, the activation energy of diffusion of all penetrants in crosslinked PDMC is much lower than it was its uncrosslinked counterpart. This results also confirms the idea that propanediol acts as a "spacer" and increases the free volume of the polymer. Note that $E_{d,H_2S} > E_{d,CH_4}$ in crosslinked PDMC, as it was in uncrosslinked PDMC; however, the difference in those activation energies of diffusion was about ~30% in uncrosslinked PDMC but is only ~17% in uncrosslinked PDMC, which means that the hypothesis of "stickiness" of H_2S molecules being mostly due to hydrogen bonding with –OH groups is likely to be correct.

163

It also suggests that in addition to this hydrogen bonding with hydroxyl groups on the DABA moiety, hydrogen-bonding with carbonyl groups also contribute to this tendency of H_2S to "stick" to the polymer. The diffusion coefficient shown in Table 6.7 was calculated using Equation 2.27, the sorption coefficient was calculated using Equation 2.28, and the permeability was calculated using equation 2.30. These coefficients were estimated to compare against the measured values of Table 6.1 and 6.3. It can be concluded that both results agree reasonably well.
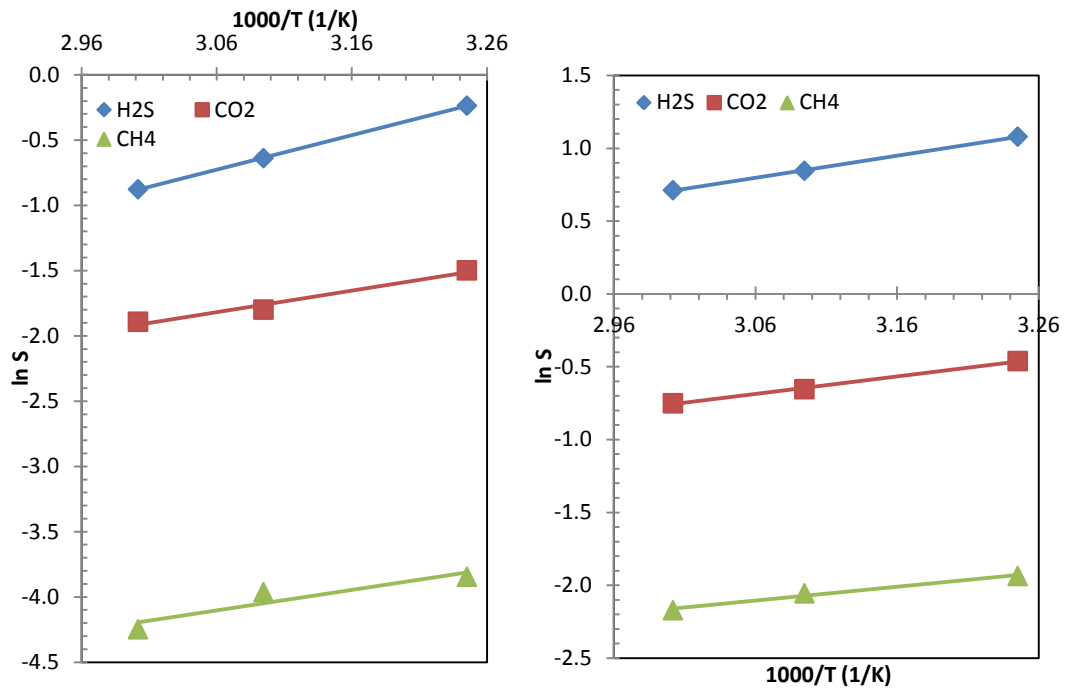
Figure 6.11: Temperature Dependence of H_2S, CO_2, and CH_4 on sorption in GCV-Modified CA and crosslinked PDMC at 65 psia.
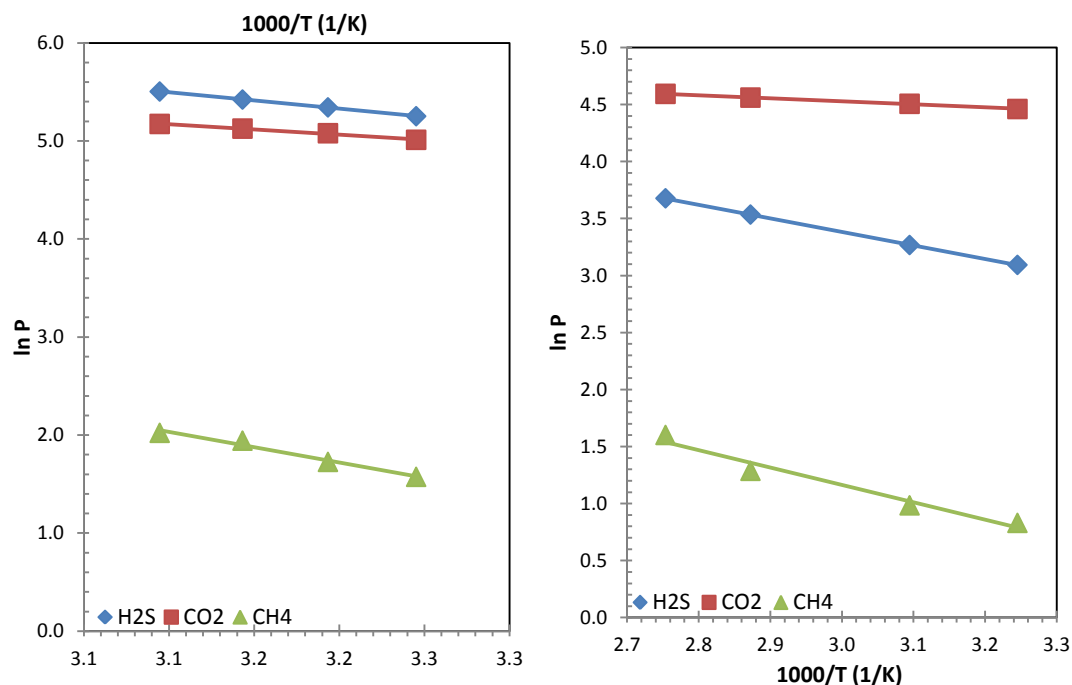
Figure 6.12: Temperature Dependence of H_2S, CO_2, and CH_4 on permeability in GCV-Modified CA and crosslinked PDMC at 65 psia.

Table 6.7: Activation energies of permeation, and diffusion, and enthalpy of sorption of H_2S, CO_2, and CH_4 in GCV-Modified CA and crosslinked PDMC at 65 psia

Parameters	GCV-CA			Crosslinked PDMC		
	H_2S	CO_2	CH_4	H_2S	CO_2	CH_4
E_p (kJ/mol)	13.85	8.52	24.80	9.99	2.22	12.66
ΔH_s (kJ/mol)	-21.92	-13.75	-13.05	-14.15	-9.96	-7.89
E_d (kJ/mol)	35.76	22.27	37.85	24.14	12.18	20.55
D ($10^{-9} cm^2$/sec)	125.4	354.6	114.3	104.6	71.33	7.85
S ($10^{-2} cm^3 STP/cm^3$ psia)	78.85	22.04	22.09	108.33	62.86	14.52
P (Barrer)	191.3	151.2	4.88	21.91	86.72	2.20

*D, S, and P were calculated using Equations 2.27, 2.28, and 2.30 at T=35°C

165

6.8 Binary Gas Permeation

Single gas permeation experiments showed very promising results for crosslinked PDMC and even more so for GCV-Modified CA; however, it is important to evaluate the performance of these materials under aggressive feed conditions. Those conditions include vacuum on the permeate side as most academic studies are reported and *also* nonvacuum downstream condition, which are industrially relevant conditions. Cellulose acetate is currently the most widely used polymer for CO_2/CH_4 separations, and numerous studies have focused on testing various mixtures but the performance of this polymer is not very well documented under nonvacuum downstream conditions. Therefore, neat CA was tested with a 50%CO_2/50%CH_4 mixture under both vacuum and nonvacuum permeate and compared with the GCV-Modified CA polymer. Figure 6.13 and Figure 6.14 show the permeability of CO_2 and CH_4 in both materials under vacuum and 14.7 psia (1 atm) downstream pressure, respectively. Their CO_2/CH_4 selectivities are shown in Figure 6.15.
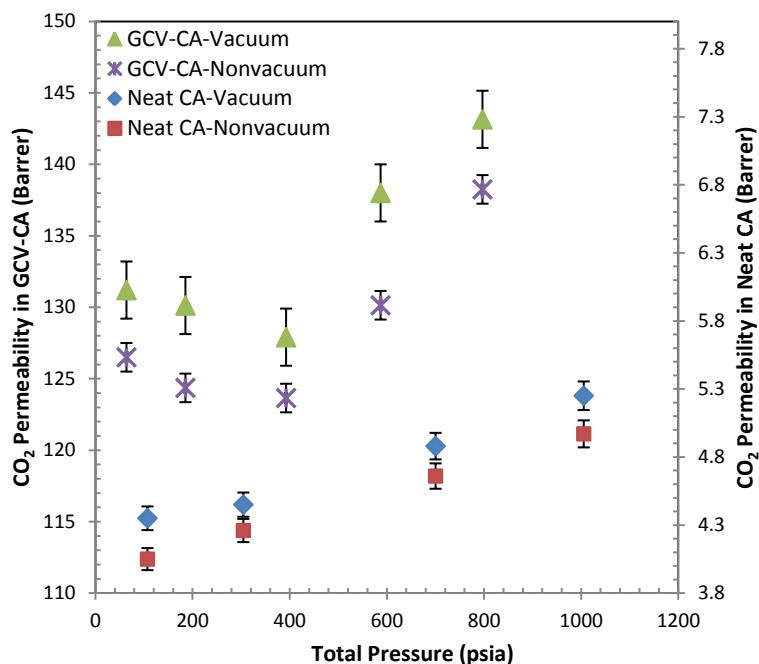
Figure 6.13: CO_2 Permeation isotherm of Neat CA (right axis) and GCV-Modified CA (left axis) under vacuum and 14.7 psia downstream pressure in a 50%CO_2/50%CH_4 mixture at 35°C.
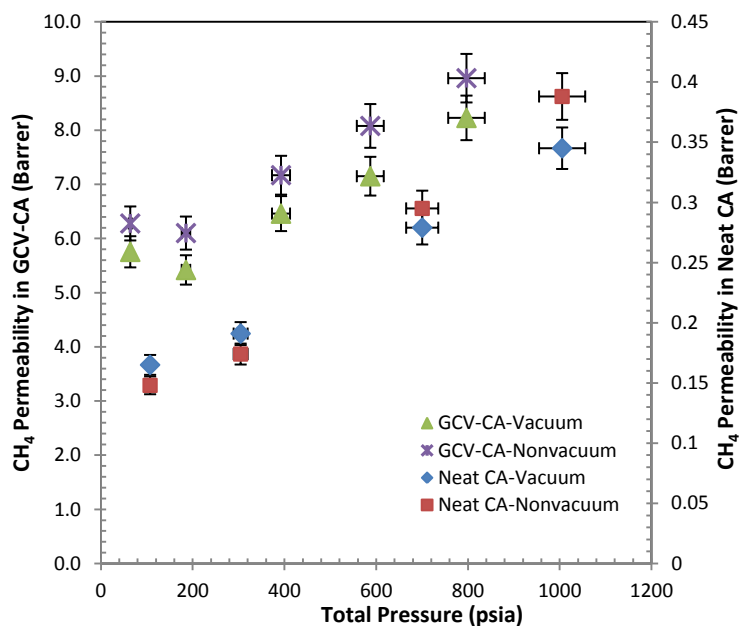
Figure 6.14: CH_4 Permeation isotherm of Neat CA (right axis) and GCV-Modified CA (left axis) with vacuum and 14.7 psia downstream pressure in a 50%CO_2/50%CH_4 mixture at 35°C.
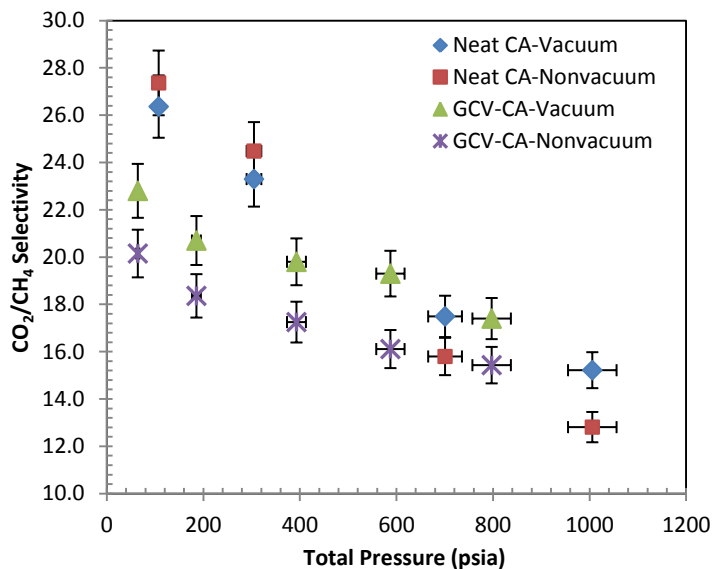
Figure 6.15: CO_2/CH_4 Selectivity of Neat CA and GCV-Modified CA with vacuum and 14.7 psia downstream pressure in a $50\%CO_2/50\%CH_4$ mixture at $35°C$.

The permeability CO_2 and CH_4 of neat CA quickly rises while that of GCV-Modified CA goes through a minimum at lower pressures, then rises at higher pressures in under both vacuum and nonvacuum. This behavior indicates a higher plasticization resistance for GCV-Modified CA. This result supports the slight improvement in CO_2 plasticization resistance observed in the section above. As a result, The CO_2/CH_4 selectivity decreases must faster for neat CA compared to GCV-Modified CA. The permeability of CO_2 under 14.7 psia downstream pressure is lower than the measured value under vacuum. The same trend is not observed for CH_4, so the overall CO_2/CH_4 selectivity is also lower under nonvacuum compared to the zero-pressure case. To better understand the reason behind these results, the general expected performance was modeled by taking into account nonideal phase thermodynamics, competitive sorption, and bulk flow contributions in the absence of plasticization as shown in Figure 6.16, Figure 6.17, and Figure 6.18 as it was done previously [22-24].
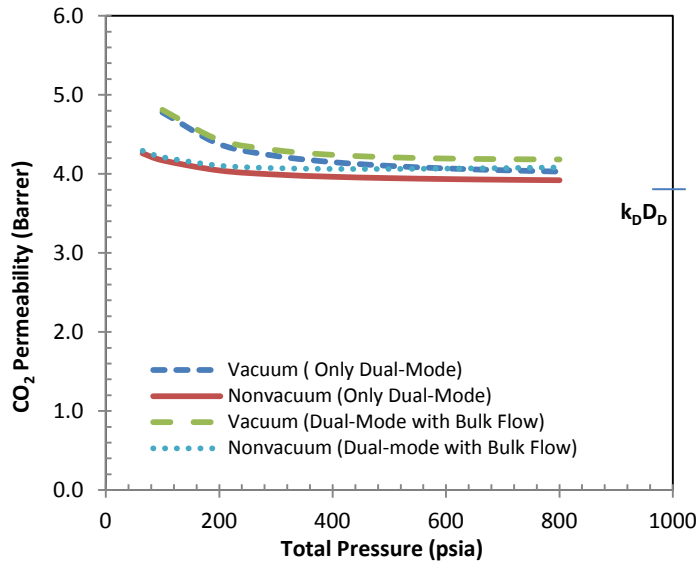
Figure 6.16: Simulation of the effect of competitive sorption and bulk flow contributions on CO_2 permeability with vacuum and 14.7 psia downstream pressure in a 50%CO_2/50%CH_4 mixture at 35°C.
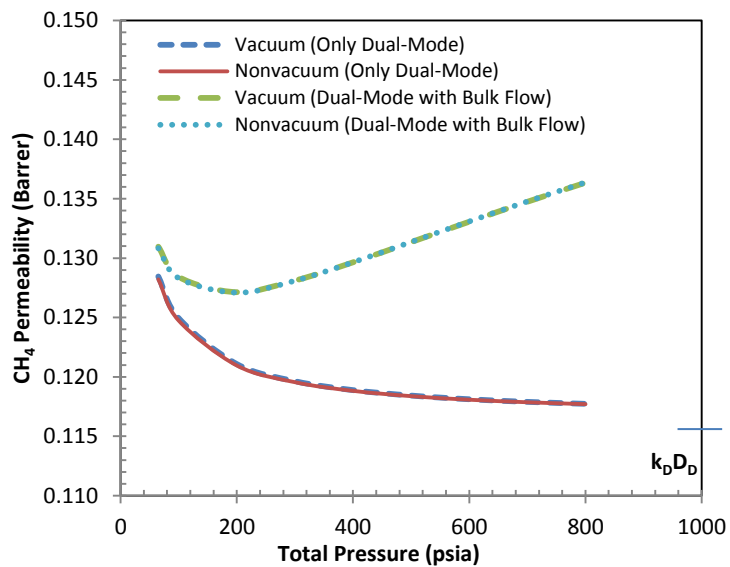
Figure 6.17: Simulation of the effect of competitive sorption and bulk flow contributions on CH_4 permeability with vacuum and 14.7 psia downstream pressure in a 50%CO_2/50%CH_4 mixture at 35°C.
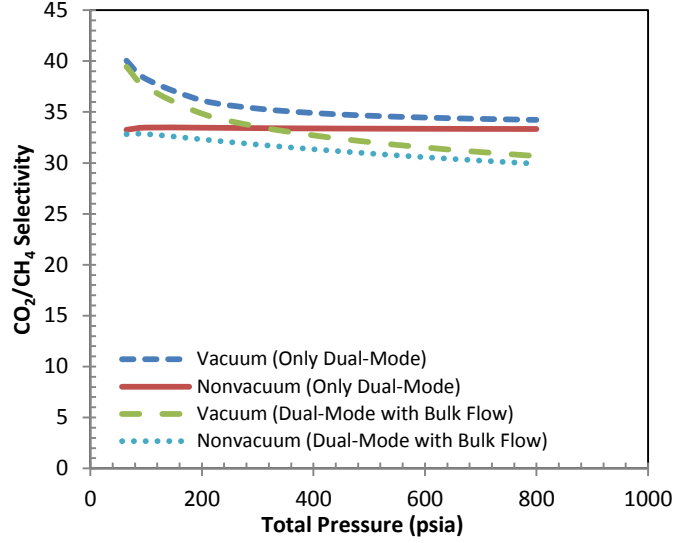
Figure 6.18: Simulation of the effect of competitive sorption and bulk flow contributions on CO_2/CH_4 selectivity with vacuum and 14.7 psia downstream pressure in a 50%CO_2/50%CH_4 mixture at 35°C.

Neat CA data from Table 4.4 were used to perform these simulations. When accounting for the dual-mode competitive sorption only, Equations C.15 and C.16 were used for the nonvacuum permeate pressure case and Equations C.17 and C.18 were used for the vacuum permeate pressure case [24]. Details on those expressions can be found in Appendix C. It should be noted that these equations only apply up to the conditions in Figure 6.8, 6.9, and 6.10 below which plasticization was not a factor.

$$P_A = \frac{k_{D_A} D_{D_A}}{(f_{A2} - f_{A1})} \left[(f_{A2} - f_{A1}) + F_A K_A \left(\frac{f_{A2}}{1 + b_A f_{A2} + b_B f_{B2}} - \frac{f_{A1}}{1 + b_A f_{A1} + b_B f_{B1}} \right) \right] \quad \text{C.15}$$

$$P_B = \frac{k_{D_B} D_{D_B}}{(f_{B2} - f_{B1})} \left[(f_{B2} - f_{B1}) + F_B K_B \left(\frac{f_{B2}}{1 + b_A f_{A2} + b_B f_{B2}} - \frac{f_{B1}}{1 + b_A f_{A1} + b_B f_{B1}} \right) \right] \quad \text{C.16}$$

$$P_A = k_{DA} D_{DA} \left[1 + \frac{F_A K_A}{1 + b_A f_{A2} + b_B f_{B2}} \right] \quad \text{C.17}$$

170

$$P_B = k_{DB} D_{DB} \left[1 + \frac{F_B K_B}{1 + b_A f_{A2} + b_B f_{B2}} \right] \qquad \text{C.18}$$

When the bulk flow contribution was taken into account in addition of the dual-mode competition effects, Equations A.60 and A.61 were used for the nonvacuum case and Equation A.62 and A.63 were used for the vacuum case [22, 23].

$$P_A = \frac{22400 n_A l}{M_A \Delta f_A} = \frac{22400 \rho D_{D_A} \ln \left[\dfrac{1 - w_{A,d} \left(1 + \dfrac{1}{r} \right)}{1 - w_{A,u} \left(1 + \dfrac{1}{r} \right)} \right]}{M_A \Delta f_A \left(1 + \dfrac{1}{r} \right)} \qquad \text{A.60}$$

$$P_B = \frac{22400 n_B l}{M_B \Delta f_B} = \frac{22400 \rho D_{D_B} \ln \left[\dfrac{1 - w_{B,d} (1 + r)}{1 - w_{B,u} (1 + r)} \right]}{M_B \Delta f_B (1 + r)} \qquad \text{A.61}$$

$$P_A = \frac{22400 \rho D_{D_A} \ln \left[\dfrac{1}{1 - w_{A,u} \left(1 + \dfrac{1}{r} \right)} \right]}{M_A \Delta f_A \left(1 + \dfrac{1}{r} \right)} \qquad \text{A.62}$$

$$P_B = \frac{22400 \rho D_{D_B} \ln \left[\dfrac{1}{1 - w_{B,u} (1 + r)} \right]}{M_B \Delta f_B (1 + r)} \qquad \text{A.63}$$

It can be inferred from Figure 6.13 and Figure 6.14 that introducing a 14.7 psia pressure on the downstream significantly decreases the CO_2 permeability with the CH_4 permeability essentially constant. The permeability of CO_2 is reduced much more than CH_4 because it permeates faster; therefore, the pressure of CO_2 on the downstream is always much higher than CH_4. This causes a decrease in CO_2/CH_4 selectivity with

increasing pressure under vacuum and a constant CO_2/CH_4 selectivity under nonvacuum. In addition, the permeability of CO_2 is lower under nonvacuum than under vacuum permeate. The latter is expected because of the increase in pressure of CO_2 on the downstream, which reduces its overall flux for the nonlinear concave sorption isotherm. More specifically, if Equation E.15 is rearranged, the following expression is obtained.

$$P_A = k_{D_A} D_{D_A} + \frac{b_A C'_{H_A} D_{H_A}}{(f_{A2} - f_{A1})} \left(\frac{f_{A2}}{1 + b_A f_{A2} + b_B f_{B2}} - \frac{f_{A1}}{1 + b_A f_{A1} + b_B f_{B1}} \right) \qquad 6.2$$

As the downstream pressure rises, only the second term of equation 6.2 decreases, which means that only the fugacity difference normalized flux through the Langmuir mode changes while the flux through the dissolved mode remains constant. This is the cause of the observed reduction in the overall CO_2 permeability under nonvacuum that was observed for neat CA and GCV-Modified CA in Figure 6.13. At higher pressures, transport through the Langmuir mode will become negligible and the permeability will be governed by the dissolved mode. This is the reason why the permeability becomes constant at higher pressures. This is also evident by the calculated limit of equation 6.2 as shown below.

$$\lim_{p \to \infty} P_A = k_{D_A} D_{D_A} \left(\text{Neglecting Bulk Flow} \right) \qquad 6.3$$

These results will be different if the permeate pressure was higher as shown by Thundyil et al. [24]. However, when the convective flux is taken into account, different trends are observed. The permeability of CO_2 and CH_4 is higher than when only competitive sorption effects were considered. There is also an increase in the permeability of CH_4 with increasing pressure that was not observed for the previous case. As expected, the latter results from the increase in the fraction of bulk mass flux of CH_4 with increasing

pressure as shown in Figure 6.19. This occurs because the bulk motion of the faster CO_2 penetrant causes the CH_4 penetrant to be "carried" along. Therefore, the overall decrease in CO_2/CH_4 selectivity observed in Figure 6.15 may be the result of not only the swelling and competitive sorption effects, but also bulk flow effects. Nevertheless the results of this aggressive binary CO_2/CH_4 feed suggest that GCV-Modified CA can be used effectively to separate these mixtures.
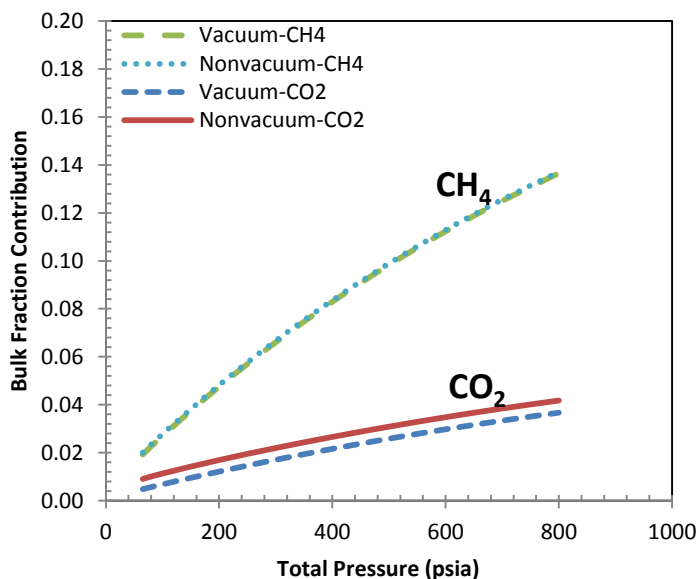
Figure 6.19: Bulk flux contribution simulation of CH_4 and CO_2 in a 50%CO_2/50%CH_4 mixture at 35°C with vacuum and 14.7 psia downstream pressure.

6.9 Ternary Gas Permeation

GCV-Modified CA showed a higher plasticization resistance for CO_2 compared to H_2S in the single gas sorption isotherms and it showed a better stability under an aggressive 50%CO_2/50%CH_4 feed compared to neat CA. This fact notwithstanding, an important goal of this work is to also separate both CO_2 and H_2S mixtures of aggressive sour gas feeds. Therefore, it is important to assess the performance of GCV-Modified CA and

crosslinked PDMC under the presence of both CO_2 and H_2S to ensure that they remain strong candidates under vacuum or nonvacuum conditions. To probe this case, a ternary mixture of 20%H_2S/20%CO_2/60%CH_4 was used to evaluate the polymers performance. In addition to the data collected, the general expected performance was also modeled by taking into account nonideal phase thermodynamics, competitive sorption, and bulk flow contributions in the absence of plasticization as shown in Figure 6.22-6.27 to understand the role of these effects in the results observed. It should be noted that these simulations have not been done previously for the ternary case, as for the binary case discussed above, and detailed derivations of the equations used can be found in Appendix A. *Crosslinked PDMC data was used for the simulation*.

Figure 6.20 shows the H_2S permeability of GCV-Modified CA and crosslinked PDMC with zero permeate pressure and 14.7 psia pressure. It can be concluded that the overall permeability of H_2S in both materials is lower with nonvacuum downstream. This result is consistent with the results obtained in the binary case. However, in this case, the permeate is always richer in H_2S and CO_2 than CH_4. Therefore, there is now even stronger competitive sorption on the feed side and permeate side of the membrane, which reduces the overall flux of H_2S compared to the vacuum case. The same trend is observed for CO_2 as shown in Figure 6.21. In addition, carbon dioxide permeability goes through a minimum and then quickly rises at higher pressures but Figure 6.24 does not predict this trend for CO_2. This is because in the model, CO_2 flux is the least affected of all penetrant in bulk flow (Figure 6.29) because it is the faster species and plasticization is

174

unaccounted for in the models. Its mass flow speeds up the slower species, giving CH_4 a higher flux.
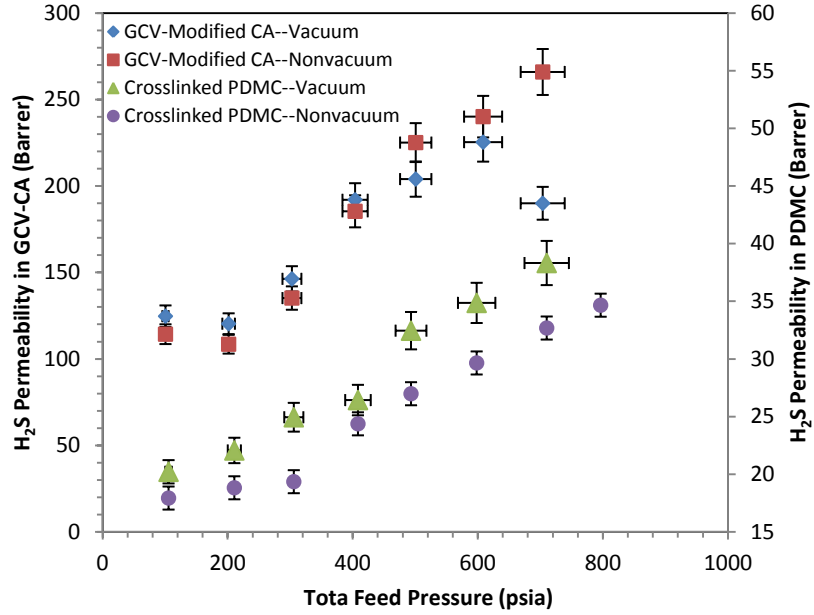
Figure 6.20: H_2S Permeation isotherm of GCV-Modified CA (left axis) and crosslinked PDMC (right axis) with vacuum and 14.7 psia downstream pressure in a 20%H_2S/20%CO_2/60%CH_4 mixture at 35°C.
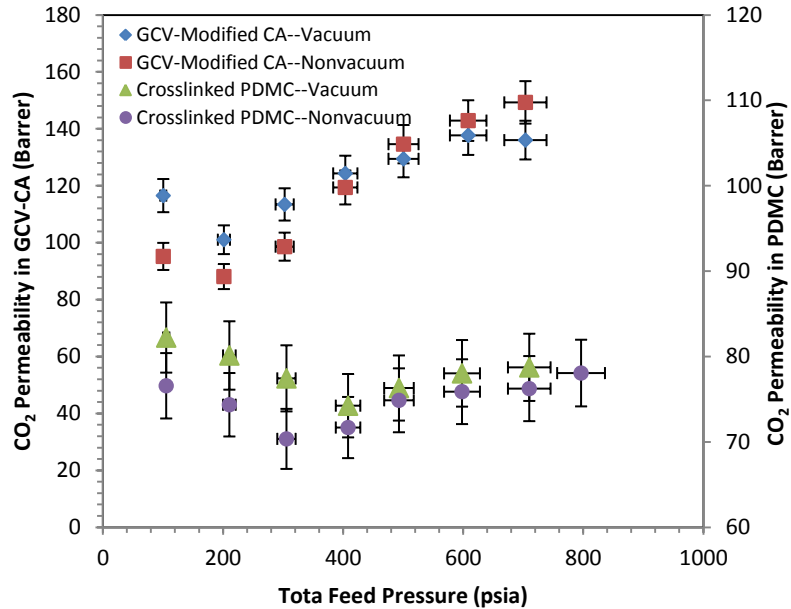
Figure 6.21: CO_2 Permeation isotherm of GCV-Modified CA (left axis) and crosslinked PDMC (right axis) with vacuum and 14.7 psia downstream pressure in a 20%H_2S/20%CO_2/60%CH_4 mixture at 35°C.
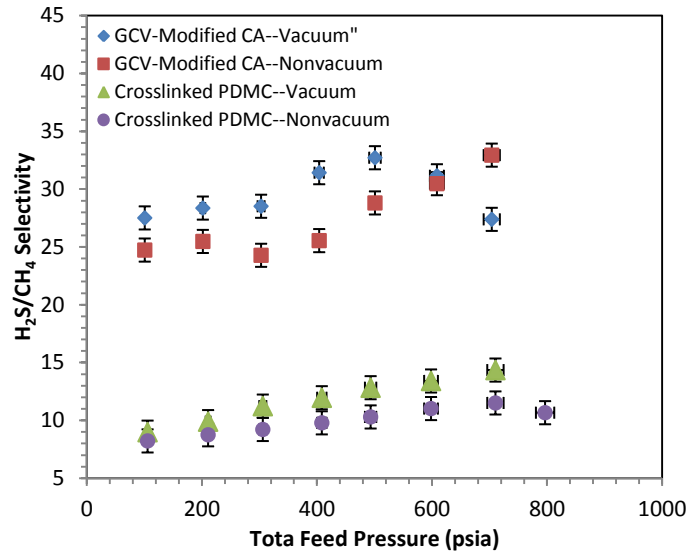
Figure 6.22: H$_2$S/CH$_4$ Selectivity of GCV-Modified CA and crosslinked PDMC with vacuum and 14.7 psia downstream pressure in a 20%H$_2$S/20%CO$_2$/60%CH$_4$ mixture at 35°C.
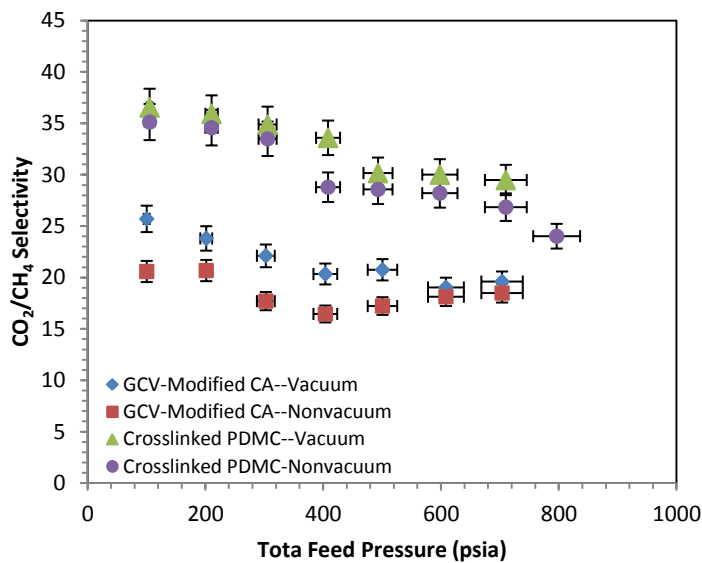
Figure 6.23: CO$_2$/CH$_4$ Selectivity of GCV-Modified CA and crosslinked PDMC with vacuum and 14.7 psia downstream pressure in a 20%H$_2$S/20%CO$_2$/60%CH$_4$ mixture at 35°C.

The H$_2$S/CH$_4$ and CO$_2$/CH$_4$ selectivities are higher for the vacuum case as shown in Figure 6.22 and Figure 6.23. The trend of increasing H$_2$S/CH$_4$ selectivity with increasing

pressure is again observed for both vacuum and nonvacuum cases for crosslinked PDMC. However, if competitive sorption effects are modeled with and without accounting for the bulk flow, this H_2S/CH_4 selectivity increase is not expected, as this is evident in Figure 6.27. Clearly, the decrease in CO_2/CH_4 is predicted by Figure 6.27 when bulk flow is taken into consideration, suggesting that this effect cannot be neglected. It is difficult to assess where plasticization occurs in a ternary system containing highly condensable gases such as CO_2 and H_2S. Therefore, understanding the contribution of these modes is paramount to interpreting the data. Figure 6.29 shows that the bulk contribution is higher for CH_4, followed by H_2S, and CO_2, which is the reason why the permeability of CH_4 is increasing at a constant rate as shown in Figure 6.25 when bulk motion is included. It should be noted that in this model, it is assumed that CO_2 is permeating faster than H_2S and CH_4, and that H_2S is permeating faster than CH_4. If H_2S is modeled to be the faster component as it is for GCV-Modified CA, then this system needs to be modeled differently; unfortunately, it is not possible to simulate this situation for GCV-CA because D_D and D_H parameters could not be obtained for H_2S due to its very low plasticization pressure. In the GCV-Modified CA ternary mixed gas results, the permeate was found to be richer in H_2S than in both CO_2 and CH_4, giving it its higher H_2S/CH_4 selectivity. Therefore, the simulation presented here mainly applies to crosslinked PDMC to give a general idea of the relative contribution of the complexity of a ternary mixture. In addition, in these figures, only a fixed downstream partial pressure of CO_2, H_2S, and CH_4 is assumed. However, data shows that these partial pressures change with feed pressure and therefore, obtaining a dynamic model, which captures these changes, will

give a better overall picture in an actual module with composition changing along the module.
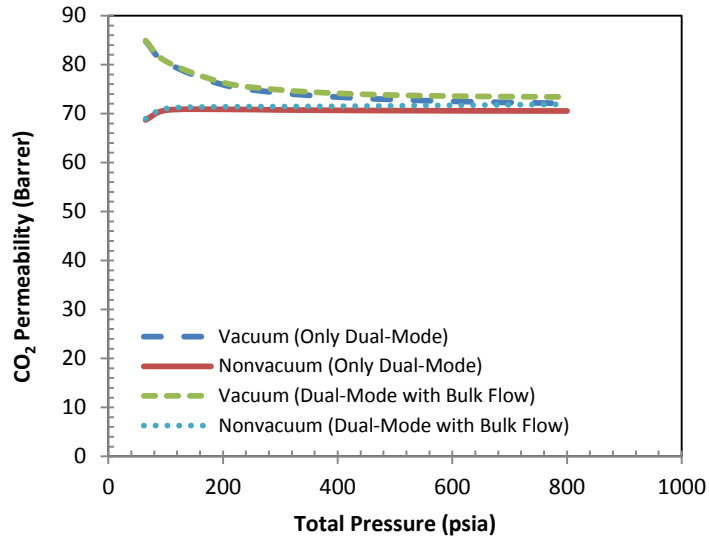
Figure 6.24: Simulation of the effect of competitive sorption and bulk flow contributions on CO_2 permeability with vacuum and 14.7 psia downstream pressure in a 20%H_2S/20%CO_2/60%CH_4 mixture at 35°C for crosslinked PDMC.
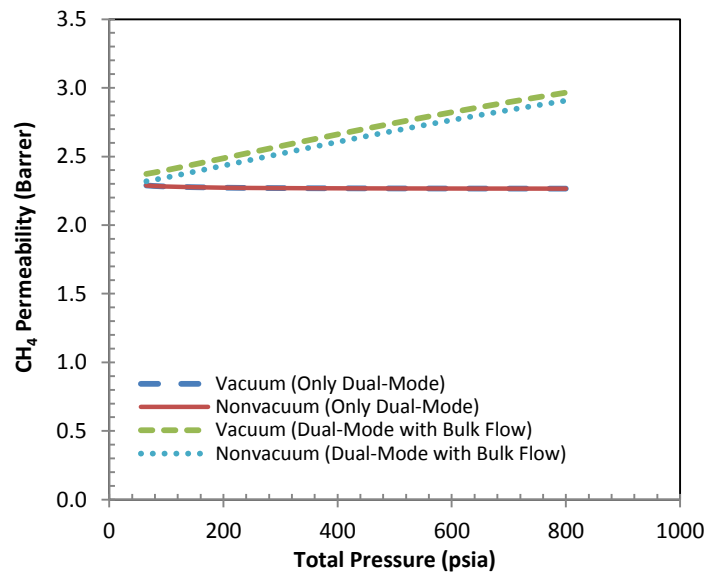
Figure 6.25: Simulation of the effect of competitive sorption and bulk flow contributions on CH_4 permeability with vacuum and 14.7 psia downstream pressure in a 20%H_2S/20%CO_2/60%CH_4 mixture at 35°C for crosslinked PDMC.
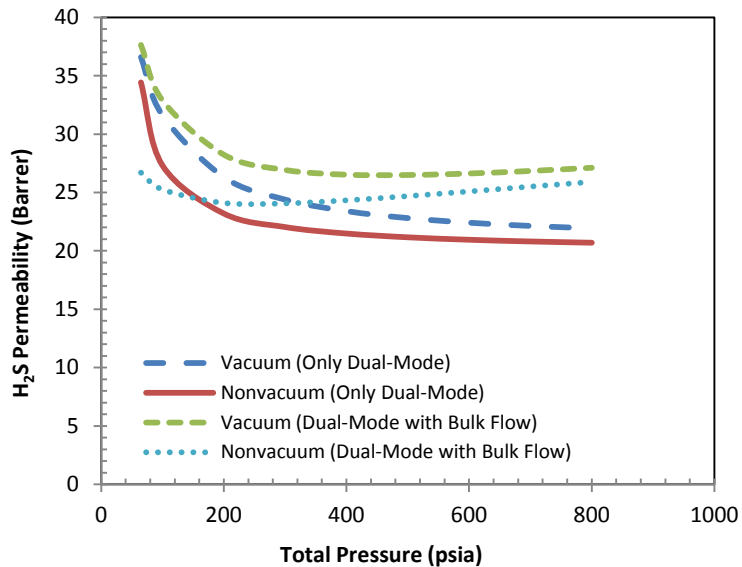
Figure 6.26: Simulation of the effect of competitive sorption and bulk flow contributions on H$_2$S permeability with vacuum and 14.7 psia downstream pressure in a 20%H$_2$S/20%CO$_2$/60%CH$_4$ mixture at 35°C for crosslinked PDMC.
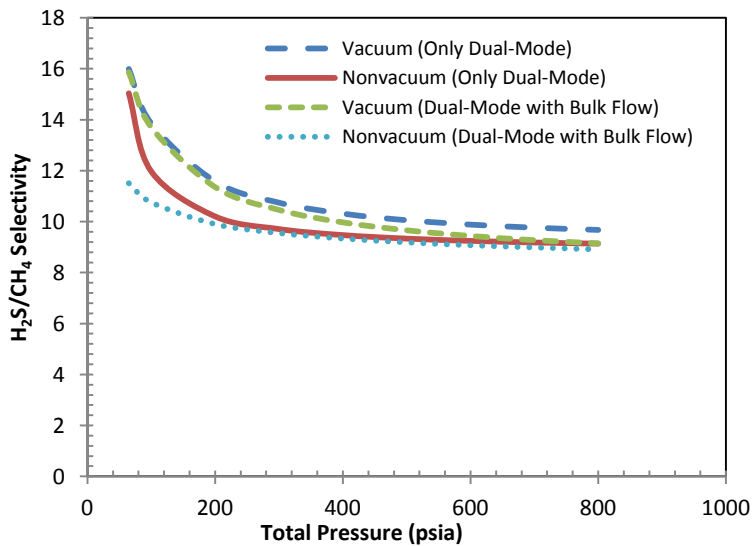
Figure 6.27: Simulation of the effect of competitive sorption and bulk flow contributions on H$_2$S/CH$_4$ selectivity with vacuum and 14.7 psia downstream pressure in a 20%H$_2$S/20%CO$_2$/60%CH$_4$ mixture at 35°C for crosslinked PDMC.
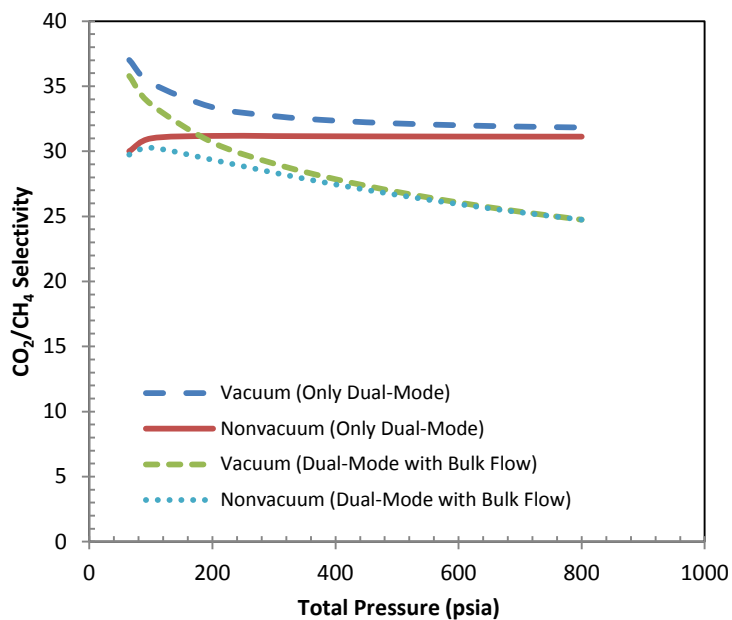
Figure 6.28: Simulation of the effect of competitive sorption and bulk flow contributions on CO_2/CH_4 selectivity with vacuum and 14.7 psia downstream pressure in a 20%H_2S/20%CO_2/60%CH_4 mixture at 35°C.
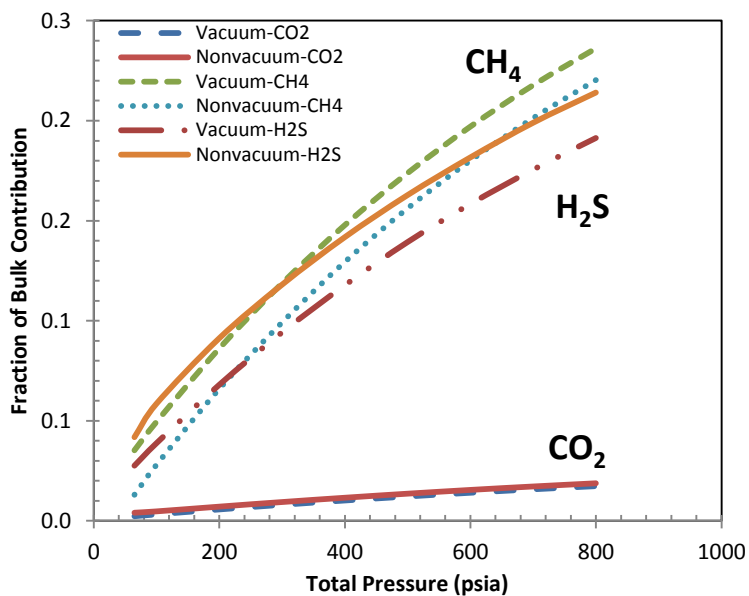
Figure 6.29: Bulk flux contribution simulation of CH_4, CO_2, and H_2S in a 20%H_2S/20%CO_2/60%CH_4 mixture at 35°C with vacuum and 14.7 psia downstream pressure.

Nevertheless the CO_2/CH_4 selectivity is about 18 and its H_2S/CH_4 selectivity is about 33 at 700 psia under nonvacuum for GCV-Modified CA, which is still remarkable. For crosslinked PDMC, its CO_2/CH_4 selectivity is about 24 with a H_2S/CH_4 selectivity of about 11 at 700 psia with nonvacuum downstream. This gives a combined acid gas selectivity of ~51 for GCV-Modified CA and about ~35 for crosslinked PDMC with a total acid gas permeability of ~113 Barrer for crosslinked PDMC and ~415 Barrer for GCV-Modified CA. Therefore, if it can be formulated into high performance asymmetric hollow fibers, GCV-Modified CA should be the material of choice not only because of this higher performance, because of its lower cost compared to PDMC. The total acid gas permeability and selectivity were calculated using Equation 6.4 and 6.5 as described previously [25, 26].

$$\text{Total Acid Gas Permeability} = P_{CO_2} + P_{H_2S} \qquad\qquad 6.4$$

$$\text{Total Acid Gas Selectivity} = \frac{P_{CO_2} + P_{H_2S}}{P_{CH_4}} \qquad\qquad 6.5$$

6.10 Assessing Materials Performance

The CO_2/CH_4 and H_2S/CH_4 separation properties of GCV-Modified CA and crosslinked PDMC are displayed through the productivity-efficiency tradeoff curves as shown in Figure 6.30 and Figure 6.31. As mentioned in Chapter 4, no upper-bound exist yet for H_2S/CH_4 separations due to the limited number of data available in literature for this gas pair. These plots were used to compare the performance of these materials against a few selected high performance polymers for CO_2/CH_4 and H_2S/CH_4 separations. The mixed gas results plotted are reported under the most aggressive conditions, which are 700-800

psia with atmospheric downstream pressure, which mimics industrially relevant conditions. It can be observed from Figure 6.31 that GCV-Modified CA lies above the prior upper-bound curve for CO_2/CH_4 separations in aggressive binary CO_2/CH_4 and ternary 20/20/60 $H_2S/CO_2/CH_4$ feeds. In addition, its H_2S/CH_4 performance is comparable to some rubbery polymers, which exhibit high H_2S permeability and H_2S/CH_4 selectivity, due to their sorption discrimination ability. It is impressive to see that GCV-Modified CA competes with rubbery polymers for H_2S/CH_4 separations and glassy polymers for CO_2/CH_4 separations, indicating that this material performs significantly better than many other high performance materials, making it a promising candidate.
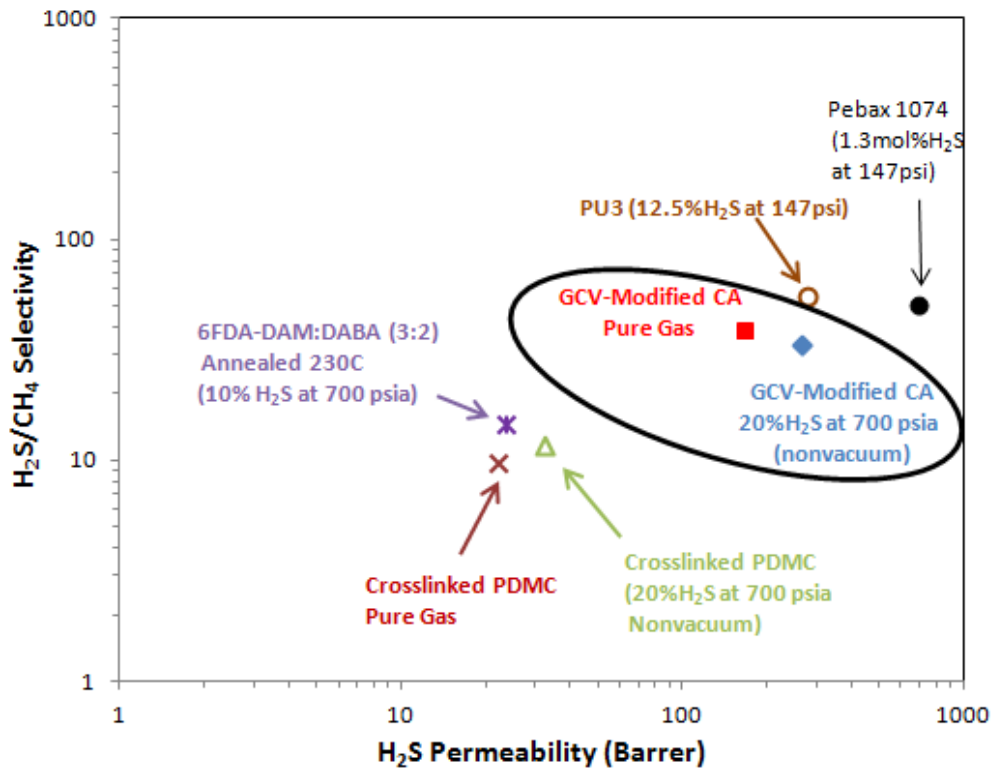
Figure 6.30: H_2S/CH_4 Permeability-selectivity tradeoff curve comparison of GCV-Modified CA and crosslinked PDMC to other materials [25, 27].
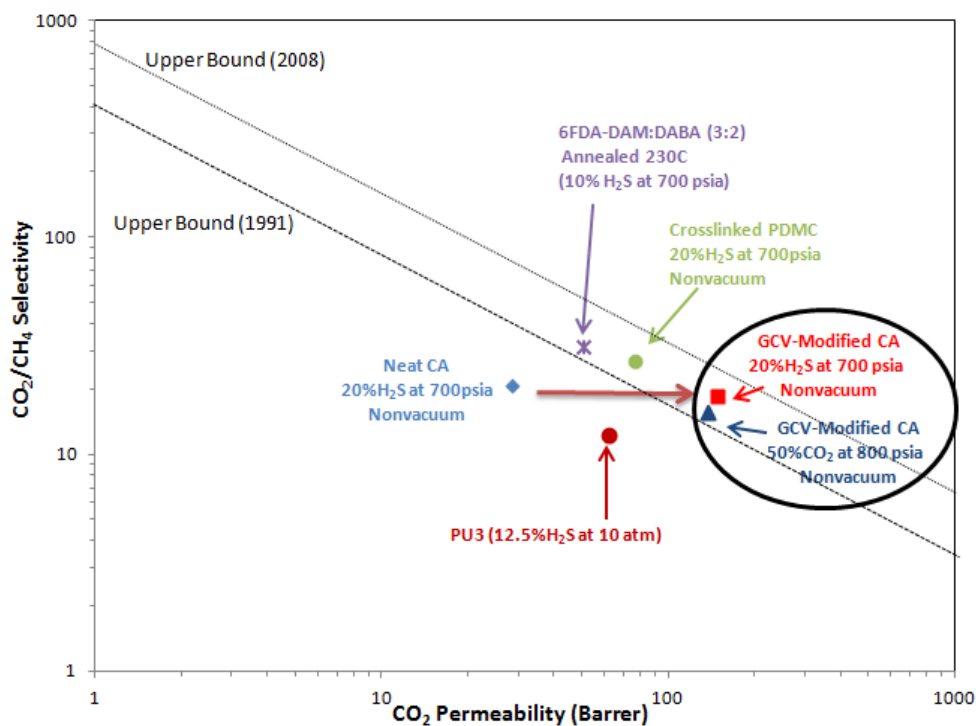
Figure 6.31: CO_2/CH_4 Permeability-selectivity tradeoff curve comparison of neat CA and uncrosslinked PDMC to other materials [25, 27-29].

6.11 References

[1] C.S.K. Achoundong, N. Bhuwania, S.K. Burgess, O. Karvan, J.R. Johnson, W.J. Koros, Silane Modification of Cellulose Acetate Dense Films as Materials for Acid Gas Removal, Macromolecules, 46 (2013) 5584-5594.

[2] A.M.W. Hillock, Crosslinkable Polyimide Mixed Matrix Membranes For Naural Gas Purification, in, Georgia Institue of Technology, PhD Thesis, 2005.

[3] A.M.W. Hillock, W.J. Koros, Cross-Linkable Polyimide Membrane for Natural Gas Purification and Carbon Dioxide Plasticization Reduction, Macromolecules, 40 (2007) 583-587.

[4] A.M.W. Hillock, S.J. Miller, W.J. Koros, Crosslinked mixed matrix membranes for the purification of natural gas: Effects of sieve surface modification, J Membrane Sci, 314 (2008) 193-199.

[5] D.W. Wallace, C. Staudt-Bickel, W.J. Koros, Efficient development of effective hollow fiber membranes for gas separations from novel polymers, J Membrane Sci, 278 (2006) 92-104.

[6] J.D. Wind, Improving Polyimide Membrane Resistance to Carbon Dioxide Plasticization in Natural Gas Separations, in: Chemical Engineering, The University of Texas at Austin, Austin, 2002, pp. 232.

[7] J.D. Wind, D.R. Paul, W.J. Koros, Natural gas permeation in polyimide membranes, J Membrane Sci, 228 (2004) 227-236.

[8] S.A. Stern, B.D. Bhide, Permeability of Silicone Polymers to Ammonia and Hydrogen-Sulfide, J Appl Polym Sci, 38 (1989) 2131-2147.

[9] C. Ma, Highly Productive Ester Crosslinkable Composite Hollow Fiber Membranes for Aggressive Natural Gas Separations, in: School of Chemical and Biomolecular Engineering, Georgia Institute of Technology, Atlanta, 2012, pp. 167.

[10] I.C. Omole, Crosslinked Polyimide Howllow Fiber Membranes for Agressive Natural Gas Feed Streams, in, Georgia Institute of Technology, PhD Thesis, 2008.

[11] C. Staudt-Bickel, W.J. Koros, Improvement of CO2/CH4 separation characteristics of polyimides by chemical crosslinking, J Membrane Sci, 155 (1999) 145-154.

[12] D.W. Wallace, Crosslinked Hollow Fiber Membranes for Natural Gas Purification and Their Manufacture from Novel Polymers, in: Chemical Engineering, University of Texas at Austin, Austin, 2004.

[13] B. Wilks, M.E. Rezac, Properties of rubbery polymers for the recovery of hydrogen sulfide from gasification gases, J Appl Polym Sci, 85 (2002) 2436-2444.

[14] D.R. Paul, I.U.P. Yampolskii, Polymeric Gas Separation Membranes, Taylor & Francis, 1994.

[15] E. Hengge, Properties and preparations of Si-Si linkages, in: Silicon Chemistry II, Springer Berlin Heidelberg, 1974, pp. 1-127.

[16] J.C. Stephen, Advanced Materials Containing the Siloxane Bond, in: Advances in Silicones and Silicone-Modified Materials, American Chemical Society, 2010, pp. 3-10.

[17] W.J. Koros, A.H. Chan, D.R. Paul, Sorption and Transport of Various Gases in Polycarbonate, J Membrane Sci, 2 (1977) 165-190.

[18] W.J. Koros, D.R. Paul, Transient and Steady-State Permeation in Poly(Ethylene Terephthlate) above and Below the Glass-Transition, J Polym Sci Pol Phys, 16 (1978) 2171-2187.

[19] S. Zhou, S.A. Stern, The Effect of Plasticization on the Transport of Gases in and through Glassy-Polymers, J Polym Sci Pol Phys, 27 (1989) 205-222.

[20] D.R. Paul, W.J. Koros, Effect of Partially Immobilizing Sorption on Permeability and Diffusion Time Lag, J Polym Sci Pol Phys, 14 (1976) 675-685.

[21] W.J. Koros, D.R. Paul, A.A. Rocha, Carbon dioxide sorption and transport in polycarbonate, Journal of Polymer Science: Polymer Physics Edition, 14 (1976) 687-702.

[22] H.D. Kamaruddin, Analysis of Methanol/Methyl Tert-Butyl Ether (MTBE) Separations using Pervaporation, in: Chemical Engineering, University of Texas, Austin, 1997.

[23] H.D. Kamaruddin, W.J. Koros, Some observations about the application of Fick's first law for membrane separation of multicomponent mixtures, J Membrane Sci, 135 (1997) 147-159.

[24] M.J. Thundyil, Y.H. Jois, W.J. Koros, Effect of permeate pressure on the mixed gas permeation of carbon dioxide and methane in a glassy polyimide, J Membrane Sci, 152 (1999) 29-40.

[25] B. Kraftschik, W.J. Koros, J.R. Johnson, O. Karvan, Dense film polyimide membranes for aggressive sour gas feed separations, J Membrane Sci, 428 (2013) 608-619.

[26] J. Vaughn, Development and Evaluation of Aromatic Polyamide-imide Membranes for H2S and CO2 Separations from Natural Gas, in: School of Chemical and Biomolecular Engineering, Georgia Instituteof Technology, Atlanta, 2013.

[27] G. Chatterjee, A.A. Houde, S.A. Stern, Poly(ether urethane) and poly(ether urethane urea) membranes with high H2S/CH4 selectivity, J Membrane Sci, 135 (1997) 99-106.

[28] L.M. Robeson, Correlation of separation factor versus permeability for polymeric membranes, J Membrane Sci, 62 (1991) 165-185.

[29] L.M. Robeson, The upper bound revisited, J Membrane Sci, 320 (2008) 390-400.

CHAPTER 7: CONCLUSIONS AND RECOMMENDATIONS

7.1 Summary and Conclusions

Natural gas is the fastest growing of all energy sources. In fact, it will grow fast enough to surpass coal and gain the second position behind oil by 2040. Demand for this lowest carbon footprint energy source will rise by more than 60% through 2040. However, as the demand grows, the need to develop technologies that will efficiently remove contaminants grows as well. Among these contaminants, hydrogen sulfide (H_2S) and carbon dioxide (CO_2), known as "acid gases", are the most important. In addition to producing subquality natural gas, these contaminants corrode pipelines. Membranes are the next-generation technologies to remove such impurities due to their higher energy efficiency, ease of process scale-up, great operational flexibility, and environmentally safety; however, limitations that include higher CH_4 losses must be addressed. The removal of CO_2 from natural gas using membranes is well documented in literature, but there is limited research on H_2S removal, mainly due to its toxic nature.

This project examined the removal of both CO_2 and H_2S from natural gas using dense film membrane materials. First, the industrial standard polymer, cellulose acetate, was studied, and then compared to the high performance crosslinkable polyimide known as PDMC. Crosslinking was examined for both polymers as a means to suppress plasticization and bulk flow effects to increase overall separation performance. Realistic feed conditions such as high concentrations and pressures of acid gases, as well as nonvacuum downstream studies were also examined. The medium of this work was on dense film membranes as a "proof of concept" study, which is the precursor for the development of hollow fiber membrane modules in a subsequent study.

The first objective of this project was to study the performance of cellulose acetate and uncrosslinked PDMC dense film membrane for H_2S separation from natural gas. It was found that uncrosslinked PDMC had a high CO_2/CH_4 selectivity (~37) but a low $H_2S/CH4$ selectivity (~14) compared to neat CA, which had both high CO_2/CH_4 selectivity (~33) and high H_2S /CH_4 (~35) in pure gas feeds. However, the latter polymer was more prone to plasticization by CO_2 and H_2S, whereas the former polymer was more resistant to CO_2 plasticization with virtually no resistance to H_2S. Mixed gas tests revealed an increase in H_2S /CH_4 selectivity with increasing pressure for both polymers with a corresponding loss in CO_2/CH_4 selectivity in aggressive binary H_2S/CH_4 and ternary $H_2S/CO_2/CH_4$ feeds. These results made the selection of one material over the other difficult. Therefore, both materials were carried along for optimization.

The second objective was to engineer these polymers to produce membrane materials with superior performance as measured by efficiency, productivity, and plasticization resistance. PDMC was crosslinked to improve its permeability and H_2S plasticization resistance as it was done by previous researchers for the case of CO_2. It was found that crosslinking PDMC gave higher CH_4, CO_2, and H_2S permeabilities with an improved $CO_2/CH4$ selectivity. The permeability of CO_2 and CH_4 nearly tripled whereas the permeability of H_2S doubled. The increase in permeability was found to be the result of higher free volume created by the introduction of propanediol as a crosslinker between the chains. This material was also found to be more resistant to plasticization compared to the uncrosslinked polymer. The reason behind this resistance to swelling is believed to be the decrease in hydrogen bonding due to the elimination of hydroxyl groups through

crosslinking, which created an interwoven polymer network in which the polymer chains became less susceptible to swelling by outside penetrants. This higher resistance to swelling was found to help the polymer remain stable under aggressive feed conditions. It was also found that H_2S has a tendency to "stick" to sorption sites in PDMC due to their highly polar nature, which gives them the ability to participate in hydrogen bonding with hydroxyl and carbonyl groups on the DABA moiety. This "stickiness" caused the activation energy of diffusion of H_2S to be greater than the activation energy of diffusion of CH_4, which is unusual as CH_4 is the larger molecule and therefore should have higher activation energy. This result was the case of the lower H_2S permeability observed compared to CO_2 in PDMC.

A new material based on cellulose acetate was also developed through a technique referred to as "*GCV-Modification*." In this technique, cellulose acetate was modified via grafting of vinyltrimethoxysilane (VTMS) to residual hydroxyl groups, followed by hydrolysis of the methoxy groups, with subsequent condensation of silanols to create a polymer network. The GCV-Modified CA membrane had CO_2 (~139 Barrer) and H_2S (~165 Barrer) productivities more than one order of magnitude higher than neat CA, with a much higher H_2S/CH_4 selectivity (~39) and maintained CO_2/CH_4 selectivity (~33) compared to other glassy polymers and some rubbery polymers, and was found to be quite stable under high aggressive feed conditions. Previous studies who used a similar approach obtained low H_2S/CH_4 and/or CO_2/CH_4 selectivities. It was found that the GCV-Modified CA film was more amorphous and had a lower glass transition temperature (T_g) than the neat polymer. The presence of the vinyl substituent on the

VTMS helped the membrane retain its transparency and increased its flexibility, and the substitution of the hydroxyl groups, which were mainly responsible for the stiffness of CA, both contributed to the overall permeability increase of the modified polymer. The significant improvement observed was found to be the result of the increase in polymer free volume caused by the incorporation of the bulky Si-O group into the polymer backbone, which helped increase the average segmental mobility and in turn the diffusion coefficient. Hydrogen sulfide was also found to have a higher sorption capacity compared to neat polymer, which was attributed to its higher affinity for the siloxane bond. The creation of the siloxane bridges helped give the polymer its size-discrimination ability, giving the polymer its high selectivity.

The last objective was to determine the separation performance of the engineered membrane materials under more aggressive, realistic natural gas feeds. It was found that it is important to take into account non ideal phase thermodynamics, competitive sorption effects, and bulk flow contributions as well as plasticization when interpreting mixed gas data. However, no one has been successful at quantifying the effect of plasticization in mixed gas feeds. Therefore, it is difficult to model a ternary gas mixture feed containing two highly plasticizing gases such as CO_2 and H_2S. Nevertheless, GCV-Modified CA was found to be rather stable even under aggressive 50% CO_2/50%CH_4 and 20%H_2S/20%CO_2/60%CH_4 feeds at 800 and 700 psia, respectively with 14.7 psia on the downstream. The CO_2/CH_4 selectivity under those conditions was found to be ~18 and the H_2S/CH_4 selectivity was found to ~33 with CO_2 and H_2S permeabilities of 149 and 265, respectively. On the other hand crosslinked PDMC had a CO_2/CH_4 selectivity of

~24 and a H_2S/CH_4 of ~10 at 700 psia in a 20%H_2S/20%CO_2/60%CH_4 with 14.7 psia downstream pressure. These results were very promising for GCV-Modified CA not only because of this remarkable performance but also due to its lower cost compared to PDMC and other high performance materials.

7.2 Cost Analysis of GCV-Modified CA vs. PDMC

Currently, many membranes used for natural gas separation applications are produced as hollow fibers modules. Hollow fibers modules allow large areas of membranes to be packaged into compact membrane modules. The cost of synthesizing high performance materials such as PDMC may vary from $1000/kg-10,000/kg [3, 4], whereas the cost of synthesizing GCV-Modified CA from cellulose acetate and vinyltrimethoxysilane may vary from $20/kg-$100/kg. Assuming that the membrane uses ~50g of polymer m^2 membrane [3], the material cost of the membrane from a material such as PDMC may range from $50/m^2-$500/m^2, whereas the material cost for GCV-Modified CA may vary from $1/m^2-$5/m^2, which may give the latter a significant advantage over PDMC. In addition, membrane costs in natural gas separation only represent a small fraction of the final membrane skid cost. High skid costs may arise because of many pressure vessels, pipes, flanges, and valves that are required [3]. One approach to reduce the skid cost is to increase membrane productivity, which will reduce the membrane surface area needed to treat the same volume of gas. In this case, GCV-Modified CA had CO_2 and H_2S permeabilities that were more than 30X higher than the neat polymer. Therefore, assuming that this GCV technique can be successfully implemented on hollow fibers and give high permeances, skid cost can be significantly reduced as well. To sum up, the

lower material cost of GCV-Modified CA coupled with its higher productivity compared to PDMC, may make it a potential candidate for natural gas separations, if it can be packaged into hollow fiber modules.

7.3 Recommendations for Future Research

7.3.1 Further Characterization of GCV-Modified CA

Permeation and sorption experiments helped us gain an understanding of the contribution of diffusion and solubility to the overall performance of this material. It was hypothesized that there is an increase in polymer free volume which lead to the significant permeability improvement. DMA and DSC studies helped understand the thermal and mechanical properties, mainly related to its glass transition, which confirmed that the material was less stiff, which led to an increase in segmental mobility. XRD gave information about the reduced crystallinity. NMR and FTIR studies helped support the proposed reaction mechanism. Elemental studies confirmed the presence of silicone in the bulk and the increase in oxygen content. However, none of these techniques helped understand the actual free volume distribution within the polymer matrix. Techniques such positron annihilation lifetime spectroscopy (PALS) can help elucidate dynamic activities at the molecular scale. A description of this length-scale may offer fundamental information about the diffusion process, which will help gain insight into the changes occurring in the polymer microstructure. This technique could also be useful for crosslinked PDMC since it was found to have a higher permeability compared to its uncrosslinked counterpart. In addition to giving a better understanding of the micromotions of these materials, the changes in polymer performance over time could also be studied.

7.3.2 Extending the GCV-Modification Technique to Hollow Fibers

The technique presented here was mainly used on dense films. However, the ultimate industrial application of these materials requires the ability to make asymmetric hollow fiber membranes. It is an advantage that cellulose acetate can be easily packaged into asymmetric fibers modules. Therefore, this technique can be mainly proposed as a post-treatment after the fiber has been formed. It is anticipated that this modification could be done at lower temperatures and shorter reaction times in hollow fibers since they do not have those diffusion limitations as the actual separation skin is much smaller. Temperatures such as 50°C or lower with reaction times ranging from 1-5 hrs should be trialed first as this reaction is expected to be much more rapid in these fibers. It is recommended to optimized reaction time, temperature, silane content, and drying conditions directly on the fiber form as dense films optimization might not give accurate predictions.

7.3.3 Use of Different Silane Agents

Even though VTMS was proven to work for this system, many improvements could be done regarding the use of this agent. In chapter 5, it was difficult to control the evolution and even characterize the reaction product because of the high reactivity of $-OCH_3$ to moisture. On the other hand, ethoxysilanes are less reactive to moisture than $-OCH_3$ and can help further increase the free volume of the polymer chains. Therefore replacing those methoxy groups with ethoxy groups could be beneficial. It is also important to limit the number of reactive sites to have a better control of the reaction. Having three methoxy groups in the structure made the reaction more difficult to control. However, if two of the

methoxy groups were replaced with a methyl groups for example, it will help control the number of grafting and crosslinking sites available for reaction. In addition, those other functional groups could be chosen based to obtain a desirable property. For example, methyl groups on PDMS were found to have make the polymer more hydrophobic [2]. Finally, exploration of other hydrocarbon substituent, such as ethyl vs. vinyl, etc… should be explored.

7.3.4 Additional Mixed Gas Studies

It was shown in Chapters 4 and 6 that in binary H_2S/CH_4 mixtures, there is an unconventional increase in H_2S/CH_4 selectivity with increasing pressure. The same result was found in ternary $10\%H_2S/20\%CO_2/70\%CH_4$ and $20\%H_2S/20\%CO_2/60\%CH_4$ mixtures, and no non-ideal thermodynamic, competitive sorption, bulk flow, and plasticization effects are useful to explain that result. Therefore, it is important to test more binary and ternary mixtures, including mixed gas sorption. The latter is suggested because all the dual-mode parameters used to model these gas pairs were pure sorption parameters and those parameters are likely to be different in binary and ternary mixture cases. These studies may provide insight into how the material structure relates to competitive sorption. It will also be important to test a range of CO_2 and H_2S feed concentrations as it may give a better estimate of the trends and operating conditions at which these materials could be most effective. In this study, it was shown that the higher the H_2S content, the higher the H_2S/CH_4 selectivity and the lower the CO_2/CH_4 selectivity in ternary gas feeds. However typical H_2S concentrations in conventional natural gas wells may be significantly lower (5ppm-10%), so even though these materials showed good performance under higher H_2S content, it is important to test feeds with lower H_2S

content and higher CO_2 content for example to assess their performance under those conditions. Furthermore, even though GCV-Modified CA performed well under aggressive CO_2 and H_2S concentrations, it is important to study their performance a well in the presence of other heavy hydrocarbons or impurities such toluene.

7.3.5 Explore Cellulose Acetate with Different Degree of Substitution

In this study, cellulose acetate with a degree of substitution (DS) of 2.45 was used, which gives 0.55 hydroxyl groups available for reaction, per repeat unit. It might also be useful to assess the performance of CA with different acetyl content such as CA with a DS of 2.0, which will have one hydroxyl groups per repeat unit available for reaction. In addition, hydrolyzing the surface to better control the number of –OH groups available for reaction might also be worth exploring.

7.3.6 Explore Polymer Materials with Hydroxyl Functionality

In this study, cellulose acetate was reacted with vinyltrimethoxysilane via residual –OH groups. The grafting reaction occurred primarily on the hydroxyl end of the polymer, which means that ideally, this technique could be used on other polymer materials with the same functionality. Other polymers could also be modified to add the hydroxyl functionality and then apply the technique. On a polymer such as uncrosslinked PDMC for example, it might be worth using this technique as a post-treatment on the fiber to further improve its performance.

7.3.7 Long-Term Stability Studies

Glassy polymers are in a nonequilibrium state, and, over time, polymer chains can slowly relax into a preferred higher density lower permeability form; this process has been defined as physical aging. This phenomenon leads to a decrease in permeability with an increase in selectivity. While GCV-Modified CA gave an impressive performance under the conditions studied, it may be susceptible to changes in performance over time due to its glassy nature. Industrially, these materials are expected to keep their separation performance over several months. Therefore, their ability to maintain their performance both under constant feed and under specified storage conditions is important. In addition to this possible aging process, researchers have shown that the Si-C bond has a better chemical stability than Si-O bond with respect to nucleophilic and electrophilic agents [1]. The susceptibility of siloxane bonds to strong electrophiles and nucleophiles, especially in the presence of water make it important to perform stability studies for such extreme cases. However, it is not anticipated that this will be an issue under dried natural feeds. In cases where the Si-O-Si bond is cleaved over time under water, introduction of bulky and rigid moieties like phenylene in the main chain may help increase their T_g and thermal stability as shown by previous researchers [1]. In addition to these long-term studies, it is important to study the material properties when they are conditioned by H_2S or CO_2. Many researchers have shown improvement in material performance under these conditions.

7.4 References

[1] A.M. Muzafarov, A. Bockholt, Silicon Polymers, Springer, 2010.

[2] J.O. Michael, Properties and Applications of Silicones, in: Advances in Silicones and Silicone-Modified Materials, American Chemical Society, 2010, pp. 13-18.

[3] R.W. Baker, K. Lokhandwala, Natural gas processing with membranes: An overview, Ind Eng Chem Res, 47 (2008) 2109-2121.

[4] R.D. Noble, S.A. Stern, Membrane Separations Technology: Principles and Applications, Elsevier Science, 1995.

APPENDIX A: FRAME OF REFERENCE MODEL DERIVATION FOR TERNARY MIXTURES

A.1 Nonzero Permeate Pressure Derivation for Ternary Mixtures

Mass is transferred as a result of chemical potential, and the concentration differences as described by Fick's law and by convection. Stefan and Maxwell used the kinetic theory of gases to prove that the mass flux relative to a fixed coordinate system resulted from the concentration gradient contribution and from the bulk motion contribution [1, 2]. Therefore, the mass flux of a component i can be written as the sum of those two contributions viz.

$$n_i = n_i^{Bulk} + n_i^{Diffusive} \qquad \text{A.1}$$

This implies that when the flux of a faster component i is large, it's coupling with a slower component can cause the convective flux and diffusive flux of the slower component to be the same order of magnitude. The diffusive flux of a component i in an isothermal, isobaric system can be defined according to Fick's law as [1]:

$$J_i = -D_{iM} \nabla c_i \qquad \text{A.2}$$

$$J_i = -\rho D_{iM} \nabla w_i \qquad \text{A.3}$$

Therefore, by taking into account both contributions, the total mass flux can be written as:

$$n_i = -\rho D_{iM} \nabla w_i + w_i \sum_{i=1}^{n} n_i \qquad \text{A.4}$$

The total individual flux of components A, B, and C in a ternary mixture becomes

$$n_A = -\rho D_{AM} \frac{dw_A}{dx} + w_A \left(n_A + n_B + n_C + n_P \right) \qquad\qquad \text{A.5}$$

$$n_B = -\rho D_{BM} \frac{dw_B}{dx} + w_B \left(n_A + n_B + n_C + n_P \right) \qquad\qquad \text{A.6}$$

$$n_C = -\rho D_{CM} \frac{dw_C}{dx} + w_C \left(n_A + n_B + n_C + n_P \right) \qquad\qquad \text{A.7}$$

$$n_P = -\rho D_{PM} \frac{dw_P}{dx} + w_P \left(n_A + n_B + n_C + n_P \right) \qquad\qquad \text{A.8}$$

The schematic of a ternary mixture gas transport process is shown in Figure A.1. Since

the membrane is immobile at steady-state, the polymeric flux n_P can be set to zero. By

replacing this polymeric flux by zero and by rearranging equation A.5-A.8, the mutually

dependent flux of each component can be expressed by Equations A.9-A.11.
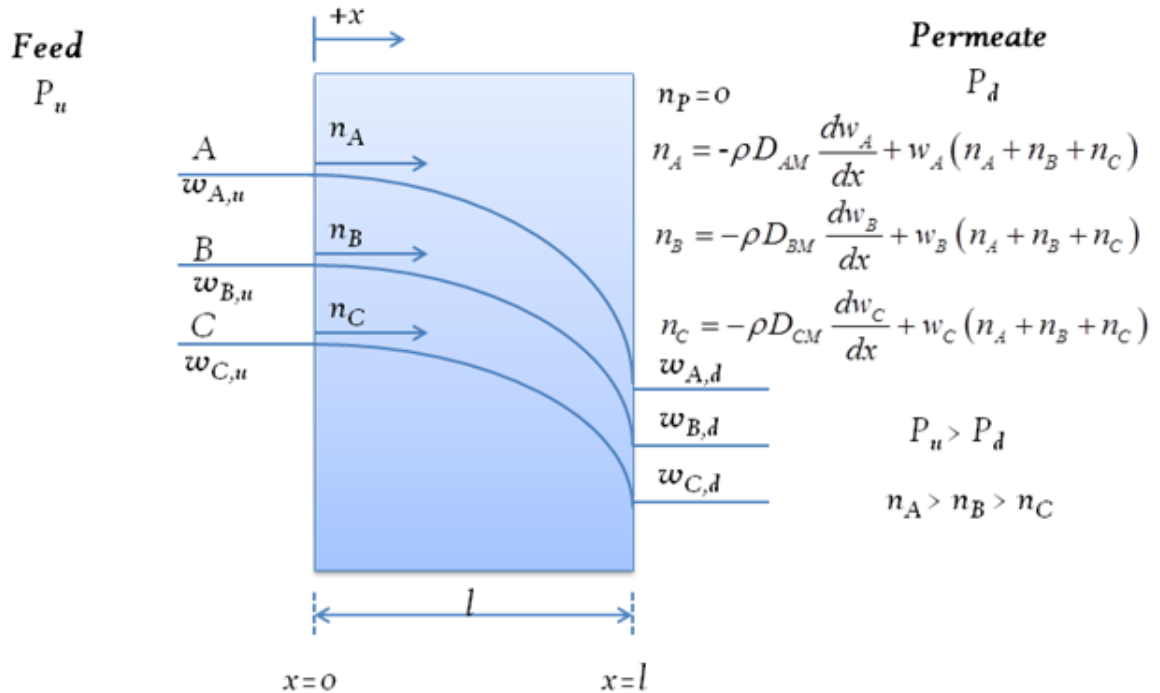
Figure A.1: Schematic of ternary mixture gas transport through a dense film membrane.

$$n_A = \frac{-\rho D_{AM} \dfrac{dw_A}{dx}}{1 - \left(1 + \dfrac{1}{r} + \dfrac{1}{p}\right) w_A} \qquad \text{A.9}$$

$$n_B = \frac{-\rho D_{BM} \dfrac{dw_B}{dx}}{1 - \left(r + 1 + \dfrac{1}{q}\right) w_B} \qquad \text{A.10}$$

$$n_C = \frac{-\rho D_{CM} \dfrac{dw_C}{dx}}{1 - (p + q + 1) w_C} \qquad \text{A.11}$$

$$r = \frac{n_A}{n_B}, \quad p = \frac{n_A}{n_C}, q = \frac{n_B}{n_C}, n_A > n_B > n_C$$

Component A is assumed to have a higher mass flux than component B and C, and component B is assumed to have a higher mass flux than component C. Therefore, "r", "p", and "q" will always be greater than or equal to one. By integrating Equations A.9-A.11 using the following boundary conditions, the mass fraction of each component can be derived as a function of x as shown in Equations A.12-A.14.

$$x = 0, w_A = w_{A,u}, w_B = w_{B,u}$$
$$x = l, w_A = w_A(x), w_B = w_B(x)$$

$$w_A(x) = \frac{1 - \left[1 - \left(1 + \dfrac{1}{r} + \dfrac{1}{p}\right) w_{A,u}\right] \exp\left[\dfrac{\left(1 + \dfrac{1}{r} + \dfrac{1}{p}\right) n_A x}{\rho D_{AM}}\right]}{\left(1 + \dfrac{1}{r} + \dfrac{1}{p}\right)} \qquad \text{A.12}$$

$$w_B(x) = \frac{1 - \left[1 - \left(1 + r + \dfrac{1}{q}\right) w_{B,u}\right] \exp\left[\dfrac{\left(1 + r + \dfrac{1}{q}\right) n_B x}{\rho D_{BM}}\right]}{\left(1 + r + \dfrac{1}{q}\right)} \tag{A.13}$$

$$w_C(x) = \frac{1 - \left[1 - (p + q + 1) w_{C,u}\right] \exp\left[\dfrac{(p + q + 1) n_C x}{\rho D_{CM}}\right]}{(p + q + 1)} \tag{A.14}$$

The concentration of components A, B, and C inside a membrane of thickness l can be averaged using Equations A.15-A.17.

$$w_A^{avg} = \frac{\int_0^l w_A(x)dx}{\int_0^l dx} \tag{A.15}$$

$$w_B^{avg} = \frac{\int_0^l w_B(x)dx}{\int_0^l dx} \tag{A.16}$$

$$w_C^{avg} = \frac{\int_0^l w_C(x)dx}{\int_0^l dx} \tag{A.17}$$

By substituting the concentration profiles equations A.12-A.14 into Equations A.15-A.17, the following expressions can be obtained

$$w_A^{avg} = \frac{1}{\left(1 + \dfrac{1}{r} + \dfrac{1}{p}\right)} \left\{ 1 + \frac{\rho D_{AM}\left[1 - \left(1 + \dfrac{1}{r} + \dfrac{1}{p}\right) w_{A,u}\right]}{n_A l \left(1 + \dfrac{1}{r} + \dfrac{1}{p}\right)} \left[1 - \exp\left(\frac{\left(1 + \dfrac{1}{r} + \dfrac{1}{p}\right) n_A l}{\rho D_{AM}}\right)\right] \right\} \tag{A.18}$$

$$w_B^{avg} = \frac{1}{\left(1+r+\dfrac{1}{q}\right)}\left\{1+\frac{\rho D_{BM}\left[1-\left(1+r+\dfrac{1}{q}\right)w_{B,u}\right]}{n_B l\left(1+r+\dfrac{1}{q}\right)}\left[1-\exp\left(\frac{\left(1+r+\dfrac{1}{q}\right)n_B l}{\rho D_{BM}}\right)\right]\right\} \qquad \text{A.19}$$

$$w_C^{avg} = \frac{1}{\left(p+q+1\right)}\left\{1+\frac{\rho D_{CM}\left[1-\left(p+q+1\right)w_{C,u}\right]}{n_C l\left(p+q+1\right)}\left[1-\exp\left(\frac{\left(p+q+1\right)n_C l}{\rho D_{CM}}\right)\right]\right\} \qquad \text{A.20}$$

By substituting the boundary conditions below into Equations A.12-A.14, Equations A.21-A.23 are derived.

$$x=0, w_A = w_{A,u}, w_B = w_{B,u}$$
$$x=l, w_A = w_{A,d}, w_B = w_{B,d}$$

$$\frac{n_A l}{\rho D_{AM}} = \frac{\ln\left[\dfrac{1-\left(1+\dfrac{1}{r}+\dfrac{1}{p}\right)w_{A,d}}{1-\left(1+\dfrac{1}{r}+\dfrac{1}{p}\right)w_{A,u}}\right]}{\left(1+\dfrac{1}{r}+\dfrac{1}{p}\right)} \qquad \text{A.21}$$

$$\frac{n_B l}{\rho D_{BM}} = \frac{\ln\left[\dfrac{1-\left(1+r+\dfrac{1}{q}\right)w_{B,d}}{1-\left(1+r+\dfrac{1}{q}\right)w_{B,u}}\right]}{\left(1+r+\dfrac{1}{q}\right)} \qquad \text{A.22}$$

$$\frac{n_C l}{\rho D_{CM}} = \frac{\ln\left[\dfrac{1-\left(p+q+1\right)w_{C,d}}{1-\left(p+q+1\right)w_{C,u}}\right]}{\left(p+q+1\right)} \qquad \text{A.23}$$

By plugging Equations A.21-A.23 into Equations A.18-A.20, the following expressions can be derived

$$w_A^{avg} = \frac{1}{\left(1+\dfrac{1}{r}+\dfrac{1}{p}\right)} + \frac{w_{A,d} - w_{A,u}}{\ln\left[\dfrac{1-w_{A,d}\left(1+\dfrac{1}{r}+\dfrac{1}{p}\right)}{1-w_{A,u}\left(1+\dfrac{1}{r}+\dfrac{1}{p}\right)}\right]} \qquad \text{A.24}$$

$$w_B^{avg} = \frac{1}{\left(1+r+\dfrac{1}{q}\right)} + \frac{w_{B,d} - w_{B,u}}{\ln\left[\dfrac{1-w_{B,d}\left(1+r+\dfrac{1}{q}\right)}{1-w_{B,u}\left(1+r+\dfrac{1}{q}\right)}\right]} \qquad \text{A.25}$$

$$w_C^{avg} = \frac{1}{\left(p+q+1\right)} + \frac{w_{C,d} - w_{C,u}}{\ln\left[\dfrac{1-w_{C,d}\left(p+q+1\right)}{1-w_{C,u}\left(p+q+1\right)}\right]} \qquad \text{A.26}$$

To quantify the importance of the bulk flow contribution, the fraction of bulk contribution can be established. It is defined as the ratio of a component bulk mass flux to the total mass flux as shown in Equations A.27-A.29.

$$\Pi_A^{Bulk} = \frac{\left(n_A + n_B + n_C + n_P\right)w_A^{avg}}{n_A} = \frac{\left(n_A + n_B + n_C\right)w_A^{avg}}{n_A} = \left(1+\frac{1}{r}+\frac{1}{p}\right)w_A^{avg} \qquad \text{A.27}$$

$$\Pi_B^{Bulk} = \frac{\left(n_A + n_B + n_C + n_P\right)w_B^{avg}}{n_B} = \frac{\left(n_A + n_B + n_C\right)w_A^{avg}}{n_A} = \left(1+r+\frac{1}{q}\right)w_B^{avg} \qquad \text{A.28}$$

$$\Pi_C^{Bulk} = \frac{\left(n_A + n_B + n_C + n_P\right)w_C^{avg}}{n_C} = \frac{\left(n_A + n_B + n_C\right)w_C^{avg}}{n_C} = \left(p+q+1\right)w_C^{avg} \qquad \text{A.29}$$

If the fraction of the bulk flux compared to the mass flux is small, the concentration profile inside the membrane will be approximately linear. In that case, the average concentration inside the membrane can be defined as follows [3]:

$$w_A^{avg} = \frac{w_{A,u} + w_{A,d}}{2} \tag{A.30}$$

$$w_B^{avg} = \frac{w_{B,u} + w_{B,d}}{2} \tag{A.31}$$

$$w_C^{avg} = \frac{w_{C,u} + w_{C,d}}{2} \tag{A.32}$$

By substituting these average concentrations values into Equations A.27-A.29, the following expressions are obtained.

$$\prod_A^{Bulk} = \left(1 + \frac{1}{r} + \frac{1}{p}\right)\left(\frac{w_{A,u} + w_{A,d}}{2}\right) \tag{A.33}$$

$$\prod_B^{Bulk} = \left(1 + r + \frac{1}{q}\right)\left(\frac{w_{B,u} + w_{B,d}}{2}\right) \tag{A.34}$$

$$\prod_C^{Bulk} = \left(p + q + 1\right)\left(\frac{w_{C,u} + w_{C,d}}{2}\right) \tag{A.35}$$

These equations are only rough approximations and will have a high percent error if the bulk flux contribution is significant. Better approximations can be found by substituting Equations A.24-A.26 into Equations A.27-A.29 to give Equations A.36-A.38.

$$\prod_A^{Bulk} = 1 + \frac{\left(w_{A,d} - w_{A,u}\right)\left(1 + \frac{1}{r} + \frac{1}{p}\right)}{\ln\left[\dfrac{1 - w_{A,d}\left(1 + \frac{1}{r} + \frac{1}{p}\right)}{1 - w_{A,u}\left(1 + \frac{1}{r} + \frac{1}{p}\right)}\right]} \tag{A.36}$$

203

$$\prod_{B}^{Bulk} = 1 + \frac{\left(w_{B,d} - w_{B,u}\right)\left(1 + r + \dfrac{1}{q}\right)}{\ln\left[\dfrac{1 - w_{B,d}\left(1 + r + \dfrac{1}{q}\right)}{1 - w_{B,u}\left(1 + r + \dfrac{1}{q}\right)}\right]} \tag{A.37}$$

$$\prod_{C}^{Bulk} = 1 + \frac{\left(w_{C,d} - w_{C,u}\right)\left(p + q + 1\right)}{\ln\left[\dfrac{1 - w_{C,d}\left(p + q + 1\right)}{1 - w_{C,u}\left(p + q + 1\right)}\right]} \tag{A.38}$$

The diffusion-based permeability of each component can be calculated using Equations A.39-A.41.

$$P_{A}^{*} = \left(1 - \prod_{A}^{Bulk}\right)P_{A} = \frac{\left(w_{A,u} - w_{A,d}\right)\left(1 + \dfrac{1}{r} + \dfrac{1}{p}\right)}{\ln\left[\dfrac{1 - w_{A,d}\left(1 + \dfrac{1}{r} + \dfrac{1}{p}\right)}{1 - w_{A,u}\left(1 + \dfrac{1}{r} + \dfrac{1}{p}\right)}\right]}P_{A} \tag{A.39}$$

$$P_{B}^{*} = \left(1 - \prod_{B}^{Bulk}\right)P_{B} = \frac{\left(w_{B,u} - w_{B,d}\right)\left(1 + r + \dfrac{1}{q}\right)}{\ln\left[\dfrac{1 - w_{B,d}\left(1 + r + \dfrac{1}{q}\right)}{1 - w_{B,u}\left(1 + r + \dfrac{1}{q}\right)}\right]}P_{B} \tag{A.40}$$

$$P_{C}^{*} = \left(1 - \prod_{C}^{Bulk}\right)P_{C} = \frac{\left(w_{C,u} - w_{C,d}\right)\left(p + q + 1\right)}{\ln\left[\dfrac{1 - w_{C,d}\left(p + q + 1\right)}{1 - w_{C,u}\left(p + q + 1\right)}\right]}P_{C} \tag{A.41}$$

P_A, P_B, and P_C are the experimentally observed permeabilities of each component. If we consider the definition of the observed permeability of a component, which takes into account the bulk and diffusion contributions, the following expressions are derived.

$$P_A = \frac{22400 n_A l}{M_A \Delta f_A} = \frac{22400 \rho D_{D_A} \ln \left[\dfrac{1 - w_{A,d}\left(1 + \dfrac{1}{r} + \dfrac{1}{p}\right)}{1 - w_{A,u}\left(1 + \dfrac{1}{r} + \dfrac{1}{p}\right)} \right]}{M_A \Delta f_A \left(1 + \dfrac{1}{r} + \dfrac{1}{p}\right)} \qquad \text{A.42}$$

$$P_B = \frac{22400 n_B l}{M_B \Delta f_B} = \frac{22400 \rho D_{D_B} \ln \left[\dfrac{1 - w_{B,d}\left(1 + r + \dfrac{1}{q}\right)}{1 - w_{B,u}\left(1 + r + \dfrac{1}{q}\right)} \right]}{M_B \Delta f_B \left(1 + r + \dfrac{1}{q}\right)} \qquad \text{A.43}$$

$$P_C = \frac{22400 n_C l}{M_C \Delta f_C} = \frac{22400 \rho D_{D_C} \ln \left[\dfrac{1 - w_{C,d}\left(p + q + 1\right)}{1 - w_{C,u}\left(p + q + 1\right)} \right]}{M_C \Delta f_C \left(p + q + 1\right)} \qquad \text{A.44}$$

As discussed in Chapter 2, sorption in glassy occurs in two populations: a Henry's and a Langmuir population. Koros et al. [4] suggested that only a fraction of the Langmuir's population can perform a diffusive jump. In their assumption, the Henry's population is fully mobile and can fully perform a diffusive jump. Therefore, most mobile species come from the Henry's population and only a fraction comes from the Langmuir population. This partial immobilization model requires that the mobile concentration is used when describing penetrant transport in a glassy polymer. The mobile concentration

of each component can be derived starting with the dual-mode sorption model to give the
following expressions.

$$w_A^m = \frac{k_{D_A} f_A M_A}{22400 \rho} \left(1 + \frac{F_A K_A}{1 + b_A f_A + b_B f_B + b_C f_C} \right)$$ A.45

$$w_B^m = \frac{k_{D_B} f_B M_B}{22400 \rho} \left(1 + \frac{F_B K_B}{1 + b_A f_A + b_B f_B + b_C f_C} \right)$$ A.46

$$w_C^m = \frac{k_{D_C} f_C M_C}{22400 \rho} \left(1 + \frac{F_C K_C}{1 + b_A f_A + b_B f_B + b_C f_C} \right)$$ A.47

A.2 Zero Permeate Pressure Derivation for Ternary Mixtures

In the case of vacuum downstream pressure, the downstream concentrations $w_{A,d}$, $w_{B,d}$, and $w_{C,d}$ are set to zero and the average concentrations (Equations A.24- A.26) reduce to:

$$w_A^{avg} = \frac{1}{\left(1 + \frac{1}{r} + \frac{1}{p} \right)} - \frac{w_{A,u}}{\ln \left[\frac{1}{1 - w_{A,u} \left(1 + \frac{1}{r} + \frac{1}{p} \right)} \right]}$$ A.48

$$w_B^{avg} = \frac{1}{\left(1 + r + \frac{1}{q} \right)} - \frac{w_{B,u}}{\ln \left[\frac{1}{1 - w_{B,u} \left(1 + r + \frac{1}{q} \right)} \right]}$$ A.49

$$w_C^{avg} = \frac{1}{\left(p + q + 1 \right)} - \frac{w_{C,u}}{\ln \left[\frac{1}{1 - w_{C,u} \left(p + q + 1 \right)} \right]}$$ A.50

Similarly, the fraction of the bulk contribution of each component when the permeate pressure is negligible can be derived as shown in Equations A.51-A.53.

$$\prod_A^{Bulk} = 1 - \frac{w_{A,u}\left(1 + \frac{1}{r} + \frac{1}{p}\right)}{\ln\left[\frac{1}{1 - w_{A,u}\left(1 + \frac{1}{r} + \frac{1}{p}\right)}\right]} \qquad\qquad \text{A.51}$$

$$\prod_B^{Bulk} = 1 - \frac{w_{B,u}\left(1 + r + \frac{1}{q}\right)}{\ln\left[\frac{1}{1 - w_{B,u}\left(1 + r + \frac{1}{q}\right)}\right]} \qquad\qquad \text{A.52}$$

$$\prod_C^{Bulk} = 1 - \frac{w_{C,u}\left(p + q + 1\right)}{\ln\left[\frac{1}{1 - w_{C,u}\left(p + q + 1\right)}\right]} \qquad\qquad \text{A.53}$$

The diffusion-based permeability can also be obtained by simplifying Equations A.39-A.41.

$$P_A^* = \frac{w_{A,u}\left(1 + \frac{1}{r} + \frac{1}{p}\right)}{\ln\left[\frac{1}{1 - w_{A,u}\left(1 + \frac{1}{r} + \frac{1}{p}\right)}\right]} P_A \qquad\qquad \text{A.54}$$

$$P_B^* = \frac{w_{B,u}\left(1 + r + \frac{1}{q}\right)}{\ln\left[\frac{1}{1 - w_{B,u}\left(1 + r + \frac{1}{q}\right)}\right]} P_B \qquad\qquad \text{A.55}$$

$$P_C^* = \frac{w_{C,u}(p+q+1)}{\ln\left[\dfrac{1}{1-w_{C,u}(p+q+1)}\right]} P_C \qquad \text{A.56}$$

Finally, Equations A.42-A.44 can be simplified to account for the zero permeate pressure to yield the following expressions:

$$P_A = \frac{22400\rho D_{D_A} \ln\left[\dfrac{1}{1-w_{A,u}\left(1+\dfrac{1}{r}+\dfrac{1}{p}\right)}\right]}{M_A \Delta f_A\left(1+\dfrac{1}{r}+\dfrac{1}{p}\right)} \qquad \text{A.57}$$

$$P_B = \frac{22400\rho D_{D_B} \ln\left[\dfrac{1}{1-w_{B,u}\left(1+r+\dfrac{1}{q}\right)}\right]}{M_B \Delta f_B\left(1+r+\dfrac{1}{q}\right)} \qquad \text{A.58}$$

$$P_C = \frac{22400\rho D_{D_C} \ln\left[\dfrac{1}{1-w_{C,u}(p+q+1)}\right]}{M_C \Delta f_C(p+q+1)} \qquad \text{A.59}$$

A.3 Expressions for Zero and Nonzero Permeate Pressure for Binary Mixtures

Kamaruddin et al. [3, 5] have derived similar expressions for binary mixtures. The following expressions of permeability were derived for the case of *nonvacuum downstream*.

$$P_A = \frac{22400 n_A l}{M_A \Delta f_A} = \frac{22400 \rho D_{D_A} \ln \left[\dfrac{1 - w_{A,d}\left(1 + \dfrac{1}{r}\right)}{1 - w_{A,u}\left(1 + \dfrac{1}{r}\right)} \right]}{M_A \Delta f_A \left(1 + \dfrac{1}{r}\right)} \qquad \text{A.60}$$

$$P_B = \frac{22400 n_B l}{M_B \Delta f_B} = \frac{22400 \rho D_{D_B} \ln \left[\dfrac{1 - w_{B,d}\left(1 + r\right)}{1 - w_{B,u}\left(1 + r\right)} \right]}{M_B \Delta f_B \left(1 + r\right)} \qquad \text{A.61}$$

For the zero pressure downstream, these equations reduce to:

$$P_A = \frac{22400 \rho D_{D_A} \ln \left[\dfrac{1}{1 - w_{A,u}\left(1 + \dfrac{1}{r}\right)} \right]}{M_A \Delta f_A \left(1 + \dfrac{1}{r}\right)} \qquad \text{A.62}$$

$$P_B = \frac{22400 \rho D_{D_B} \ln \left[\dfrac{1}{1 - w_{B,u}\left(1 + r\right)} \right]}{M_B \Delta f_B \left(1 + r\right)} \qquad \text{A.63}$$

The bulk fraction contribution of each species was estimated by Equations A.64-A.65.

$$\prod_A^{Bulk} = 1 + \frac{\left(w_{A,d} - w_{A,u}\right)\left(1 + \dfrac{1}{r}\right)}{\ln\left[\dfrac{1 - w_{A,d}\left(1 + \dfrac{1}{r}\right)}{1 - w_{A,u}\left(1 + \dfrac{1}{r}\right)}\right]} \qquad \text{A.64}$$

$$\prod_B^{Bulk} = 1 + \frac{\left(w_{B,d} - w_{B,u}\right)\left(1 + r\right)}{\ln\left[\dfrac{1 - w_{B,d}\left(1 + r\right)}{1 - w_{B,u}\left(1 + r\right)}\right]} \qquad \text{A.65}$$

A.4 Limiting Cases

It is also important to assess the limits of these expressions in extreme cases. For binary mixtures with nonvacuum downstream, the limiting cases are given by the following equations.

$$\lim_{r \to \infty} P_A = \frac{22400 \rho D_{D_A}}{M_A \Delta f_A} \ln\left[\frac{w_{A,d} - 1}{w_{A,u} - 1}\right] \qquad \text{A.66}$$

$$\lim_{r \to 0} P_A = 0 \qquad \text{A.67}$$

$$\lim_{r \to 0} P_B = \frac{22400 \rho D_{D_B}}{M_B \Delta f_B} \ln\left[\frac{w_{B,d} - 1}{w_{B,u} - 1}\right] \qquad \text{A.68}$$

$$\lim_{r \to \infty} P_B = 0 \qquad \text{A.69}$$

Equations A.66-A.69 means that in the limit that that the flux of A is very large compared to the flux of B, that is, the permeability of the slower component B will be negligible and the permeability of the faster component A will be equal to a constant given by

210

Equation A.66. For binary mixtures with nonvacuum downstream, Equation A.67 and

A.69 remain the same while Equations A.66 and A.68 become:

$$\lim_{r \to \infty} P_A = \frac{22400 \rho D_{D_A}}{M_A \Delta f_A} \ln \left[\frac{1}{1 - w_{A,u}} \right] \qquad \text{A.70}$$

$$\lim_{r \to 0} P_B = \frac{22400 \rho D_{D_B}}{M_B \Delta f_B} \ln \left[\frac{1}{1 - w_{B,u}} \right] \qquad \text{A.71}$$

For ternary mixtures with nonvacuum downstream, the limits of the permeability

coefficients of A, B, and C are given by the following expressions.

$$\lim_{r \to 0} P_A = 0 \qquad \text{A.72}$$

$$\lim_{r \to \infty} P_A = \frac{22400 \rho D_{D_A} p \ln \left[\dfrac{w_{A,d} - p + p w_{A,d}}{w_{A,u} - p + p w_{A,u}} \right]}{M_A \Delta f_A (1 + p)} \qquad \text{A.73}$$

$$\lim_{p \to 0} P_A = 0 \qquad \text{A.74}$$

$$\lim_{p \to \infty} P_A = \frac{22400 \rho D_{D_A} r \ln \left[\dfrac{w_{A,d} - r + r w_{A,d}}{w_{A,u} - r + r w_{A,u}} \right]}{M_A \Delta f_A (1 + r)} \qquad \text{A.75}$$

$$\lim_{r \to 0} P_B = \frac{22400 \rho D_{D_A} q \ln \left[\dfrac{w_{A,d} - q + q w_{A,d}}{w_{A,u} - q + q w_{A,u}} \right]}{M_A \Delta f_A (1 + q)} \qquad \text{A.76}$$

$$\lim_{r \to \infty} P_B = 0 \qquad \text{A.77}$$

$$\lim_{q \to 0} P_B = 0 \qquad \text{A.78}$$

$$\lim_{q \to \infty} P_B = \frac{22400 \rho D_{D_A} \ln \left[\dfrac{-1 + w_{A,d} + r w_{A,d}}{-1 + w_{A,u} + r w_{A,u}} \right]}{M_A \Delta f_A (1 + r)} \qquad\qquad \text{A.79}$$

$$\lim_{p \to \infty} P_C = 0 \qquad\qquad \text{A.80}$$

$$\lim_{p \to 0} P_C = \frac{22400 \rho D_{D_A} \ln \left[\dfrac{-1 + w_{A,d} + q w_{A,d}}{-1 + w_{A,u} + q w_{A,u}} \right]}{M_A \Delta f_A (1 + q)} \qquad\qquad \text{A.81}$$

$$\lim_{q \to 0} P_C = \frac{22400 \rho D_{D_A} \ln \left[\dfrac{-1 + w_{A,d} + p w_{A,d}}{-1 + w_{A,u} + p w_{A,u}} \right]}{M_A \Delta f_A (1 + p)} \qquad\qquad \text{A.82}$$

$$\lim_{q \to \infty} P_C = 0 \qquad\qquad \text{A.83}$$

A.5 References

[1] J. Welty, Fundamentals of Momentum, Heat, and Mass Transfer, Wiley, 2001.

[2] L.S. Darken, Diffusion, mobility and their interrelation through free energy in binary metallic systems, Trans. Aime, 175 (1948) 41.

[3] H.D. Kamaruddin, W.J. Koros, Some observations about the application of Fick's first law for membrane separation of multicomponent mixtures, J Membrane Sci, 135 (1997) 147-159.

[4] W.J. Koros, R.T. Chern, V. Stannett, H.B. Hopfenberg, A model for permeation of mixed gases and vapors in glassy polymers, Journal of Polymer Science: Polymer Physics Edition, 19 (1981) 1513-1530.

[5] H.D. Kamaruddin, Analysis of Methanol/Methyl Tert-Butyl Ether (MTBE) Separations using Pervaporation, in: Chemical Engineering, University of Texas, Austin, 1997.

APPENDIX B: DERIVATION OF NON IDEAL MIXED GAS SELECTIVITY WITH NONVACUUM DOWNSTREAM

The steady-state permeability coefficients of components A and B through a membrane of thickness l are defined as:

$$P_A = \frac{N_A l}{f_{A2} - f_{A1}} \qquad \text{B.1}$$

$$P_B = \frac{N_B l}{f_{B2} - f_{B1}} \qquad \text{B.2}$$

where N_A and N_B are the steady-state fluxes of components A and B through the membrane and f_{i2} and f_{i1} are the penetrant fugacities in the feed and permeate, respectively. The mole fraction y_A and y_B of components A and B in the permeate can be written in terms of the total mass flux N_T across the membrane as follows:

$$y_A = \frac{N_A}{N_T} \qquad \text{B.3}$$

$$y_B = \frac{N_B}{N_T} \qquad \text{B.4}$$

If Equations B.3 and B.4 are plugged into Equations B.1 and B.2, respectively, equations B.5 and B.6 are obtained.

$$P_A = \frac{y_A N_T l}{f_{A2} - f_{A1}} \qquad \text{B.5}$$

$$P_B = \frac{y_B N_T l}{f_{B2} - f_{B1}}$$

B.6

The fugacities of each penetrant on either side of the membrane can be written as

$$f_{A2} = x_A \hat{\varphi}_{A,2} P_2$$

B.7

$$f_{A1} = y_A \hat{\varphi}_{A,1} P_1$$

B.8

$$f_{B2} = x_B \hat{\varphi}_{B,2} P_2$$

B.9

$$f_{B1} = y_B \hat{\varphi}_{B,1} P_1$$

B.10

x_A and x_B are the mole fraction of components A and B in the feed. $\hat{\varphi}_{A,2}$ and $\hat{\varphi}_{B,2}$ are the fugacity coefficients of components A and B in the feed mixture. $\hat{\varphi}_{A,1}$ and $\hat{\varphi}_{B,1}$ are the fugacity coefficients of components A and B in the permeate mixture. The fugacity coefficients of the mixtures considered in this study can be found in Appendix D along with the derivations. By substituting equations B.7 through B.10 into Equations B.5 and B.6, the following expressions are obtained.

$$P_A = \frac{y_A N_T l}{x_A \hat{\varphi}_{A,2} P_2 - y_A \hat{\varphi}_{A,1} P_1}$$

B.11

$$P_B = \frac{y_B N_T l}{x_B \hat{\varphi}_{B,2} P_2 - y_B \hat{\varphi}_{B,1} P_1}$$

B.12

If the separation factor is defined as the ratio of permeabilities of both penetrants, the ratio of Equation B.11 to B.12 can be taken to yield Equation B.14.

$$\alpha^*_{A/B} = \frac{P_A}{P_B} \qquad \text{B.13}$$

$$\alpha^*_{A/B} = \left(\frac{y_A}{y_B}\right)\left(\frac{x_B \hat{\varphi}_{B,2}\, p_2 - y_B \hat{\varphi}_{B,1}\, p_1}{x_A \hat{\varphi}_{A,2}\, p_2 - y_A \hat{\varphi}_{A,1}\, p_1}\right) \qquad \text{B.14}$$

If the permeate pressure is neglected, p_1 is set to zero and the separation factor becomes

$$\alpha^*_{A/B} = \left(\frac{y_A}{y_B}\right) \times \left(\frac{x_B}{x_A}\right) \times \left(\frac{\hat{\varphi}_{B,2}}{\hat{\varphi}_{A,2}}\right) \qquad \text{B.15}$$

In addition, if the penetrants behave ideally, $\hat{\varphi}_{A,2} = \hat{\varphi}_{B,2} = 1$ and Equation B.15 reduce to

$$\alpha^*_{A/B} = \left(\frac{y_A}{y_B}\right) \times \left(\frac{x_B}{x_A}\right) \qquad \text{B.16}$$

Equation B.16 is the expression that is mostly used in literature to calculate the separation factor. However, in this study, the penetrants (CO_2 and H_2S) are highly compressible and the case of nonzero permeate pressure is explored so Equation B.14 and B.15 were used in those cases.

APPENDIX C: GENERAL EXPRESSIONS OF DUAL-MODEL PERMEABILITY COEFFICIENTS IN BINARY AND TERNARY GAS MIXTURES

C.1 Binary Gas Mixture Expressions (Zero and Nonzero Permeate Pressure)

At steady-state, the permeability coefficient of a component A through a membrane of thickness l is given by:

$$P_A = \frac{N_A l}{f_{A2} - f_{A1}} \qquad \text{C.1}$$

As discussed in Chapter 2, according to the partial immobilization model, the flux of component A can also be expressed as [1]:

$$N_A = -D_{DA} \frac{\partial C_{DA}}{\partial x} - D_{HA} \frac{\partial C_{HA}}{\partial x} \qquad \text{C.2}$$

$$N_A = -D_{DA} \left[\frac{\partial C_{DA}}{\partial x} + \frac{D_{HA}}{D_{DA}} \frac{\partial C_{HA}}{\partial x} \right] \qquad \text{C.3}$$

where C_{DA} and C_{HA} are the local concentration of penetrant A in the Henry's and Langmuir populations, respectively. If we let

$$C_{MA} = C_{DA} + \frac{D_{HA}}{D_{DA}} C_{HA} \qquad \text{C.4}$$

Equation C.3 can be rewritten as:

$$N_A = -D_{DA} \frac{\partial C_{MA}}{\partial x}$$

C.5

By integrating this expression using the following boundary conditions, equation C.6 is derived.

$$x = 0, C_{MA} = C_{MA2}$$
$$x = l, C_{MA} = C_{MA1}$$

$$N_A l = D_{DA} \left(C_{MA2} - C_{MA1} \right)$$

C.6

Koros et al [2] showed that by taking into account competitive sorption in the Langmuir population, the concentration of components A and B in a binary mixture can be defined by Equations C.7 and C.8.

$$C_{HA} = \frac{b_A C'_{HA} f_A}{1 + b_A f_A + b_B f_B}$$

C.7

$$C_{HB} = \frac{b_B C'_{HB} f_B}{1 + b_A f_A + b_B f_B}$$

C.8

By substituting Equations C.7 and C.8 into Equation C.4, the following expressions are obtained.

$$C_{MA} = C_{DA} + F_A \left[\frac{b_A C'_{HA} f_A}{1 + b_A f_A + b_B f_B} \right]$$

C.9

$$C_{MB} = C_{DB} + F_B \left[\frac{b_B C'_{HB} f_B}{1 + b_A f_A + b_B f_B} \right]$$

C.10

Where $F_A = \dfrac{D_{HA}}{D_{DA}}$

By substituting the expression for the local concentration in the Langmuir environment and by plugging Equations C.9 and C.10 into equation C.6, Equations C.11 and C.12 are derived.

$$N_A = \frac{k_{DA}D_{DA}}{l}\left[\left(f_{A2} - f_{A1}\right) + \frac{F_A K_A f_{A2}}{1 + b_A f_{A2} + b_B f_{B2}} - \frac{F_A K_A f_{A1}}{1 + b_A f_{A1} + b_B f_{B1}}\right] \qquad \text{C.11}$$

$$N_B = \frac{k_{DB}D_{DB}}{l}\left[\left(f_{B2} - f_{B1}\right) + \frac{F_B K_B f_{B2}}{1 + b_A f_{A2} + b_B f_{B2}} - \frac{F_B K_B f_{B1}}{1 + b_A f_{A1} + b_B f_{B1}}\right] \qquad \text{C.12}$$

Where $K_A = \dfrac{C_{HA}' b_A}{k_{DA}}$ and $K_B = \dfrac{C_{HB}' b_B}{k_{DB}}$

Therefore, the permeability coefficients of components A and B can be derived as shown in Equations C.13 and C.14.

$$P_A = k_{DA}D_{DA}\left[1 + \frac{F_A K_A f_{A2}/\left(f_{A2} - f_{A1}\right)}{1 + b_A f_{A2} + b_B f_{B2}} - \frac{F_A K_A f_{A1}/\left(f_{A2} - f_{A1}\right)}{1 + b_A f_{A1} + b_B f_{B1}}\right] \qquad \text{C.13}$$

$$P_B = k_{DB}D_{DB}\left[1 + \frac{F_B K_B f_{B2}/\left(f_{B2} - f_{B1}\right)}{1 + b_A f_{A2} + b_B f_{B2}} - \frac{F_B K_B f_{B1}/\left(f_{B2} - f_{B1}\right)}{1 + b_A f_{A1} + b_B f_{B1}}\right] \qquad \text{C.14}$$

Equations C.13 and C.14 can be rearranged to yield the following expressions (Equations 2.41 and 2.42 as shown in Chapter 2).

$$P_A = \frac{k_{D_A} D_{D_A}}{\left(f_{A2} - f_{A1}\right)} \left[\left(f_{A2} - f_{A1}\right) + F_A K_A \left(\frac{f_{A2}}{1 + b_A f_{A2} + b_B f_{B2}} - \frac{f_{A1}}{1 + b_A f_{A1} + b_B f_{B1}} \right) \right] \qquad \text{C.15}$$

$$P_B = \frac{k_{D_B} D_{D_B}}{\left(f_{B2} - f_{B1}\right)} \left[\left(f_{B2} - f_{B1}\right) + F_B K_B \left(\frac{f_{B2}}{1 + b_A f_{A2} + b_B f_{B2}} - \frac{f_{B1}}{1 + b_A f_{A1} + b_B f_{B1}} \right) \right] \qquad \text{C.16}$$

In the limit that the permeate pressure is neglected, Equations C.13 and C.14 can be simplified to give Equations C.17 and C.18.

$$P_A = k_{DA} D_{DA} \left[1 + \frac{F_A K_A}{1 + b_A f_{A2} + b_B f_{B2}} \right] \qquad \text{C.17}$$

$$P_B = k_{DB} D_{DB} \left[1 + \frac{F_B K_B}{1 + b_A f_{A2} + b_B f_{B2}} \right] \qquad \text{C.18}$$

C.2 Ternary Gas Mixture Expressions (Zero and Nonzero Permeate Pressure)

The above equations are valid for a binary gas mixture. However, in ternary gas mixtures, those equations are modified to account for an additional component. In this case, Equations C.7 and C.8 become

$$C_{HA} = \frac{b_A C'_{HA} f_A}{1 + b_A f_A + b_B f_B + b_C f_C} \qquad \text{C.19}$$

$$C_{HB} = \frac{b_B C'_{HB} f_B}{1 + b_A f_A + b_B f_B + b_C f_C} \qquad \text{C.20}$$

$$C_{HC} = \frac{b_C C'_{HC} f_C}{1 + b_A f_A + b_B f_B + b_C f_C} \qquad \text{C.21}$$

With these expressions in mind, the permeability coefficient can be derived in the same

manner as it was done for the binary case to yield Equations C.22-C.24.

$$P_A = \frac{k_{D_A} D_{D_A}}{\left(f_{A2} - f_{A1}\right)} \left[\left(f_{A2} - f_{A1}\right) + F_A K_A \left(\frac{f_{A2}}{1 + b_A f_{A2} + b_B f_{B2} + + b_C f_{C2}} - \frac{f_{A1}}{1 + b_A f_{A1} + b_B f_{B1} + b_C f_{C1}} \right) \right] \quad \text{C.22}$$

$$P_B = \frac{k_{D_B} D_{D_B}}{\left(f_{B2} - f_{B1}\right)} \left[\left(f_{B2} - f_{B1}\right) + F_B K_B \left(\frac{f_{B2}}{1 + b_A f_{A2} + b_B f_{B2} + b_C f_{C2}} - \frac{f_{B1}}{1 + b_A f_{A1} + b_B f_{B1} + b_C f_{C1}} \right) \right] \quad \text{C.23}$$

$$P_C = \frac{k_{D_C} D_{D_C}}{\left(f_{C2} - f_{C1}\right)} \left[\left(f_{C2} - f_{C1}\right) + F_C K_C \left(\frac{f_{C2}}{1 + b_A f_{A2} + b_B f_{B2} + b_C f_{C2}} - \frac{f_{C1}}{1 + b_A f_{A1} + b_B f_{B1} + b_C f_{C1}} \right) \right] \quad \text{C.24}$$

If the downstream pressure is negligible, Equations C.22-C.24 reduce to Equations C.25-

C.27.

$$P_A = k_{D_A} D_{D_A} \left[1 + \frac{F_A K_A}{1 + b_A f_{A2} + b_B f_{B2} + + b_C f_{C2}} \right] \qquad \text{C.25}$$

$$P_B = k_{D_B} D_{D_B} \left[1 + \frac{F_B K_B}{1 + b_A f_{A2} + b_B f_{B2} + b_C f_{C2}} \right] \qquad \text{C.26}$$

$$P_C = k_{D_C} D_{D_C} \left[1 + \frac{F_C K_C}{1 + b_A f_{A2} + b_B f_{B2} + b_C f_{C2}} \right] \qquad \text{C.27}$$

C.3 References

[1] W.J. Koros, R.T. Chern, V. Stannett, H.B. Hopfenberg, A model for permeation of mixed gases and vapors in glassy polymers, Journal of Polymer Science: Polymer Physics Edition, 19 (1981) 1513-1530.

[2] W.J. Koros, Model for Sorption of Mixed Gases in Glassy-Polymers, J Polym Sci Pol Phys, 18 (1980) 981-992.

APPENDIX D: COMPRESSIBILITY FACTOR AND FUGACITY COEFFICIENTS

D.1 Compressibility Factor

The ideal gas law provides a simple way of describing fluid behavior. However, to determine a more quantitative description of real-fluid behavior, the compressibility factor z is used. Equations of state (EOS) are used to account for those deviations from ideal behavior. The Peng-Robinson (PR) EOS was used in this study as it is often used to determine the compressibility factor [1-3] as shown in Equation D.1.

$$P = \frac{RT}{v-b} - \frac{a(T)}{v(v+b)+b(v-b)}$$
D.1

For a pure fluid, constant b is given by

$$b = 0.07780 \frac{RT_c}{P_c}$$
D.2

while $a(T)$ is a function of temperature and is defined as

$$a(T) = a(T_c)\alpha(T)$$
D.3

$$a(T_c) = 0.45724 \frac{(RT_c)^2}{P_c}$$
D.4

$$\alpha(T) = \left[1 + \left(0.37464 + 1.54226\omega - 0.26992\omega^2\right)\left(1 - \sqrt{T/T_c}\right)\right]^2$$
D.5

$$0 \leq \omega \leq 0.5$$

ω is the acentric factor, T_c and P_c are the gas critical temperature and pressure, respectively. The acentric factor is a measure of the non-sphericity of molecules.

Equation D.1 can be rearranged to yield Equation D.6, which is solved iteratively to determine the compressibility factor. Table D.1 shows the critical parameters and acentric factors of all gases used in this study.

$$Z^3 - (1-B)Z^2 + (A - 3B^2 - 2B)Z - (AB - B^2 - B^3) = 0 \qquad \text{D.6}$$

$$A = \frac{a\alpha P}{(RT)^2} \qquad\qquad z = \frac{Pv}{RT} \qquad\qquad B = \frac{bP}{RT}$$

Table D.1: Critical parameters of gases used in this study [4]

	T_c (K)	T_c (psi)	Acentric Factor ω
Methane (CH_4)	190.6	667.2	0.008
Carbon Dioxide (CO_2)	304.2	1070	0.225
Hydrogen Sulfide (H_2S)	373.2	1296	0.10

By applying these equations, the compressibility factor of each penetrant at different temperatures and pressures can be calculated as showed in Figures D.1-D.3. Since H_2S is highly condensable, its saturation pressure was considered during experiments. Table D.2 shows the saturation pressure of H_2S at different experimental temperatures, calculated using the Antoine equation as shown in Equation D.7 [5].

$$\log_{10} P^{sat} (bar) = A - \frac{B}{T(K) + C} \qquad \text{D.7}$$

$$A = 4.52887, B = 958.587, \ C = -0.539 \quad (T = 212.8 - 349.5K)$$

Table D.2: Saturation pressure of H₂S at different temperatures

P$_{sat}$ (psia)	T=35°C	T=50°C	T=60°C
Hydrogen Sulfide (H$_2$S)	375.1	523.6	643.2
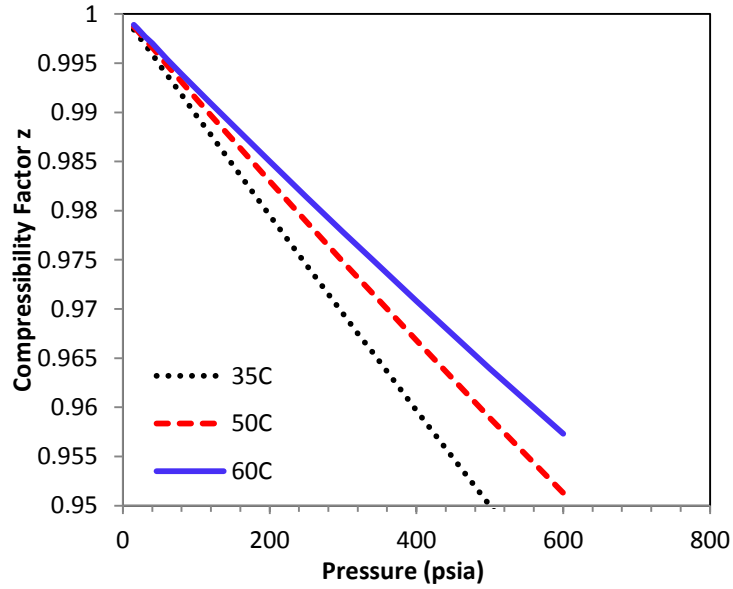
Figure D.1. Compressibility Factor of CH$_4$ at different temperatures.
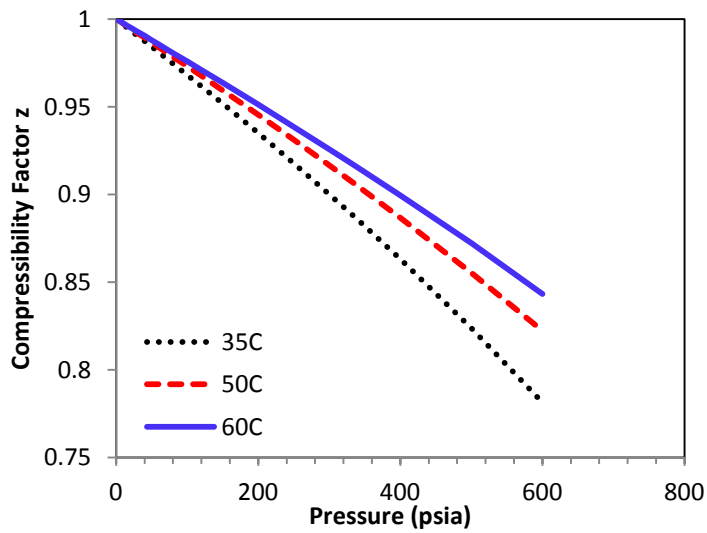
Figure D.2. Compressibility Factor of CO$_2$ at different temperatures.
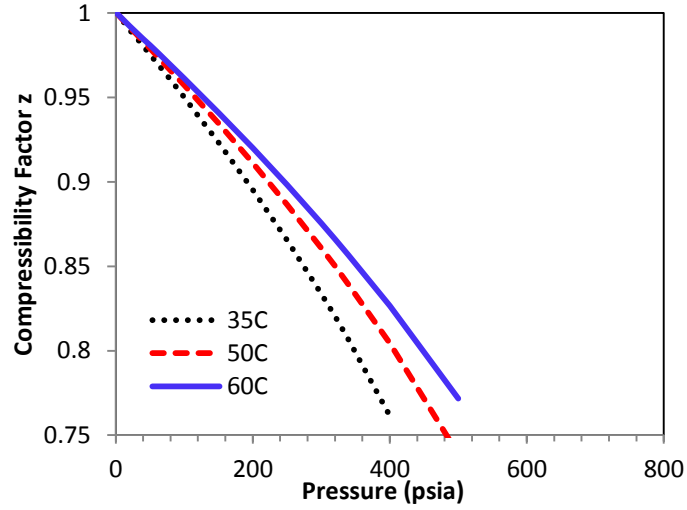
Figure D.3. Compressibility Factor of H_2S at different temperatures.

D.2 Pure Gas Fugacity Coefficient

The fugacity coefficient of pure species was calculated from the PR fugacity using the Lewis fugacity rule as shown in the equations below [2, 3].

$$\ln \varphi_i = z_i - 1 - \ln(z_i - B_i) - \frac{A_i}{2.8284 B_i} \ln\left(\frac{z_i + 2.4142 B_i}{z_i - 0.4142 B_i}\right) \qquad \text{D.8}$$

$$z_i = \frac{P v_i}{RT} \qquad A_i = \frac{a_i \alpha_i P}{(RT)^2} \qquad B_i = \frac{b_i P}{RT}$$

$$a_i = 0.45724 \frac{(RT_{c,i})^2}{P_{c,i}} \qquad b_i = 0.07780 \frac{RT_{c,i}}{P_{c,i}}$$

$$\alpha_i = \left[1 + \left(0.37464 + 1.54226 \omega_i - 0.26992 \omega_i^2\right)\left(1 - \sqrt{T/T_{c,i}}\right)\right]^2$$

v_i can be solved directly from the EOS shown in Equation D.1. The fugacity coefficient of CH_4, CO_2, and H_2S were calculated using these equations and are shown in Figure D.4.
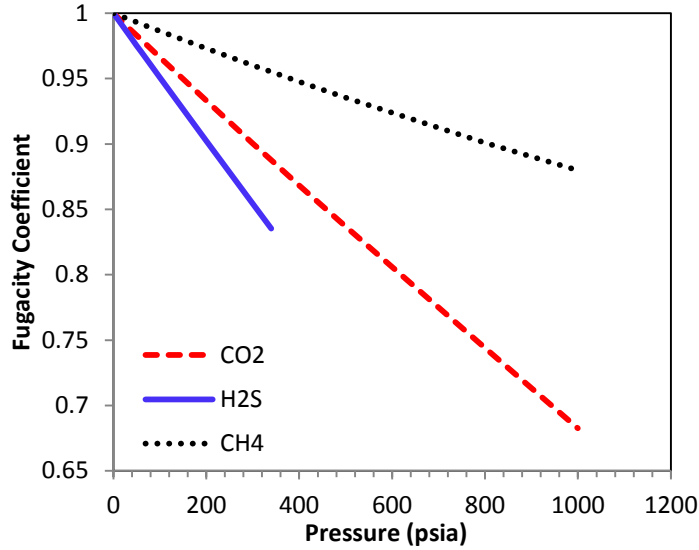
Figure D.4. Pure component fugacity coefficients of species used in this study.

D.3 Mixed Gas Fugacity Coefficient

The fugacity coefficient of each species in a mixture was calculated from the full rigor

PR EOS using ThermoSolver via Equation D.9 [2, 3].

$$\ln \hat{\varphi}_i = \frac{B_i}{B}(z-1) - \ln(z-B) - \frac{A}{2.8284B}\left[\frac{B_i}{B} - \frac{2}{a\alpha}\sum_j y_j (a\alpha)_{ij}\right]\ln\left(\frac{z+2.4142B}{z-0.4142B}\right) \quad \text{D.9}$$

$$A = \sum\sum y_j y_k A_{jk} \qquad A_{jk} = \sqrt{A_{jj} A_{kk}} \qquad A_{jj} = \frac{(a\alpha)_{jj} P}{(RT)^2}$$

$$B = \frac{bP}{RT} \qquad B_i = \frac{b_i P}{RT} \qquad b = \sum y_j b_j$$

$$(a\alpha)_{jk} = \sqrt{(a\alpha)_{jj}(a\alpha)_{kk}} \qquad (a\alpha)_{jj} = a_j\alpha_j \qquad a\alpha = \sum\sum y_j y_k (a\alpha)_{jk}$$

$$\alpha_j = \left[1 + \left(0.37464 + 1.54226\omega_j - 0.26992\omega_j^2\right)\left(1 - \sqrt{T/T_{c,j}}\right)\right]^2$$

The fugacity coefficient of CH_4, CO_2, and H_2S in various mixtures considered in this study is shown in Figure D.5.
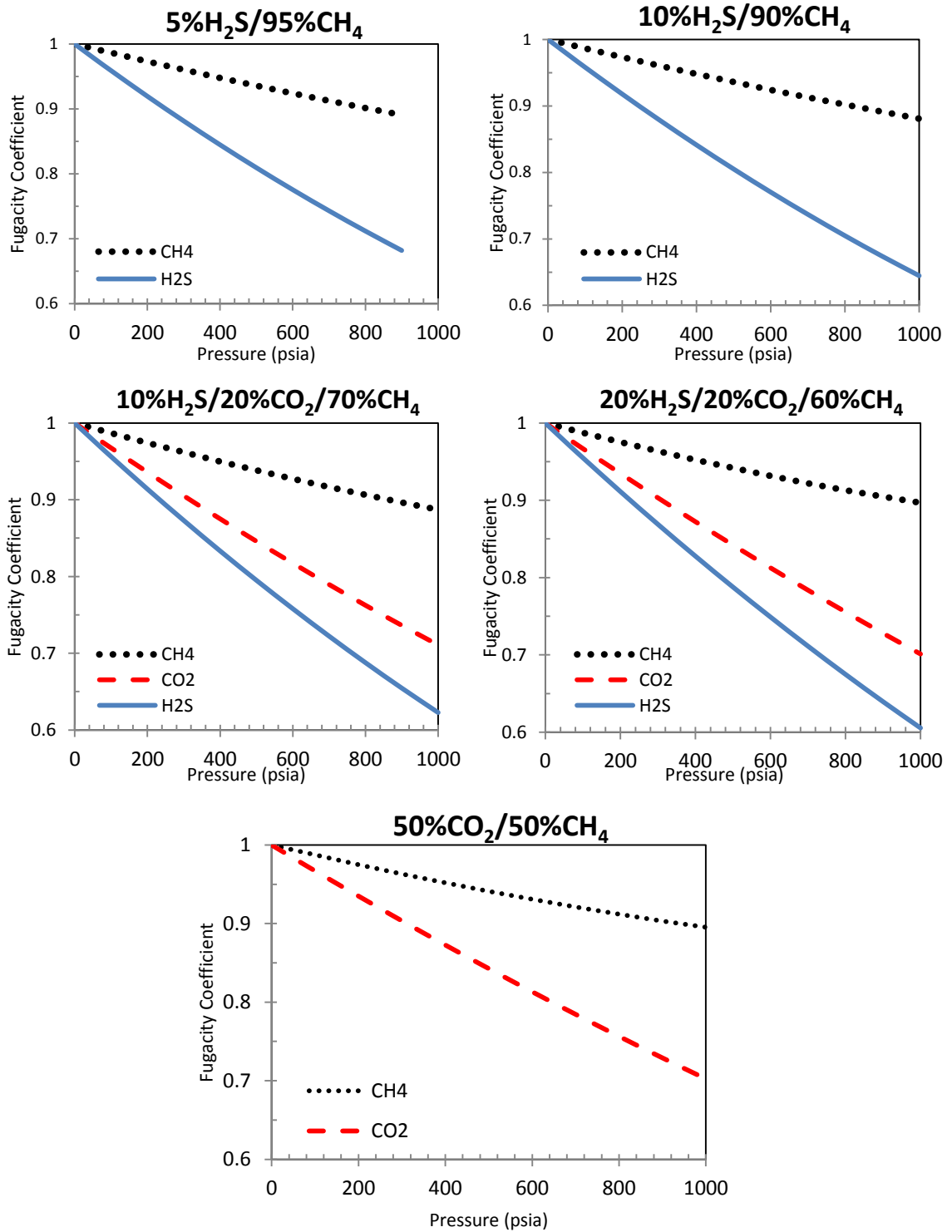
Figure D.5. Fugacity coefficients of species in various mixtures used in this study.

D.4 References

[1] D. Peng, D.B. Robinson, New 2-Constant Equation of State, Ind Eng Chem Fund, 15 (1976) 59-64.

[2] J.M. Smith, H.C. Van Ness, M.M. Abbott, Introduction to chemical engineering thermodynamics, McGraw-Hill, 2005.

[3] J.M. Prausnitz, R.N. Lichtenthaler, E.G. de Azevedo, Molecular Thermodynamics of Fluid-Phase Equilibria, Pearson Education, 1998.

[4] B. Poling, J. Prausnitz, J.O. Connell, The Properties of Gases and Liquids, Mcgraw-hill, 2000.

[5] D.R. Stull, Vapor Pressure of Pure Substances - Organic Compounds, Ind Eng Chem, 39 (1947) 517-540.

APPENDIX E: FILM DENSITY CALCULATIONS

As mentioned in Chapter 3, the density of the polymer films used in this study was measured using a Techne DC-1 density gradient column. The column was filled with both a low and a high density $Ca(NO_3)_2$ solutions, and calibrated weights spanning the density range selected were added in the column. The position of those calibrated weights was recorded and is tabulated in Table E.1. The density of those calibrated weights was plotted against their position in the column as shown in Figure E.1 to ensure the linearity of the column. Once an approximately linear density gradient was established, the samples were introduced. The position of those films in the columns was recorded and the density of the samples was determined based on the known equation in Figure E.1.

Table E.1: Position of calibrated weights in column

Column Height (cm)	Bead Density
0.5	1.3193
8.75	1.3006
15.5	1.2900
20.75	1.2700
25	1.2598
40	1.2202
52.75	1.1901
66.5	1.1494

Three different pieces of the same sample type were introduced into the column for comparison and error estimates. Table E.2 lists all the different positions that were recorded for a set of samples along with the calculated density using the equation of Figure E.1.
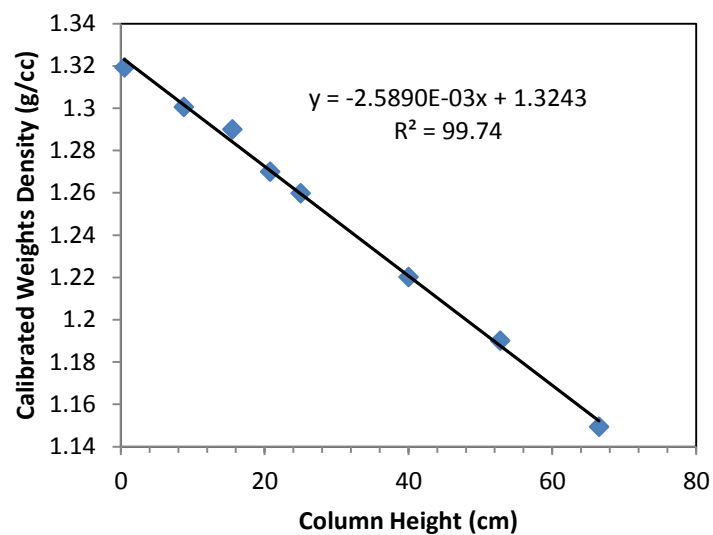
Figure E.1. Density Calibration Plot.

Table E.2: Position of neat CA and GCV-Modified CA samples in the column

Column Height (cm)	Density (Neat CA)	Column Height (cm)	GCV-Modified CA
4.25	1.3133	**19.80**	1.2730
4.60	1.3124	**19.45**	1.2739
5.45	1.3102	**21.35**	1.2690
Average	1.3120	**Average**	1.2720

APPENDIX F: SAMPLE CALCULATIONS

F.1 Pure Gas Calculations

The permeability coefficient of each gas was calculated from the steady-state rate of permeation of penetrants based on the data obtained from pressure vs. time experiments. As an example, Figure F.1 shows the data recorded from a CO_2 permeability measurement in neat cellulose acetate. This example will show the typical process taken to obtain the permeability coefficient.
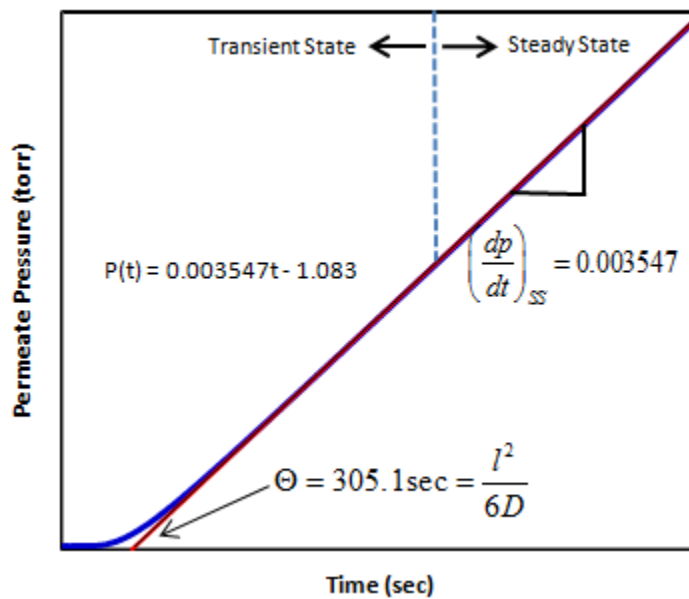
Figure F.1. Example of pressure vs. time plot for permeability measurement (CO_2 in neat CA).

From the steady-state fit equation of Figure F.1, the time lag was calculated as the time-intercept as follows

$$P(\Theta) = 0.003547\Theta - 1.083 = 0$$

$$\Theta = \frac{1.083}{0.003547} = 305.1\,\text{sec}$$

Based on this value of the time lag, the diffusion coefficient was calculated using Equation 3.3 as follows

$$D_{CO_2} = \frac{l^2}{6\Theta} = \frac{\left(3.795 \times 10^{-3}\,cm\right)^2}{6 \times 305.1\,\text{sec}} = 7.87 \times 10^{-9}\,\frac{cm^2}{\text{sec}}$$

As mentioned in Chapter 3, the following general expression was used to calculate the permeability coefficient.

$$P(Barrer) = \frac{\left\{\left(\dfrac{dp}{dt}\right)_{SS} - \left(\dfrac{dp}{dt}\right)_{leak}\right\}\left(\dfrac{torr}{\text{sec}}\right) \times V_d(cm^3) \times l(cm) \times V_{STP}\left(\dfrac{cm^3(STP)}{mol}\right)}{\Delta f(psia) \times \left(\dfrac{psia}{5.1715cmHg}\right) \times R\left(\dfrac{cm^3 torr}{mol.K}\right) \times T(K) \times A(cm^2) \times 1 \times 10^{-10}\left(\dfrac{cm^3(STP).cm}{cmHg.cm}\right)}$$

V_d : Downstream volume

V_{STP} : Standard molar volume $\cong 22{,}413$ cm^3(STP)/mol

l : Membrane thickness

R : Universal gas constant $\cong 62{,}356$ cm^{3}torr/mol K

By further simplifying the above equation, the following expressions are obtained.

$$P_i(Barrer) = \frac{6.95 \times 10^8 \times \left\{\left(\dfrac{dp}{dt}\right)_{SS} - \left(\dfrac{dp}{dt}\right)_{leak}\right\}\left(\dfrac{torr}{\text{sec}}\right) \times V_d(cm^3) \times l(cm)}{\left(f_{i,upstream} - f_{i,downstream}\right)(psia) \times T(K) \times A(cm^2)}$$

$$P_i(Barrer) = \frac{6.95 \times 10^8 \times \left\{ \left(\dfrac{dp}{dt}\right)_{SS} - \left(\dfrac{dp}{dt}\right)_{leak} \right\} \left(\dfrac{torr}{\sec}\right) \times V_d(cm^3) \times l(cm)}{\left(\varphi_{i,u} \times p_{T,u} - \varphi_{i,d} \times p_{T,d}\right)(psia) \times T(K) \times A(cm^2)}$$

Assuming that the downstream pressure is negligible, the permeability coefficient was calculated using the parameters of Table F.1.

Table F.1: Parameters used in the pure gas permeability calculation example

Thickness (cm)	A (cm²)	V$_d$ (cm³)	Temperature (K)	Leak Rate (torr/sec)
3.795x10^{-3}	1.756	15.8	308.15	9.17x10^{-6}

$$P_{CO_2}(Barrer) = \frac{6.95 \times 10^8 \times \left(3.55 \times 10^{-3} - 9.17 \times 10^{-6}\right)\left(\dfrac{torr}{\sec}\right) \times 15.8 cm^3 \times 3.795 \times 10^{-3} cm}{\left(0.9778 \times 65.4 - 0\right) psia \times 308.15 K \times 1.756 cm^2}$$

$$P_{CO_2} = 4.26 \; Barrer$$

A simple Matlab® code like the one shown below was written to execute these calculations.

```
function [P,theta,D]= permeabilitypure(dpdt,leaktest,upres,phiu,temp,thickness,area)
%%This code takes in the pressure rise, leaktest value, total upstream
%%pressure, fugacity coefficient, system temperature, film thickness, and
%%area and return the permeability coefficient, the time lag, and the
%%diffusion coefficient

dvol=15.8;R=62356;
temp=temp+273.15;  %%This converts the temperature from celsius to Kelvin
thickness=thickness/10; %%converts the thickness from mm to cm

dpdt_real=dpdt-leaktest;
upres=upres*phiu; %%this adjusts the pressure for fugacity
dpdt_p=dpdt_real/upres;
dndt_p=(dpdt_p*dvol)/(R*temp*5.171);
rate_dp=dndt_p*22400;

P=(rate_dp*thickness)/(area*10^-10);
b=input('Enter y intercept b value:');%%y=mx+b
theta=b/dpdt;
D=thickness^2/(6*theta);
```

Figure F.2 Matlab® code used for pure gas permeability with vacuum downstream calculations.

F.2 Mixed Gas Calculations

As mentioned in Chapter 3, in the case of multicomponent permeation, with **vacuum downstream**, the pressure rise was adjusted to account for each gas contribution to the overall flow to give rise to Equation 3.8:

$$P_i(Barrer) = \frac{6.95 \times 10^8 \times y_i \left\{ \left(\dfrac{dp}{dt}\right)_{SS} - \left(\dfrac{dp}{dt}\right)_{leak} \right\} \left(\dfrac{torr}{\sec}\right) \times V_d(cm^3) \times l(cm)}{\left(x_i \, \hat{\varphi}_{i,u} \, p_u \right)(psia) \times T(K) \times A(cm^2)}$$

y_i : Mole fraction of component i downstream

x_i : Mole fraction of component i upstream

$\hat{\varphi}_{i,u}$: Fugacity of component i in the feed mixture at pressure p_u

p_u: Total Upstream Pressure

$f_{i,u} = x_i \, \hat{\varphi}_{i,u} \, p_u$

233

As an example, actual data from a permeation experiment of uncrosslinked PDMC in a binary 5%H_2S/95%CH_4 mixture. Table F.2 shows the general parameters used in the calculation and Table F.3 shows the upstream and downstream gas compositions, with the later obtained from the gas chromatograph.

Table F.2: Parameters used in the binary gas permeability calculation example

Thickness (cm)	A (cm²)	V_d (cm³)	Temperature (K)
6.16x10⁻³	2.13	46.9	308.15
Total Upstream Pressure (psia)	$\hat{\varphi}_{CH_4,u}$	$\hat{\varphi}_{H_2S,u}$	**Leak (torr/sec)**
98.7	0.9866	0.9596	2.28x10⁻⁶

Table F.3: Mole fraction of each species on the upstream and downstream sides in the binary gas permeability calculation example

Upstream (x_i)%		Downstream (y_i)%	
H₂S	**CH₄**	**H₂S**	**CH₄**
5.0	95.0	39.67	60.33

$$P_{CH_4}(Barrer) = \frac{6.95 \times 10^8 \times 0.6033 \left(4.01 \times 10^{-4} - 2.28 \times 10^{-6}\right)\left(\frac{torr}{sec}\right) \times 46.9 cm^3 \times 6.16 \times 10^{-3} cm}{\left(0.95 \times 0.9866 \times 98.7\right) psia \times 308.15 K \times 2.13 cm^2}$$

$$P_{CH_4} = 0.795$$

$$P_{H_2S}(Barrer) = \frac{6.95 \times 10^8 \times 0.3967 \left(4.01 \times 10^{-4} - 2.28 \times 10^{-6}\right)\left(\frac{torr}{sec}\right) \times 46.9 cm^3 \times 6.16 \times 10^{-3} cm}{\left(0.05 \times 0.9596 \times 98.7\right) psia \times 308.15 K \times 2.13 cm^2}$$

$$P_{H_2S} = 10.22$$

The separation factor was calculated using two methods as shown below to assess the extent of deviation when nonideal mixtures are considered.

$$\alpha^*_{H_2S/CH_4} = \frac{P_i}{P_j} = \frac{10.22}{0.795} = 12.85$$

$$\alpha^*_{H_2S/CH_4} = \left(\frac{y_{H_2S}}{y_{CH_4}}\right) \times \left(\frac{x_{CH_4}}{x_{H_2S}}\right) \times \left(\frac{\hat{\varphi}_{CH_4,u}}{\hat{\varphi}_{H_2S,u}}\right) = \left(\frac{0.3967}{0.6033}\right) \times \left(\frac{0.95}{0.05}\right) \times \left(\frac{0.9866}{0.9596}\right) = 12.84$$

If the fugacities are not taken into the account, the separation factor becomes

$$\alpha^*_{H_2S/CH_4} = \left(\frac{y_{H_2S}}{y_{CH_4}}\right) \times \left(\frac{x_{CH_4}}{x_{H_2S}}\right) = \left(\frac{0.3967}{0.6033}\right) \times \left(\frac{0.95}{0.05}\right) = 12.49$$

There is a 2.8% underestimation of the separation factor when the nonidealities of the system are not taken into account, this error may become more significant at higher pressures. Therefore, both methods were always used to compare the results. Ultimately, the results reported in this study were calculated using the method that accounted for fugacities as shown above. The Matlab® code used for calculations involving binary H_2S/CH_4 mixtures is shown in Figure F.3 and the code used for ternary mixtures of $H_2S/CO_2/CH_4$ is shown in Figure F.4. These codes were also used for vacuum calculations by simply setting the downstream pressure to zero. These codes were always adjusted depending on the conditions under study such as changes in downstream volume when using one permeation system versus another.

```matlab
function [Ph,Pm,selectivity]= permeabilitybinarynonvac(dpdt,leaktest,yhd,Pd,phihd,phimd,
Pu,yhu,phihu,phimu,area,thickness,temp)
%%This code takes in the pressure rise, leaktest value, mole fraction of
%%H2S downstream, downstream pressure, fugacity coefficient of H2S downstream,
%%fugacity coefficient of CH4 downstream, total average upstream
%%pressure, mole fraction of H2S upstream, fugacity coefficient of H2S
%%upstream,fugacity coefficient of CH4 upstream , film area, film thickness
%%and system temperature,and returns the permeability coefficient of H2S
%%and CH4, the selectivity
%%Pu is in psia, Pd is in torr, area is in cm^2

dvol=15.8;R=62356;vstp=22400;
temp=temp+273.15;
thickness=thickness*2.54/1000; %%mils converts to cm

ymd=1-yhd; %%this calculates the mole fraction of CH4 downstream
ymu=1-yhu; %%%%this calculates the mole fraction of CH4 upstream

term1=dvol*vstp*thickness;
term2=area*R*temp;

dpdt=dpdt-leaktest;

Pm=((term1/term2)*(14.5038/75.0061)*1e10*(ymd*dpdt))/((ymu*phimu*Pu)-(ymd*phimd*Pd*14.696/760));
Ph=((term1/term2)*(14.5038/75.0061)*1e10*(yhd*dpdt))/((yhu*phihu*Pu)-(yhd*phihd*Pd*14.696/760));

selectivity=Ph/Pm;

sel1=(yhd/ymd)*(ymu/yhu)*(phimu/phihu);
```

Figure F.3. Matlab® code used for permeability and selectivity calculations in binary H_2S/CH_4 mixtures.

```matlab
function [Pm,Pc,Ph,sel_cm,sel_hm,sel_ch]= permeabilityternarynonvac(dpdt,leaktest,ymd,ycd,phimd,
phicd,phihd,Pd,ymu,ycu,phimu,phicu,phihu,Pu,temp,thickness,area)
%%This code takes in the pressure rise, leaktest value, mole fraction of
%%CH4 downstream, mole fraction of CO2 downstream, fugacity coefficient of
%%CH4 downstream,fugacity coefficient of
%%CO2 downstream , fugacity coefficient of H2S downstream, downstream
%%pressure, mole fraction of CH4 upstream, mole fraction of CO2,
%%fugacity coefficient of CH4 upstream,fugacity coefficient of
%%CO2 upstream , fugacity coefficient of H2S upstream,total average upstream
%%pressure, system temperature,film thickness, and film area,
%%and returns the permeability coefficient of CH4, CO2, and H2S and their selectivity

dvol=15.8;R=62356;vstp=22400;
temp=temp+273.15;
thickness=thickness*2.54/1000; %%mils converts to cm
area=area*2.54^2/40000; %%converts to cm^2

yhd=1-ymd-ycd; %%H2S downstream mole fraction from GC
yhu=1-ymu-ycu; %%H2S upstream mole fraction from GC

term1=dvol*vstp*thickness;
term2=area*R*temp;

dpdt=dpdt-leaktest;

Pm=((term1/term2)*(14.5038/75.0061)*1e10*(ymd*dpdt))/((ymu*phimu*Pu)-(ymd*phimd*Pd*14.696/760));
Ph=((term1/term2)*(14.5038/75.0061)*1e10*(yhd*dpdt))/((yhu*phihu*Pu)-(yhd*phihd*Pd*14.696/760));
Pc=((term1/term2)*(14.5038/75.0061)*1e10*(ycd*dpdt))/((ycu*phicu*Pu)-(ycd*phicd*Pd*14.696/760));

sel_hm=Ph/Pm;
sel_cm=Pc/Pm;
sel_ch=Pc/Ph;


sfhm=(yhd/ymd)*(ymu/yhu); %%Another way to calculate selectivity for comparison
sfcm=(ycd/ymd)*(ymu/ycu);
sfch=(ycd/yhd)*(yhu/ycu);
```

Figure F.4. Matlab® code used for permeability and selectivity calculations in ternary $H_2S/CO_2/CH_4$ mixtures.

F.3 Pure Gas Sorption Calculations

As discussed previously, the concentration of sorbed species in a glassy polymer can be described using the dual-mode model. Figure F.5 shows real data of a CH_4 sorption isotherm in neat CA along with the dual-mode fit parameters.

237
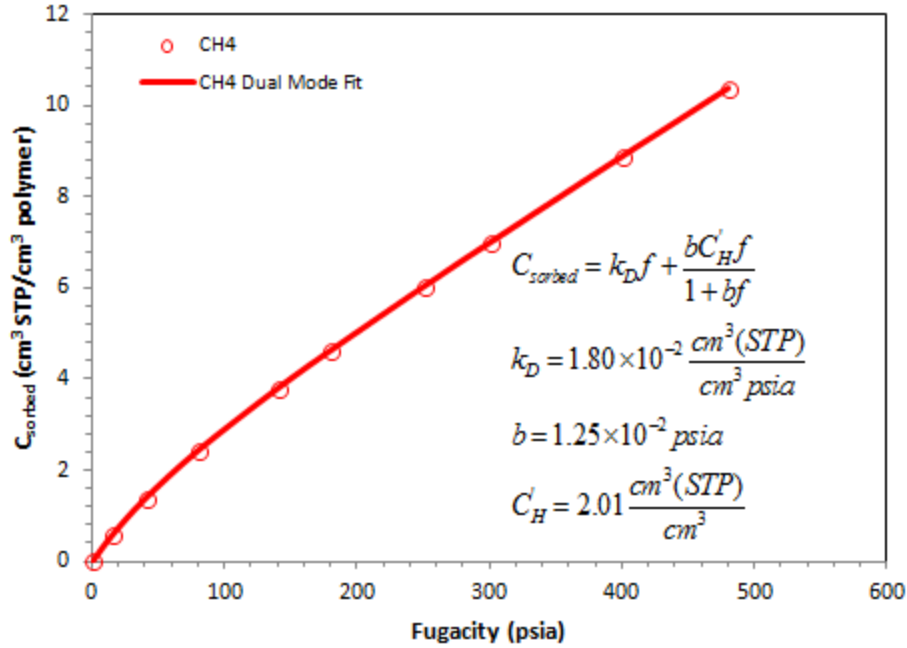
Figure F.5. Example of dual-mode fit parameters for CH_4 in neat cellulose acetate.

As an example, the concentration of sorbed penetrant at a fugacity of 65 psia can be calculated from these parameters.

$$C_{CH_4} = \left(1.80 \times 10^{-2} \frac{cm^3(STP)}{cm^3 \, psia} \times 65 \, psia\right) + \left(\frac{1.25 \times 10^{-2} \, psia^{-1} \times 2.01 \frac{cm^3(STP)}{cm^3} \times 65 \, psia}{1 + \left(1.25 \times 10^{-2} \, psia^{-1} \times 65 \, psia\right)}\right)$$

$$C_{CH_4} = 2.071 \frac{cm^3(STP)}{cm^3}$$

Similarly, the sorption coefficient can be calculated as

$$S_{CH_4} = \frac{C_{CH_4}}{f_{CH_4}} = \frac{2.071 \frac{cm^3(STP)}{cm^3}}{65 \, psia}$$

$$S_{CH_4} = 3.19 \times 10^{-2} \frac{cm^3(STP)}{cm^3 \, psia}$$

238

As discussed in Chapter 4 ad 6, in addition to the diffusivity obtained from the time lag, the diffusivity was also calculated using the sorption coefficient experimental value as shown below for CH_4 in neat CA:

$$P = DS$$

$$D_{CH_4} = \frac{P_{CH_4}}{S_{CH_4}} = 0.13 Barrer \times \frac{1 \times 10^{-10} cm^3 (STP) cm.cmHg^{-1} s^{-1} cm^{-2}}{1 Barrer} \times \frac{cm^3 psia}{3.19 \times 10^{-2} cm^3 (STP)} \times \frac{cmHg}{0.1934 psia}$$

$$D_{CH_4} = 2.11 \times 10^{-9} \frac{cm^2}{s}$$

Similarly, when the diffusion coefficient is obtained using the time lag from the permeation experiment, the sorption coefficient was calculated as shown below. In this example, the permeability and diffusivity of CH_4 in neat CA was used.

$$S_{CH_4} = \frac{P_{CH_4}}{D_{CH_4}} = 0.13 Barrer \times \frac{1 \times 10^{-10} cm^3 (STP) cm.cmHg^{-1} s^{-1} cm^{-2}}{1 Barrer} \times \frac{\sec}{1.95 \times 10^{-9} cm^2} \times \frac{cmHg}{0.1934 psia}$$

$$S_{CH_4} = 3.45 \times 10^{-2} \frac{cm^3 (STP)}{cm^3 psia}$$

F.3 Determination of Local Diffusion Coefficients D_D and D_H

The permeability of a penetrant was defined previously using the dual-mode model as a function of local diffusion coefficients in the Henry and Langmuir environments as

$$P = k_D D_D + \frac{bC_H' D_H}{1 + bf}$$

$$P = \left(\frac{1}{1 + bf} \right) \times bC_H' D_H + k_D D_D \qquad \text{F.1}$$

239

Therefore, the local diffusion coefficients D_D and D_H were obtained for CH_4 in CA for example by plotting permeability versus $1/(+bf)$ as shown in Figure F.6 using the value of the affinity constant b obtained from the sorption experiments (Table F.4).

Table F.4: Sorption parameters of CH_4 in neat CA

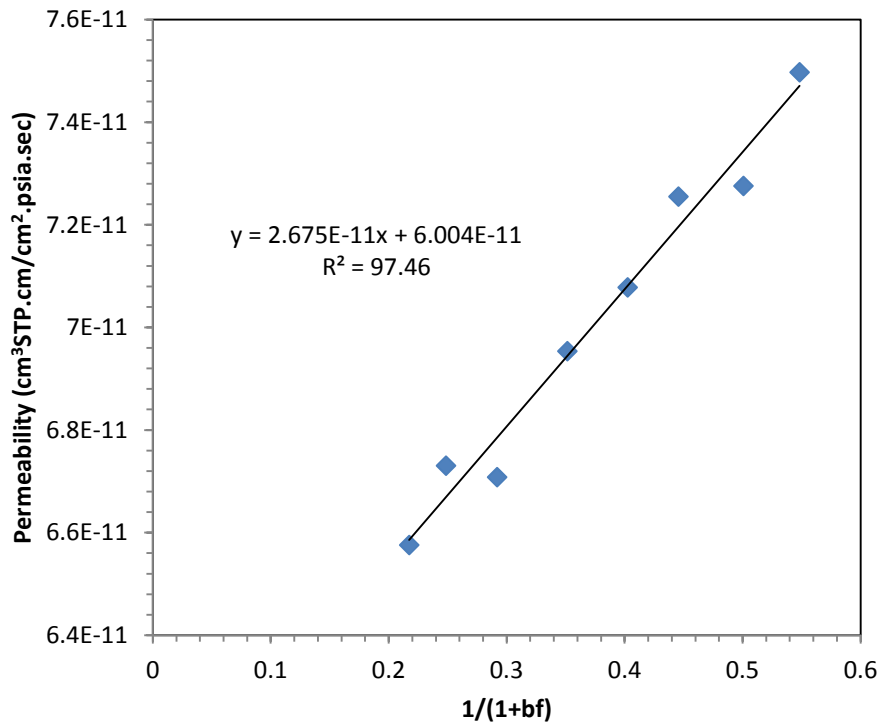| k_d (cm^3(STP)/cm^{3}psia)	b (1/psia)	C_H'(cm^3(STP)/cm^3)
0.0180	0.0125	2.0100

Figure F.6: Plot of permeability versus $1/(1+bf)$ to determine local diffusion coefficients.

The diffusion coefficient in the Langmuir region or "holes" D_H was calculated from the slope of the plot of Figure F.6.

$$Slope = bC'_H D_H = 2.675 \times 10^{-11} \frac{cm^2}{\sec}$$

$$D_H = \frac{2.675 \times 10^{-11} \dfrac{cm^2}{\sec}}{1.25 \times 10^{-2} \, psia^{-1} \times 2.01 \dfrac{cm^3(STP)}{cm^3}}$$

$$D_H = 1.06 \times 10^{-9} \frac{cm^2}{\sec}$$

Similarly, the diffusion coefficient in the dissolved or Henry's region D_D was calculated from the intercept of the plot of Figure F.6.

$$Intercept = k_D D_D = 6.004 \times 10^{-11} \frac{cm^2}{\sec}$$

$$D_D = \frac{6.004 \times 10^{-11} \dfrac{cm^2}{\sec}}{1.80 \times 10^{-2} \dfrac{cm^3(STP)}{cm^3 \, psia}}$$

$$D_D = 3.34 \times 10^{-9} \frac{cm^2}{\sec}$$

The coefficient K, which measures the amount of penetrant immobilized in the Langmuir environment relative to the amount dissolved, was calculated as shown below.

$$K = \frac{bC'_H}{k_D} = \frac{1.25 \times 10^{-2} \, psia^{-1} \times 2.01 \dfrac{cm^3(STP)}{cm^3}}{1.80 \times 10^{-2} \dfrac{cm^3(STP)}{cm^3 \, psia}} = 1.39$$

The coefficient F, which is the ratio of the diffusivity in the microvoids to the diffusivity in the Henry's region, a measure of the degree of immobilization, was calculated viz.,

$$F = \frac{D_H}{D_D} = \frac{1.06 \times 10^{-9} \dfrac{cm^2}{\sec}}{3.34 \times 10^{-9} \dfrac{cm^2}{\sec}} = 0.32$$

The effective diffusion coefficient as discussed in Chapter 4 and 6 was calculated using these parameters assuming a fugacity of 65 psia.

$$D_{eff} = D_D \left[\frac{1 + FK/(1+bf)^2}{1 + K/(1+bf)^2} \right]$$

$$D_{eff} = 3.34 \times 10^{-9} \left[\frac{1 + \dfrac{0.32 \times 1.39}{\left(1 + 1.25 \times 10^{-2} \times 65\right)^2}}{1 + \dfrac{0.32 \times 1.39}{\left(1 + 1.25 \times 10^{-2} \times 65\right)^2}} \right]$$

$$D_{eff} = 2.66 \times 10^{-9} \frac{cm^2}{\sec}$$

The dual-mode permeability coefficient was calculated as follows

$$P = k_D D_D \left[1 + \frac{FK}{1+bf} \right] = k_D D_D + \frac{bC_H' D_D}{1+bf}$$

$$P_{CH_4} = \left(1.80 \times 10^{-2} \frac{cm^3(STP)}{cm^3 \, psia} \times 3.34 \times 10^{-9} \frac{cm^2}{s} \right) + \left(\frac{1.25 \times 10^{-2} \, psia^{-1} \times 2.01 \dfrac{cm^3(STP)}{cm^3} \times 1.06 \times 10^{-9} \dfrac{cm^2}{s}}{1 + \left(1.25 \times 10^{-2} \, psia^{-1} \times 65 \, psia\right)} \right)$$

$$P_{CH_4} = \frac{7.48 \times 10^{-11} cm^3(STP)cm}{cm^2.s.psia} \times \frac{1 Barrer}{1 \times 10^{-10} cm^3(STP)cm.cmHg^{-1}s^{-1}cm^{-2}} \times \frac{0.1934 \, psia}{cmHg}$$

$$P_{CH_4} = 0.14 \, Barrer$$

F.4 Temperature Dependence Calculations

In Chapter 4 and 6, the activation energy of permeation and diffusion, and enthalpy of sorption were presented. This section shows an example of how those energies were obtained.

$$S = S_o \exp\left(\frac{-\Delta H_S}{RT}\right) \qquad 2.28$$

$$P = P_o \exp\left(\frac{-E_p}{RT}\right) \qquad 2.30$$

Rearranging Equations 2.28 and 2.30 give the following expressions

$$\ln S = \left(\frac{-\Delta H_S}{R}\right)\frac{1}{T} + \ln S_o \qquad F.2$$

$$\ln P = \left(\frac{-E_P}{R}\right)\frac{1}{T} + \ln P_o \qquad F.3$$

From these equations, a plot of ln S versus 1/T and ln P versus 1/T were constructed.

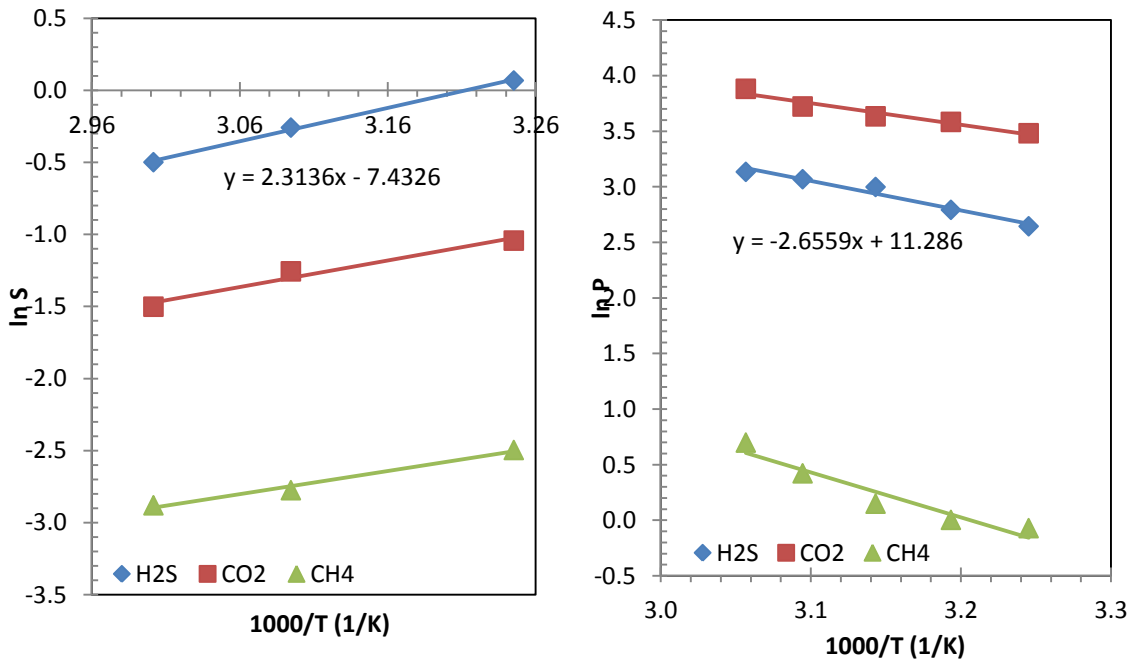Figure F.7: Plot of ln S and ln P versus 1000/T for uncrosslinked PDMC.

243

The activation energy of permeation and enthalpy of sorption of H_2S for example was calculated from the slope of the line of Figure F.6, given $R = 8.314 kJ / mol$.

$$slope = \frac{-\Delta H_S}{R} = 2.3136$$

$$\Delta H_S = -19.23 \frac{kJ}{mol}$$

$$slope = \frac{-E_P}{R} = -2.6659$$

$$E_P = 22.08 \frac{kJ}{mol}$$

Therefore, the activation energy of diffusion can be calculated

$$E_d = E_P - \Delta H_S = 22.08 - (-19.23)$$

$$E_d = 41.31 \frac{kJ}{mol}$$

Each pre-exponential factor P_o and S_o can be calculated using those values of the activation energies and known values of P and T. Since the permeability is the product of the diffusion coefficient and the sorption coefficient, the pre-exponential factor of the diffusivity was calculated using the equation below

$$P_o = D_o S_o$$

Using those values of the pre-exponential factors, general expressions of the diffusivity, permeability, and sorption coefficient as a function of temperature were obtained.

F.5 Bulk Flow Contribution Simulation Calculations

A sample calculation for predicting 20/20/60 $H_2S/CO_2/CH_4$ mixed-gas permeation data in crosslinked PDMC using pure H_2S, CO_2, and CH_4 data is illustrated in this section. Table F.5 summarizes the parameters used this calculation. As an example, a total upstream pressure of 400 psia with zero vacuum downstream pressure is illustrated.

Table F.5: Crosslinked PDMC parameters used in the bulk flow simulation example

	CH$_4$	CO$_2$	H$_2$S
D_D (cm^2/sec)	1.49E-08	2.40E-07	1.91E-08
D_H (cm^2/sec)	8.95E-10	1.98E-08	4.45E-09
k_d	7.85E-02	1.51E-01	5.30E-01
b	3.23E-03	4.67E-02	2.65E-01
C_H'	24.63	41.48	37.80
K	1.01	12.83	18.90
$F=D_H/D_D$	0.060	0.083	0.233
M (g/mol)	16.04	44.01	34.08
$k_D D_D$	1.17E-9	3.62E-8	1.01E-8
ϕ	0.9519	0.8727	0.8278
Fugacity (psia)	228.46	69.82	66.22

Based on these parameters, the mobile concentration of H_2S, CO_2, and CH_4 were first computed using Equations A.45-A.47.

$$w_{CO_2}^m = \frac{k_{D_{CO_2}} f_{CO_2} M_{CO_2}}{22400\rho} \left(1 + \frac{F_{CO_2} K_{CO_2}}{1 + b_{CO_2} f_{CO_2} + b_{H_2S} f_{H_2S} + b_{CH_4} f_{CH_4}}\right)$$

$$w_{CO_2}^m = \frac{0.151 \times 69.82 \times 44}{22400 \times 1.402} \left(1 + \frac{0.083 \times 12.83}{1 + (0.0467 \times 69.82) + (0.265 \times 66.22) + (3.23 \times 10^{-3} \times 228.46)}\right)$$

$$w_{CO_2}^m = 0.0148 \text{ g/g}$$

$$w_{H_2S}^m = \frac{k_{D_{H_2S}} f_{H_2S} M_{H_2S}}{22400\rho}\left(1+\frac{F_{H_2S} K_{H_2S}}{1+b_{CO_2} f_{CO_2} + b_{H_2S} f_{H_2S} + b_{CH_4} f_{CH_4}}\right)$$

$$w_{H_2S}^m = \frac{0.53\times 66.22\times 34}{22400\times 1.402}\left(1+\frac{0.233\times 18.90}{1+(0.0467\times 69.82)+(0.265\times 66.22)+(3.23\times 10^{-3}\times 228.46)}\right)$$

$$w_{H_2S}^m = 0.0455 \text{ g/g}$$

$$w_{CH_4}^m = \frac{k_{D_{CH_4}} f_{CH_4} M_{CH_4}}{22400\rho}\left(1+\frac{F_{CH_4} K_{CH_4}}{1+b_{CO_2} f_{CO_2} + b_{H_2S} f_{H_2S} + b_{CH_4} f_{CH_4}}\right)$$

$$w_{CH_4}^m = \frac{0.0785\times 228.46\times 16}{22400\times 1.402}\left(1+\frac{0.060\times 1.01}{1+(0.0467\times 69.82)+(0.265\times 66.22)+(3.23\times 10^{-3}\times 228.46)}\right)$$

$$w_{CH_4}^m = 0.0092 \text{ g/g}$$

From these values of the mobile concentrations, the thickness-normalized flux can be obtained via Equations A.21-A.23. However, there are 3 equations with 6 unknowns (n_A, n_B, n_C, r, p, and p) but some of these unknowns are dependents. Trial and error will be required to solve these equations. First, initial guesses of r, p, and q need to be computed. Equations C.25-C.27 can be used as first approximations for r, p, and q.

$$P_{CO_2}^* = k_{D_{CO_2}} D_{D_{CO_2}}\left(1+\frac{F_{CO_2} K_{CO_2}}{1+b_{CO_2} f_{CO_2} + b_{H_2S} f_{H_2S} + b_{CH_4} f_{CH_4}}\right) \qquad \text{C.25}$$

$$P_{CO_2}^* = 3.62\times 10^{-8}\times\left(1+\frac{0.083\times 12.83}{1+(0.0467\times 69.82)+(0.265\times 66.22)+(3.23\times 10^{-3}\times 228.46)}\right)\times\frac{0.1934}{1\times 10^{-10}}$$

$$P_{CO_2}^* = 73.32 \text{ Barrer}$$

$$P_{H_2S}^* = k_{D_{H_2S}} D_{D_{H_2S}} \left(1 + \frac{F_{H_2S} K_{H_2S}}{1 + b_{CO_2} f_{CO_2} + b_{H_2S} f_{H_2S} + b_{CH_4} f_{CH_4}} \right) \qquad \text{C.26}$$

$$P_{H_2S}^* = 1.01 \times 10^{-8} \times \left(1 + \frac{0.233 \times 18.90}{1 + (0.0467 \times 69.82) + (0.265 \times 66.22) + (3.23 \times 10^{-3} \times 228.46)} \right) \times \frac{0.1934}{1 \times 10^{-10}}$$

$$P_{H_2S}^* = 23.35 \text{ Barrer}$$

$$P_{CH_4}^* = k_{D_{CH_4}} D_{D_{CH_4}} \left(1 + \frac{F_{CH_4} K_{CH_4}}{1 + b_{CO_2} f_{CO_2} + b_{H_2S} f_{H_2S} + b_{CH_4} f_{CH_4}} \right) \qquad \text{C.27}$$

$$P_{CH_4}^* = 1.17 \times 10^{-9} \times \left(1 + \frac{0.060 \times 1.01}{1 + (0.0467 \times 69.82) + (0.265 \times 66.22) + (3.23 \times 10^{-3} \times 228.46)} \right) \times \frac{0.1934}{1 \times 10^{-10}}$$

$$P_{CH_4}^* = 2.26 \text{ Barrer}$$

$$r = \frac{P_{CO_2}^*}{P_{H_2S}^*} = \frac{73.32}{23.35} = 3.14$$

$$p = \frac{P_{CO_2}^*}{P_{CH_4}^*} = \frac{73.32}{2.26} = 32.4$$

$$q = \frac{P_{H_2S}^*}{P_{CH_4}^*} = \frac{23.35}{2.26} = 10.3$$

Using these approximations for r, p, and q, the thickness-normalized flux can be

computed as:

$$\frac{n_A l}{\rho D_{AM}} = \frac{\ln\left[\dfrac{1-\left(1+\dfrac{1}{r}+\dfrac{1}{p}\right)w_{A,d}}{1-\left(1+\dfrac{1}{r}+\dfrac{1}{p}\right)w_{A,u}}\right]}{\left(1+\dfrac{1}{r}+\dfrac{1}{p}\right)} \qquad\text{A.21}$$

$$n_{CO_2}l = \frac{1.402\times2.40\times10^{-7}\times\ln\left[\dfrac{1-0}{1-\left(1+\dfrac{1}{3.14}+\dfrac{1}{32.4}\right)\times0.0148}\right]}{\left(1+\dfrac{1}{3.14}+\dfrac{1}{32.4}\right)} = 5.03\times10^{-9}$$

$$\frac{n_B l}{\rho D_{BM}} = \frac{\ln\left[\dfrac{1-\left(1+r+\dfrac{1}{q}\right)w_{B,d}}{1-\left(1+r+\dfrac{1}{q}\right)w_{B,u}}\right]}{\left(1+r+\dfrac{1}{q}\right)} \qquad\text{A.22}$$

$$n_{H_2S}l = \frac{1.402\times1.91\times10^{-8}\times\ln\left[\dfrac{1-0}{1-\left(1+3.14+\dfrac{1}{10.3}\right)\times0.0454}\right]}{\left(1+3.14+\dfrac{1}{10.3}\right)} = 1.35\times10^{-9}$$

$$\frac{n_C l}{\rho D_{CM}} = \frac{\ln\left[\dfrac{1-(p+q+1)w_{C,d}}{1-(p+q+1)w_{C,u}}\right]}{(p+q+1)} \qquad\text{A.23}$$

$$n_{CH_4}l = \frac{1.402 \times 1.49 \times 10^{-8} \times \ln\left[\dfrac{1-0}{1-(1+32.4+10.3)\times 0.0092}\right]}{(1+32.4+10.3)} = 2.46 \times 10^{-10}$$

First approximations of r, p, and q can be checked against the proper expression of these parameters.

$$r = \frac{n_{CO_2}}{n_{H_2S}} = 3.73 \neq 3.14$$

$$p = \frac{n_{CO_2}}{n_{CH_4}} = 20.4 \neq 32.4$$

$$q = \frac{n_{H_2S}}{n_{CH_4}} = 5.49 \neq 10.3$$

Therefore, a trial and error calculation is performed by using these calculated values as new first approximations and by repeating the calculations until values of r, p, and q converge. From the converged values, the bulk flow contributions could be calculated as well as permeabilities and selectivities values as shown in Chapter 6 simulations results.

VITA

Carine Saha Kuete Achoundong

Carine Achoundong was born on August 27, 1986 in Yaoundé, Cameroon. She moved to the United States after graduating from high school in Cameroon to continue higher education. She obtained a Bachelor of Science (BSc) in Chemical Engineering at Georgia Institute of Technology with Highest Honors in December 2007. She worked as a pilot plant process supervisor at Bristol-Myers Squibb for one year. In August 2009, she was admitted in the School of Chemical & Biomolecular Engineering at Georgia Institute of Technology to pursue a doctorate, under the guidance of Dr. William Koros. Carine got married in December 2011 in Cameroon, and she received a Master of Science (MSc) in Chemical & Biomolecular Engineering from Georgia Institute of Technology in May 2012. She will be completing her Doctor of Philosophy degree in December 2013. Upon graduation, Carine will be starting her professional career in the PhD Professional Development Program (PhD PDP) at BASF, The Chemical Company. She is fluent in French, and has traveled to five different continents.